

CLASSIFICATION OF THE X-RAY
SOURCE POPULATION IN THE M 33
FIELD



Dissertation

Der Fakultät für Physik
der Ludwig-Maximilians-Universität München

zur Erlangung des Grades
Doktor der Naturwissenschaften
Dr. rer. nat.
vorgelegt von

Zdenka Misanovic

aus Tuzla, Bosnia and Herzegovina

München, den 16. Dezember 2005

1. Gutachter: Prof. Dr. Ralf Bender
2. Gutachter: PD. Dr. Werner Becker

Tag der mündlichen Prüfung: 13. Jan 2006

Summary

Classification of individual sources of X-ray emission in a galaxy plays a crucial role in understanding its structure, dynamical history and evolution. This dissertation presents the X-ray source population study of the nearest face-on, late-type spiral galaxy M 33, using an XMM-Newton raster survey. I present a total of 447 sources in the M 33 field, including their positions, fluxes in five energy bands, hardness ratios (X-ray colours), flux variability amplitudes, and cross-correlations with optical, infrared and radio data. A classification method was established based, to a great extent, only on the X-ray spectral and temporal characteristics. As objects in M 33 we identified or classified a total of 18 supernova remnants (SNRs) and 20 SNR candidates, 8 X-ray binary (XRB) candidates (only the 2 brightest XRBs in M 33 were known from previous studies), and 12 supersoft source (SSS) candidates, all of which are reported here for the first time. In addition, a total of 15 active galactic nuclei (AGN) and galaxies, and 7 foreground Galactic stars and 30 star candidates were detected in the field of view. A total of 271 sources could only be classified as 'hard', half of which are either XRBs or Crab-like SNRs in M 33, while the other half are, most probably, background objects. The detailed spectral analysis of the brightest objects extends our hardness ratio method, by revealing two basic spectral shapes, and further distinguishing the class of 'hard' sources that we could not separate based on their hardness ratios. We found that the luminosity distribution of the classified SNRs is similar to that of M 31, and slightly steeper than the Large Magelanic Cloud distribution. The sample of the classified XRBs, although small, indicates that the binary population of this late type spiral may be different than that of M 31. We detected a region to the South of the M 33 nucleus with 8 SNRs concentrated very close to each other, which could indicate a region of a recent star-formation episode. There is no pronounced bulge in this late-type spiral galaxy, in agreement with other wavelength studies. As part of this project, optical follow-up observations at the 1.3-m Skinakas telescope in Crete, Greece, confirmed the proposed X-ray classifications of the brightest optical counterparts (one background galaxy and 20 foreground stars). The detailed spectral and temporal properties of one of the brightest X-ray sources in M 33 indicates that the compact object of this system is most probably a black hole. Confirmation of this result would make this object the first detected eclipsing high mass black hole X-ray binary. The presented largest sample of the classified sources in the M 33 field forms a basis for further studies of the X-ray source population of the M 33 galaxy. Deeper X-ray and optical follow up observations are needed to fully explore the properties of the detected objects.

Zusammenfassung

Die Klassifizierung einzelner Röntgenquellen innerhalb einer Galaxie ist entscheidend für das Verständnis ihrer Struktur sowie ihrer früheren und künftigen Entwicklung. In dieser Dissertation werden die Ergebnisse einer auf XMM-Newton - Daten beruhenden Durchmusterung der Röntgenquellen der uns am nächsten stehenden Spiralgalaxie, M 33, zusammengefasst. Für insgesamt 447 Quellen in M 33 werden die Koordinaten, Flüsse (in 5 Energiebändern), “Hardness-Ratios”, Variabilitäten der Flussamplituden sowie Korrelationen mit Daten aus Beobachtungen im Bereich von Radio- bis Infrarotfrequenzen angegeben. Eine Klassifikationsmethode wurde entwickelt, welche im wesentlichen auf den spektralen und zeitlichen Charakteristiken der Röntgenbeobachtungen beruht. In M 33 wurden insgesamt 18 Supernovaüberreste (SNR) und 20 solche Kandidaten, 8 Kandidaten für Röntgendoppelsterne (XRB, davon 6 bislang unbekannte) und 12 mögliche superweiche Quellen, die bislang unbekannt waren, identifiziert oder klassifiziert. Zusätzlich wurden im Sichtfeld von XMM-Newton 15 aktive galaktische Kerne, 7 Vordergrundsterne der Milchstrasse und 30 weitere Sternkandidaten entdeckt. Insgesamt wurden 271 Quellen als “hart” klassifiziert, wovon etwa die Hälfte aus XRBs oder dem Krebsnebel ähnlichen SNR besteht, während die andere Hälfte höchstwahrscheinlich aus Hintergrundobjekten gebildet wird. Die detaillierte Spektralanalyse der hellsten Objekte ermöglichte eine Erweiterung der bekannten “hardness ratio”-Methode durch die Entdeckung von 2 qualitativ verschiedenen Spektren. Dadurch konnten “harte” Quellen genauer klassifiziert werden, als das mit der bisher verfügbaren Methode möglich war. Während die Helligkeitsverteilung der in M 33 klassifizierten SNR der von SNR in der Galaxie M 31 ähnlich ist, ist sie etwas steiler als in der LMC. Obwohl die Zahl der in M 33 klassifizierten XRB relativ klein ist, gibt es Hinweise auf eine deutlich unterschiedliche Population von XRBs in M 33 im Vergleich zu der in der älteren Galaxie M 31. Es wurde ein Gebiet im Süden des Kernes von M 33 entdeckt, in welchem SNR auf sehr engem Raum konzentriert sind. In dieser Region könnte kürzlich eine Episode von Sternentstehungsprozessen stattgefunden haben. In Übereinstimmung mit Studien in anderen Wellenlängenbereichen konnte in M 33 keine ausgeprägte zentrale Aufwölbung gefunden werden. Die im Rahmen dieses Projektes mit dem 1.3-m Skinakas Teleskope auf Kreta durchgeführten Folgebeobachtungen der hellsten optischen Pendants (eine Hintergrundgalaxie und 20 Vordergrundsterne) der Röntgenquellen bestätigten deren vorgeschlagene Klassifikation. Die Spektren und die zeitliche Veränderung einer der hellsten Röntgenquellen in M 33 deuten darauf hin, dass dieses kompakte Objekt sehr wahrscheinlich ein Schwarzes Loch ist. Sollte sich diese Beobachtung bestätigen, so wäre das die erste Beobachtung eines massiven, bedeckungsveränderlichen XRB, welches ein Schwarzes Loch enthält. Die hier vorgestellte bislang grösste Auswahl von klassifizierten Röntgenquellen in M 33 ist die Grundlage für weitere Untersuchungen ihrer Röntgenquellenpopulation. Es sind jedoch tiefer in M 33 hineinreichende Beobachtungen im Röntgen - und optischen Energiebereich erforderlich, um die Eigenschaften der gefundenen Objekte vollständig zu verstehen.

Acknowledgements

I am deeply grateful to many people for their help and support during my PhD. In particular, I would like to thank Professor Günther Hasinger, Dr Wolfgang Pietsch and Dr Frank Haberl for supervising my PhD, and for giving me an opportunity to work in such a fascinating field of astronomy. It has been a great experience to work in the X-ray Group at Max Planck Institut für Extraterrestrische Physik, as part of IMPRS. I would also like to express my gratitude to my LMU affiliated advisor, Professor Ralf Bender.

I am very, very grateful to Günther Hasinger for all his help, support and advice during my PhD. I would especially like to thank him for reading the thesis and for giving me very helpful comments and advice on how to significantly improve it. I also very much appreciate his help in organising the exam in a very short time, and I am also grateful for additional financial support, for sending letters of recommendation for me, and for allowing me to present my work at various conferences and meetings. His invaluable help is very, very much appreciated.

I would also like to thank my project supervisors, Wolfgang Pietsch and Frank Haberl. I am very grateful to them for allowing me to participate in the M33 project, for guiding my research efforts, and for providing constant help and advice. I have benefited so much from their expertise during my PhD. I would also like to thank them for reading the thesis and for helping me to improve it. I am especially thankful to Wolfgang Pietsch for allowing me to include his publications in the thesis, and for reading and checking it many times.

A big thank you goes to Werner Becker, who, although not directly involved in my research project, had always have time for a chat, and who always tried to help and give me useful advice. I am also grateful to him for sending letters of recommendation, and for helping me with so many things.

I would also like to thank my co-authors, Ginevra Trinchieri, Despina Hatzidimitriou and Matthias Ehle. I consider myself very lucky to have had an opportunity to collaborate with them during my PhD, and to learn from them during this time. I am especially thankful to Despina Hatzidimitriou for involving me in the optical follow up observations and for allowing me to include her publication in this dissertation. I would also like to thank her very much for writing and sending letters of recommendation for me. I am also very grateful to Ginevra Trinchieri for critical reading (“pretending to be a referee”), useful comments and practical advice.

I would also like to thank my Thesis Committee members, Vadim Burwitz and Konrad Dennerl, for their help and for attending my Thesis Committee meetings. Also a big thank you to Vadim Burwitz for the help with Chandra data reduction and submissions (in the very last moment) of my proposals.

I am grateful to the Max Planck Society for the IMPRS PhD Fellowship.

It was very nice to share the office with Ulrich Geppert, who I am very grateful for many things. I would like to thank for helpful advice and also for answering many physics questions, and especially for letting me to practice my German. I am also very grateful for a constant supply of vitamins in a form of fresh fruits I would also like to thank him very, very much for translating my thesis abstract.

I would also like to thank Stefanie Komossa for helpful advice, Hermann Brunner for help with SAS problems, and Harald Baumgartner for a lot of disk space and for being always so helpful with my numerous computing problems.

I am also grateful to Birgit Boller and Hans Gschnell for being very helpful with administrative support, and especially Hans Gschnell for his help in dealing with my dental bills.

I am very grateful to George Pavlov for giving me postdoc position, and for waiting a bit longer that I finish my PhD and start working.

I would also like to thank my former supervisor from the University of Sydney, Lawrence Cram, for writing and sending letters of recommendation for me, despite being very busy.

Many thanks to Jens Chluba for the first version of German abstract, and Aga for convincing him to do it. Many thanks to Aga for help in emergency situations, and for being very very helpful. I would also like to thank Luigi Gallo for involving me in his project with ATCA data, and Yas Hashimoto for a short and efficient introduction to IDL.

I would also like to thank all of my friends for really nice time out of work, and also for help and encouragement, when needed. Especially, Alina, Aga, Melanija, Paulo, Thomas, Manami, Yu-ying, Katya, Dorina, Linda, Darren and many others. I would especially like to thank Alina for many things, like fixing my (boring) latex, and providing moral support whenever I needed it, and also for making sure that I always have something to do and never get bored.

I would like to thank my family, especially my aunty Sanja Timosok for being always there for me and just an email away; and also to Dejan and BLP for sending me a lot of jokes to keep me awake during many early-morning hours.

Finally, I am grateful to my parents, Zora and Ivica Misanovic, and my sister Sonja for their unconditional love, support and help during my PhD and throughout my life.

This publication makes use of the USNOFS Image and Catalogue Archive operated by the United States Naval Observatory, Flagstaff Station (<http://www.nofs.navy.mil/data/fchpix/>), of data products from the Two Micron All Sky Survey, which is a joint project of the University of Massachusetts and the Infrared Processing and Analysis Center/California Institute of Technology, funded by the National Aeronautics and Space Administration and the National Science Foundation, of the SIMBAD database, operated at CDS, Strasbourg, France, and of the NASA/IPAC Extragalactic Database (NED) which is operated by the Jet Propulsion Laboratory, California Institute of Technology, under contract with the National Aeronautics and Space Administration. The compressed files of the “Palomar Observatory - Space Telescope Science Institute Digital Sky Survey” of the northern sky, based on scans of the Second Palomar Sky Survey, are copyright (c) 1993-1995 by the California Institute of Technology and are distributed herein by agreement. All Rights Reserved. Produced under Contract No. NAS 5-26555 with the National Aeronautics and Space Administration. The XMM-Newton project is supported by the Bundesministerium für Bildung und Forschung / Deutsches Zentrum für Luft- und Raumfahrt (BMBF/DLR), the Max-Planck Society and the Heidenhain-Stiftung.

Contents

List of Figures	xii
List of Tables	xiii
1 Introduction	1
1.1 X-ray observations of nearby galaxies	1
1.2 Basic concepts of accretion	2
1.2.1 Accretion onto compact objects	2
1.2.2 Accretion disk	4
1.2.3 Comptonisation	4
1.3 Sources of X-ray emission in normal galaxies	5
1.3.1 X-ray binaries (XRBs)	5
1.3.2 Ultra-luminous sources (ULXs)	14
1.3.3 Supersoft sources (SSS)	16
1.3.4 Supernova remnants (SNRs)	18
1.3.5 Diffuse X-ray emission	19
1.3.6 Supermassive black holes in normal galaxies	19
1.4 Background and foreground sources in fields of normal galaxies	20
1.4.1 Active galactic nuclei (AGN)	20
1.4.2 Foreground stars	21
1.5 X-ray source population studies	22
1.5.1 Hardness ratio diagrams	22
1.5.2 The X-ray luminosity function (XLF)	23
1.6 Previous X-ray observations of M 33	24
1.7 The XMM-Newton Observatory	27
1.8 Scope of this dissertation	27
1.8.1 Thesis outline	28
2 XMM-Newton survey of the Local Group galaxy M 33	31
2.1 Introduction	31
2.2 Observations and data analysis	34
2.3 Source catalogue	37
2.4 Images	42
2.5 Cross-correlation with other M 33 X-ray catalogues	42
2.6 Classes of point-like X-ray sources detected in the direction of M 33	48

2.6.1	Foreground stars (fgStar)	51
2.6.2	Galaxies (GAL) and AGN	51
2.6.3	Super-Soft Sources (SSS)	52
2.6.4	Supernova remnants (SNR)	52
2.6.5	X-ray binaries (XRB)	53
2.7	Discussion	54
3	An XMM-Newton survey of the Local Group galaxy M 33 - variability of the detected sources	57
3.1	Introduction	58
3.2	Observations and data reduction	59
3.3	Production of the catalogue	61
3.3.1	Source detection	61
3.3.2	Source positions	62
3.3.3	Hardness ratios, fluxes, and variability factors	63
3.4	Description of the catalogue	65
3.5	Images	67
3.6	Comparison to the PMH2004 catalogue	67
3.7	Cross-correlations with other catalogues	69
3.8	Variability	71
3.9	Classification of the detected sources	73
3.9.1	Foreground stars (fgStar)	74
3.9.2	Galaxies (GAL) and AGN	75
3.9.3	Super-soft sources (SSS)	75
3.9.4	Supernova remnants (SNR)	76
3.9.5	X-ray binaries (XRB)	78
3.9.6	Spatial distribution	79
3.9.7	Luminosity distribution	80
3.10	Summary and conclusion	81
4	XMM-Newton survey of the Local Group galaxy M 33 – bright individual sources	87
4.1	Introduction	87
4.2	Source spectra	88
5	Spectroscopy of the brightest optical counterparts of X-ray sources in the direction of M 31 and M 33	91
5.1	Introduction	91
5.2	Optical Observations	93
5.3	Data Reduction	95
5.4	Spectral Classification	96
5.5	Discussion of results	99
5.5.1	[PFH2005] 464 in M 31 field (USNO1311-0013521)	99
5.5.2	Source south-west of [PMH2004] 3 in M 33 field	99
5.5.3	[PMH2004] 122 in M 33 field	101
5.5.4	[PMH2004] 196 in M 33 field (2MASS01334186+3038491)	101

5.5.5	[PMH2004] 206 in M 33 field (USNO1209-0020969)	102
5.5.6	[PMH2004] 297 in M 33 field (USNO1209-0021478)	103
5.5.7	[PMH2004] 337 in M 33 field (USNO 1204-0021198)	104
5.5.8	[PMH2004] 358 in M 33 field (LEDA 5899)	104
5.6	Summary	105
6	The eclipsing massive X-ray binary M33 X-7: New X-ray observations and optical identification	107
6.1	Introduction	107
6.2	X-ray observations and results	108
6.2.1	Time variability	111
6.2.2	Improved position	114
6.2.3	Energy spectra	115
6.3	Optical observations and results	118
6.3.1	Observations	118
6.3.2	Data reduction and calibration	119
6.3.3	Results	119
6.4	Discussion	121
6.4.1	Improved ephemeris	121
6.4.2	The optical companion	121
6.4.3	M 33 X-7, an eclipsing black hole XRB?	122
6.5	Conclusions	123
7	Conclusions	125
7.1	Results	125
7.2	Future prospects	127
A	Full band images	145
B	Light-curves of the individual sources	153
C	Read-Me file Table 2.3	159
D	Read-Me file Table 3.4	165
E	Read-Me file Table 3.5	171

List of Figures

1.1	The physical components and sites of emission in an XRB	7
1.2	Corbert diagram	9
1.3	Spectral states of black hole binary systems	10
1.4	Hardness ratios of sources detected in a ROSAT survey of M 33	23
1.5	MECS photon spectra of the brightests sources im M 33	26
2.1	XMM-Newton EPIC “PN equivalent” exposure map	35
2.2	Combined XMM-Newton EPIC image of M 33	43
2.3	XMM-Newton EPIC M 33 images	44
2.3	XMM-Newton EPIC M 33 images (continued)	45
2.4	Three-colour XMM-Newton EPIC combined image of M 33	46
2.5	Hardness ratios of sources detected by XMM-Newton EPIC	49
2.6	An optical image of M 33 with the (0.2-2.0) keV band contours	55
3.1	The XMM-Newton EPIC observation fields	59
3.2	The RA and DEC offsets	62
3.3	The RA and DEC offsets with respect to USNO-B1 and 2MASS catalogues	63
3.4	Three-colour image of observation 1c	66
3.5	Histograms of the total positional errors	68
3.6	The maximum and minimum XID fluxes for a sample of SNRs	69
3.7	The long-term X-ray light-curve of an SNR	70
3.8	The maximum and minimum XID fluxes for variable sources	71
3.9	The long-term X-ray light-curve of source #44	72
3.10	The variability factor vs. XID flux and HR1	83
3.11	The regions around sources #44, 41, and 37	84
3.12	Spatial distribution of classified X-ray sources	85
3.13	The cumulative luminosity distribution of SNR	86
3.14	The cumulative luminosity distribution of XRB	86
4.1	Spectra of bright X-ray sources detected in M 33	89
5.1	X-ray positions overlaid on an optical image	95
5.2	Examples of spectra of optical counterparts	96
5.3	Results of cross-correlation between the spectrum of object USNO 1201-0020193 with the standard star spectra	97
5.4	Derived versus standard spectral type	98

5.5	Frequency distribution of spectral types	101
5.6	X-ray properties of the observed sources	102
5.7	X-ray contours of the USNO source 1204-0019500 overlaid on an optical R image	103
5.8	Optical spectrum of the counterpart of PMH2004 196	104
5.9	Hardness ratio of PMH2004 206 as a function of epoch of observation .	105
5.10	Images of the galaxy LEDA 5899 in U and V	106
5.11	Optical spectrum of Galaxy LEDA 5899	106
6.1	<i>Chandra</i> ACIS I light curve and hardness ratio of M 33 X-7	111
6.2	Light curves and hardness ratio of M 33 X-7	112
6.3	Grey-scale XMM-Newton and <i>Chandra</i> images of of M 33 X-7	113
6.4	Light curve of the XRB M 33 X7 folded over the 3.45 d orbital period .	114
6.5	Position of M 33 X-7 shown on a V image of the DIRECT survey . . .	115
6.6	M 33 X-7 spectra	118
A.1	The broad band images of the observations 1(a), 1(b), 1(c), and 15(a) .	146
A.2	The broad band images of the observations 2(a), 14(a), 9(a), and 9(b) .	147
A.3	The broad band images of the observations 8(a), 8(b), 6(c), and 6(b) .	148
A.4	The broad band images of the observations 4(a), 4(b), 12(a), and 12(b)	149
A.5	The broad band images of the observations 5(a), 11(a), 7(a), and 13(a)	150
A.6	The broad band images of the observations 3(a), 3(b), 10(a), and 10(b)	151
B.1	The long-term X-ray light-curves of sources #41 to #113	154
B.2	The long-term X-ray light-curves of sources #124 to #175	155
B.3	The long-term X-ray light-curves of sources #180 to #246	156
B.4	The long-term X-ray light-curves of sources #248 to #321	157

List of Tables

2.1	XMM-Newton M 33 observation log	32
2.2	Count rate to energy conversion factor for different spectral models . .	34
2.3	X-ray source catalogue	38
2.3	X-ray source catalogue - continued	39
2.3	X-ray source catalogue - continued	40
2.4	Cross-correlation with the M 33 ROSAT catalogue	47
2.5	Summary of identifications and classifications	50
3.1	The XMM-Newton M 33 observations	60
3.2	The RA and DEC offsets	64
3.3	Count rate to energy conversion factors	64
5.1	Log and spectral types of the observed stars	94
5.2	X-ray properties of the observed objects	100
6.1	M 33 X-7 XMM-Newton observations	109
6.2	Spectral modeling results for M 33 X-7	116
6.3	Spectral modeling results for the out of eclipse XMM-Newton observations	117
6.4	Optical light curve of the star identified with M 33 X-7	120

Chapter 1

Introduction

1.1 X-ray observations of nearby galaxies

The new generation of X-ray satellites, XMM-Newton (Jansen et al. 2001) and Chandra (Weisskopf et al. 2000), has made significant progress in studies of X-ray emission from external galaxies. The unprecedented spatial and spectral resolution over a broad energy band, combined with large sensitivity and throughput of the instruments on-board XMM-Newton and Chandra, have made it possible to detect and classify a large number of individual X-ray sources in nearest galaxies and beyond (e.g. the first identification of an eclipsing binary outside the Local Group by Pietsch et al. 2003b, or a population of LMXBs resolved in faint elliptical galaxies by Sivakoff et al. (2003)). Detailed spectral and temporal properties of the brightest objects have been determined and compared with Galactic sources (see reviews by Fabbiano & White 2003; Fabbiano 2003). Furthermore, these large uniform samples of particular source classes (e.g X-ray binaries of different types, supernova remnants etc.) in external galaxies have been used to study how their global properties depend on the environment of parent galaxies, in particular on the temperature and distribution of the hot interstellar medium (ISM), which is closely related to the star formation activity (Humphrey et al. 2003; Soria et al. 2005b; Gilfanov et al. 2004). For example, a large number of bright discrete X-ray sources and hot gas have been detected in galaxies and in galactic regions with enhanced star formation (Matsumoto et al. 2001; Soria & Wu 2003; Fabbiano et al. 2003).

In addition to the X-ray source populations also found in our own Galaxy, recent surveys of external galaxies have collected more data about a new class of objects with very high intrinsic luminosities apparently exceeding the Eddington luminosity for a stellar mass compact object (Fabbiano 2004). These sources are generally referred to as ultra-luminous X-ray sources (ULXs), although their nature is still under debate. However, with new XMM-Newton and Chandra observations, the evidence is emerging that at least some of ULXs are normal X-ray binary systems associated with regions of active star formation in galaxies (Soria et al. 2005a). The alternative explanation is that ULXs harbour intermediate black holes with masses of about $10^2 - 10^4 M_{\odot}$ (Colbert & Miller 2003).

Finally, the hot ISM, only marginally detected with previous missions, has been analysed in detail in nearby galaxies (e.g. LMC, M31; Sasaki et al. 2002; Nazé et al. 2004; Trudolyubov et al. 2005).

This dissertation presents detailed X-ray properties of the Local Group spiral galaxy M33, using the XMM-Newton observations made between July 2000 and August 2003. Located at a distance of 795 kpc (van den Bergh 1991) with relatively face-on inclination (56° , Zaritsky et al. 1989), M33 allows a detailed investigation of its X-ray source population and, hence, it has been a target of all previous and present X-ray missions. In addition, an extensive set of M33 observations in optical/UV (Regan & Wilson 1993; Rowe et al. 2005; Thilker et al. 2005), infrared (Hippelein et al. 2003; Hinz et al. 2004), and radio regimes (HI, Newton 1980a) provides a unique opportunity for investigating how the spatial distribution of the X-ray emission within the galaxy correlates with the distribution of stars, and the ISM and dust seen at these other wavelengths. These results for M33 and other nearby galaxies can then be used to establish the relationship between X-ray emission and star formation rate, and to apply it to more distant unresolved galaxies.

Since the brightest objects discussed in this dissertation are accreting binary systems, this chapter will largely focus on the models of accretion, believed to be responsible for most of the X-ray emission from normal galaxies (Fabbiano 1995). The first part summarises the basic concepts of accretion, including the standard accretion disk model and comptonisation. The remaining part introduces the source classes commonly detected in X-ray surveys of nearby galaxies. The observed spectral and temporal properties of these sources are discussed, together with the models which attempt to explain these observational results. Finally, the main results from population studies of various source classes in nearby spiral galaxies are described, with emphasis on how these results can be used to infer the star formation activity. The main results of previous X-ray observations of M33, and comparison to other neighbouring galaxies are also summarised. A short description of the XMM-Newton Observatory and the thesis outline are presented in the end.

1.2 Basic concepts of accretion

Accretion as a source of energy in XRBs, and the accretion disk and various Comptonisation models are presented and discussed in detail by Rybicki & Lightman (1979), Longair (1981), Longair (1994), Frank et al. (2002), and reviewed by Reynolds & Nowak (2003), McClintock & Remillard (2004), and Liedahl & Torres (2005). Based on these works, the most relevant results for this dissertation are briefly summarised in the next three sections.

1.2.1 Accretion onto compact objects

Accretion is defined as the capture of material by the gravitational field of an object, and conversion of its gravitational potential energy into radiation. Since the gravita-

tional potential energy of an accreted mass m is equal:

$$\Delta E_{acc} = GMm/R, \quad (1.1)$$

where M and R are the mass and radius of the accreting object, the efficiency of this process depends on the compactness of the accreting body. For compact objects e.g. neutron stars and black holes, it can be shown that this process can produce an energy of about 10^{20} erg g^{-1} , which is approximately 20 times more efficient than nuclear fusion.

The radiation produced near the surface of the compact object exerts pressure on the accreted mass m , so that the radiation pressure force on each electron-proton pair at the distance r from the accreting object is equal:

$$F_{rad} = \frac{\sigma_T L}{4\pi cr^2}, \quad (1.2)$$

where L is the luminosity of the accreting source, and σ_T is the Thomson cross-section. The formula is derived assuming spherical symmetry and fully ionised hydrogen plasma, and ignoring relativistic corrections for σ_T .

This radiation force, which cannot be greater than gravity for accretion to proceed, sets an upper limit for the accretion luminosity called the *Eddington luminosity*:

$$L_E = \frac{4\pi G m_p c M}{\sigma_T} = 1.3 \times 10^{38} \frac{M}{M_\odot} \text{ erg s}^{-1}, \quad (1.3)$$

where m_p is the proton mass.

Assuming that all of the kinetic energy of the infalling matter is transferred into radiation at the compact object's surface (e.g. a white dwarf or neutron star of a radius R and mass M), then the accretion luminosity is given by:

$$L_{acc} = GM\dot{M}/R, \quad (1.4)$$

where \dot{M} is the accretion rate. Typical values of M and R for white dwarfs and neutron stars, and an accretion rate of $\sim 10^{-10} M_\odot$ per year yield an accretion luminosity of the order of 10^{33} and 10^{36} erg s^{-1} , respectively, which is consistent with the observed values for these systems.

If the accreting object is a black hole with the Schwarzschild radius $R = 2GM/c^2$, since there is no material surface, only a fraction of the infalling mass may be radiated away, while the remaining part could disappear beyond the event horizon, increasing the black hole mass. This is expressed by the accretion efficiency η , so that:

$$L_{acc} = \eta \dot{M} c^2. \quad (1.5)$$

It has been estimated that η is of the order of ~ 0.1 (see next section). This value is similar to the value that can be calculated for a neutron star. For example, from 1.4 and 1.5 it follows that $\eta = GM/Rc^2 = 0.2$, for a typical neutron star mass of $1.4 M_\odot$ and a radius of 10^6 cm (e.g. see Liedahl & Torres 2005).

Assuming that the total accretion luminosity is released over a spherical surface of a radius R as optically thick blackbody radiation, then the blackbody temperature can be calculated as:

$$T_{bb} = (L_{acc}/(4\pi R^2\sigma))^{1/4}, \quad (1.6)$$

where σ is the Stefan-Boltzmann constant. For a typical luminosity value of about 10^{36} erg s⁻¹ the blackbody temperature would be $\sim 10^7$ K, or $kT \sim 1$ keV, which implies that the energy will be radiated mainly in the X-ray band.

1.2.2 Accretion disk

When a star in a binary system evolves and fills completely its *Roche lobe*, part of its mass can be accreted onto the other (compact) star via *Roche lobe overflow*. Since the stars are in a relative orbiting motion, the accreted mass will have an angular momentum and hence, it will go into Keplerian orbit and form a geometrically thin disk around the accreting object. The accreted mass will lose angular momentum through viscosity, probably due to magneto-hydrodynamical turbulence (e.g. Balbus & Hawley 1998), and will flow inwards approaching the compact object.

An analytical model of disk accretion was derived by Shakura & Sunayev (1973), assuming that the dissipated energy is radiated locally as blackbody emission with the temperature:

$$T_{bb}(r) = \left[\frac{3GM\dot{M}}{8\pi\sigma r^3} (1 - \sqrt{R/r}) \right]^{1/4}, \quad (1.7)$$

where R is the radius of the compact star (or the radius of the innermost stable circular orbit $r_{in} = 6GM/c^2$, in the case of a non-rotating black hole). The total disk luminosity is approximated to be $L = GM\dot{M}/(2R)$, as the outer disk radius $R_{outer} \rightarrow \infty$. For a non-rotating black hole the last two equations yield $L \approx 0.1\dot{M}c^2$. If the source radiates at a constant fraction of its Eddington luminosity, from (1.7) follows:

$$T_{bb}(x) \sim M^{-1/4}, \quad (1.8)$$

for the scaled radius $x = r/R$.

1.2.3 Comptonisation

Comptonisation in astrophysics refers usually to the inverse Compton scattering i.e. the average gain of energy by photons scattered off energetic electrons in hot ionised plasma.

When a photon encounters an electron at rest, the energy of the incident photon after the scattering process is given by:

$$E' = \frac{E}{1 + \frac{E}{m_e c^2}(1 - \cos\theta)}, \quad (1.9)$$

where θ is the scattering angle and $E = h\nu$ is the initial photon energy.

The scattering electrons in hot ionised plasma have a Maxwellian velocity distribution i.e. $kT_e/m_e c^2 \ll 1$, where T_e is the electron temperature. Assuming this non-relativistic case, and averaging over all scattering angles, the average relative photon energy change can be calculated as:

$$\frac{\Delta E}{E} = \frac{4kT_e - E}{m_e c^2}. \quad (1.10)$$

If the scattering electrons are energetic ($4kT_e > E$, e.g. see equation 4.40 in Longair 1981), the incident photons will on average gain energy in this process. The resulting Comptonised spectrum will have a power law shape with an exponential cutoff determined by the electron temperature T_e and by the optical depth of the Comptonising plasma. The increase of the electron temperature and/or the optical depth will produce a harder spectrum.

1.3 Sources of X-ray emission in normal galaxies

The X-ray emission of the Local Group galaxies is dominated by bright discrete sources, mostly X-ray binaries (XRBs) and supernova remnants (SNRs) (Fabbiano 1989). Both classes of objects are endpoints of stellar evolution. However their X-ray spectra and light-curves are quite different, reflecting the different physical processes giving rise to their X-ray emission.

Comprising the brightest class of X-ray sources in external galaxies, XRBs alone span a huge range of observed luminosities and spectral shapes, including a class of highly luminous ULXs. Another distinct class of accreting binary systems are objects called super-soft sources (SSS) named after their extremely soft X-ray spectra.

Finally, there are two additional components of X-ray emission in normal galaxies: diffuse X-ray emission from a hot gas, and possible weak activity from central supermassive black holes, if present.

1.3.1 X-ray binaries (XRBs)

An X-ray binary (XRB) consists of a compact object which accretes material from its companion star. Depending on the mass of the companion, XRBs are divided into high-mass (HMXB), accreting from an O or B giant star; and low-mass X-ray binaries (LMXB), with a main sequence star of $\sim M_\odot$ as a donor (White 1989). The compact object is a remnant of a relatively massive star, at the endpoint of its stellar evolution, and can be either a neutron star or a black hole¹. The observations of about 300 well-known XRBs in our own Galaxy (catalogued by e.g. van Paradijs & McClintock 1995; Liu et al. 2000, 2001) show that, depending on the nature of the compact object, the companion star, and the accretion geometry, XRBs show a broad range of the observed X-ray properties, including their total luminosity range, spectral

¹The compact object in an X-ray binary system can also be a white dwarf but, in that case, accretion is often not the main source of the X-ray emission (see Sect. 1.3.3).

shapes and temporal behaviour. Moreover, XRBs belong to a class of highly variable sources, often displaying significant spectral and flux variability on time scales from milliseconds to years (Hasinger & van der Klis 1989; van der Klis 2004)

The source of emitted energy in all binary systems is the same: conversion of gravitational potential energy into radiation, as mass from the companion star is transferred onto the compact object by accretion (Shklovsky 1967; Shapiro & Teukolsky 1983; Frank et al. 1992). The efficiency of this process depends on the accretion mass rate \dot{M} , and on the compactness of the accreting object, and is proportional to $M\dot{M}/R$, where M and R are the mass and radius of the compact object, respectively (Liedahl & Torres 2005). Hence, for a typical neutron star or a stellar mass black hole, the accretion rates of approximately $10^{-10} M_{\odot}$ per year are already capable of producing the observed luminosities.

Mass transfer mechanism

Although in both HMXBs and LMXBs the accretion onto the compact object is responsible for most of their X-ray emission, it is the nature of the companion star that largely determines the mass transfer mechanism and the geometry of the accretion flow. The mass transfer mechanism in HMXBs is believed to be, in most cases, the stellar wind capture via spherical accretion (Davidson & Ostriker 1972). The produced X-ray emission propagates through the stellar wind and can sometimes be significantly absorbed (White et al. 1995). A simple model of a spherically symmetrical wind capture by a neutron star predicts already the values found by observations, although for a black hole as a compact object, the spherical accretion must be replaced by a disk accretion model to account for the observed luminosities (Liedahl & Torres 2005).

Disk accretion models (Pringle & Rees 1972; Shakura & Sunyaev 1973; Novikov et al. 1973; Li et al. 2005) are also used to describe X-ray emission in LMXBs, which is illustrated in Fig. 1.1 (see also Sect. 1.2 for more details). The mass transfer of LMXBs is dominated by the Roche lobe overflow, when matter from the donor star reaches the inner Lagrangian point and falls onto the compact object. Since the inflowing matter has a high specific angular momentum, due to the relative motion of the stars, it does not strike the compact object directly but goes into a Keplerian orbit, and forms a geometrically thin accretion disk around the compact object. As already discussed in Sect. 1.2 the standard disk model (Shakura & Sunyaev 1973) explains the spreading of the disk by viscosity. The dissipated energy is emitted locally as thermal radiation at all disk radii, resulting in a relatively cold ($kT \sim 1$ keV) accretion flow. When an evolved star expands and fills the Roche lobe, a constant overflow of material can be supplied to power a highly luminous X-ray source. In contrast to HMXBs, the disk itself radiates significant part of the energy. For example, if a compact object is a neutron star then approximately half of the energy comes from the disk, while the other half emerges from the boundary layer between the accretion disk and the surface of the neutron star (Psaltis 2004).

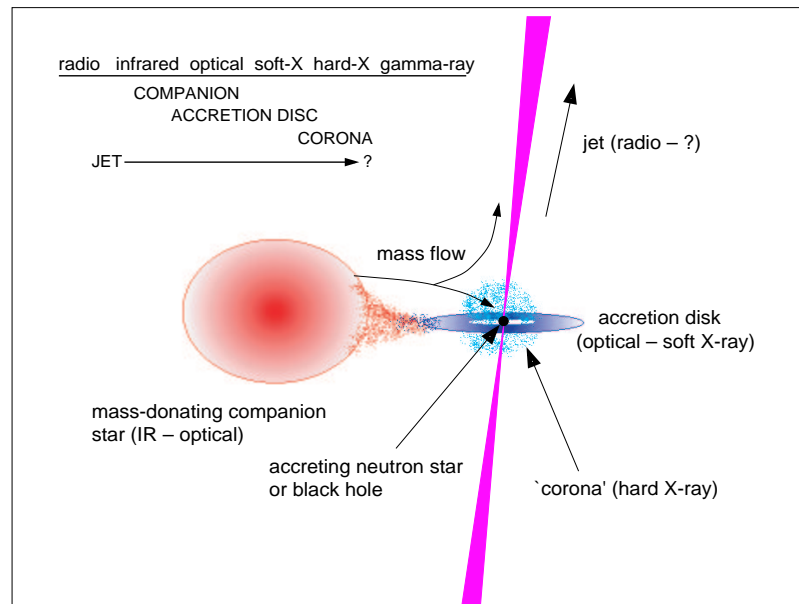


Figure 1.1: Current basic understanding of the physical components and sites of emission in an X-ray binary system. In this example, the companion loses mass to the compact object through Roche lobe overflow. The accreting matter forms a disk, which can be thought of as a series of annular rings in quasi-Keplerian orbits, whose radii decrease under the action of stresses between neighboring annuli. Energy is released, giving rise to X-ray emission at small radii. Hard X-ray emission impinges on the optically thick disk, which “reflects” a fraction of the incident flux, with spectral imprinting in the form of lines, absorption, and deformed continuum. A fraction of the accretion energy is redirected into kinetic energy, giving rise to the jets. A hot corona surrounds the disk at small radii, which can affect the reflection spectrum through Compton scattering. From Fender & Maccarone (2004).

Accreting X-ray pulsars

The emission region and properties of the accretion flow in an XRB system are determined by the nature of the compact object, and in particular, by the strength of its magnetic field. For example, an accreting neutron star with a strong magnetic field will collimate the accreting flow along the field lines, and the accreted mass will fall onto the magnetic polar caps. The accreted energy will be released as X-rays in a shock near, or at the neutron star surface (Pringle & Rees 1972; Davidson & Ostriker 1972; Trümper 1986). As the neutron star spins, this X-ray emission will be changing its direction with respect to the line of sight² and will be observed as pulsations (Wang & Welter 1981). This type of XRBs are classified as the accreting X-ray pulsars, and their pulsation periods can be of the order of typically a few hundred seconds (*slow pulsars* mostly encountered in HMXBs, see e.g. Haberl & Pietsch 2005), or a millisecond (*millisecond pulsars* found in XRBs with short orbital periods, Becker & Trümper

²This will happen only if the rotational and magnetic axes are not aligned.

1999). However, not all spinning neutron stars with strong magnetic fields will be observed as pulsars, as the accretion flow may obscure the view of the magnetic poles, depending on the relative orientation of the spinning and magnetic axes (Psaltis 2004).

Magnetic field lines can transfer angular momentum either to the accreting material or to the neutron star, depending on their relative orbiting velocities, which results in a spin-down or spin-up, respectively. It has been suggested that the long duration of accretion in LMXBs can spin-up the pulsar up to millisecond periods and several such objects have been detected (Chakrabarty & Morgan 1998).

The relationship between the spin and orbital period of slow pulsars is still not well understood, although it seems that it is connected to the mass transfer mechanism, in some way (Waters & van Kerkwijk 1989). For instance, no correlation is found between the spin and orbital periods for stellar wind powered pulsars, while the Roche lobe overflow systems have these two periods strongly anti-correlated. On the other hand, the pulsation periods of Be X-ray binary systems are well correlated with their orbital periods as shown in Fig. 1.2 (Bildsten et al. 1997).

The shortest observed spin periods of millisecond pulsars (see e.g. Becker 2001) are longer than the minimum periods allowed by their equation of state, suggesting that either the equation of state should be modified, or that there is some mechanism which reduces the spin. As one possibility, Bildsten (1998) suggests that rapidly spinning neutron stars lose their spin angular momenta via emission of gravitational radiation.

If the neutron star spin frequency is larger than the orbital frequency of the accretion flow, the centrifugal force will be too strong for material to be accreted. It is assumed, in that case, that material will eventually escape the neutron star as a wind (the propeller effect, Illarionov & Sunyaev 1975).

If the neutron star magnetic field is too weak, it will not be able to channel the accreting flow. For such weakly magnetised neutron stars the X-ray emission originates from the accretion disk, and also from the boundary layer between the accretion disk and the neutron star (Mitsuda et al. 1984), or from the neutron star surface - if the disk touches the neutron star (White et al. 1995).

Black hole binaries

Black hole binaries (BHBs) are observed in five distinct spectral/temporal states which are believed to be related to different accretion conditions (Fig. 1.3): the high³/soft state, dominated by thermal emission from the accretion disk and a weak steep power law component; the low/hard state, with non-thermal power law emission exhibiting rapid variability; and the very high and intermediate states, with similar spectral shapes including both, the power law with a much steeper slope and the thermal disk component. Finally, the quiescent state is characterised by very faint, power law dominated emission. At lower mass accretion rates a BHB is in the low/hard or quiescent state, when its spectrum is dominated by a hard, power law component with a photon index of ~ 1.4 – 1.8 (e.g. McClintock & Remillard 2004).

³The terms *high* and *low* in the state nomenclature refer to the luminosity in the ~ 0.2 – 10 keV band, corresponding to the energy range limit of the first X-ray detectors.

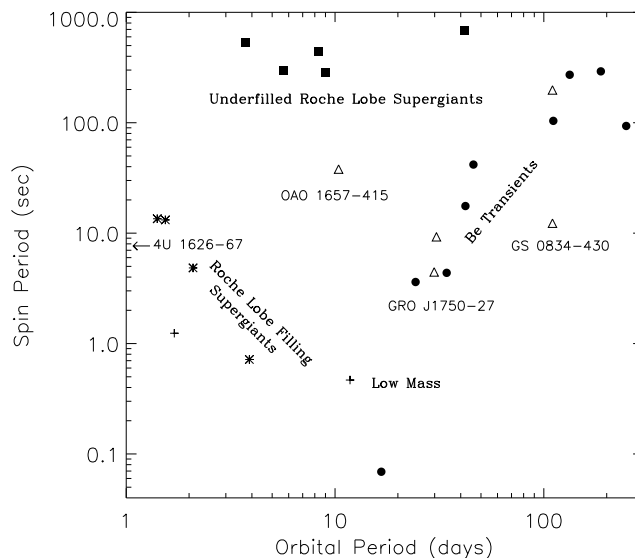


Figure 1.2: The spin period of accreting neutron stars versus binary period (Corbet diagram). The different symbols refer to the type of binary the neutron star resides in. Asterisks are supergiant companions which are Roche-Lobe filling, squares are supergiant companions that underfill their Roche lobe, circles are confirmed Be transient binaries, and crosses are those with low mass ($< 2M_{\odot}$) companions (Her X-1, GRO J1744-28, 4U 1626-67). Triangles refer to sources for which there are no optical companions yet identified, though orbits have been measured (GS 0834-430, OAO 1657-415 and GRO J1750-27). From Bildsten et al. (1997).

This non-thermal component is usually assumed to be due to the Comptonization of soft disk photons by hot electrons in a surrounding corona (Haardt & Maraschi 1991; Dove et al. 1997; Zdziarski 2000; Nowak et al. 2002). The corona is also thought to be the source of the powerful jets and outflows observed at radio frequencies (Merloni & Fabian 2002). In all corona models, the temperature of the hot coronal plasma is about 100–300 keV and the optical depth is assumed to be less than 1, but the physical properties, origin and geometry of the corona are different in each model, or not entirely explained.

An advection dominated accretion flow (ADAF) model has also been proposed to account for the observed spectral properties and quiescent states (Narayan 1996; Quataert & Narayan 1999). According to this model the disk does not extend to the last innermost circular orbit, but is truncated at some larger radius, while the interior is filled with a hot ADAF, which does not radiate the dissipated energy so efficiently as the disk does. Hence, most of the potential energy is not radiated away but it is rather advected towards the compact object.

The ADAF model has been used together with the disk accretion and corona in an attempt to unify the observed states (Esin et al. 1997). The observed properties in the five distinct states are explained by the geometry of the accretion flow. In the very high and high/soft states the accretion rate is high and dominated by the soft

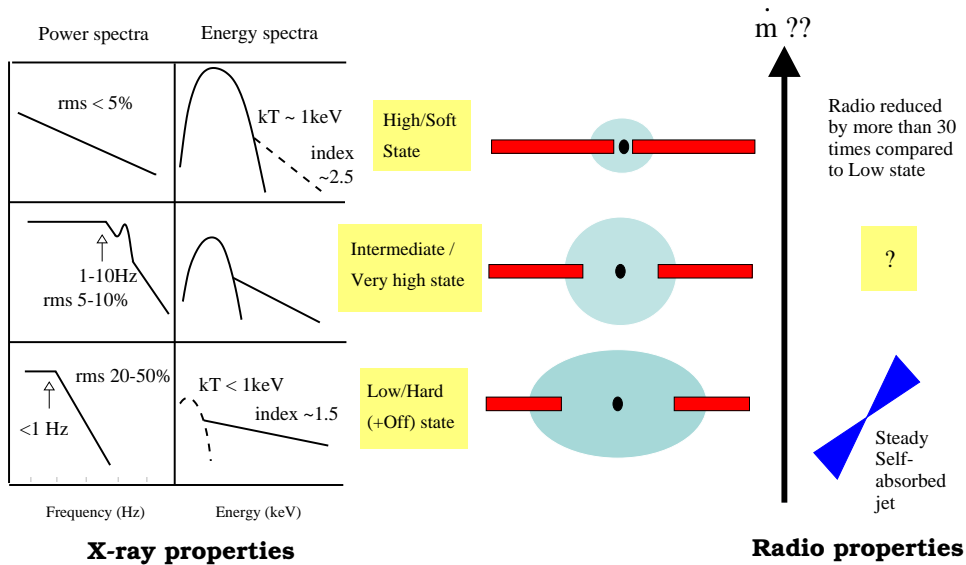


Figure 1.3: Black hole binary spectral states, as classified by their X-ray spectral and timing properties. A rough physical interpretation, based on the X-ray data alone, is indicated, as is the relation to radio emission. Black hole binary transients typically, although not exclusively, transit from undetectable levels to the soft state in a short period of time. The relation of states to mass accretion rate, previously thought to be quite clear, is now less certain. From Fender (2002).

disk component, because the disk extends down to the innermost stable circular orbit. As the disk moves further away, the ADAF becomes more dominant, and the BHB evolves to the low/hard and quiescent state.

However, this unified model does not explain the hard power law component extending up to several hundred keV, observed in the very high state of many BHBs (McClintock & Remillard 2004). The radio emission, strong flares and low-frequency quasi-periodic oscillation observed in many BHBs, are also not accounted for in this simple model, and hence other models have been proposed. At present, however, no single model can explain all complex spectral and timing properties of BHBs in all five states (McClintock & Remillard 2004).

Models representing the X-ray spectra

Many models have been developed to fit spectra of different types of XRBs. In general, most HMXBs can be fitted by a single component power law model with an exponential cutoff, while the spectral shapes of LMXBs are more complex, requiring typically two components – a thermal component for the disk emission, and a hard, non-thermal component, believed to originate from an ADAF or an accretion disk

corona. The hard component can be approximated to first order by a power law, and various Comptonisation models with different assumptions and corona geometries have been put forward to explain it. Some of these models assume that the thermal disk component provides seed photons for Comptonisation (e.g. Gierliński et al. 1999; Zdziarski 2001; Zdziarski & Gierliński 2004), while others are not constrained i.e the seed photons originate from an unspecified source.

There are several models which can be used to approximate the thermal emission from an optically thick accretion disk in black hole LMXBs (Shakura & Sunyaev 1973; Mitsuda et al. 1984; Stella & Rosner 1984; Makishima et al. 1986). The multicolour disk black body model (the *diskbb* model in XSPEC), a simple non-relativistic approximation of the standard disk model of Shakura & Sunyaev (1973), has been proposed by Mitsuda et al. (1984). In this model the disk temperature varies from a low value at the outer edge, to the maximum value T_{in} at the inner edge of the disk with the radius R_{in} . All gravitational potential energy of the accreted mass is released locally as black body radiation with the effective temperature $T(r)$, depending on the disk radius r as $T(r) \sim r^{-0.75}$ (see Sect. 1.2, equation 1.7). Hence, the observed spectrum is composed of multiple black body spectra with temperatures $T(r)$. The model normalisation parameter is given by $R_{in}^2 \cos\theta/d^2$, where θ is the inclination angle of the disk and d is the distance to the source. The R_{in} is usually assumed to be the radius of the innermost stable circular orbit (approximately three times the Schwarzschild radius $r_g = 2GM/c^2$ for non-rotating black holes, where M is the mass of the compact object⁴). However, detailed calculations suggest that several corrections need to be applied when using this model, in order to derive more realistic physical parameters. For example, the model needs to be corrected for a weak Comptonisation in the inner region of the disk, the difference between the intrinsic and apparent radii of the peak temperature, and relativistic effects (see e.g. Kubota 1998).

Spectra of weakly magnetised neutron star LMXBs are also well fitted with the multicolour disk model, as expected, since neutron star LMXBs and black hole systems have accretion disks of a similar structure (Tanaka & Lewin 1995). Observations have shown however, that neutron star binaries have systematically lower normalizations by a factor of $\sim 3-4$, implying that the masses of the neutron stars in these systems are lower by approximately the same factor than the masses of black holes (Mitsuda et al. 1984; Ebisawa et al. 1991). The measured temperatures kT_{in} for the black hole systems are less than ~ 1.3 keV, while the luminous neutron star LMXBs show slightly higher values of about 1.5 keV. This is consistent with the the lower masses of neutron stars, since T_{in} scales with the compact object mass as $T_{in} \sim M^{-0.25}$ (Tanaka & Lewin 1995, see also Sect. 1.2). In addition to the disk component, neutron star LMXBs sometimes require an additional soft black body component with a temperature of ~ 2 keV, interpreted as emission from the neutron star surface (Mitsuda et al. 1984).

Although the multicolour disk model is a simple approximation of the soft disk emission, it has been used successfully to determine the characteristic inner disk radius and temperature from the observed X-ray spectra, other models have also been

⁴For magnetised neutron stars R_{in} may represent the Alfvén radius, hence it could be larger than $3r_g$.

proposed. For example, Sunyaev & Titarchuk (1980) showed that the observed soft spectra of LMXBs can be approximated equally well by an unsaturated Comptonisation model, when low-energy photons are injected into a high-temperature plasma of a particular electron temperature T_e . The X-ray flux is proportional to the rate of the injected photons, although the source of the low-energy photons cannot be explained with this model.

However, these simple single-component models do not provide adequate fits for LMXB spectra, as they require an additional power law component with a photon index of 2.0–2.5 to approximate the hard-energy tail, and in some cases, an iron line at ~ 6.4 keV and disk reflection (e.g. Tanaka 1991; Ebisawa et al. 1991). Both of these additional spectral features are explained by the irradiation of relatively cold gas in the accretion disk near the central compact object. The fluorescent Fe $K\alpha$ line is observed as a prominent feature in many sources, due to relatively high abundance of iron as the end point of thermonuclear fusion, and also as a result of its high K fluorescence yield (e.g. see review by Fabian et al. 2000).

Spectra of neutron star HMXBs are hard and can be fitted by a power law model with a photon index of < 1 , up to a high energy cutoff at 10–20 keV (White et al. 1983b; Nagase 1989). A few LMXB pulsars have softer spectra in the 1–20 keV range (White et al. 1983b), while some show significantly steeper spectra, with a photon index of ~ 2 (White et al. 1983b; Koyama et al. 1991). The most plausible physical interpretation of these spectra is unsaturated Comptonisation of soft seed photons in a hot fully ionised medium (Eardley et al. 1975), most probably, in the accretion columns above the magnetic polar caps (Meszaros 1992). If the neutron star in an HMXB has a strong magnetic field, cyclotron lines may also be present in the X-ray spectra, mostly at higher energies. High-resolution XMM-Newton and Chandra spectra of HMXBs often show an additional soft thermal component from the ionized stellar wind, which is sometimes resolved into emission lines (e.g. Vela X-1, Schulz et al. 2002).

Although these various simple models have been used to approximate spectra of many XRBs providing deeper insights about global properties of accretion flows around neutron stars and black holes, they are still not detailed enough to infer all physical mechanisms responsible for the observed continuum radiation. For instance, various physical mechanisms can produce similar spectral shapes, especially in a relatively narrow energy band (e.g. Vacca et al. 1987), and it is not possible to distinguish these physical processes based on the spectral data alone. Hence, attempts have been made to include the temporal behaviour during different spectral states in the models, to better constrain the model parameters. For example, Lamb & Miller (1995) and Psaltis et al. (1995) have developed a physically self-consistent model, describing spectral properties and QSOs for disk accretion onto weakly magnetised stars. According to this model, the electron cyclotron emission in the magnetosphere is responsible for producing soft seed photons, which are then Comptonized within the magnetosphere, or in a hot corona that forms around the magnetosphere.

Flux variability of XRBs

XRBs belong to the most variable X-ray sources, changing their intrinsic or apparent X-ray flux by many orders of magnitude, sometimes on time scales as short as milliseconds to years. The flux variations can be periodic or aperiodic, and are sometimes accompanied by significant spectral variability tracing out coherent patterns (Hasinger & van der Klis 1989). Apart from pulsations (with periods of several milliseconds to more than two hours (e.g. Skinner et al. 1982; Koyama et al. 1990) from rotating neutron stars with strong magnetic fields, the orbital motion of the stars can cause apparent periodic variability like eclipsing, when the companion star blocks the X-ray emission in the line of sights partially or almost completely. Orbital motion can also cause smooth periodic modulations and periodic dips to be observed (see review by White et al. 1995, and references therein). The LMXB orbital periods range from less than one hour (e.g. X1820-303 with a 0.19h period, Stella et al. 1987), to several days (Cir X-1 with a 398h period, Kaluziński et al. 1976). The orbital periods of high mass systems are longer, from several hours (e.g. 0.2 days for Cyg X-3, Sanford et al. 1974) up to several months (Hen 715, 187.5 days, Watson et al. 1981, see also Fig. 1.2).

Neutron star XRBs exhibit another aperiodic variability observed as an isolated flux increase, with a short rise time of ~ 1 sec or less, and a decay with a distinct spectral softening lasting up to several minutes (Lewin et al. 1993, and references therein). These X-ray bursts are believed to be caused by thermonuclear burning when a sufficient amount of hot, compressed material is accreted onto the neutron star surface (type-I bursts, observed only in LMXBs), or by instabilities in the accretion disk (type-II bursts). The X-ray bursts show a large variety of profiles depending on photon energy, with much shorter decays at lower energies (Strohmayer & Bildsten 2003).

Lower luminosity ($< 10^{37}$ erg s $^{-1}$), stellar-wind-driven HMXBs sometimes show absorption variability, which is due to the non-symmetric or unstable stellar winds (Haberl & White 1990), or sometimes by the inhomogeneities in the wind (White et al. 1983a). Haberl et al. (1989) suggest that these inhomogeneities might be caused by the disruption of the wind by the X-ray source.

Most of black hole LMXBs, and also many neutron star low-mass binary systems show a transient behaviour (X-ray novae), when they change their X-ray flux by a factor of $10^3 - 10^4$, exhibiting repeated periodic or irregular outbursts on time scales of less than one month to tens of years or more (Priedhorsky & Holt 1987; Bradt et al. 2000; Tanaka & Lewin 1995). There are two models interpreting these transient outbursts as being caused by thermal disk instabilities (e.g. Lasota 2001; Dubus et al. 2001), or by irradiation-induced instabilities (e.g. King 1995). According to the disk instability model, during the quiescent phase almost all mass is accumulated at the outer edges of the accretion disk, with only a small amount of material accreted by the compact object. At such large radii the disk temperatures can be as low as $\sim 10^4$ K, which can cause a thermal disk instability, due to anomalous opacity related to the ionisation of hydrogen. The instability of the disk triggers the accumulated mass to move towards the compact object, increasing the accretion rate. As a result

an X-ray nova outburst is observed. The second model explains the increase of the mass transfers rate by the expansion of the atmosphere of the companion star due to the X-ray heating.

Finally, quasi-periodic oscillations (QPOs) or flickering, observed in the power density spectra of all types of XRBs, is rapid aperiodic variability caused by the irregularities in the inner accretion disk (see review by van der Klis 2004). QPOs at high frequencies (40-450 Hz) in BHBs are believed to originate from the region very near the event horizon.

Optical and radio counterparts of XRBs

Although XRBs are detected as bright X-ray sources, the observations at other wavelengths are crucial not only for their classification (LMXB or HMXB), but also for determining many of their important properties. For example, from the optical spectroscopy of the companion star and the determination of the Doppler shifts in the line emission, the orbital velocities and mass functions of many systems are measured (Orosz et al. 2002). In addition, detailed optical studies of XRBs provide valuable information about the temperatures, ionisation fractions and abundances of accretion disks.

Radio emission in the form of collimated outflows of matter ejected at relativistic speeds, or jets has been detected from several Galactic XRBs (Fender et al. 1999, see also Fig. 1.1 for sites of emission at various wavelengths). Because of their similarity to quasars, these sources were dubbed ‘micro-quasars’ (Mirabel & Rodriguez 1998).

1.3.2 Ultra-luminous sources (ULXs)

Ultra-luminous sources (ULXs) are usually defined as non-nuclear point sources in external galaxies, with luminosities of $\sim 10^{39} - 10^{40}$ erg s⁻¹, i.e greatly exceeding the Eddington luminosity for a spherically accreting stellar mass compact object. Ever since their discovery with the *Einstein* Observatory (Fabbiano & Trinchieri 1987), the unusual properties of these extremely luminous sources made them a subject of intense studies with all X-ray missions, including ROSAT (Roberts & Warwick 2000; Colbert & Mushotzky 1999; Colbert & Ptak 2002), ASCA (Makishima et al. 2000), and in the last several years also XMM-Newton (Miller et al. 2003; Strohmayer & Mushotzky 2003), and *Chandra* (Miller & Colbert 2004). However, despite the large amount of accumulated data, the nature of these extraordinary sources remains controversial. A conclusion that could be reached so far, from observations of many such sources, is that the sample of detected ULXs might be heterogeneous.

The first suggestion about the nature of ULXs was that they are young luminous SNRs (Fabbiano 1989), but although similarly luminous SNRs were detected and identified (Bregman & Pildis 1992; Fabian & Terlevich 1996; Immler et al. 1998), it was soon recognised that most ULXs exhibit X-ray flux variability (La Parola et al. 2001; Matsumoto & Tsuru 2001; Kaaret et al. 2001) and have many other properties that are reminiscent of accreting binary systems. However, if these accreting systems contain

a stellar mass compact object, then their apparent luminosities greatly exceeds the Eddington limit for isotropic emission.

The most intriguing idea put forward to explain the observed high luminosities of ULXs is that they represent a new class of accreting black holes with masses in the range of $10^2 - 10^4 M_\odot$ (Fabbiano 1989; Colbert & Mushotzky 1999; Kaaret et al. 2001). The proposed masses would make the observed luminosities of these systems consistent with the Eddington limit. The existence of these *intermediate mass black holes (IMBHs)* would be of great relevance, as they would provide the missing link between already established stellar mass (in accreting black hole binaries), and super-massive black holes, believed to power AGN.

The observational evidence supporting the hypothesis that at least some of the most luminous ULXs ($> 10^{40}$ erg s $^{-1}$) are IMBHs includes their X-ray spectra revealing a cool ($T_{in} = 0.1 - 0.2$ keV) accretion disk component⁵, implying very massive black holes of $\sim 1000 M_\odot$ in these systems (Swartz 2002; Miller et al. 2003; Roberts & Colbert 2003). In addition, the observed power density spectra and frequency breaks are consistent with IMBHs rather than stellar mass black holes (Colbert & Miller 2003). For example, Strohmayer & Mushotzky (2003), have detected a 54 mHz QPO from the most luminous ULX in M 82 ($\sim 10^{40}$ erg s $^{-1}$) suggesting a compact object of $\sim 100 - 10000 M_\odot$. The detection of a broad Fe K line in the XMM-Newton spectrum of this source further supports this scenario, since very few XRBs show significant iron line emission.

Although indirect evidence for the existence of IMBHs is intriguing, it is still not entirely clear how to explain their origin. Because of their spatial coincidence with globular clusters, Miller & Hamilton (2002), suggest that IMBHs could be formed in dense old globular clusters, while Portegies Zwart et al. (2004) and Gürkan et al. (2004) propose a merger of stellar objects in young dense stellar cluster cores. However, *Chandra* observations of the Antennae galaxies and comparison with HST data show that the ULXs are displaced from star-forming stellar clusters (Zezas & Fabbiano 2002). Soria et al. (2005a) argue that nuclear star clusters in late-type spirals may offer another natural environment for formation of IMBHs, while Madau & Rees (2001) suggest that they may be the remnants of primordial Population III stars.

However, most ULXs display spectral shapes and have other properties in common with stellar mass black hole systems (Kubota et al. 2001). For example, already ASCA observations of several ULXs in nearby galaxies (Makishima et al. 2000) showed that they have typical XRB spectra, including an accretion disk with characteristic temperatures of ~ 1 keV and a hard power law tail, implying that their compact objects have stellar size masses. Furthermore, super-Eddington luminosities have also been observed from neutron star and stellar mass black hole systems in our Galaxy (McClintock & Remillard 2003, and references therein) further supporting this idea, and several models have been suggested to explain the observed super-Eddington luminosities of these objects. King et al. (2001); King (2002) propose that ULXs are XRBs with geometrically beamed radiation during a short evolutionary stage characterised by high mass accretion. However, optical observations have identified emission

⁵ $kT_{in} \sim 1.2 keV (M/10 M_\odot)^{1/4}$ (Makishima et al. 2000), see also Sect. 1.2 for details.

nebulae with some ULXs (e.g Holmberg II; Pakull & Mirioni 2001; Lehmann et al. 2005), which excludes the strong beaming model, at least for these sources. Mirabel & Rodríguez (2000) and Koerding et al. (2001) suggest that ULXs are extragalactic counterparts of microquasars, i.e. their apparent super-Eddington luminosity is due to the relativistic jet emission pointing along the line-of-sight, while Begelman (2002) argues that a thin super-Eddington accretion disk may be responsible for such high luminosities.

Observations with XMM-Newton and Chandra have revealed a large number of ULXs in external galaxies providing an opportunity to study detailed properties of these sources and constrain their nature. In addition, with these large samples it is now also possible to investigate their population properties, and in particular, the connection with the host galaxy type and local environments of ULXs, which provides further insight into the nature of X-ray emission from these objects. For example, a relatively large number of ULXs has been found in regions of current star formation in starburst galaxies Tennant et al. (2001); Zezas & Fabbiano (2002); Roberts et al. (2002); Zezas et al. (2003); Swartz et al. (2003), which implies their association with a young stellar population. In addition, Grimm et al. (2003) finds no apparent deviation from the power law in the universal luminosity function of star-forming galaxies, which is consistent with the assumption that ULXs are not exceptional sources, but a stage in XRB evolution. However, a small ULX fraction, detected in elliptical and S0 galaxies, suggests their connection with much older stellar population (Angelini et al. 2001; Irwin et al. 2003).

ULXs remain an important theme in studies of normal galaxies, as more data are needed to explain their X-ray emission and origin. The observational evidence so far seems to suggest that less luminous ULXs are probably young XRBs with beamed emission during a short stage in their evolution. However, very luminous systems (above 10^{40}) cannot easily fit into this picture, and are more likely to be IMBHs.

1.3.3 Supersoft sources (SSS)

Luminous supersoft X-ray sources (SSSs) were recognised as a new source class by Trümper et al. (1991, see also Greiner et al. (1991); Hasinger (1994)), following their first observations with ROSAT. Although SSSs were originally detected with *Einstein* (e.g. CAL 83 and CAL 87 in LMC by Long et al. 1981b, also in SMC two SSSs by Seward & Mitchell (1981)), their extremely soft emission could be clearly distinguished from other soft sources (e.g. stellar coronae) only with the softer energy response and higher spectral resolution of the ROSAT satellite. Supersoft sources belong to the source populations much better studied in nearby galaxies, since only a few of the nearby objects could be detected in the Milky Way. This is due to their extremely soft emission that is largely absorbed by interstellar medium. Large samples of SSSs have been detected in nearby galaxies like LMC (Greiner et al. 1994; Cowley et al. 1996), SMC (Wang & Wu 1992; Orío et al. 1994), M 31 (Greiner et al. 1996), M 33 (Haberl & Pietsch 2001). A large number of SSSs have been catalogued (Hasinger 1994; Kahabka & Trümper 1996; Greiner 2000). It has been estimated (Rappaport

et al. 1994) that around 1000 of these sources populate large spiral galaxies like the Milky Way or M 31, representing a major distinct class of accreting binary systems. This is recently being confirmed by deep XMM-Newton and *Chandra* observations (Di Stefano & Kong 2003, 2004; Greiner et al. 2004; Pietsch et al. 2005a).

The spectra of SSSs are extremely soft and can be approximated by blackbody models with temperatures of $\sim 20 - 80$ eV (on average $20 - 40$ eV), which corresponds to effective blackbody temperatures of $10^5 - 10^6$ K. The observed luminosities of SSSs are in the range $10^{36} - 10^{38}$ erg s $^{-1}$, which means that most of them are intrinsically luminous objects approaching the Eddington luminosity limit.

Supersoft sources are a highly variable source class, probably more variable than any other class of XRBs (Greiner et al. 2004). In a systematic survey of SSSs in M 31 using ROSAT, XMM-Newton and Chandra data, Greiner et al. (2004) and Di Stefano et al. (2004) find that about 30% of the detected SSSs are transients or recurrent transients on a time scale of several months. Greiner et al. suggest that most of these SSSs are accreting binary white dwarf systems, and explain their rapid variability by photospheric expansion and contraction of the white dwarf envelope. Pietsch et al. (2005a) also find that many optical novae in M 31 and M 33 appear as SSSs in less than one year or several years after the optical outburst. In one of the SSSs in M 31, Osborne et al. (2001) detect a 865-s periodicity, most probably the spin period of a white dwarf (King et al. 2002).

The observed spectral properties and timing behaviour of most SSSs are consistent with a white dwarf binary system model. According to the model, an SSS consists of a white dwarf as a compact object and a more massive ($\sim 1.3 - 3.0 M_{\odot}$) donor star, supplying the mass for accretion at a rate of $\sim 10^{-7} M_{\odot}$ per year. This mass is accreted onto the white dwarf's surface where X-rays are produced by nuclear burning (see review by Kahabka & van den Heuvel 1997; Greiner 2000). This model was proposed after realising that an estimated radius⁶ of the compact object of the observed SSS systems would be in the range of 5000–10000 km, i.e. a typical white dwarf radius. However, if the source of energy of SSSs would be the accretion as in neutron star and black hole binary systems, a huge amount of the accreted mass ($> 2 \times 10^{-6} M_{\odot}$) would be required to produce the observed luminosities. Moreover, the inflowing matter would be optically thick, for such large accretion rates, and the soft emission could not be radiated away. As a solution, van den Heuvel et al. (1992) have suggested that the source of energy is nuclear burning on a white dwarf's surface, which is approximately 30 times more efficient (see Sect. 1.2 for details). This would reduce the required accretion rate to $\sim 10^{-7} M_{\odot}$ per year, and account for the observed luminosities and soft spectra of SSSs. Various models (Nomoto et al. 1979; Livio 1994; Di Stefano & Rappaport 1995) predict that, for a limited mass transfer range of $\sim 1 - 4 \times 10^{-7} M_{\odot}$ per year, nuclear burning on the solar mass white dwarf is steady, producing a soft luminous X-ray source. However, for lower accretion rates ($\sim 10^{-8} M_{\odot}$ per year), the accreted matter will burn in flashes, producing a typical nova or cataclysmic variable (CV).

⁶The radius is estimated from the observed luminosities and effective temperatures using Stefan-Boltzman's law.

1.3.4 Supernova remnants (SNRs)

In addition to XRBs, supernova remnants (SNRs) represent the second major class of discrete X-ray sources detected in normal galaxies. X-ray emission from SNRs in our Galaxy has been extensively studied, providing details about the interaction of high velocity ejecta with the ISM and circumstellar material (CSM) (e.g. Aschenbach 2002), and in some cases, the identification of the central neutron star and its associated synchrotron nebula (e.g. Slane 2000, see also review by Becker & Pavlov (2001)). However, despite large amount of data about individual objects (see Galactic SNR catalogue, Green 2004), the population studies of Galactic SNRs have been limited due to high interstellar absorption and high level of confusion, which results in incomplete SNR samples. For example, despite many searches (e.g. Misanovic et al. 2002), very young and very old populations of Galactic SNRs are underrepresented in the current SNR catalogues. Furthermore, the distance estimates for Galactic SNRs are not reliable, which makes their comparison difficult.

The nearest external face-on galaxies, in contrast, reveal a large number of SNRs at approximately the same distance, so that it is possible to derive complete samples. These samples can be used to study their luminosity and spatial distribution, which determines the structure of the ISM. For example, since the heated interiors of SNRs are the source of most of the hot gas phase of the ISM, the fraction of the hot gas depends directly on the frequency and distribution of SNRs. In addition, the metal enrichment and distribution of cavities produced by the SNR expansion, are closely related to the SNR population. Hence, large surveys have been undertaken, using XMM-Newton and Chandra, to study SNRs in normal galaxies (Sasaki et al. 2002; Ghavamian et al. 2005).

The thermal X-ray emission from SNRs arises when a shock wave, after the supernova explosion, heats the surrounding CSM and ISM. In this process, most of the initial kinetic energy is radiated as thermal X-rays. The expansion of the shock wave and the emission from the SNR are strongly influenced by the density and distribution of the surrounding CSM and ISM (Lozinskaya 1992). The X-ray plasma is produced in the shocked environment and in the interface between hot and cold gas. The thermal X-ray continuum emission is produced by Bremsstrahlung (free-free radiation), when high speed electrons are decelerated in close encounters with ions.

X-ray line emission is also produced in SNR shocks, and it is dominated, in particular by iron lines Raymond & Smith (1977); Gaetz & Salpeter (1983). Due to low density and corresponding long average collision time, non-equilibrium ionisation (NEI) conditions are expected in the X-ray plasma, producing characteristic spectral lines that arise from inner-shell excitation and ionisation (Hughes 1998).

Recently, thermal X-ray emission has been detected from point-like sources in central regions of several SNRs (Pavlov et al. 2004). The X-ray spectra of these sources can be described as blackbody emission with temperatures of 0.2-0.5 keV, and they show no pulsations. Pavlov et al. (2004) suggest that these sources are, most probably neutron stars born in supernova explosions, similar to pulsars, but with weak magnetic fields.

In addition to the thermal X-ray emission, particularly rapid shocks may generate non-thermal X-rays in some SNRs (e.g. first detected in SN1006 by Koyama et al. 1995). Relativistic electrons, accelerated at the shock front, produce synchrotron emission when they interact with the compressed magnetic field (Kardashev 1962; Shklovskii 1976). For sufficiently high relativistic electron speeds (e.g. with energies close to the knee in the electron spectrum of cosmic rays i.e. 1000 TeV), the produced synchrotron radiation is observed in X-rays. TeV observations Tanimori et al. (1998) have confirmed the existence of such high velocity electrons in SNRs. This also confirms the hypothesis that the cosmic rays are accelerated by supernova shocks. If the SNR contains a pulsar then additional synchrotron radiation is produced. In this case, the relativistic electrons, which are accelerated by pulsar magnetic dipole radiation, interact with the magnetic field to produce synchrotron emission. This type of SNRs are referred to as *plerions*, while the SNRs whose emission is dominated by thermal processes are known as *shell remnants* (Lozinskaya 1992).

Most SNRs are bright radio sources at most stages of their evolution. The radio emission of SNRs is non-thermal, and it is produced by the same process as non-thermal X-rays, although less energetic electrons are required to generate radio emission. Optical IR and UV spectra of SNRs are dominated by line emission, which is produced by collisional excitation and ionisation of atomic species, due to the increased density and temperature of the shocked material. This is reflected in characteristic line strengths and line ratios, which are used as a diagnostic tool in SNR classification.

The observed X-ray spectra of shell SNRs are characterised as 'soft' in comparison to e.g. the spectra of XRBs, and they are usually modelled by various plasma models (Raymond & Smith, NEI). If non-thermal X-rays are produced as well, the spectra can be approximated by additional power law components (Duric 2000a).

1.3.5 Diffuse X-ray emission

A very hot gas ($10^6 - 10^7$ K) is the source of diffuse X-ray emission detected in many spiral galaxies. This hot gas component, mainly associated with the spiral arms and disks, is most probably produced and heated in supernova explosions and stellar winds (Trudolyubov et al. 2005).

The hot ISM component, probably produced by large-scale outflows in form of galactic super-winds, has also been observed in halos of starburst galaxies (e.g. Pietsch et al. 2000).

1.3.6 Supermassive black holes in normal galaxies

Many late-type spiral galaxies with pronounced bulges have been found to contain central black holes, with masses which correlate with the velocity dispersion of the bulge (Bender et al. 2005). The best studied example is an accreting super-massive black hole in the Galactic Centre (Schödel et al. 2002), which shows weak activity detected as rapid flares in X-rays (Baganoff et al. 2001; Porquet et al. 2003) and infrared (Eckart et al. 2004). A possible detection of X-ray emission from the central

supermassive black hole in M 31 has also been recently reported by Garcia et al. (2004). However, no such massive black holes are detected in bulgeless galaxies like M 33 (Gebhardt et al. 2001).

1.4 Background and foreground sources in fields of normal galaxies

Finally, in face-on, sufficiently resolved, nearby galaxies like M 33, a significant fraction of the observed sources, in the field of view, are also foreground (Galactic stars) and background objects (AGN). A small contribution in the soft band may come from galaxy groups and clusters.

1.4.1 Active galactic nuclei (AGN)

A significant fraction of the X-ray sources detected in surveys of nearby normal galaxies does not belong to the host galaxy, but has clear extragalactic origin. As demonstrated by the recent deepest available surveys of the X-ray background, the majority of these extragalactic sources belong to a class of active galactic nuclei (AGN), Mushotzky et al. 2000; Hasinger et al. 2001; Brandt & Hasinger 2005), believed to be powered by an accretion of the gas and dust onto a supermassive black hole (Peterson 1997).

AGN are highly luminous sources, with their luminosities emanating from a small spatially unresolved galactic core, sometimes exceeding 10^{46} erg s⁻¹. This small emitting region is implied by the X-ray flux variability on time scales as short as several minutes (to years), observed in many AGN. However, the degree of the AGN variability is less than that of XRBs, and large flux variations on short time scales are observed only in a small fraction of AGN (Boller et al. 2003; Gallo et al. 2004). Based on their optical line widths (Osterbrock 1998) and absorption values, AGN are divided into two basic types: type-1 AGN (unabsorbed sources showing broad emission lines) and type-2 AGN (absorbed sources with narrow emission lines). However, according to the unification scheme proposed by Antonucci (1993), these two AGN types are intrinsically similar, with their observed differences being due to the different viewing directions.

The physical mechanism for producing X-ray emission emerging from AGN is believed to be essentially the same as for XRBs, the main difference being the mass of the compact object. Many orders of magnitude more massive black holes ($\sim 10^6$ – 10^9 M_⊙), residing at cores of host AGN galaxies, accrete galactic matter through an accretion disk. According to the standard AGN model, the disk is surrounded by an extended dusty molecular torus and a corona populated by hot electrons. These corona electrons are believed to Comptonise the UV photons⁷ emerging from the disk, producing the observed hard X-ray continuum in AGN. As for XRBs, there are various models try-

⁷The AGN disk emission is expected to peak in the UV band, since according to the standard accretion disk model $T_{bb} \sim M^{-1/4}$. See also Sect. 1.2(eq. 1.8) for details.

ing to explain the origin and geometry of the corona (e.g. Meyer & Meyer-Hofmeister 1994).

The observed AGN X-ray spectrum in the 0.2–10 keV energy range can be approximated by a simple power-law model, with the photon index Γ in the range 1.5–2.0. Mushotzky (e.g. 1984). The additional spectral components (e.g. the iron line, Compton hump, soft excess and etc.) that are sometimes observed, are believed to be due to the effects of reflection and reprocessing of the underlying power law emission in the optically thick accretion disk. The most prominent spectral feature, an Fe K_α line emission at 6.4–6.7 keV, has an equivalent width in the range 100–300 eV (in type-1 AGN), or up to 1 keV in type-2 AGN (Pounds et al. 1990). Sensitive observations have revealed relativistically broadened Fe line profiles in bright nearby AGN, believed to be due to gravitational redshift and other effects in the vicinity of the black hole event horizon (Tanaka 1995). Similar Fe K_α line shapes have been observed in the combined spectra of the most distant AGN (Streblyanska et al. 2005), confirming the standard AGN model.

In contrast to the deep surveys, where AGN constitute up to 90% of the total number of detected sources, AGN detected in significantly shorter observations of nearby galaxies are mostly bright, nearby ($z < 1$) objects. The total number of detected background AGN in the field of view can be inferred from the flux distribution of the X-ray background sources (Hasinger et al. 2005).

1.4.2 Foreground stars

Although not initially predicted, the first imaging X-ray observations with the *Einstein* Observatory have shown that normal stars emit X-rays (Vaiana et al. 1981; Pakull 1981). X-ray emission has been detected from many late-type, as well as from hot OB stars (see review by Schmitt 2000). Hence, X-ray surveys of nearby galaxies also reveal a significant fraction of Galactic normal stars, seen as relatively soft X-ray sources homogeneously distributed across the field of view.

The X-ray emission from late-type (spectral types F, G, K and M) stars is interpreted as coronal activity, similar to that observed in the Sun, but on a much larger scale in some stars. For example, many M-type stars show significant coronal activity and strong flares. In addition, the fraction of the observed X-ray emission in late-type stars is found to be correlated with the rotational period (Schmitt 2000). There is also a strong correlation between relatively strong X-ray and $H\alpha$ emission, which is also an indicator of strong coronal activity (Fleming et al. 1989). According to the current understanding, the X-ray emission in the stellar coronae is produced by plasma heated by the interaction of the convective layers with magnetic fields in the star's outer convection zone (e.g. Haisch et al. 1991). Two temperature components are usually required to model the X-ray emission from the stellar coronae. X-ray variability on time scales of several hours, caused by flaring, has been observed in the most active stellar coronae. Flaring coronae may also require additional spectral temperature components (e.g. Güdel et al. 2001a).

Relatively soft X-ray emission is also observed from hot stars (Harnden et al. 1979),

which do not have an outer convection zone. It has been suggested that X-ray emission from hot OB stars is produced by heating due to hydrodynamic shocks caused by instabilities in strong stellar winds emerging from such stars (Feldmeier et al. 1997). The X-ray spectra can also be described by two temperature models with additional absorption by warm wind (Corcoran et al. 1994).

X-ray emission has been detected from A-type stars as well, although it is not clear which mechanism is responsible for producing it, since A-type stars do not have strong stellar winds. In some cases, X-ray emission from A stars is due to their late-type companions (e.g. Stelzer & Burwitz 2003).

1.5 X-ray source population studies

Although Galactic observations provide much more detail about individual sources, due to their proximity, the study of population properties of different source classes is, to a great extent, only possible in external galaxies. As already discussed for SNRs (see Sect. 1.3.4), population studies in our Galaxy are limited because of the uncertainties in the distance measurements and, hence, non-accurate flux determination. Furthermore, due to the large extinction in the Galactic plane, the samples of the detected and classified Galactic sources are incomplete. The Local Group and nearby galaxies, on the other hand, provide large uniform samples (complete or nearly complete, down to a limiting flux) of XRBs, SNRs and other source classes at approximately the same distance, so that it is possible to conduct statistical studies of source populations i.e. their spatial and luminosity distribution. These studies in a wide range of different environments, for instance in galaxies of different types, or in different galactic components (bulge, disk, spiral arms), are needed to establish the relationship between the X-ray properties and the galactic structure and star formation activity. The results can then be applied to distant galaxies as well, to probe star formation at high redshift (Soria 2003).

In statistical studies of nearby galaxies in X-rays, two methods are often used: hardness ratios, or colour-colour diagrams, and luminosity functions.

1.5.1 Hardness ratio diagrams

In addition to using X-ray flux and spectral variability and cross-correlation with source counterparts at other wavelengths, hardness ratio or X-ray colour diagrams have also been an efficient tool to distinguish between different source classes. The unique spectral shape of each class of objects determines their positions in the hardness ratio diagram, so that a large number of sources can be classified. The advantage of this method is that it can also be used when only a limited number of photons are detected. However, the hardness ratio diagrams must be calibrated for each instrument separately, and the results obtained with different detectors cannot be directly compared.

X-ray colour diagrams have been widely used (e.g. Haberl & Pietsch 2001; Prestwich et al. 2003). Fig. 1.4 shows an example of a hardness ratio diagram used to

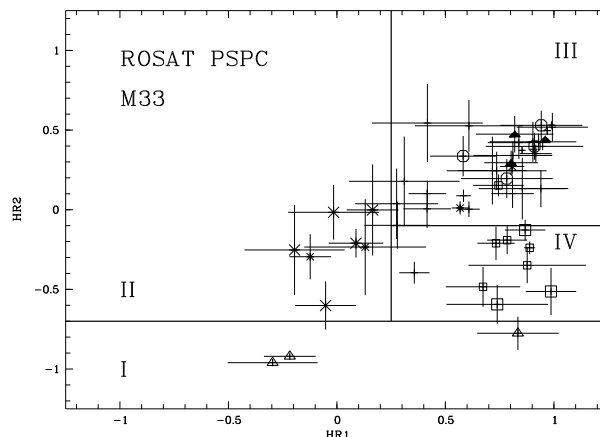


Figure 1.4: Hardness ratios of sources detected by the PSPC. Shown are only values with errors smaller than 0.3 on both HR1 and HR2. In part I of the parameter space candidates for SSSs (triangles), in II foreground stars (x), and in IV SNRs (squares) are found. Part III mainly contains XRBs (filled triangles) and AGN (circles) but can also include some foreground stars and SNRs. Small symbols indicate X-ray sources with likely counterpart found from spatial correlations, which is supported in most cases by the hardness ratio criteria (only for foreground stars and SNRs). Large symbols mark the candidates classified from hardness ratios only. (from Haberl & Pietsch 2001).

classify X-ray sources in a ROSAT survey of M33 by Haberl & Pietsch 2001. They and others have developed this method for classifying the SMC and LMC sources, and have used it successfully to distinguish SSSs, SNRs and foreground stars from intrinsically hard sources like XRBs and AGN. However, as the figure shows, XRBs and AGN occupy the same region in the diagram and, hence, could not be separated.

1.5.2 The X-ray luminosity function (XLF)

The cumulative X-ray luminosity function (XLF) is defined as the number of sources $N > L_X$ (usually normalised per unit area) with luminosities greater than L_X . The XLF provides information about the formation, evolution and physical properties of the X-ray source population (Fabbiano & White 2003). The XLFs are fitted either by single or broken power laws. A broken power law luminosity distribution indicates some change in the X-ray source population.

Recent sensitive, high-resolution observations of nearby galaxies have revealed large populations of X-ray sources, so that it has been possible to derive XLFs for relatively large number of galaxies, and even for different galactic components. These observations have shown that the power law normalisation, slope and break in the XLFs of XRBs are indicative of the star-formation history (Soria & Wu 2002). Wu (2001) suggests that a simple birth-death model of XRBs can explain these observed XLF shapes. For example, Wu (2001) shows that an unbroken power law distribution of XRBs can be derived assuming on-going star formation, while a break in the XLF is

a signature of a starburst episode in the recent past.

The shape of the XLF also indicates the star-formation rate, since the XLF slopes are found to be significantly flatter for galaxies with vigorous star formation activity (e.g. Matsumoto et al. 2001; Zezas & Fabbiano 2002). A recent survey of 32 nearby galaxies observed with Chandra confirms these results. Colbert et al. (2003) find a cumulative slope of ~ 1.4 for elliptical galaxies characterised by quiescent star-formation activity, while the slopes of actively star-forming spirals are in the range ~ 0.6 – 0.8 . In addition, Grimm et al. (2002) suggest that the power law normalisation (i.e. the total number of XRBs) is correlated either with the star-formation rate or with the total mass of the galaxy.

The observed power law slopes of the XLF of spiral galaxies are broadly in agreement with the results obtained for our own Galaxy. However, the Galactic XLF studies consider different XRB populations, so that XLFs have been derived for HMXBs and LMXBs separately. Grimm et al. (2003) find that HMXBs have a power law cumulative luminosity distribution with a slope of ~ 0.6 , which is universal i.e. applies to all star-forming galaxies. They also suggest that the power law normalisation is proportional to the star-formation rate, while Gilfanov (2004) suggests that the total number of LMXBs is correlated with the total galactic mass. This result is expected since HMXBs are younger systems distributed in galactic disks, with lifetimes of $\sim 10^5$ – 10^7 yr, determined by the fast evolution of their massive companions. Hence, they can be used to trace star formation activity. In contrast, the lifetimes of LMXBs ($\sim 10^7$ – 10^9 yr) are much longer, since they are determined by the mass-transfer process. This old stellar population is found in galactic bulges and globular clusters.

To make similar detailed studies in external galaxies, larger samples and an efficient method for separating HMXBs and LMXBs are needed. However, some limited studies have been done for the nearest galaxies. For example, XLFs of M 31 are different for the bulge and disk regions, consistent with the different XRB populations in these regions (Kong et al. 2003). Similar differences have also been observed in M 81 (Tennant et al. 2001).

1.6 Previous X-ray observations of M 33

M 33 has been surveyed with all X-ray observatories and belongs to the galaxies best studied in X-rays. The observations with the *Einstein* X-ray Observatory (Long et al. 1981a; Markert & Rallis 1983; Trinchieri et al. 1988b) have revealed 17 discrete sources and some diffuse emission in the spiral arms near the nucleus. In a systematic study of variability in M 33 using *Einstein* data, Peres et al. (1989) have found two sources exhibiting significant variability: the nuclear source X–8, and the eclipsing binary X–7.

A total of 57 sources have been detected in ROSAT HRI and PSPC observations (Schulman & Bregman 1995; Long et al. 1996). Combining all ROSAT data, Haberl & Pietsch (2001) have compiled the most complete catalogue of M 33, which contains 184 sources down to a limiting luminosity of $\sim 10^{36}$ erg s $^{-1}$, and also the classification of the brightest objects. In this survey Haberl & Pietsch have developed a method for source classification based on their X-ray properties (hardness ratio), and also on

the identification with optical and radio counterparts. A total of 7 SSS candidates, and 16 SNRs and SNR candidates have been classified in M 33, and also 4 foreground stars and 5 star candidates, and 5 AGN candidates, in the field of view. In addition, by comparing the luminosity distribution of the detected SNRs in M 33 and the LMC Haberl & Pietsch (2001) have suggested that M 33 has relatively lower metallicity.

M 33 has also been observed by ASCA (Takano & Mitsuda 1994) and BeppoSAX (Parmar et al. 2001). Figure 1.5 shows the BeppoSAX spectra of the brightest sources in the field of M 33, showing either thermal (fitted by bremsstrahlung models) or non-thermal (power law) spectral shapes, although the BeppoSAX spectral resolution and a limited soft band response had made it difficult to discriminate between these models.

M 33 X-7

The variable X-ray source M 33 X-7 has been detected in *Einstein* and ROSAT observations (Long et al. 1981a; Markert & Rallis 1983; Trinchieri et al. 1988a,b). Peres et al. (1989) has suggested that the source is an eclipsing HMXB with a period of 1.78 d, which was later confirmed by Schulman et al. (1993, 1994) using ROSAT data. However, Larson & Schulman (1997) and Dubus et al. (1999) have proposed a 3.45-d orbital period with gradual ingress (0.1 in phase), eclipse duration (0.2), and eclipse egress (0.01). In addition, Dubus et al. (1999) have found indications for possible 0.31-s pulsations, suggesting that the source is a neutron star HMXB similar to e.g. SMC X-1.

M 33 X-8

The source M 33 X-8 is the most luminous source in the Local Group ($\sim 10^{39}$ erg s $^{-1}$) and the nearest ULX. Hence, detailed spectral and timing properties of this source have been studied with all X-ray missions. High spatial resolution Chandra observations have confirmed that the position of X-8 coincides with the optical nucleus of M 33 (Dubus et al. 2004). However, the low-activity AGN interpretation was rejected since the measured velocity dispersion did not support it (Gebhardt et al. 2001, see also Sect. 1.3). In addition, Dubus et al. (1997) have detected a small amplitude flux modulation (20%) with a period of 106 days, consistent with an XRB interpretation. Recently Foschini et al. (2004) have analysed an XMM-Newton spectrum of X-8 (using one of the observations from the raster survey analysed in this dissertation), and have found that the best-fitting model is a multicolour disk plus a hard blackbody component. From the model parameters Foschini et al. (2004) propose that the source is a stellar mass black hole XRB in a very high state, and estimate the black hole mass to be in the range 6–12 M_{\odot} . They also suggest that the observed super-Eddington luminosity is most probably due to orientation effects in the accretion disk.

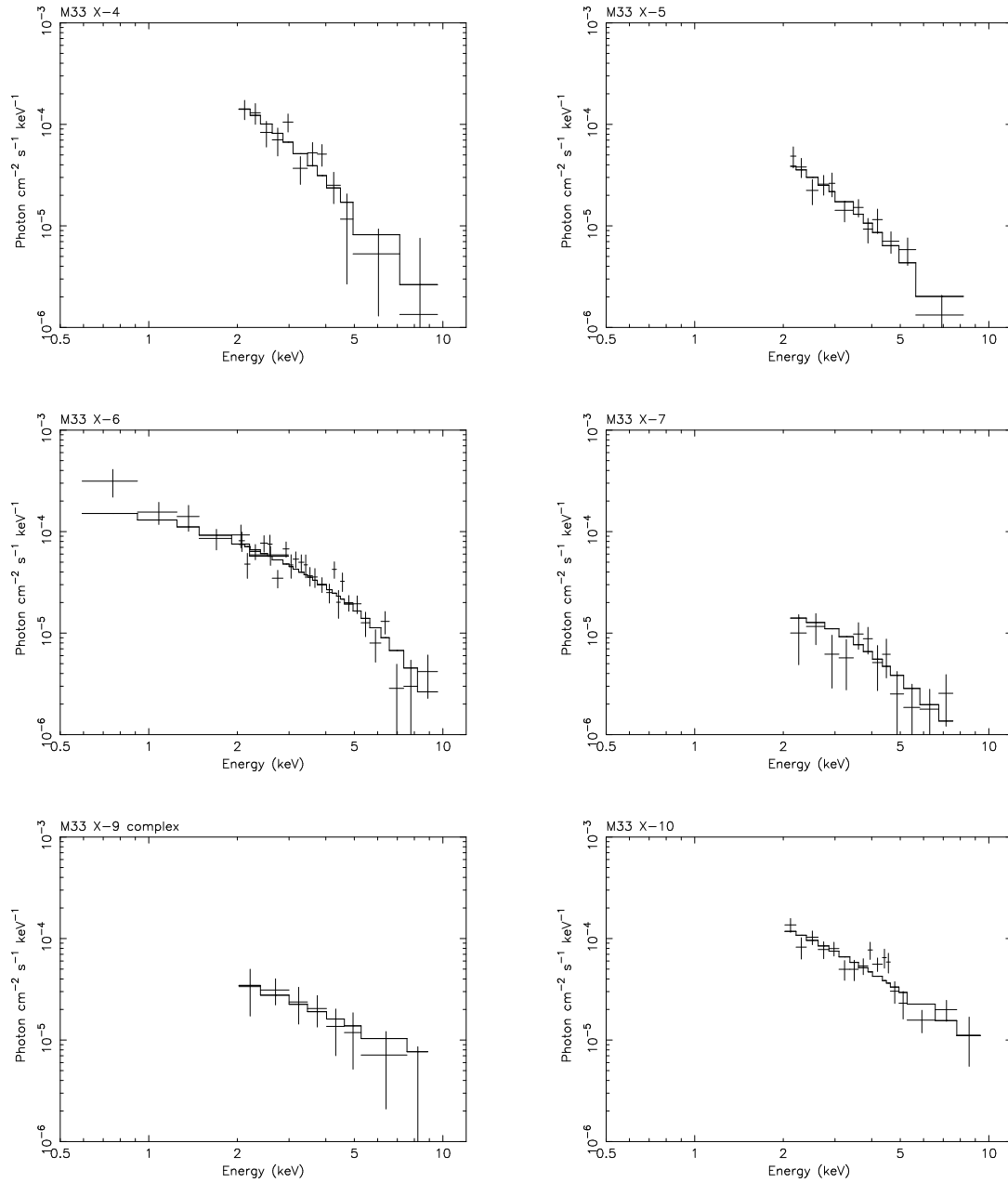


Figure 1.5: MECS photon spectra of the point sources detected in the M33 galaxy deconvolved using an absorbed power-law model except M33 X-6 where the LECS spectrum is included and an absorbed disk-blackbody model is used. Data from all 3 observations are included, except for M33 X-4 where the 1998 August observation is excluded. The plots all have the same extrema to aid comparison (from Parmar et al. 2001).

1.7 The XMM-Newton Observatory

The XMM-Newton Observatory (Jansen et al. 2001) consists of three co-aligned highly nested grazing incidence X-ray telescopes, which focus in-coming X-ray photons onto three detectors of the European Photon Imaging Camera (EPIC), and two Reflection Grating Spectrometers (RGS; den Herder et al. 2001). In addition, there is an optical/UV instrument (the Optical Monitor - OM, Mason et al. 2001) on board XMM-Newton, which can be operated simultaneously with the X-ray detectors. One of the X-ray telescopes focuses all X-rays onto a single spectroscopic imaging camera called EPIC-pn (Strüder et al. 2001), while each of the other two telescopes is equipped with a MOS imaging detector (EPIC-MOS, Turner et al. 2001) and a diffraction grating (RGS). The EPIC cameras can be operated in several science modes. The imaging modes include the 'full frame' (all pixels of all CCDs are read out), and 'partial window' mode (which reads out only part of the CCD chip). In the timing mode, with much better time resolution (0.007 s for the pn burst mode), photons are collected only in one dimension along the column axis. The EPIC-pn CCD detector has a pixel size of 4.1" and a time resolution of 73.4 ms in the full frame imaging mode. The pixel size of the EPIC-MOS CCD detectors is 1.1" with a time resolution of 2.6 seconds, in the full frame imaging mode. Both detectors cover a field of view of approximately 30 arcmin.

The main characteristics of XMM-Newton are (XMM-Newton user's handbook):

- High sensitivity

A total effective area of 4650 cm² at 1.5 keV makes XMM-Newton the most sensitive focusing X-ray telescope to date. The EPIC detectors are sensitive to photons in the 0.2–12 keV energy range, and can detect X-ray sources down to $\sim 10^{-15}$ erg s⁻¹ in a few tens of kilo-seconds.

- Good angular resolution

The on-axis point-spread function is of the order of 6" (FWHM) and varies little over a wide energy range of 0.1–4 keV. The half energy width (HEW), at which 50% of the total energy is encircled, is of the order of 15".

- moderate and high spectral resolution

The EPIC cameras have a moderate spectral resolution $\Delta E/E \sim 20 - 50$, while the RGS spectrometers have a much higher resolving power of 200–800.

1.8 Scope of this dissertation

This dissertation presents classifications and X-ray properties of discrete sources detected in a raster X-ray survey of the Local Group late-type spiral galaxy M 33. The survey consists of 24 overlapping observations carried out between August 2000 and July 2003 with the XMM-Newton Observatory, covering the full D_{25} area of M 33. A

complete census of the X-ray source population in M 33 is presented down to a limiting luminosity of $\sim 10^{35}$ erg s⁻¹ (ten times deeper than in previous X-ray surveys).

The main aims of the project are:

- to detect and catalogue all sources of X-ray emission in the field of view
- to cross-correlate all detected sources with known classes of objects from optical/radio/infrared observations
- to develop the methods for source classification based on X-ray properties alone (hardness ratio, detailed spectra, variability)
- to present statistical properties of the detected source classes, including spatial and luminosity distribution
- to present detailed spectral and timing properties of the sample of brightest sources
- to study properties of the luminous eclipsing XRB X-7
- to analyse optical follow-up observations of the detected foreground stars

1.8.1 Thesis outline

Most of the work presented in this thesis has already been published in refereed journals. The presented work has been done in collaboration with Wolfgang Pietsch and Frank Haberl, from the Max Planck Institute for Extraterrestrial Physics, Garching, Germany; Despina Hatzidimitriou, from the Department of Physics, University of Crete, Heraklion, Greece; Ginevra Trinchieri, Osservatorio Astronomico di Brera, via Brera, Milano, Italy; Matthias Ehle, XMM-Newton Science Operations Centre, ESAC, ESA, Madrid, Spain, and Barbara Mochejska, Harvard-Smithsonian Center for Astrophysics, Cambridge, USA.

Chapter 2: XMM-Newton survey of the Local Group galaxy M 33, Pietsch, W., Misanovic, Z., Haberl, F., Hatzidimitriou, D., Ehle, M., Trinchieri, G., 2004, A&A, 426, 11.

This paper presents the analysis of the combined images of our XMM-Newton raster survey, including the calibration of the hardness ratio plots. The classification method, based on these plots and also on cross-correlations with optical and radio counterparts, was established. The first list of the classified objects in the M 33 field is presented. Part of this work is an on-line data catalogue (one table) available in electronic form at CDS. The Read-Me file for the on-line catalogue is presented in Appendix C.

Chapter 3: An XMM-Newton survey of the Local Group galaxy M 33 - variability of the detected sources, Misanovic, Z., Pietsch, W., Haberl, F., Hatzidimitriou, D., Ehle, M., Trinchieri, G., 2005, A&A, in press.

In this paper an analysis of all individual observations is presented, including a systematic search for flux variability. The second source catalogue is presented, and the detected variability was used as an additional tool for source classification. In addition, we also included cross-correlations with infrared data to classify the detected sources. This paper also presents the spatial and luminosity distribution of the classified sources. Part of this work is an on-line data catalogue (two tables) that will be available in electronic form at CDS. The Read-Me file for the first table in the on-line catalogue is presented in Appendix D, and for the second table in Appendix E.

Chapter 4: An XMM-Newton survey of the Local Group galaxy M 33 – bright individual sources, Misanovic, Z., Pietsch, W., Haberl, F., Trinchieri, G., Ehle, M., Hatzidimitriou, D., 2005, Proceedings IAU Symposium No. 130, Dublin, E. J.A. Meurs & G. Fabbiano, eds.

In this chapter we present X-ray spectra of the brightest objects detected in our survey. The detailed spectral analysis shows that these spectra can be used to extend the hardness ratio method for source classification, at least for the brightest sources.

Chapter 5: Spectroscopy of the brightest optical counterparts of X-ray sources in the direction of M 31 and M 33, Hatzidimitriou, D., Pietsch, W., Misanovic, Z., Reig, P., Haberl, F., 2005, A&A, submitted.

This paper presents the results of optical spectroscopy of the brightest optical counterparts of X-ray sources detected in our survey. Optical follow up observations were made at the 1.3-m Skinakas telescope in Grete, Greece.

Chapter 6: The eclipsing massive X-ray binary M 33 X-7: New X-ray observations and optical identification, Pietsch, W., Mochejska, B. J., Misanovic, Z., Haberl, F., Ehle, M., Trinchieri, G., 2004, A&A, 413, 879.

This paper presents a detailed spectral and timing analysis of one of the brightest objects in our field - the high mass X-ray binary system X-7. The presented analysis includes the identification of the optical counterpart obtained in a special analysis of DIRECT observations made with the 2.1-m telescope at the Kitt Peak National Observatory.

The following publications, which were also done as part of this project, are not included in this dissertation:

- Deep XMM-Newton survey of M33, Pietsch, W., Ehle, M., Haberl, F., Misanovic, Z., Trinchieri, G., 2003, AN, 324, 85.
- An XMM-Newton survey of the Local Group galaxy M 33 – catalogue results and

global properties, Misanovic, Z., Pietsch, W., Haberl, F., Ehle, M., Hatzidimitriou, D.; Trinchieri, G., 2005, Proceedings IAU Symposium No. 130, Dublin, E.J.A. Meurs & G. Fabbiano, eds.

- Variability of the X-ray sources detected in XMM-Newton survey of M33, Misanovic, Z., Pietsch, W., Haberl, F., Ehle, M., Hatzidimitriou, D., Trinchieri, G., 2005, XMM-Newton Consortium Meeting: 5 Years of Science with XMM-Newton, eds. U. Briel, S. Sembay, A. Read

Chapter 2

XMM-Newton survey of the Local Group galaxy M 33

W. Pietsch, Z. Misanovic, F. Haberl, D. Hatzidimitriou, M. Ehle, G. Trinchieri, 2004, A&A, 426, 11

Abstract: In an XMM-Newton raster observation of the bright Local Group spiral galaxy M 33 we study the population of X-ray sources (X-ray binaries, supernova remnants) down to a (0.2–4.5) keV luminosity of 10^{35} erg s⁻¹ – more than a factor of 10 deeper than earlier ROSAT observations. EPIC hardness ratios and optical and radio information are used to distinguish between different source classes. The survey detects 408 sources in an area of 0.80 square degree. We correlate these newly detected sources with earlier M 33 X-ray catalogues and information from optical, infra-red and radio wavelengths. As M 33 sources we detect 21 supernova remnants (SNR) and 23 SNR candidates, 5 super-soft sources and 2 X-ray binaries (XRBs). There are 267 sources classified as hard, which may either be XRBs or Crab-like SNRs in M 33 or background AGN. The 44 confirmed and candidate SNRs more than double the number of X-ray detected SNRs in M 33. 16 of these are proposed as SNR candidates from the X-ray data for the first time. On the other hand, there are several sources not connected to M 33: five foreground stars, 30 foreground star candidates, 12 active galactic nucleus candidates, one background galaxy and one background galaxy candidate. Extrapolating from deep field observations we would expect 175 to 210 background sources in this field. This indicates that about half of the sources detected are within M 33.

2.1 Introduction

The Local Group Sc galaxy M 33, located at a distance of 795 kpc (van den Bergh 1991, i.e. 1'' corresponds to 3.9 pc and the flux to luminosity conversion factor is 7.6×10^{49} cm²), is seen under a relatively low inclination of 56° (Zaritsky et al. 1989)

Table 2.1: XMM-Newton M33 observation log (proposal numbers 010264 and 014198).

Field	Obs. id.	Obs. dates	Pointing direction		EPIC PN		EPIC MOS1		EPIC MOS2	
M33			RA/DEC (J2000)		Mode ⁺ /Filter	T _{exp} [†]	Mode ⁺ /Filter	T _{exp} [†]	Mode ⁺ /Filter	T _{exp} [†]
(1)	(2)	(3)	(4)	(5)	(6)	(7)	(8)	(9)	(10)	(11)
1	0102640101	2000-08-04	1:33:51.0	30:39:37	FF/medium	6.29	PW2/medium	6.23	PW2/medium	6.22
1	0141980501	2003-01-22	1:33:51.0	30:39:37	FF/medium	1.23	FF/medium	1.51	FF/medium	1.51
1	0141980801	2003-02-12	1:33:51.0	30:39:37	FF/medium	7.25	FF/medium	8.86	FF/medium	8.87
2	0102640201	2000-08-04	1:34:40.0	30:57:48	EFF/medium	11.40	FF/medium	15.24	FF/medium	15.24
3	0102640301	2000-08-07	1:33:32.0	30:52:13	EFF/medium	3.80	FF/medium	4.58	FF/thin	4.58
3	0141980401	2003-01-24	1:33:32.0	30:52:13	FF/medium	0.00	FF/medium	0.00	FF/medium	0.00
4	0102640401	2000-08-02	1:32:51.0	30:36:49	EFF/thick	8.66	FF/thick	12.99	FF/thick	12.99
4	0141980601	2003-01-23	1:32:51.0	30:36:49	FF/medium	11.18	FF/medium	12.56	FF/medium	12.56
5	0102640501	2001-07-05	1:33:02.0	30:21:24	FF/medium	9.26	FF/medium	11.76	FF/medium	11.76
6	0102640601	2001-07-05	1:34:08.0	30:46:06	FF/medium	2.86	FF/medium	3.42	FF/medium	3.42
6	0141980301	2003-07-25	1:34:08.0	30:46:06	FF/medium	4.12	FF/medium	4.82	FF/medium	4.82
7	0102640701	2001-07-05	1:34:10.0	30:27:00	FF/medium	6.97	FF/medium	10.96	FF/medium	10.95
8	0102640801	2001-07-07	1:34:51.0	30:42:22	FF/medium	-	FF/medium	1.19	FF/medium	1.19
8	0102642001	2001-08-15	1:34:51.0	30:42:22	FF/medium	8.65	FF/medium	11.15	FF/medium	11.15
9	0102640901	2001-07-07	1:34:04.0	30:57:25	FF/medium	2.42	FF/medium	3.15	FF/medium	3.15
9	0141980201	2003-07-11	1:34:04.0	30:57:25	FF/medium	3.74	FF/medium	4.02	FF/medium	4.02
10	0102641001	2001-07-08	1:33:07.0	30:45:02	FF/medium	1.25	FF/medium	8.33	FF/medium	8.37
10	0141980101	2003-07-11	1:33:07.0	30:45:02	FF/medium	5.45	FF/medium	5.75	FF/medium	5.77
11	0102641101	2001-07-08	1:32:46.0	30:28:19	FF/medium	8.10	FF/medium	10.36	FF/medium	10.36
12	0102641201	2000-08-02	1:33:38.0	30:21:49	EFF/thick	11.34	FF/thick	3.67	FF/thick	3.66
12	0141980701	2003-01-24	1:33:38.0	30:21:49	FF/medium	4.40	FF/medium	5.72	FF/medium	5.73
13	0102642101	2002-01-25	1:34:34.0	30:34:11	FF/medium	10.00	FF/medium	12.27	FF/medium	12.27
14	0102642201	2002-01-25	1:34:56.0	30:50:52	FF/medium	11.60	FF/medium	13.87	FF/medium	13.87
15	0102642301	2002-01-27	1:33:33.0	30:33:07	FF/medium	10.00	FF/medium	12.27	FF/medium	12.27

Notes:

+ : FF: full frame, EFF: extended full frame, PW2: partial window 2

† : Exposure time in units of ks after screening for high background (see text)

and the optical extent can be approximated by an inclination-corrected D_{25} ellipse with large diameter of $64'.4$ and axes ratio of 1.66 (de Vaucouleurs et al. 1991; Tully 1988). With its moderate Galactic foreground absorption ($N_H = 6 \times 10^{20} \text{ cm}^{-2}$, Stark et al. 1992) M33 is ideally suited to study the X-ray source population and diffuse emission in a nearby spiral galaxy. The *Einstein* X-ray Observatory detected diffuse emission from a hot gas in M33 and 17 unresolved sources (Long et al. 1981a; Markert & Rallis 1983; Trinchieri et al. 1988b). First ROSAT HRI and PSPC observations revealed 57 sources and confirmed the detection of diffuse X-ray emission which may trace the spiral arms within a $10'$ radius around the nucleus (Schulman & Bregman 1995; Long et al. 1996). Combining all archival ROSAT observations of the field, Haberl & Pietsch (2001, hereafter HP01) found 184 X-ray sources within a $50'$ radius around the nucleus, identified some of the sources by correlations with previous X-ray, optical and radio catalogues, and in addition classified sources according to their X-ray properties. They found candidates for super-soft X-ray sources (SSS), X-ray binaries (XRBs), supernova remnants (SNRs), foreground stars and active galactic nuclei (AGN).

To follow up on these findings, we proposed as part of the telescope scientist guaranteed time (GT) program a deep homogeneous XMM-Newton survey of M33 with a sensitivity of $10^{35} \text{ erg s}^{-1}$ in the 0.5–10 keV band, a factor of ten deeper than previous surveys. The survey consisted of a raster of 15 pointings of about 10 ks each. The directions were selected in a way that each area within the M33 optical D_{25} extent was covered by the XMM-Newton EPIC detectors at least three times with the medium filter. The survey was complemented by an additional AO2 program, initiated to fill observation gaps due to high detector background, or, because the thick filter was used during the GT observations. First results of this survey were presented in Pietsch et al. (2003a).

Two M33 sources are known for their outstanding X-ray properties (Peres et al. 1989). The brightest source (X–8 in the nomenclature of Long et al. 1981a, luminosity of $10^{39-40} \text{ erg s}^{-1}$) is the most luminous X-ray source in the Local Group of galaxies and coincides with the optical center of M33. Its time variability (Dubus et al. 1997), its point-like nature seen by ROSAT HRI (Pietsch & Haberl 2000) and *Chandra* (Dubus & Rutledge 2002) and its X-ray spectrum best described by an absorbed power law plus disk blackbody model (e.g., Ehle et al. 2001; La Parola et al. 2003; Foschini et al. 2004), point towards a black hole XRB. A possible periodicity of 106 days was not confirmed in later observations (see Parmar et al. 2001). The second source X–7 is an eclipsing high mass XRB (HMXB) with a binary period of 3.45 d and possible 0.31 s pulsations, discovered in ROSAT PSPC and HRI observations (Schulman et al. 1993; Dubus et al. 1997, 1999; Larson & Schulman 1997). Pietsch et al. (2004b) analyzed XMM-Newton and *Chandra* data and determined improved binary parameters, however, they could not confirm the proposed pulsations. In a special analysis of DIRECT data, they identified an O7I star of 18.89 mag in V, as the optical counterpart, which shows the ellipsoidal heating light curve of a HMXB with the X–7 binary ephemeris. X–7 was the most distant eclipsing XRB until the detection of another such source in XMM-Newton and *Chandra* observations of the starburst galaxy NGC 253, which is located

Table 2.2: Count rate to energy conversion factor for different spectral models for EPIC instruments in energy band 1 to 5 (B1–B5). Models are a power law with photon index of 1.7 (PL), a thin thermal model with temperature of 1 keV (TT), and a black body with a temperature of 30 eV (BB). All models assume galactic foreground absorption of $6 \times 10^{20} \text{ cm}^{-2}$ (Stark et al. 1992).

Detector	Spec	B1	B2	B3	B4	B5
($10^{-12} \text{ erg cm}^{-2} \text{ ct}^{-1}$)						
EPIC PN	PL	1.03	1.10	1.71	4.9	21.
	TT	1.03	1.14	1.55	4.0	
	BB	1.09	0.97	1.30		
EPIC MOS	PL	6.2	4.9	4.8	12.9	66.
	TT	6.0	4.5	4.6	11.0	
	BB	10.1	4.8	4.2		

at more than three times the distance of M 33 (Pietsch et al. 2003b).

Here we present merged medium and thin filter images for the three EPIC instruments, in five energy bands, using only times of low background from our XMM-Newton survey of M 33, as well as a source catalogue and source population study based on these images. An analysis of the individual pointings with less stringent background rejection and using all filters is in progress, and will result in a source catalogue with improved positions (taking care of individual pointing offsets), that will also provide information on source variability and spectral characteristics.

2.2 Observations and data analysis

Table 2.1 summarizes the XMM-Newton (Jansen et al. 2001) EPIC (Strüder et al. 2001; Turner et al. 2001) observations. For each observation we give the field number of our M 33 raster (col. 1), the observation identification (2), date (3), pointing direction (4,5), as well as instrument mode, filter and exposure time after screening for high background for EPIC PN (6,7), MOS1 (8,9), and MOS2 (10,11). Observation 0102640801 was affected by a satellite “slew failure” and only the EPIC MOS instruments got some exposure time.

In the XMM-Newton observations the EPIC PN and MOS instruments were mostly operated in the full frame mode resulting in a time resolution of 73.4 ms and 2.6 s, respectively. Only for four early observations was the PN detector operated in the extended full frame mode (time resolution 200 ms). During observation 0102640101 the MOS detectors were operated in the small window mode (0.3 s time resolution for the inner CCDs to avoid pile-up for the bright source X–8). The medium filter was in front of the EPIC cameras in all but the first two observations which were performed

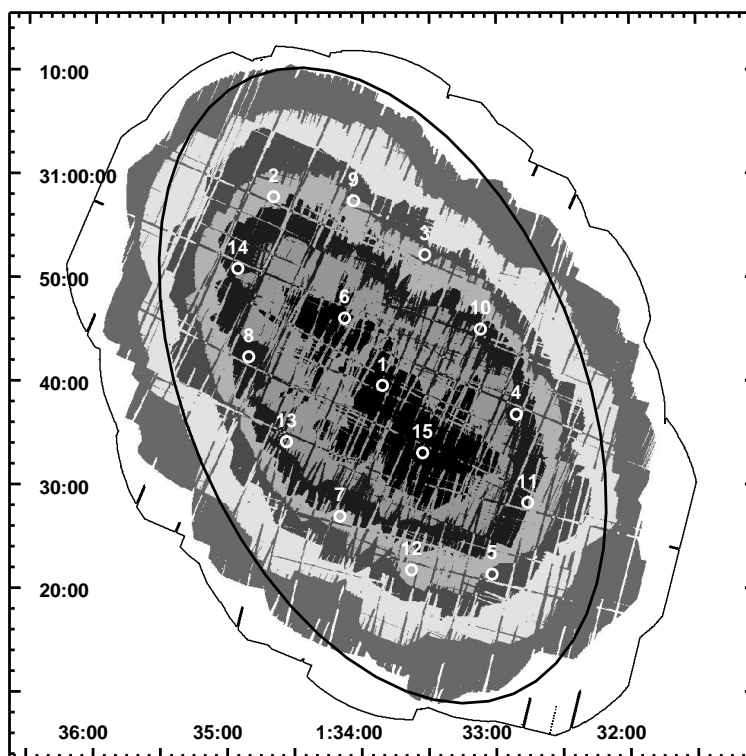


Figure 2.1: XMM-Newton EPIC “PN equivalent” exposure map combining all low background observation times of the fields of the M33 raster. The outer contour indicates 0 ks, gray-scale steps every 10 ks. The maximum PN equivalent exposure (see text) is 89 ks in the center area of M33. The optical extent of M33 is marked by the white inclination-corrected D_{25} ellipse. The center of the fields of our raster (see Table 2.1) are indicated and numbered.

with the thick filter (0102640401, 0102641201) and observation 0102640301 for which the MOS2 detector was operated with the thin filter. For creating the merged images and for source detection, we only used medium and thin filter observations.

The data analysis was performed using tools in the XMM-Newton Science Analysis System (SAS) v5.4.1 and some later versions from the development area as specially mentioned, EXSAS/MIDAS 1.2/1.4, and FTOOLS v5.2 software packages, the imaging application DS9 v2.3b1 and the spectral analysis software XSPEC v11.2.

For MOS, we used the SAS task `emchain` with task `emevent` v7.10 that removes flickering pixels. We carefully screened the event files for bad CCD pixels, remaining after the standard processing. To create a homogeneous combined image with similar background level for all fields we had to carefully screen the data for high background periods. In most observations the background light curves at all energies follow the high energy (7-15 keV) background light curves provided by the SAS tasks `epchain` and `emchain` and allowed us to efficiently screen the data. In some observations, however, the low energy background (below 1 keV) was higher during high energy selected good time intervals (GTIs) and had to be used for additional screening. GTIs were determined from the higher signal-to-noise PN light curves and also used for the MOS

cameras. Outside the PN time coverage, GTIs were determined from the combined MOS light curves. The corresponding low background times for the individual observations are listed for the PN and MOS cameras in Table 2.1. The combined “PN equivalent” vignettted EPIC exposure (1-2 keV) is significantly above 20 ks within most of the optical extent of M 33 (indicated by the inclination-corrected D_{25} ellipse in Fig. 2.1). Only in the NW and S the exposure does not reach this limit. For the “PN equivalent” EPIC exposure map we added MOS1 and MOS2 exposure maps (scaled by a factor of 0.36 as expected for a 5 keV thermal bremsstrahlung spectrum with an absorption of $6 \times 10^{20} \text{cm}^{-1}$, as expected for XRBs in M 33) to the PN exposure.

For the analysis we used five energy bands: (0.2–0.5) keV, (0.5–1.0) keV, (1.0–2.0) keV, (2.0–4.5) keV, and (4.5–12) keV as band 1 to 5. We intentionally split the 0.5–2.0 keV band used in the 1XMM XMM-Newton Serendipitous Source Catalogue¹ to get, on average, a more homogeneous distribution of the source counts to the energy bands, which leads to a better spread of the hardness ratio values and allows effective source classification (see Sect. 2.6).

For PN we selected only “singles” (PATTERN=0) in band 1, for the other bands “singles and doubles” (PATTERN \leq 4). For MOS we used “singles” to “quadruples” (PATTERN \leq 12). To avoid background variability over the PN images we omitted the energy range (7.2–9.2) keV in band 5 where strong fluorescence lines cause higher background in the outer detector area (Freyberg et al. 2004). To convert source count rates in the individual bands to fluxes we calculated count rate to energy conversion factors (ECF) for PN and MOS medium filter observations using W3PIMMS and assuming the same spectrum as for the first XMM-Newton source catalogue, i.e. a power law spectrum with photon index 1.7 absorbed by the galactic foreground column of $6 \times 10^{20} \text{cm}^{-2}$ (Table 2.2). The assumed spectrum represents hard sources like XRBs or AGN. We also give ECF values for a typical SNR (absorbed 1 keV thin thermal) and SSS (absorbed 30 eV black body) in M 33. Table 2.2 demonstrates that for EPIC PN, ECF values only vary by about 20% for the different spectra in bands 1 to 4. The same is true for EPIC MOS, with the exception of the black body ECF in the 0.2–0.5 keV band where the MOS sensitivity is much lower. For both PN and MOS, the sensitivity is strongly reduced at energies above 4.5 keV. On the other hand, background count rates are similar in the hard band. Therefore, only bright hard sources are detected in this band.

To classify the source spectra we computed four hardness ratios from the source count rates. These hardness ratios are defined as $\text{HR}_i = (B_{i+1} - B_i) / (B_{i+1} + B_i)$, for $i = 1$ to 4, where B_i denotes count rates in band i , as defined above. In the standard source detection products, hardness ratios and count rates in individual energy bands are not combined for all instruments. To improve the statistics, we have combined the count rates (and fluxes) from all three EPIC instruments and have then derived hardness ratios for them. We are aware that these products have some jitter in their meaning, as the relative integration times for individual sources in the EPIC instruments differ slightly. Due to the better signal in the combined products, they are still very valuable

¹Prepared by the XMM-Newton Survey Science Centre Consortium (<http://xmmssc-www.star.le.ac.uk/>)

for source classification. For investigations needing accurate calibration, values derived for each instrument separately should be used.

As discussed above, band 5 suffers from the combined effect of lower sensitivity in both PN and MOS, and a large contamination from the hard background, reducing the significance of any detection due to the much higher noise. We therefore give total count rates and errors derived from all instruments in the “XID” band that comprises bands 1–4, and derive fluxes in the corresponding 0.2–4.5 keV range. A larger band would artificially increase the overall noise of all but extremely hard sources. For very soft sources, or for sources detected only in one of the instruments (*e.g.* soft sources in PN), even with this choice the quoted errors are overestimated, however the number of sources of this nature is small.

For PN, MOS1 and MOS2 we created images, background images, exposure maps (without and with vignetting correction) and masked them for the acceptable detector area in each of the five energy bands. For PN, the background maps contain the contribution from the “out of time (OOT)” events (parameter `withootset=true` in task `esplinemap`). The images of the individual observations were then merged for source detection into images covering the full M33 field. The maximum vignettted exposure was 44.3 ks, 58.6 ks and 58.7 ks in the 1–2 keV band for the PN, MOS1 and MOS2 cameras, respectively, and was nearly the same for bands 1 to 4. In the hardest band, the maximum exposure is smaller by 30% due to the larger vignetting effects. To allow us an easy merging of images, we calculated for the events of all observations projected sky coordinates (X,Y) with respect to the center reference position RA=01^h33^m50^s.4, DEC=+30°39′36″(J2000). At the borders, due to the different field of view of the EPIC instruments, the merged images for PN, MOS1 and MOS2 do not fully overlap. Nevertheless, we used the full area for source detection.

2.3 Source catalogue

We searched for sources in these merged images simultaneously using 5×3 images (5 energy bands and PN, MOS1 and MOS2 camera). A preliminary source list created with the task `boxdetect` with a low likelihood threshold was used as starting point for the task `emldetect v4.31`. As photons collected with different off-axis angles contribute to the source counts in the merged image, we prepared a specific point spread function (PSF) calibration file. It assumed a constant PSF over the total field of view that was degraded as if 6′ off-axis. This is the most degraded but still “circular” PSF in the EPIC calibration files and a first approximation for the PSF when source counts are collected at many different off-axis angles as in the M33 raster observation. To resolve sources that overlap due to the PSF, we used parameter `multisourcefit=4`.

A detection probability above 4σ is equivalent to a single band limiting detection likelihood of 10. This threshold has been successfully used by HP01 for the ROSAT PSPC detections (see Sect. 2.5). In the case of simultaneous detection with a large number of images this equivalence is no longer valid due to the small number of counts in the individual images contributing to a source at the detection threshold. We have established for the task `emldetect` that for the case of simultaneously using

Table 2.3: X-ray source catalogue of the XMM-Newton EPIC M 33 raster observation.

Src	RA(J2000)	DEC(J2000)	$r_{1\sigma}$	M_{Lexi}	Count rate*	Flux*	HR1	HR2	HR3	HR4	Val
(1)	(h mm ss.ss)	(+dd mm ss.s)	($''$)	(10)	(ct s $^{-1}$)	(erg cm $^{-2}$ s $^{-1}$)	(15,16)	(17,18)	(19,20)	(21,22)	(23)
1	1 31 42.93	+30 23 29.5	1.78	3.41e+01	1.18e-02±2.2e-03	1.55e-14±4.0e-15	0.44±0.21	-0.39±0.21	-0.84±0.34	*± *	TFF
2	1 31 46.89	+30 22 01.3	1.03	1.43e+02	3.86e-02±4.1e-03	4.17e-14±5.7e-15	0.44±0.11	-0.17±0.12	-0.75±0.14	*± *	TTF
3	1 31 54.90	+30 29 54.5	1.86	2.48e+01	7.15e-03±1.6e-03	6.33e-15±1.7e-15	0.37±0.21	-0.64±0.26	*± *	*± *	TTT
4	1 31 55.12	+30 28 56.9	1.62	1.49e+01	6.37e-03±1.7e-03	7.72e-15±2.7e-15	*± *	0.31±0.31	-0.11±0.29	0.20±0.35	TTT
5	1 31 59.18	+30 35 06.9	1.60	1.58e+01	5.00e-03±1.0e-03	6.96e-15±1.7e-15	0.38±0.27	-0.37±0.27	0.37±0.28	-1.00±0.90	TTT
...											
408	1 36 01.07	+30 51 28.0	1.10	1.10e+02	2.52e-02±2.7e-03	2.72e-14±4.1e-15	0.82±0.13	0.06±0.11	-0.32±0.14	-0.20±0.31	TTT

EPIC PN parameters										
Expo	M_{Lexi}	Count rate*	Flux*	HR1	HR2	HR3	HR4			
(ks)	(25)	(ct s $^{-1}$)	(erg cm $^{-2}$ s $^{-1}$)	(30,31)	(32,33)	(34,35)	(36,37)			
(24)	(25)	(26,27)	(28,29)	(30,31)	(32,33)	(34,35)	(36,37)			
2.7	3.41e+01	1.18e-02±2.2e-03	1.55e-14±4.0e-15	0.44±0.21	-0.39±0.21	-0.84±0.34	*± *			
2.7	1.32e+02	3.30e-02±3.7e-03	4.94e-14±7.2e-15	0.38±0.12	-0.14±0.13	-0.71±0.16	*± *			
3.8	1.04e+01	4.40e-03±1.4e-03	5.91e-15±2.4e-15	0.65±0.33	-0.59±0.32	*± *	*± *			
3.8	1.46e+01	4.42e-03±1.4e-03	1.05e-14±4.1e-15	*± *	0.27±0.34	-0.32±0.36	*± *			
8.4	1.57e+01	3.50e-03±8.5e-04	9.23e-15±2.8e-15	0.43±0.32	-0.45±0.31	0.48±0.31	-1.00±1.02			
4.1	5.06e+01	1.17e-02±1.7e-03	2.14e-14±4.7e-15	1.00±0.08	-0.07±0.14	-0.54±0.22	*± *			

Table 2.3: X-ray source catalogue - continued

EPIC MOS1 parameters							
Expo (ks) (38)	ML _{exi} (39)	Count rate* (ct s ⁻¹) (40,41)	Flux* (erg cm ⁻² s ⁻¹) (42,43)	HR1 (44,45)	HR2 (46,47)	HR3 (48,49)	HR4 (50,51)
*	*	*± *	*± *	*± *	*± *	*± *	*± *
2.8	1.42e+01	5.61e-03±1.7e-03	2.78e-14±9.6e-15	0.76±0.30	-0.28±0.30	*± *	*± *
9.5	2.64e-01	4.38e-04±4.5e-04	2.60e-15±3.2e-15	*± *	*± *	*± *	*± *
4.9	1.38e-01	3.15e-04±4.2e-04	2.57e-15±4.1e-15	*± *	*± *	*± *	*± *
10.7	1.65e+00	5.80e-04±3.2e-04	5.14e-15±3.2e-15	*± *	*± *	*± *	*± *
4.1	3.84e+01	7.34e-03±1.5e-03	5.23e-14±1.3e-14	1.00±0.34	0.23±0.22	-0.23±0.23	-0.02±0.39
EPIC MOS2 parameters							
Expo (ks) (52)	ML _{exi} (53)	Count rate* (ct s ⁻¹) (54,55)	Flux* (erg cm ⁻² s ⁻¹) (56,57)	HR1 (58,59)	HR2 (60,61)	HR3 (62,63)	HR4 (64,65)
*	*	*± *	*± *	*± *	*± *	*± *	*± *
*	*	*± *	*± *	*± *	*± *	*± *	*± *
9.4	1.84e+01	2.32e-03±6.1e-04	1.26e-14±3.8e-15	0.01±0.26	-0.72±0.31	*± *	*± *
4.7	4.22e+00	1.64e-03±7.6e-04	1.54e-14±7.4e-15	*± *	*± *	*± *	*± *
10.4	1.83e+00	9.21e-04±4.5e-04	5.84e-15±3.1e-15	*± *	*± *	*± *	*± *
4.0	2.35e+01	6.09e-03±1.5e-03	4.43e-14±1.3e-14	*± *	0.17±0.32	-0.10±0.33	-0.38±0.58

Table 2.3: X-ray source catalogue - continued

XID (66)	USNO-B1 name (67)	Mul (68)	Δ (") (69)	B2 (mag) (70)	R2 (mag) (71)	I2 (mag) (72)	$\log(\frac{f_x}{f_{opt}})$ (73)	Class (74)	Remarks (75)
LCB2(Var(flare)),HP8	1203-0020312	1	3.1	15.8	13.5	11.3	-2.6	fg Star	W UMa Var(SIM)
	2293-01403-1	1	2.7	11.1	10.8	10.6	-3.6	fg Star	beta Lyrae EB(SIM)
	2293-01131-1	1	2.7	12.4	11.3	10.9	-4.1	< fgStar >	< G8 >
		*	*	*	*	*	*	< hard >	
		*	*	*	*	*	*	< hard >	

Notes:

*: in XID band (0.2–4.5 keV)

References:

in XID: X-n: Long et al. (1981a), Trinchieri et al. (1988b), SBn: Schulman & Bregman (1995), LCBn: Long et al. (1996), DCL97: Dubus et al. (1997), DCL99: Dubus et al. (1999), HPn: Haberl & Pietsch (2001)

in remarks: SIM: SIMBAD database, NED: NASA Extragalactic Database, NVSS: Condon et al. (1998), CS82: Christian & Schommer (1982), [MC83]25: Massey & Conti (1983), IFM*: Ivanov et al. (1993), GKLn: Gordon et al. (1998), GDKn: Gordon et al. (1999), IV74: Israel & van der Kruit (1974), VBW78: von Kap-Herr et al. (1978), M98: Massey (1998), MCM2001: Magrini et al. (2001), MBH96: Massey et al. (1996), PMM2004: Pietsch et al. (2004b), GM94: Giovagnoli & Mould (1994), FSZ: Fabrika et al. (1997), D33: Macri et al. (2001a), Mochejska et al. (2001a), RW93: Regan & Wilson (1993), VHK: Hubble (1926), CGC97: Crampton et al. (1997), BCLMP: Boulesteix et al. (1974)

15 images, a detection probability above 4σ corresponds to a combined likelihood of 7. This threshold was used to select sources for the catalogue. The detection procedure produced acceptable results as can be checked from the overlay of the detected sources onto the smoothed X-ray images (see Sect. 2.4).

Two emission peaks were resolved into several sources with no sign of multiplicity from the smoothed images and are better described as extended. In a detection run including extent determination we found that these two sources (#125 and #299) can be characterized by a Gaussian with FWHM of $18''.0$ and $16''.2$, respectively, and the extent likelihood is high. In total we detected 408 sources in the field.

The source parameters are summarized in Table 2.3 (EPIC combined products and products for EPIC PN, MOS1 and MOS2, separately). We only show the first five and the last row in the paper. The full table is available in electronic form at the CDS.

Table 2.3 gives the source number (col. 1), position (2 to 8) with 1σ uncertainty radius (9), likelihood of existence (10), integrated PN, MOS1 and MOS2 count rate and error (11,12) and flux and error (13,14) in the 0.2–4.5 keV band, and hardness ratios and errors (15–22). Hardness ratios are calculated only for sources for which at least one of the two band count rates has a significance greater than 2σ . Errors are the properly combined statistical errors in each band and can extend beyond the range of allowed values of hardness ratios as defined previously (-1.0 to 1.0). The EPIC instruments contributing to the source detection, are indicated in the “Val” parameter (col. 23, first character for PN, second MOS1, third MOS2) as “T”, if inside the field of view (FOV), or “F”, if outside of FOV. There are only nine sources at the periphery of the FOV where only part of the EPIC instruments contribute. The positional error does not include intrinsic systematic errors which, according to the Users Guide of the 1XMM XMM-Newton Serendipitous Source Catalogue, amount to $1''.5$ and should be quadratically added to the statistical errors in col. 9.

Table 2.3 then gives for EPIC PN exposure (24), source existence likelihood (25), count rate and error (26,27) and flux and error (28,29) in the 0.2–4.5 keV band, and hardness ratios and error (30–37). Columns 38 to 51 and 52 to 65 give the same information corresponding to cols. 24 to 37, but now for the EPIC MOS1 and MOS2 instruments. Hardness ratios for the individual instruments were again screened as described above. From the comparison of the hardness ratios derived from integrated PN, MOS1 and MOS2 count rates (cols. 15–22) and the hardness ratios of the individual instruments (cols. 30–37, 44–51 and 58–65) it is clear that combining the instrument count rate information yielded significantly more hardness ratios above the chosen significance threshold.

In the remaining columns of Table 2.3, we give cross correlation information, which is further described in Sect. 2.5. We only want to mention here, that we used the foreground stars and candidates, to verify the assumed source position errors. All 35 foreground stars and candidates are located within the 3σ statistical plus systematic positional error given above.

The faintest sources detected have a flux of $1.0 \times 10^{-15} \text{erg cm}^{-2} \text{s}^{-1}$, the brightest source (X-8) $1.1 \times 10^{-11} \text{erg cm}^{-2} \text{s}^{-1}$ in the 0.2–4.5 keV band. This corresponds to an absorbed luminosity range in M33 of $7.6 \times 10^{34} \text{erg s}^{-1}$ to $8.4 \times 10^{38} \text{erg s}^{-1}$.

2.4 Images

For Figs. 2.2, 2.3 and 2.4 we smoothed the images and un-vignetted exposure maps per band and observation (created as described in Sect. 2) with a Gaussian (FWHM of $20''$) and masked them for acceptable detector area. For PN, we subtracted OOT images, that were masked and smoothed in the same way as the images. We normalized the images with the un-vignetted exposure maps to avoid an over-correction of the partly un-vignetted detector background. For the EPIC combined images, we added the images of the individual cameras scaled according to the background in the individual energy bands. For the colour image and the broad band image we added images for the individual bands as needed and masked them to a total un-vignetted exposure of 10 ks. To better visualize faint structures we add contours. We indicate the detected sources by boxes and the optical extent of M 33 by the inclination-corrected D_{25} ellipse.

The XID band (0.2–4.5 keV) image (Fig. 2.2) gives an overview on the sources detected in the XMM-Newton analysis. Two of the sources (1 and 7) are bright sources detected in areas with low exposure that were masked out for the images. In Fig. 2.3 we rotated the images of the individual band so that the major axis of the D_{25} ellipse is oriented vertically. We over-plotted the positions of the sources of our catalogue. By comparing the different energy bands it is clear that many sources only show up in some of the images, a fact that indicates spectral diversity and is further quantified in the different hardness ratios of the sources. This fact can be visualized even more clearly in the combined EPIC colour image where we coded the 0.2–1.0 keV band in red, 1.0–2.0 keV band in green and above 2.0 keV in blue (see Fig. 2.4). The image is a demonstration of the colourful X-ray sky. SSS, thermal SNRs and foreground stars appear red or yellow, XRBs, Crab-like SNRs and AGN green to blue. Diffuse emission fills the inner area of the disk and the southern spiral arm (red, see also Fig. 2.3, band 1–3). A detailed analysis of this emission is outside the scope of this paper.

The images reveal that there is additional emission that has not been resolved into individual sources. This may be due to really diffuse emission or due to sources that did not reach the detection threshold. Examples are, structures in the area around the three bright sources X–9a,b,c (277, 297, 310) in the NE, source X–4 (124) in the NW and source X–6 (155) in the SSW. There seems to be a relatively bright source which was missed by the detection procedure between sources 235 and 258. Faint structure appears between sources 55 and 65 and south of source 91. Only deeper and/or higher resolution observations will allow us to clarify the nature of this emission.

2.5 Cross-correlation with other M 33 X-ray catalogues

In this section we discuss the cross-correlation of the XMM-Newton detected sources with sources reported in earlier X-ray catalogues. All correlations (together with other X-ray information like variability, reported in these catalogues, or extent, detected in this work) are indicated in the XID column of Table 2.3 (col. 66).

From the 17 *Einstein* sources reported in Trinchieri et al. (1988b) we detected

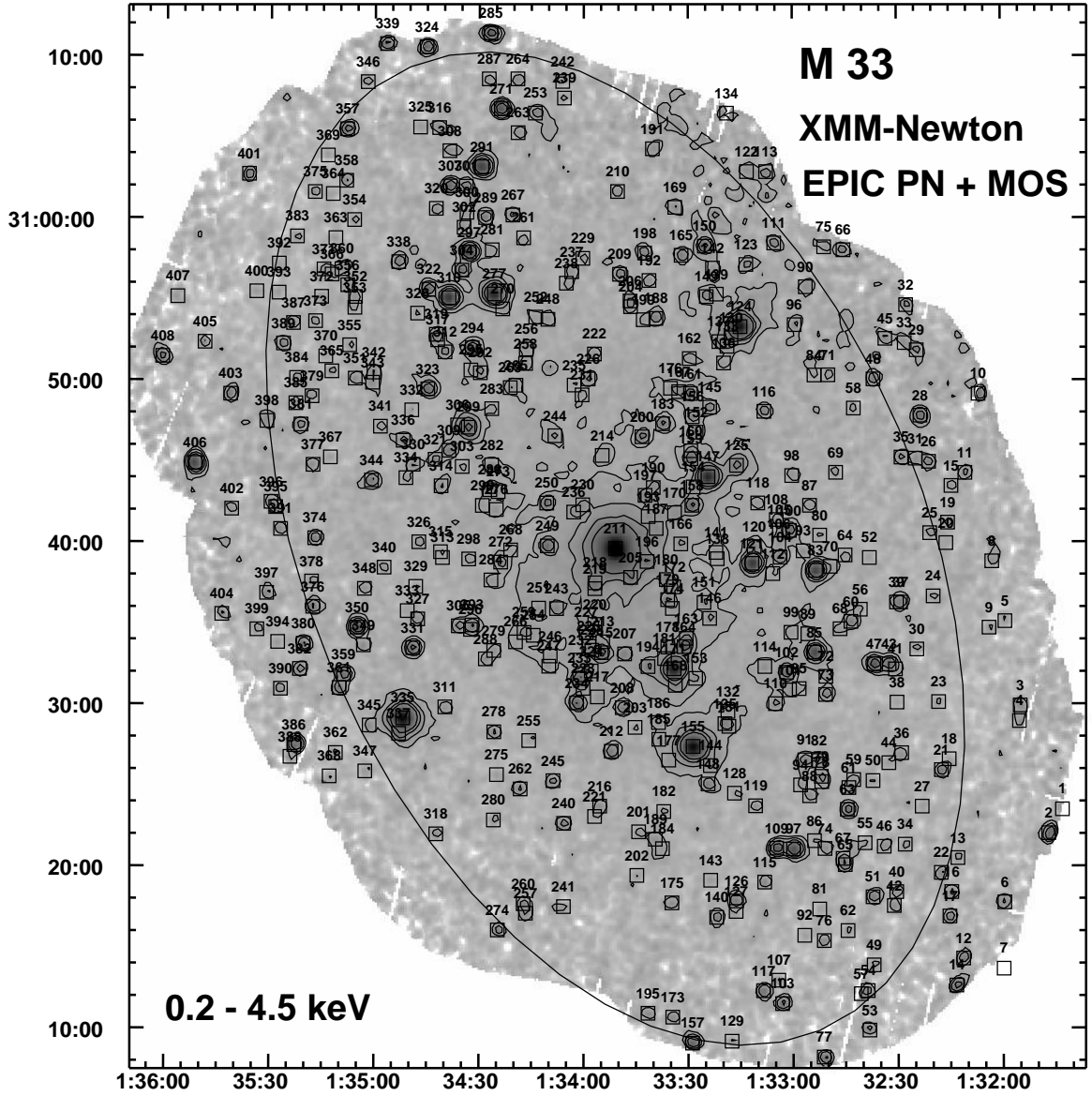


Figure 2.2: Logarithmically-scaled XMM-Newton EPIC low background image of the M33 medium and thin filter observations combining PN and MOS1 and MOS2 cameras in the (0.2–4.5) keV band. The data are smoothed with a Gaussian of FWHM $20''$ which corresponds to the average point spread function of the combined observations with different off-axis angles. The image is corrected for un-vignetted exposure and masked for exposure above 14 ks. Contours are at $(0.8, 1.2, 2.0, 3.6) \times 10^{-5}$ $ct\ s^{-1}$. Sources from the catalogue, RA, DEC (J2000.0) coordinates, and the optical D_{25} ellipse of M33 are marked.

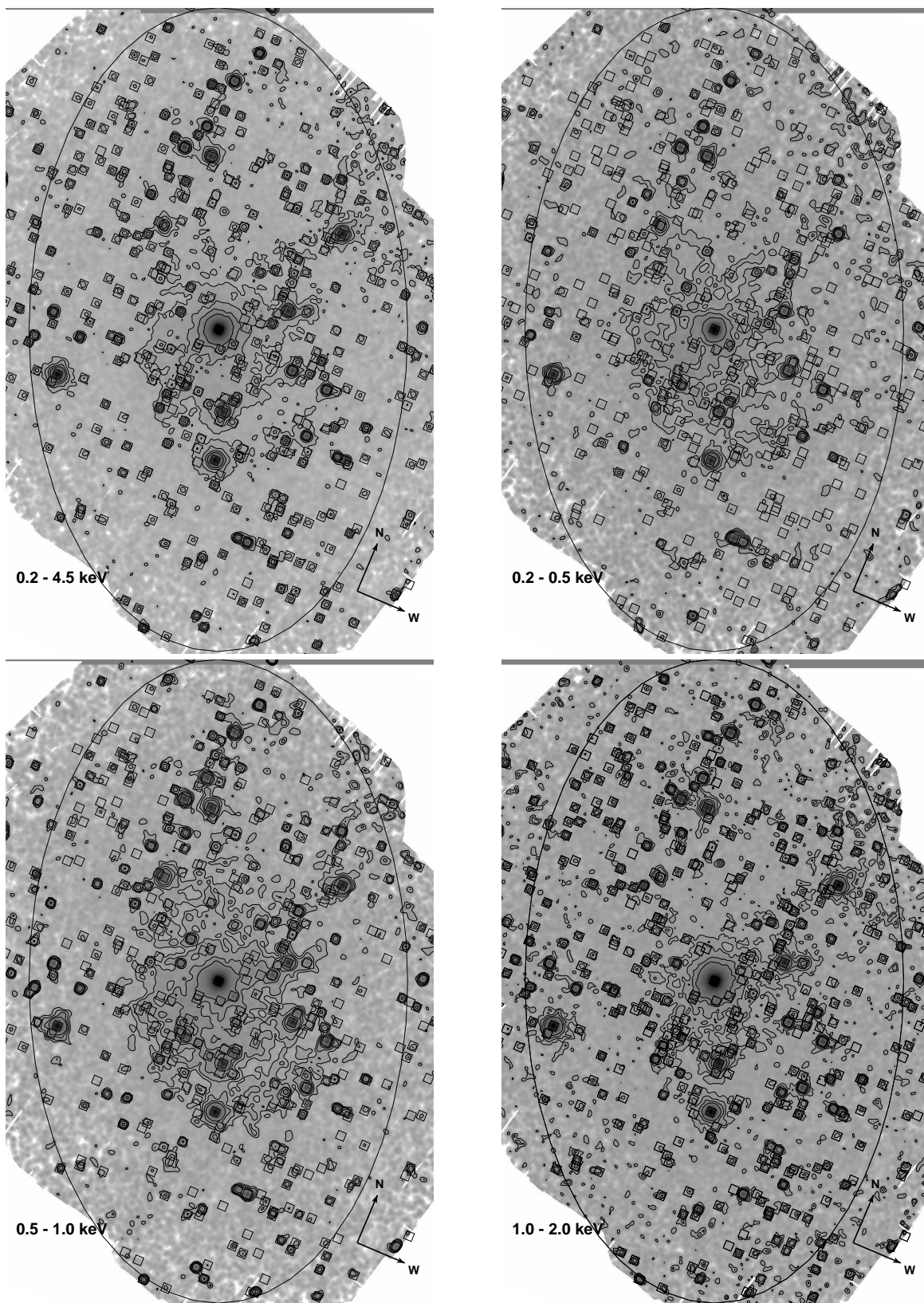


Figure 2.3: XMM-Newton EPIC M33 images: band 1-4 (upper left), band 1 (upper right), band 2 (lower left), and band 3 (lower right).

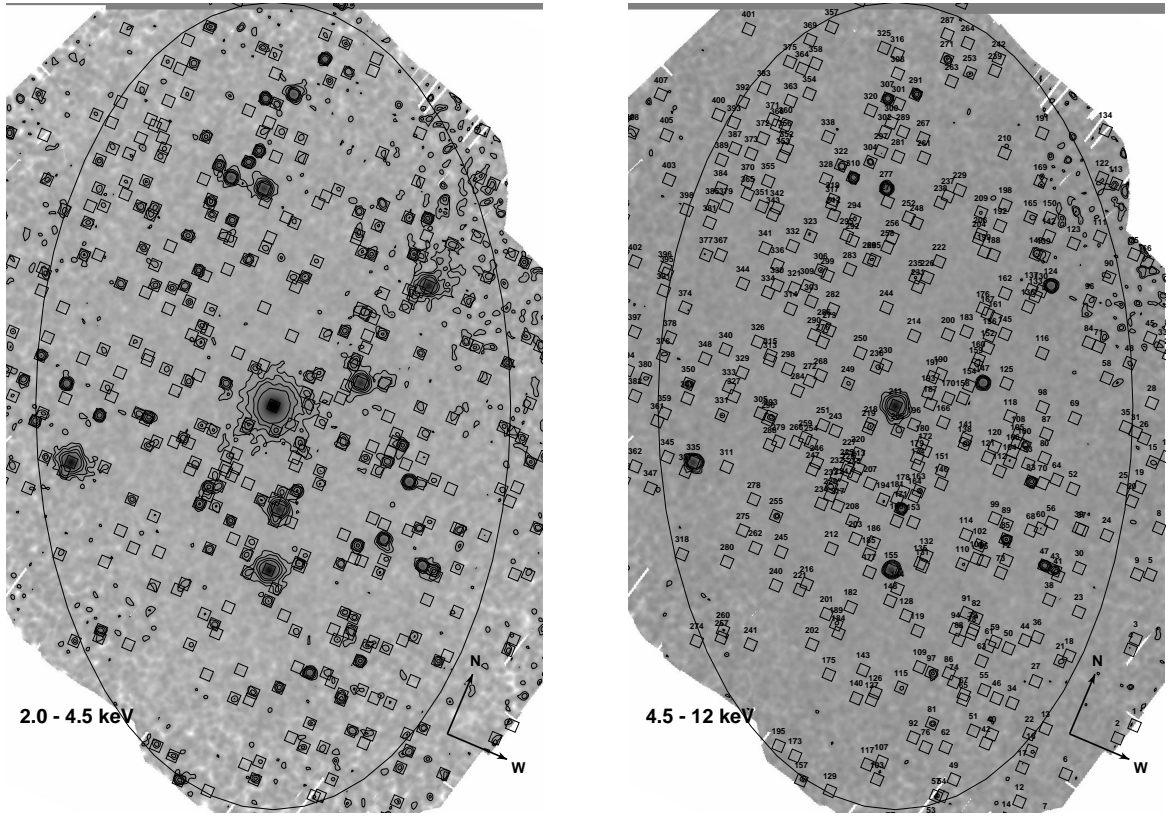


Figure 2.3: (continued) XMM-Newton EPIC M33 images: band 4 (left) and band 5 (right). The images are smoothed with a Gaussian of FWHM $20''$, corrected for un-vignetted exposure and masked for exposure above 14 ks. Contour levels are $(8, 12, 20, 36) \times 10^{-6} \text{ ct s}^{-1}$ for the merged band 1–4, $(1.5, 2, 3, 5) \times 10^{-6} \text{ ct s}^{-1}$ for the band 1, $(1.7, 2.2, 3.2, 5.2) \times 10^{-6} \text{ ct s}^{-1}$ for the band 2, $(3, 4, 6, 10) \times 10^{-6} \text{ ct s}^{-1}$ for the band 3, $(2.5, 3.5, 5.5, 9.5) \times 10^{-6} \text{ ct s}^{-1}$ for the band 4, and $(5, 6, 8, 12) \times 10^{-6} \text{ ct s}^{-1}$ for the band 5 images. The inclination-corrected optical D_{25} ellipse of M33, the sky orientation, and the sources from the catalogue - including source numbers in the (4.5–12) keV band image - are indicated.

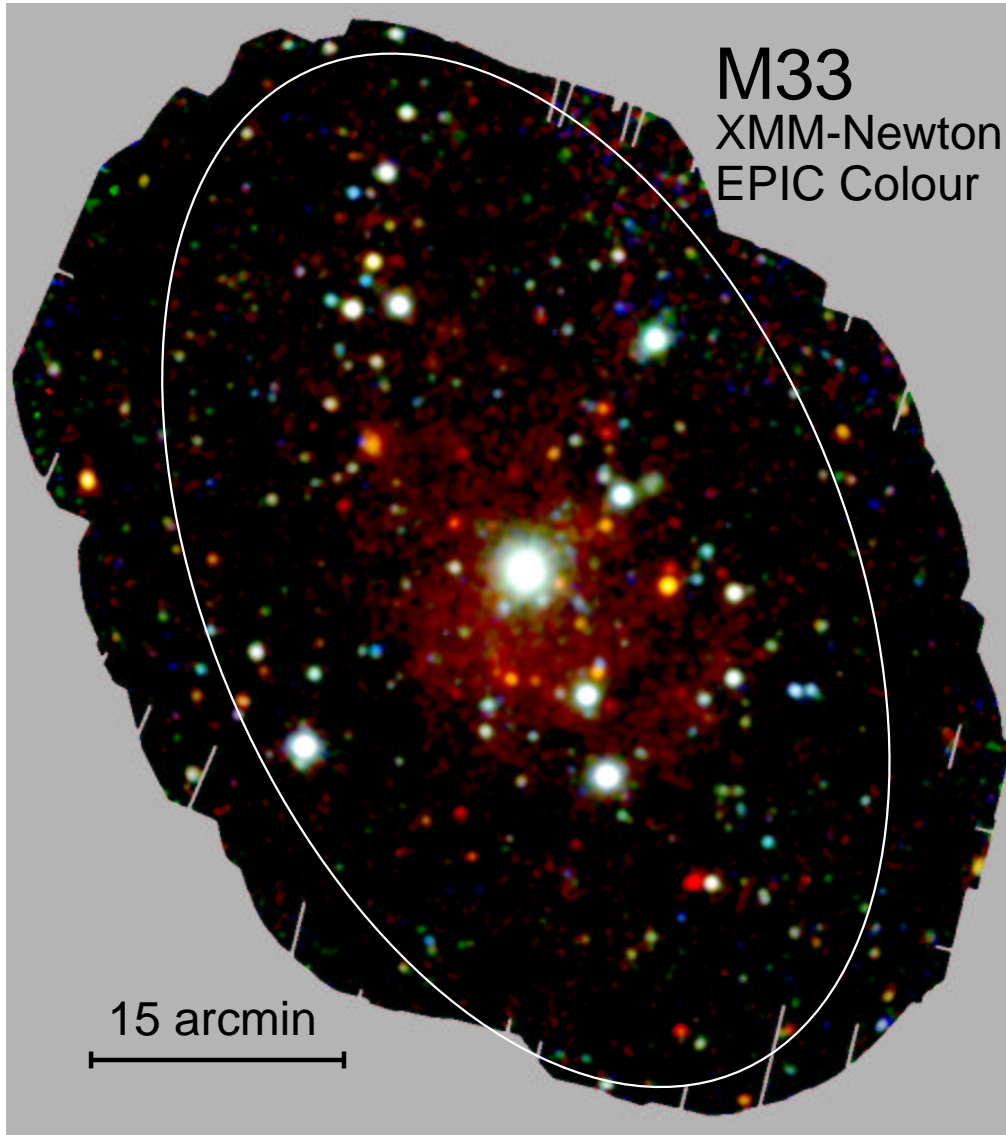


Figure 2.4: Logarithmically-scaled, three-colour XMM-Newton EPIC low background image of the M 33 medium and thin filter observations combining PN and MOS1 and MOS2 cameras. Red, green and blue show respectively the (0.2–1.0) keV, (1.0–2.0) keV and (2.0–12.0) keV bands. The data in each energy band have been smoothed with a Gaussian of FWHM $20''$ which corresponds to the average point spread function of the combined observations with different off-axis angles. The image has been corrected for un-vignetted exposure and masked for exposure above 14 ks. The image scale and the inclination-corrected D_{25} ellipse of M 33 are marked.

Table 2.4: Summary of cross-correlation with the M33 ROSAT catalogue of HP01. ROSAT sources, not detected in our XMM-Newton analysis, are arranged according to their ROSAT detection likelihood LH.

classification	HP01 source numbers
outside XMM-Newton field	1,2,3,4,5,6,7,10,11,46,167,171, 176,177,180,181,182,183,184
within extended source 125	48,50,51
resolved by <i>XMM-Newton</i>	22,29,59,121,172
not detected: LH<9 (28 of 34 sources)	14,16,24,35,37,38,65,73,79,85,88, 89,94,105,107,108,116,127,131, 135,138,149,153,155,159,166,175
not detected: 9<LH<10 (13 of 19 sources)	23,36,43,47,56,72,90,99,100,101, 113,125,142
not detected: LH \geq 10	9(LH=29),30(59),41(44),53(13), 68(42),69(11),82(27),83(14), 93(198,near nucleus),97(11), 98(21,near nucleus),119(14,near nucleus),128(18),133(20)

all but the relatively bright source X-12 in the northern disk and the less than 3σ detection X-15 which was located about $90''$ to the East of the nucleus. Both of these sources were also not detected by ROSAT (Schulman & Bregman 1995; Long et al. 1996, HP01). While one may question the original existence of X-15, X-12 was detected by *Einstein* with high significance and has to be strongly time variable.

In the correlation with ROSAT detected sources, we concentrated on the catalogue derived by HP01 from all archival observations of the field, which contains 184 sources within $50'$ of the nucleus. It re-detects all 37 sources detected in the ROSAT PSPC analysis of Long et al. (1996) and 21 of the 27 sources from the first ROSAT HRI analysis of the central area of M 33 by Schulman & Bregman (1995). We searched for these low signal-to-noise sources (numbers 18, 19, 20, 23, 24, and 27) without success in the more sensitive XMM-Newton data. The sources therefore most likely are not just time variable, but rather false detections.

In Table 2.4, we classified sources of HP01 who analyzed all archival ROSAT PSPC and HRI observations of the M33 field: 19 sources are positioned outside the field covered by the XMM-Newton observations, three are detected within the extended emission of XMM-Newton source 125, 5 are resolved into multiple components in the XMM-Newton catalogue. We did not detect 41 out of 51 sources with a ROSAT detection likelihood below 10. All these sources originate from the ROSAT HRI detections list which, following the experience at the time, was generated with a likelihood

limit of 8 for detection compared to the limit of 10 used for PSPC sources. If still at the ROSAT brightness, these HRI sources should have been detected by the deeper XMM-Newton observations. While, in principle, they could all have dimmed by such an amount that we did not detect them, this seems rather unlikely and probably most of these sources were spurious detections. The situation is certainly different for the HP01 sources with likelihood above 10. Many of these sources were detected with both ROSAT detectors and the non-detection with XMM-Newton indicates time variability. HP01 source 30 was already found to vary by more than a factor of 7.5 during the ROSAT observations, two other sources (69 and 82) were classified by HP01 as SSS candidates, which as a class are known to show strong time variability, and another two were classified as foreground stars (9 and 133), which might have been flaring during the ROSAT observations. The HP01 sources close to the nucleus of M33 (93, 98, and 119) may have been missed in our XMM-Newton analysis due to contamination from the bright nuclear source X-8 or could be spurious detections due to structures in the ROSAT PSF. One other HP01 source (128) is clearly visible in the XMM-Newton band 3 and 4 images (see Fig. 2.3) between XMM-Newton sources 235 and 258, however it was not picked up by the detection algorithms. Besides these special cases, there are 92 clear and four questionable (214, 256, 258, 338) XMM-Newton and HP01 correlations listed in col. 66 of Table 2.3.

2.6 Classes of point-like X-ray sources detected in the direction of M 33

To identify the M 33 X-ray sources we searched for correlations around the X-ray source positions (within a radius of $3 \times (\sigma_{stat} + \sigma_{syst})$ in the SIMBAD and NED archives and within several catalogues. In cols. 67 to 72 of Table 2.3, we give extraction information from the USNO-B1 catalogue (name, number of objects within search area, distance, B2, R2 and I2 magnitude of the brightest object). We omitted information, when the digitization was fooled by extended emission within HII regions (mostly only some colours available and rather bright). To improve on the reliability of identifications we used the B and R magnitudes to calculate the ratio of X-ray-to-optical flux, given by $\log(\frac{f_x}{f_{opt}}) = \log(f_x) + (m_{B2} + m_{R2}) / (2 \times 2.5) + 5.37$, following Maccacaro et al. (1988, see col. 73).

The catalogued X-ray sources are identified or classified based on properties in X-rays (hardness ratios (HR), variability, extent) and of correlated objects in other wavelength regimes (Table 2.3, cols. 74, 75). The criteria used are summarized in Table 2.5. We counted a source as identified, if at least two criteria secure the identification. Otherwise, we only counted a source as classified (indicated by pointed brackets).

We plotted X-ray colour/colour diagrams based on the HRs (see Fig. 2.5). Unclassified sources are only plotted if the error in both contributing HRs is below 0.2. To identify areas of specific source classes in the plots, we over-plotted colours of sources, derived from measured XMM-Newton spectra and model simulations (see discussion

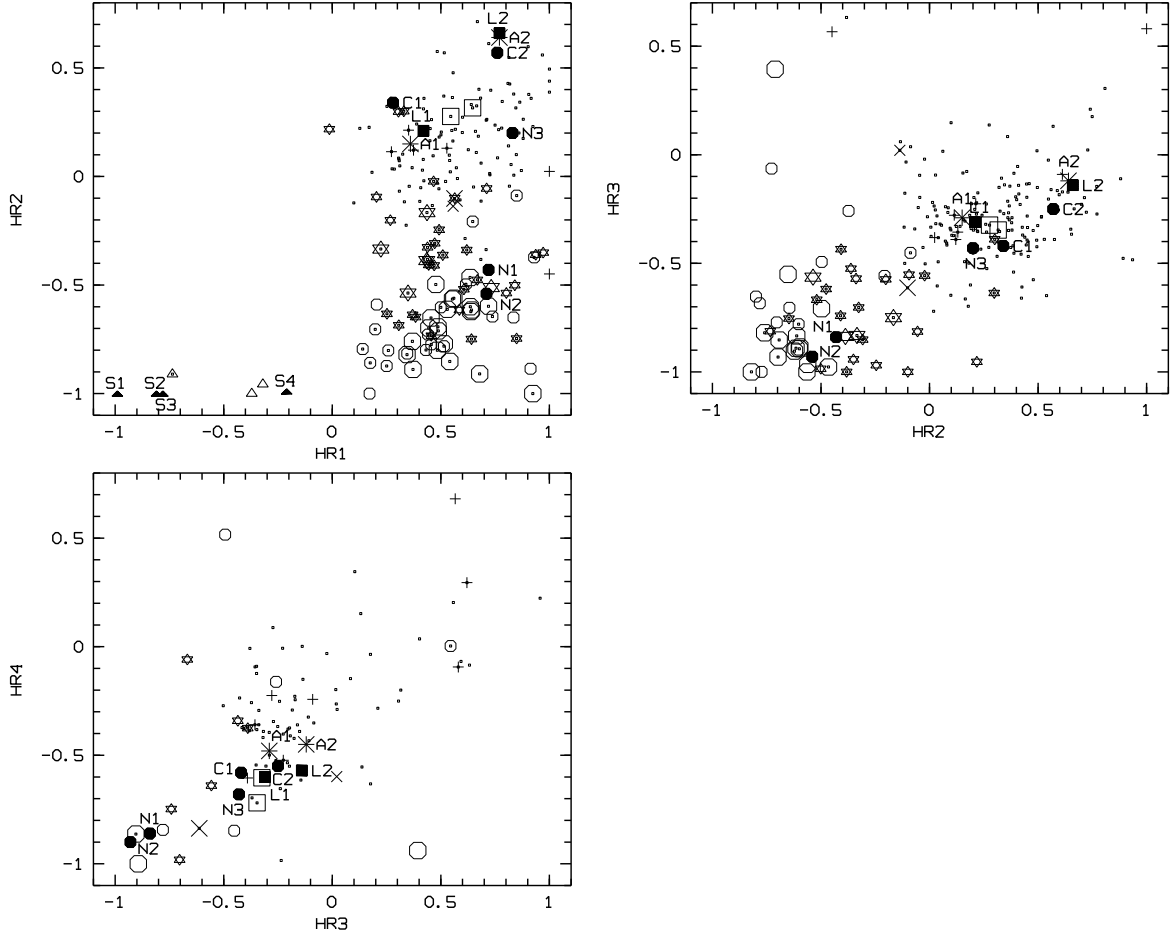


Figure 2.5: Hardness ratios of sources detected by XMM-Newton EPIC. Shown as dots are only values with errors smaller than 0.20 on both $HR(i)$ and $HR(i+1)$. Foreground stars and candidate are marked as big and small stars, galaxies and candidates as big and small x, AGN candidates as crosses, SSS candidates as triangles, SNR and candidates as big and small hexagons, XRBs as squares. In addition, we mark positions derived from measured XMM-Newton EPIC spectra and models for SSS (S1 to S4) as filled triangles, low mass XRBs (L1 and L2) as filled squares, SNRs (N132D as N1, 1E 0102.2-7219 as N2, N157B as N3, Crab spectra as C1 and C2) as filled hexagons, AGN (A1 and A2) as asterisks.

Table 2.5: Summary of identifications and classifications.

Source type	Selection criteria	identified	classified
fg Star	$\log(\frac{f_x}{f_{\text{opt}}}) < -1.0$ and $\text{HR2} < 0.3$ and $\text{HR3} < -0.4$ or not defined	5	30
AGN	Radio source and not classification as SNR from HR2		12
GAL	optical id with galaxy and $\text{HR2} < 0.0$	1	1
SSS	$\text{HR1} < -0.2$, $\text{HR2} - \text{EHR2} < -0.99$ or HR2 not defined, HR3 , HR4 not defined		5
SNR	$\text{HR1} > 0.1$ and $\text{HR2} < -0.4$ and not a fg Star	21	23
XRB	optical identification or X-ray variability	2	
hard	$\text{HR2-EHR2} > -0.2$ or only HR3 and HR4 defined, and no other classification		267

in subsections below).

Identification and classification criteria and results are discussed in detail in the subsections on individual source classes below. Many foreground stars, SSS and SNRs can be classified or identified. However, besides a few clearly identified XRBs and AGN, and SNR candidates with known positions at other wavelengths, we have no clear hardness ratio criteria (see below) to select XRBs, Crab-like SNR or AGN. They are all “hard” sources and we therefore introduced a class <hard> for sources with HR2 minus HR2-error greater than -0.2 (see Tab. 2.5).

A total of 43 sources remained unidentified or without classification.

2.6.1 Foreground stars (fgStar)

Foreground stars are a class of X-ray sources that is homogeneously distributed over the FOV of the M 33 survey. The good positioning of XMM-Newton and the available catalogue USNO-B1 allowed us to effectively select this type of sources. We identified five sources with stars of known type in the SIMBAD data base. Their X-ray fluxes were in the range expected for these sources. In addition, we classified 30 sources as foreground stars ($\log(\frac{f_x}{f_{opt}}) < -1$, see Maccacaro et al. (1988) and in addition HR2 < 0.3 and HR3 < -0.4). For several of the star candidates we estimated the type from the colours in the USNO-B1 catalogue using the stellar spectral flux library from Pickles (1998). For ten candidates we could not determine the type from the colours (28, 54, 77, 122, 128, 262, 308, 337, 371, 393). This may indicate that these sources are not isolated stars but more complicated systems or even, in some cases, galaxies. This expectation could, for instance, be confirmed for source 262, which was resolved into two sources in DSS2 images.

A special case was source 196, only $\sim 2'$ WSW of the nucleus. The source correlated with 2MASS J01334186+3038491, and was catalogued by Ivanov et al. (1993) as red star 184. The X-ray HRs, optical colour and $\log(\frac{f_x}{f_{opt}})$ point towards a foreground star of type M6 as the identification of this source.

From the HRs, sources 7 and 10 should be foreground stars. However, there was no candidate star within the error box. As these sources were at the border of the field, the systematic error may be underestimated and nearby stars may be candidates for the optical identification.

For source 240, the HRs indicated a foreground star, however $\log(\frac{f_x}{f_{opt}}) = -0.7$, larger than the assumed limit for classification. The optical colours would indicate a M10 III star. Also the other candidate stars of type late M have a rather high $\log(\frac{f_x}{f_{opt}})$.

For several sources, $\log(\frac{f_x}{f_{opt}})$ pointed towards a stellar identification (8, 38, 72, 176, 206, 209, 226, 234). However, only for three sources the HRs including errors were within the limits we assume for foreground stars (72, 176, 234).

2.6.2 Galaxies (GAL) and AGN

Already after the *Einstein* observations, the X-ray bright source X-9c (297) has been identified by Christian & Schommer (1982) with an elliptical galaxy at $z=0.03$. The

XMM-Newton X-ray luminosity of 1.35×10^{41} erg s⁻¹ (0.2–4.5 keV) was typical and the HRs were compatible with an elliptical galaxy spectrum (see HR plots).

From SIMBAD and NED searches, we found an additional galaxy correlation (namely source 358 = LEDA5899).

There were no correlations with AGN with known redshift within SIMBAD or NED. We therefore only classified 12 sources as AGN based on SIMBAD, NED, and other radio source correlations (NVSS, Gordon et al. (1999)) with the additional condition of being a <hard> X-ray source. A final decision will only be possible using optical spectra. In Fig. 2.5, we included typical HRs for an AGN spectrum (power law with photon index of 1.7 assuming Galactic foreground absorption (6×10^{20} cm⁻², A1) and absorption through the densest areas of M 33 (Newton 1980b, 4.8×10^{21} cm⁻², A2).

Sources 150 and 373 could be classified as SNRs, as well as AGN. They were identified as radio sources within the inclination-corrected M 33 D₂₅ ellipse, without optical identification as SNR by Gordon et al. (1999) and the radio spectral index did not clearly classify them as AGN.

2.6.3 Super-Soft Sources (SSS)

SSS show black body spectra with temperatures below 50 eV, they radiate close to the Eddington luminosity of a 1 M_⊙ object and they are believed to be white dwarf systems steadily burning hydrogen at the surface. They were identified as a class of X-ray sources by ROSAT and are often observed as transient X-ray sources (see Greiner 2000, and references therein). In the catalogue, SSS were only classified using their HRs. To guide the classification, we calculated SSS HRs assuming a 25 and 50 eV black body model spectrum assuming Galactic foreground absorption (S1 and S3) and absorption through the densest areas of M 33 (S2 and S4). This led to the selection criteria in Table 2.5 and the classification of five M 33 SSS (52, 109, 223, 247, 332). They were detected with absorbed luminosities of $(1-8) \times 10^{35}$ erg s⁻¹ in the 0.2-0.5 keV band. Only three of the sources (and the model HRs) could be plotted in Fig. 2.5. For the other two, HR2 was not determined.

2.6.4 Supernova remnants (SNR)

SNRs can be identified as sources where thermal components dominate the X-ray spectrum below 2 keV (examples are N132D in the Large Magellanic Cloud and 1E 0102.2-7219 in the Small Magellanic Cloud) and as so called “plerions” with power law spectra (examples are the Crab nebula and N157B in the Large Magellanic Cloud). To guide the classification we calculated HRs from archival XMM-Newton spectra of these SNRs. Spectra of N132D (N1), 1E 0102.2-7219 (N2), and N157B (N3) could be directly compared to M 33 SNRs, as they are seen through comparable foreground absorption. For the Crab nebula spectrum, we assumed Galactic foreground absorption (C1) and absorption through the densest areas of M 33 (C2). It is clear from Fig. 2.5, that “thermal” SNRs are located in areas of the X-ray colour/colour plots that only

overlap with foreground stars. If we assumed that we have identified all foreground star candidates from the optical correlation and inspection of the optical images, the remaining sources could be classified as SNRs with the criteria given in Table 2.5.

Extensive searches for SNRs in M33 were performed in the optical (see Gordon et al. 1998, and references therein) and radio (see Gordon et al. 1999, and references therein). Many X-ray sources in the catalogue correlated with optical and/or radio SNRs (see Table 2.3). We counted such sources as SNR identifications (21), if in addition they fulfilled the HR criteria (see above). We counted sources as classified SNRs (23), if they either just fulfilled the HR criteria (16) and were not identified or classified as foreground star, or if they correlated with optical/radio SNRs and did not fulfill the HR criteria (7).

From these classified SNRs, source 20 fulfilled the HR criteria, but was positioned outside the inclination-corrected optical D_{25} ellipse, while sources 101 and 266 were located between two optical SNR candidates and may represent the combined emission of both. As already mentioned in the subsection on AGN, we classify sources 150 and 373 as SNR as well as AGN due to the radio correlation.

A special case was source 227, which correlated with radio source 126 of Gordon et al. (1999), who classified it as a background source with no optical identification. The XMM-Newton HRs clearly indicated a SNR nature and we therefore classified the source as a SNR.

The giant HII regions BCLMP 290 and NGC 604 were detected as extended X-ray sources (125 and 299). While the HRs of source 299 indicated a spectrum similar to thermal SNRs (several SNRs would be necessary to explain the X-ray emission), the HRs of source 125 indicated a hard spectrum which may originate from several point sources (XRBs) or Crab-like SNRs. In the catalogue we only classified source 299 as a SNR.

Four additional sources in the catalogue (137, 154, 162, 280) had HRs compatible with the selection criteria in Table 2.5, within the errors. They are good candidates for further SNR investigations in M33.

2.6.5 X-ray binaries (XRB)

As already mentioned in the introduction to this section, expected spectra of XRBs are similar to AGN and Crab-like SNRs. To guide the classification, we calculated HRs as expected for low mass XRBs (5 keV thermal Bremsstrahlung spectrum assuming Galactic foreground absorption (L1) and absorption through the densest areas of M33 (L2)), which show soft spectra for XRBs. As can be seen in Fig. 2.5 these different source classes did not separate.

Therefore we only listed the black hole XRB X-8 close to the nucleus (211) and the 3.4 d eclipsing HMXB X-7 (171) as identified X-ray binaries.

SIMBAD searches indicated 16 more good XRB candidates from positional coincidences with optical stars of different type in M33 (see Table 2.3). Source 110 correlated with an emission line object and is a good candidate for a Be XRB, source 174 correlated with an eclipsing binary candidate (398 d period), and sources 194, 197,

and 323 with variable stars. Of historical interest is the optical candidate for source 323, VHK6. This source was discussed as one of four irregular variables in the paper by Hubble (1926), in which he proposed the spiral nebula M33 as a stellar system outside the Milky Way.

All the candidates mentioned above need further X-ray work to confirm their XRB nature.

2.7 Discussion

Besides the large number of point-like sources, there was a strong component of unresolved X-ray emission in the energy band below 2 keV. The overlay of X-ray on the DSS2 red image (Fig. 2.6) clearly showed the strong correlation with the inner disk and the southern and NW spiral arm. While some of this emission certainly is due to unresolved point sources, there is a significant contribution from hot gas in the disk which is more concentrated in the spiral arms and HII regions like NGC 604 12' NE and BCLMP 290 15' NW of the nucleus. A detailed analysis of this emission will be presented in a separate paper.

In the XMM-Newton source catalogue we presented 408 sources in the M33 field, 35 of which could be identified or classified as foreground stars and 14 as background AGN or galaxies. As sources in M33 we identified or classified 5 SSS, 44 SNRs, and 2 XRBs. 267 sources were classified as hard and may be either XRBs or Crab-like SNRs in M33 or background AGN. There remained 43 sources unclassified.

We can estimate the contribution of background sources to the source catalogue extrapolating from X-ray deep field number counts in the 0.5–2.0 keV and 2.0–8.0 keV bands (see e.g. Brandt et al. 2001; Rosati et al. 2002). We used rough sensitivity maps for our survey created by the SAS task `esensmap` for the 0.5–2.0 keV and 2.0–4.5 keV bands and an estimate for additional absorption in the line-of-sight. One expects about 175 to 210 background sources detected in our field-of-view, if we assume an overlap of sources detected in the hard and soft band of 75% or only 50%. Fourteen of the background sources have already been identified (see Sect. 2.6.2. Taking these numbers into account, up to 50% of the hard or unclassified sources should be sources within M33 (mostly XRBs or Crab-like SNRs).

We compared the XMM-Newton source catalogue with the ROSAT catalogue of HP01. While most of the bright ROSAT sources were also detected by XMM-Newton, many of the sources, only detected with the ROSAT HRI with a detection likelihood below 10, were not detected by XMM-Newton and seem to be spurious detections. From the seven ROSAT sources classified as SSS, we did not detect four. As expected for this source class, these might be transients, that were not active during the XMM-Newton observations (HP01 sources 43, 69, 76, 82). The remaining three seem to be false identifications: HP01 source 61 is now classified by XMM-Newton as a SNR, 84 as a foreground star and 124 as a hard source. Two ROSAT correlations with radio sources are no longer valid with the improved XMM-Newton positions (HP01 sources 63 and 147).

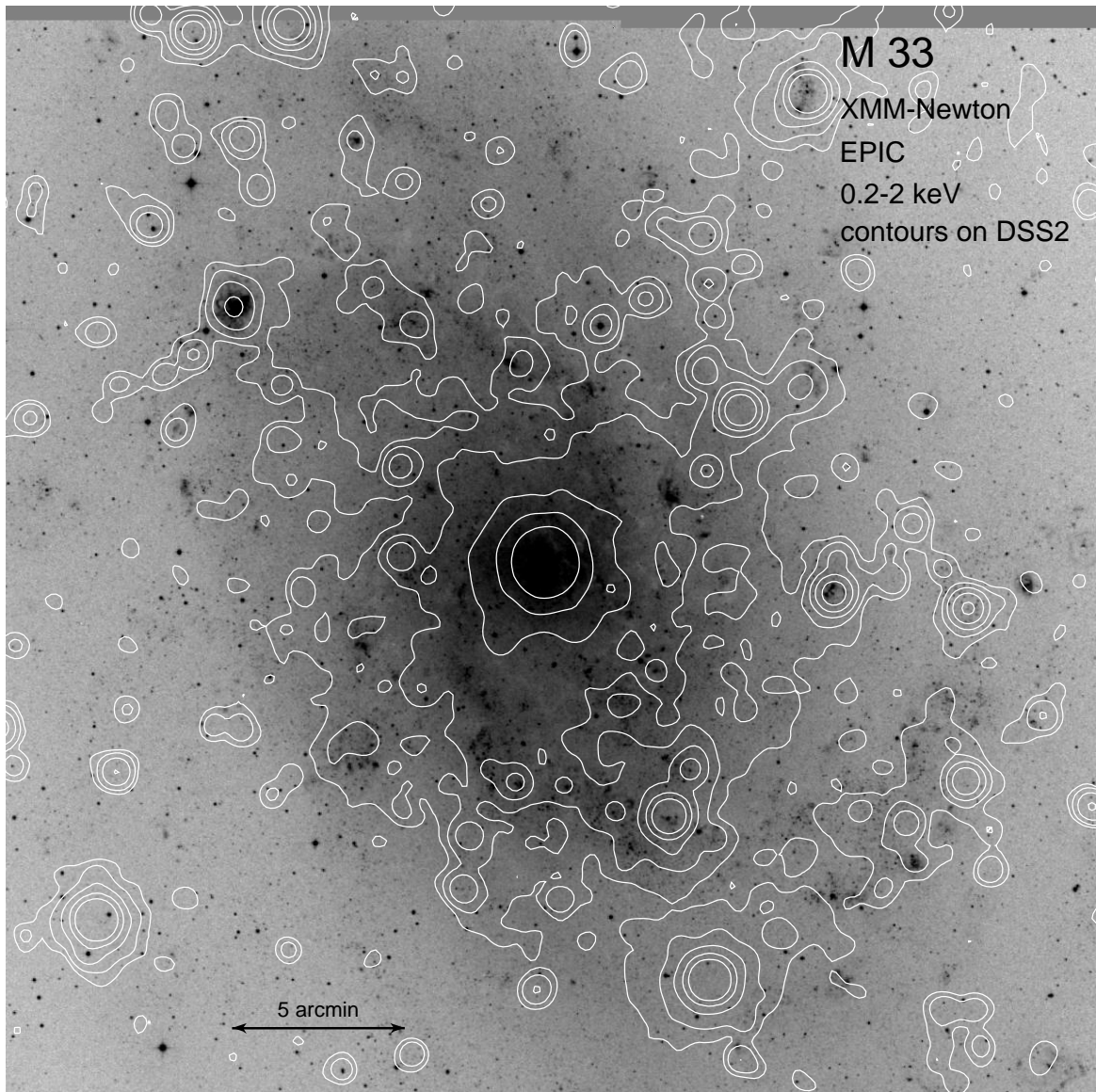


Figure 2.6: XMM-Newton EPIC 0.2-2 keV band contours of $(6,8,14,32,86) \times 10^{-5} \text{ ct s}^{-1}$ overlaid on an optical image of M33 extracted from the digitized sky survey (DSS2) red plates. The image scale is marked.

HP01 identified and classified 17 SNRs. The XMM-Newton source catalogue marks 21 identifications and 23 classifications. While the HR criteria seem to be rather robust for thermal SNRs, the identification of Crab-like remnants is doubtful and can only be secured by measurement of source extent. This may be possible with XMM-Newton EPIC for very extended SNRs (optical extent of SNR in M 33 vary from 9" to 126" according to Gordon et al. (1998)). Most of the sources, however, will need dedicated *Chandra* on-axis observations for a final decision on the extent. The *Chandra* count rates will not be sufficient to get good spectra and a combined XMM-Newton and *Chandra* analysis will be important for this class of sources.

The importance of combined XMM-Newton and *Chandra* data for M 33 XRB research was demonstrated in Pietsch et al. (2004b). This type of analysis extended to all brighter sources will be the subject of a future paper.

Chapter 3

An XMM-Newton survey of the Local Group galaxy M 33 - variability of the detected sources

Z. Misanovic, W. Pietsch, F. Haberl, M. Ehle, D. Hatzidimitriou, G. Trinchieri, 2005, A&A, in press

Abstract: We present an analysis of the individual observations of a deep XMM-Newton survey of the Local Group spiral galaxy M 33. We detected a total of 350 sources with fluxes (in the 0.2–4.5 keV energy band) in the range $6.7 \times 10^{-16} - 1.5 \times 10^{-11}$ erg s⁻¹. This comprehensive study considers flux variability, spectral characteristics, and classification of the detected objects. Thirty-nine objects in our catalogue are new sources, while 311 were already detected in a previous analysis of most of the same data using combined images. We present improved positions of these sources and the X-ray parameters of each source in each individual observation that covers the source. We then used these parameters to systematically search for flux variability on time scales of hours to months or years. The long-term light-curves were generated for the 61 sources showing a significant variability of the (0.2–4.5) keV flux, by a factor of 1.2 to 144. The detected variability was then used to classify 8 new X-ray binary candidates in M 33. Together with the hardness ratio method and cross-correlation with optical, infrared, and radio data, we also classify or confirm previous classification of 25 supernova remnants and candidates, 2 X-ray binaries, and 11 super-soft source candidates (7 of which are new SSS candidates). In addition, we classify 13 active galactic nuclei and background galaxies, 6 stars, and 23 foreground star candidates in the direction of M 33. Further 206 objects are classified as 'hard', approximately half of which are sources intrinsic to M 33. The relative contribution of the classified XRB and SSS in M 33 is now comparable to M 31. The luminosity distribution of SNRs in both spiral galaxies is almost the same, although the number of the detected SNRs in M 33 remains much higher.

3.1 Introduction

The nearby Sc type galaxy M 33 has been extensively studied in X-rays. Located at a distance of 795 kpc (van den Bergh 1991) and seen under a relatively low inclination angle of 56 deg (Zaritsky et al. 1989), M 33 allows detailed investigation of its source population and diffuse emission from hot gas in the disk.

A total of 17 discrete sources and some diffuse emission of the spiral arms in the vicinity of the nucleus were detected with the *Einstein* X-ray Observatory (Long et al. 1981a; Markert & Rallis 1983; Trinchieri et al. 1988b). These results were later confirmed with ROSAT HRI and PSPC observations, which also revealed a number of new point-like sources (Schulman & Bregman 1995; Long et al. 1996). Combining all ROSAT data, Haberl & Pietsch (2001) compiled a catalogue of 184 sources in the direction of M 33, and classified the brightest objects using their X-ray properties and identification with optical and radio counterparts.

Pietsch et al. (2004a) (hereafter PMH2004) and Pietsch et al. (2003a) have presented the first results of a deep homogeneous XMM-Newton survey of M 33. With a sensitivity of 10^{35} erg s⁻¹ in the 0.2–4.5 keV band, this survey is ten times more sensitive than any previous X-ray observation of M 33. It consists of 24 raster 10-ks observations of 15 overlapping fields covering the whole optical D₂₅ extent of M 33 (some fields are re-observed), performed between August 2000 and July 2003. PMH2004 have analysed combined images of the 22 observations made with the medium and thin filters, and detected a total of 408 objects. Having obtained the largest sample of X-ray sources in M 33 to-date, PMH2004 have made use of the broader spectral coverage provided by XMM-Newton to establish criteria for source classification based on hardness ratios. Applying this method, together with cross-correlations with optical and radio catalogues, PMH2004 were able to classify approximately 350 of the detected X-ray sources.

In this paper we present the results of analysis applied to all 24 XMM-Newton observations of M 33 individually, using a less stringent background rejection than in PMH2004 and a more accurate description of the Point Spread Function (PSF). Since our data span a period of almost three years, we were able to study long-term X-ray flux variability of our sample and to use it, together with other methods, to constrain the nature of the detected sources. In addition, we detected new sources in the individual images, and present more accurate X-ray positions of the majority of the sources already detected in the combined data. The paper is organised as follows: in Sect. 3.2 we present XMM-Newton EPIC observations and data reduction techniques; Sect. 3.3 describes how the new catalogue was produced; Sect. 3.4 and Sect. 3.5 present the catalogue and the images of the individual observations. We compare the new catalogue with the combined data catalogue of PMH2004 in Sect. 3.6, and also cross-correlate it with optical, infrared and radio catalogues (Sect. 3.7). Section 3.8 summarises statistical properties of the variable X-ray source population in M 33. Finally, classification and properties of the detected X-ray sources, including their spatial and luminosity distribution, are presented in Sect. 3.9, while Sect. 3.10 summarises our results. We also include the full band images of all 24 observations showing the detected sources

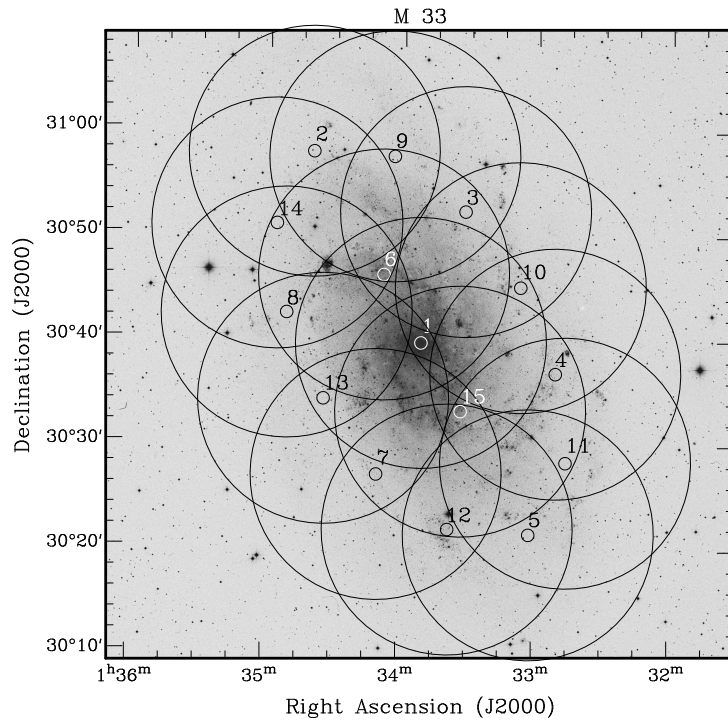


Figure 3.1: The XMM-Newton EPIC observation fields overlaid on an optical (DSS-2 red) image of M 33. The fields of view (FoV) are approximated by circles of $15'$ radius centred at the positions given in Table 3.1.

(Appendix A) and long-term light-curves of all variable sources detected in our sample (Appendix B).

3.2 Observations and data reduction

We present analysis of all 24 archival raster XMM-Newton (Jansen et al. 2001) observations of M 33. The data analysis was performed using the XMM-Newton Science Analysis System (SAS) v6.0, IDL v6.0, EXSAS/MIDAS 1.4, and FTOOLS v5.3 software packages, the imaging applications DS9 v3.0b6 and KVIS v0.0.11 and the count rate simulator W3PIMMS v3.6a. Most observations were obtained in the Full Frame mode and medium filter, two with the thick filter, and only one exposure of EPIC MOS2 was obtained with the thin filter, as summarised in Table 3.1. Table 3.1 also lists the observation ID and date, and the exposure times for EPIC PN (Strüder et al. 2001), MOS1, and MOS2 (Turner et al. 2001) that we have obtained after cleaning for episodes of high background, as we explain later. Figure 3.1 shows the location of the observed fields overlaid on an optical (DSS-2) image of M 33.

For each pointing we produced PN, MOS1, and MOS2 event files using the SAS tasks `epchain` and `emchain`, and then manually flagged the remaining bad CCD pixels, which we recognised visually on the images but could not clean with the standard

Table 3.1: The XMM-Newton M 33 observation log (proposal numbers 010264 and 014198).

Field	Obs. ID.	Date	Pointing direction		EPIC PN	EPIC MOS1			EPIC MOS2	
M 33			RA/DEC (J2000)		Mode ⁺ /Filter	T _{exp} [†]	Mode ⁺ /Filter	T _{exp} [†]	Mode ⁺ /Filter	T _{exp} [†]
(1)	(2)	(3)	(4)	(5)	(6)	(7)	(8)	(9)	(10)	(11)
1a	0102640101	2000-08-04	1:33:51.0	30:39:37	FF/medium	6.09	PW2/medium	10.11	PW2/medium	9.81
1b	0141980501	2003-01-22	1:33:51.0	30:39:37	FF/medium	3.63	FF/medium	7.86	FF/medium	7.86
1c	0141980801	2003-02-12	1:33:51.0	30:39:37	FF/medium	8.55	FF/medium	10.16	FF/medium	10.16
2a	0102640201	2000-08-04	1:34:40.0	30:57:48	EFF/medium	12.10	FF/medium	16.24	FF/medium	15.94
3a	0102640301	2000-08-07	1:33:32.0	30:52:13	EFF/medium	9.10	FF/medium	13.69	FF/thin	13.69
3b	0141980401	2003-01-24	1:33:32.0	30:52:13	FF/medium	7.71	FF/medium	11.53	FF/medium	11.64
4a	0102640401	2000-08-02	1:32:51.0	30:36:49	EFF/thick	9.20	FF/thick	12.69	FF/thick	12.99
4b	0141980601	2003-01-23	1:32:51.0	30:36:49	FF/medium	11.38	FF/medium	13.31	FF/medium	13.59
5a	0102640501	2001-07-05	1:33:02.0	30:21:24	FF/medium	9.26	FF/medium	11.76	FF/medium	11.76
6a	0102640601	2001-07-05	1:34:08.0	30:46:06	FF/medium	6.56	FF/medium	11.76	FF/medium	11.76
6b	0141980301	2003-07-25	1:34:08.0	30:46:06	FF/medium	9.52	FF/medium	11.20	FF/medium	11.50
7a	0102640701	2001-07-05	1:34:10.0	30:27:00	FF/medium	6.86	FF/medium	11.40	FF/medium	11.39
8a	0102640801	2001-07-07	1:34:51.0	30:42:22	FF/medium	-	FF/medium	2.54	FF/medium	2.55
8b	0102642001	2001-08-15	1:34:51.0	30:42:22	FF/medium	8.65	FF/medium	11.46	FF/medium	11.46
9a	0102640901	2001-07-07	1:34:04.0	30:57:25	FF/medium	7.31	FF/medium	12.51	FF/medium	12.51
9b	0141980201	2003-07-11	1:34:04.0	30:57:25	FF/medium	12.14	FF/medium	15.57	FF/medium	15.57
10a	0102641001	2001-07-08	1:33:07.0	30:45:02	FF/medium	4.06	FF/medium	8.74	FF/medium	8.73
10b	0141980101	2003-07-11	1:33:07.0	30:45:02	FF/medium	9.68	FF/medium	6.81	FF/medium	6.84
11a	0102641101	2001-07-08	1:32:46.0	30:28:19	FF/medium	7.50	FF/medium	10.50	FF/medium	10.20
12a	0102641201	2000-08-02	1:33:38.0	30:21:49	EFF/thick	11.30	FF/thick	3.07	FF/thick	2.75
12b	0141980701	2003-01-24	1:33:38.0	30:21:49	FF/medium	7.48	FF/medium	5.40	FF/medium	5.40
13a	0102642101	2002-01-25	1:34:34.0	30:34:11	FF/medium	9.96	FF/medium	12.27	FF/medium	12.27
14a	0102642201	2002-01-25	1:34:56.0	30:50:52	FF/medium	11.60	FF/medium	13.87	FF/medium	13.87
15a	0102642301	2002-01-27	1:33:33.0	30:33:07	FF/medium	10.00	FF/medium	12.27	FF/medium	12.27

Notes:

+ : FF: full frame; EFF: extended full frame; PW2: partial window 2

† : Exposure time in units of ks after background screening to produce the maximum signal-to-noise ratio (see text).

processing. The calibration index files appropriate for the times of observations were generated using the SAS task `cifbuild`. To optimise the source detection in each field, we then selected the good time intervals (GTIs), which produced the maximum signal-to-noise ratio (S/N) in each exposure. The maximum S/N was calculated using the formula: $S/N \sim t_{exp}/(R_{bkg})^{1/2}$, where t_{exp} is the total exposure time after the background screening, and R_{bkg} is the remaining background rate in the image. Such a selection of GTIs results in longer exposure times than those used in PMH2004, since there they had to apply a homogeneous, hence more restrictive, criterion for high background rejection. In addition, PMH2004 had to exclude the (7.2–9.2) keV energy range in order to avoid background variability caused by strong fluorescence lines (Freyberg et al. 2004). When analysing each field individually, however, this was not required.

We produced images from each PN, MOS1, and MOS2 event list in five energy bands: (0.2–0.5) keV, (0.5–1.0) keV, (1.0–2.0) keV, (2.0–4.5) keV, and (4.5–12.0) keV (bands B1 to B5, respectively). We split the standard (0.5–2.0) keV band into two (0.5–1.0 and 1.0–2.0 keV) bands, to be able to apply the hardness ratio method for source classification, introduced by PMH2004. For our PN images in band 1 we selected only single-pixel events (`PATTERN=0`), and single and double-pixel events (`PATTERN≤4`) for the other energy bands. We used this `PATTERN` selection because of the relatively higher noise in the softest PN band. For all five bands of the MOS data, we used 1–4 pixel events (`PATTERN≤12`), and for each image we produced the corresponding exposure map corrected for vignetting, and also the detector masks to limit the source detection to the detector areas only. These images were then used to run the source detection procedures (described in Sect. 3.3) separately for each observation.

3.3 Production of the catalogue

3.3.1 Source detection

We run our source detection procedure separately for each pointing, for the 5 energy bands and 3 instruments (in total 15 images) simultaneously, and following the standard method (see e.g. Haberl et al. 2003). Our PN background maps also included the out-of-time (OOT) events, so they did not affect our source detection results. The SAS task `emldetect` was used to determine the parameters of the detected sources by using a maximum likelihood fit. We selected the likelihood threshold value (`DET_ML`) of 7 to include a source in the list of the detected sources. As noted by PMH2004, this value was found to be approximately equivalent to the single instrument likelihood of ten, and it corresponds to a 3 – 4 σ detection.

Since the fields of view overlap, we cross-correlated the individual source lists to eliminate multiple detections of the same source. The final position was taken from the observation in which the source has the smallest statistical positional error, which corresponds to the smallest off-axis angle, in most cases.

The positions of the sources common to more than one field were also used to determine the relative astrometry of the observations (see Sect. 3.3.2). All positions

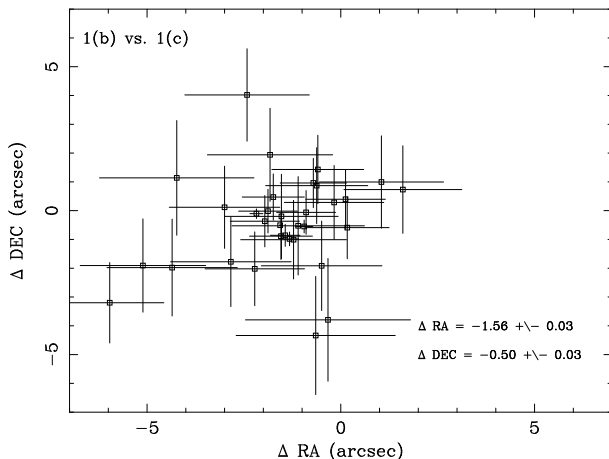


Figure 3.2: The RA and DEC offsets of the cross-correlated sources in the observations 0141980501 (1b) and 0141980801 (1c). The error bars represent the combined statistical errors of both X-ray positions. The relative offsets between the two observations are given as the weighted mean of RA and DEC in arcsec.

listed in the final catalogue are corrected for that offset.

We determined the X-ray parameters (likelihoods of existence, count rates, fluxes, and hardness ratios) for each source in each individual observation, even when the source is below the detection threshold in that particular observation. This was done by running `emldetect` again with the final position of each source as an input parameter (`'fitposition=no'`). By selecting the detection threshold of zero, we obtained the vignetting corrected count rates and corresponding fluxes for each source within the field of view of each observation. For non-detections, we determined a 3σ upper limit of the flux.

Finally, to search for extended emission in our sources we repeated the whole procedure optimised for the extended source detection (`'fitextent=yes'` in `emldetect`).

3.3.2 Source positions

We determined the relative shifts between our overlapping observations using the positions of the common sources. Sources were considered detected in two different fields if their positions were closer than $3\times$ the combined statistical errors. We corrected all X-ray positions relative to the observation 0141980801 (1c), since the X-ray source positions in this observation showed the smallest offset with respect to optical and infrared counterparts in our preliminary analysis. Moreover, this field has sources in common with all other fields.

As one example, we show the RA and DEC offsets of the observation 0141980501 (1b) with respect to the reference observation 0141980801 (1c) in Fig. 3.2. Similarly, we calculated the average offsets of all observations with respect to our reference pointing (listed in Table 3.2), and corrected all catalogued X-ray positions.

To determine the systematic errors in the X-ray positions we cross-correlated the final X-ray catalogue with optical (USNO-B1, Monet 1998) and infrared (2MASS,

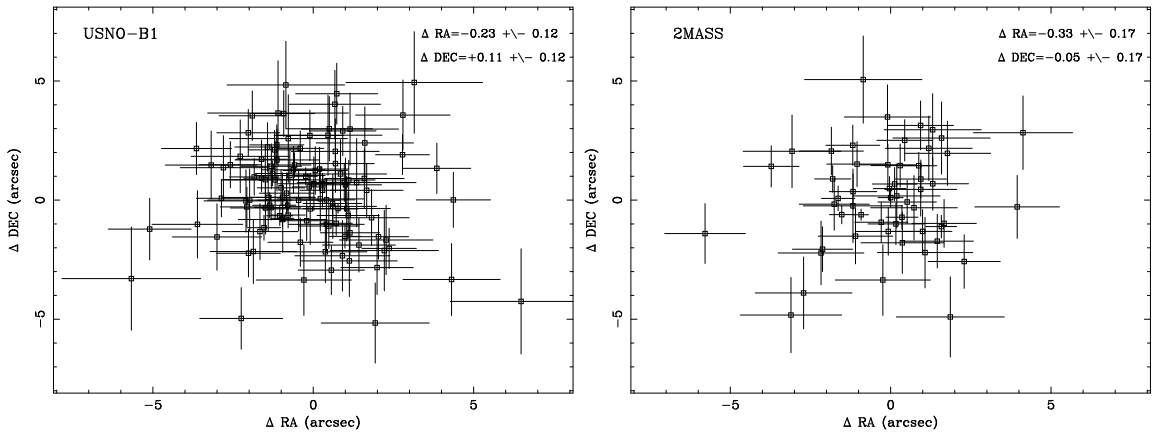


Figure 3.3: *Left: The RA and DEC offsets of the USNO-B1 counterparts. The error bars represent the combined errors of the statistical error of the X-ray position and corresponding optical source error. The shifts of the X-ray observation with respect to optical data are given as the weighted mean of RA and DEC in arcsec. Right: The RA and DEC offsets of the 2MASS counterparts. The error bars represent the combined errors of the statistical error of the X-ray position and corresponding infrared source error. The shift of the X-ray observation with respect to 2MASS data are given as the weighted mean of RA and DEC in arcsec.*

Skrutskie et al. 1997) catalogues. We used a distance of $< 3 \times$ the combined X-ray and optical/IR positional error to associate the object to the X-ray source. We identified 113 counterparts in USNO-B1 and 54 in the 2MASS catalogue (Fig. 3.3), but could not find any significant offset in RA and DEC when compared to either of the catalogues. The 1σ residual systematic positional error of $0''.5$ was then added quadratically to the statistical uncertainties of the detected sources.

3.3.3 Hardness ratios, fluxes, and variability factors

To characterise the spectra of the detected sources, we computed four hardness ratios (HR) for each instrument, defined as $HR_i = (R_{i+1} - R_i) / (R_{i+1} + R_i)$, for $i = 1$ to 4, where R_i denotes the count rate in band Bi. In addition, we calculated the total count rates in each energy band by combining the count rates from all three instruments in a given band and used them to compute the combined hardness ratios. As discussed by PMH2004, due to improved statistics, these combined hardness ratios are useful for source classification.

To convert the vignetting corrected count rates to fluxes in the individual energy bands, we used the energy conversion factors (ECF) for the PN and MOS medium, thin and thick filters calculated using W3PIMMS, taking 100% of the source counts and assuming a power law spectrum with a photon index of 1.7 absorbed by the Galactic foreground column of $6 \times 10^{20} \text{ cm}^{-2}$ (Table 3.3). The assumed model fits the majority of the sources in our sample well i.e. XRBs, AGN, or 'hard' sources, while it leads to an underestimation of the flux of soft sources (SNR, foreground stars, SSS) by approximately 10–20%, or even higher for extremely soft sources like SSS, especially

Table 3.2: The RA and DEC offsets of the M33 XMM-Newton observations with respect to observation 1c.

Field	Obs. ID.	Offsets	
M33		$\Delta\text{RA}(\prime\prime)$	$\Delta\text{DEC}(\prime\prime)$
(1)	(2)	(3)	(4)
1a	0102640101	-0.38 ± 0.04	$+0.31\pm 0.04$
1b	0141980501	-1.56 ± 0.03	-0.50 ± 0.03
1c	0141980801	–	–
2a	0102640201	$+2.48\pm 0.09$	$+0.16\pm 0.09$
3a	0102640301	$+1.12\pm 0.05$	$+0.25\pm 0.05$
3b	0141980401	-0.62 ± 0.06	$+1.89\pm 0.06$
4a	0102640401	$+1.57\pm 0.06$	-0.54 ± 0.06
4b	0141980601	-1.41 ± 0.07	$+0.00\pm 0.07$
5a	0102640501	-1.11 ± 0.25	-0.93 ± 0.25
6a	0102640601	$+1.44\pm 0.04$	-1.73 ± 0.04
6b	0141980301	$+0.93\pm 0.04$	-1.41 ± 0.04
7a	0102640701	-1.12 ± 0.07	-1.28 ± 0.07
8a	0102640801	$+0.37\pm 0.21$	-2.29 ± 0.21
8b	0102642001	$+1.87\pm 0.06$	-0.74 ± 0.06
9a	0102640901	-0.54 ± 0.22	-1.00 ± 0.22
9b	0141980201	-1.32 ± 0.23	$+0.56\pm 0.23$
10a	0102641001	-0.32 ± 0.05	$+0.09\pm 0.05$
10b	0141980101	-1.28 ± 0.05	-1.13 ± 0.05
11a	0102641101	-2.00 ± 0.24	-0.41 ± 0.24
12a	0102641201	-0.03 ± 0.02	-0.41 ± 0.02
12b	0141980701	-1.43 ± 0.17	-0.79 ± 0.17
13a	0102642101	-0.74 ± 0.03	-1.08 ± 0.03
14a	0102642201	$+0.54\pm 0.18$	-0.14 ± 0.18
15a	0102642301	$+0.33\pm 0.12$	-0.92 ± 0.12

Table 3.3: Count rate to energy conversion factors for different filters of the EPIC instruments in the energy bands B1–B5, assuming a power law model with a photon index of 1.7 and the Galactic foreground absorption of $6 \times 10^{20} \text{ cm}^{-2}$ (Stark et al. 1992).

Detector	Filter	B1	B2	B3	B4	B5
EPIC		$(10^{-12} \text{ erg cm}^{-2} \text{ ct}^{-1})$				
PN	Medium	1.03	1.10	1.71	4.90	17.07
	Thin	0.87	1.07	1.68	4.83	17.05
	Thick	1.82	1.45	1.96	5.12	17.27
MOS	Medium	6.16	4.89	4.83	12.93	65.71
	Thin	5.33	4.72	4.75	12.78	65.61
	Thick	10.36	6.34	5.53	13.50	66.61

if they are detected only in MOS data (see Table 2 in PMH2004).

To be able to compare our results with the combined data catalogue, we present the total count rates and corresponding fluxes in the “XID” band (0.2–4.5 keV), introduced by PMH2004. As they note, band B5 suffers from the combined effect of lower sensitivity and a large contamination from the hard background, increasing the noise of all but extremely hard sources.

Since the analysed observations span a period of three years, and are separated by several hours to several months or years, we used them to study X-ray variability on the corresponding time scales. To search for variable sources in our sample, we compared their XID fluxes (or upper limits for non-detections) in different observations. We characterise X-ray variability of each source by its variability factor, defined as $V = F_{max}/F_{min}$, where F_{max} and F_{min} are the source XID maximum and minimum (or upper limit) flux, respectively. In addition, we calculate a linear significance parameter defined as $S = (F_{max} - F_{min})/\sqrt{(\sigma_{max}^2 + \sigma_{min}^2)}$, where σ_{max}^2 and σ_{min}^2 are the errors of the maximum and minimum flux, respectively (Primini et al. 1993). We define a source as “variable” if $S > 3$. If the minimum XID flux is a non-detection, we use the 3σ XID flux upper limit to calculate the lower limit of the variability factor. This is indicated by the variability flag (V_FLAG) value of 1 in Table 3.4 (V_FLAG=0 for detections).

3.4 Description of the catalogue

We detected 350 X-ray sources in the 24 individual observations of the XMM-Newton survey of M 33. Most of the sources in our catalogue have been detected in more than one pointing, which gives us an opportunity to study their X-ray variability (Sect. 3.8). The results of the survey are summarised in Tables 3.4 and 3.5 (available only in electronic form at the CDS).

Table 3.4 lists the source identification number (col. 1), source number from the catalogue of PMH2004 when available (col 2), and the final source position (3, 4) (see Sect. 3.3.2). The total positional error, which includes the statistical and systematic error of 0."5 quadratically summed, is listed in col. 5, while columns 6, 7, 8, 9, and 10 present the maximum of the detected XID flux and error, variability factor V, significance parameter S and variability flag (as described in Sect. 3.3.3). The remaining columns of Table 3.4 list the results of the cross-correlation with X-ray, optical, infrared, and radio catalogues, which are described in detail in Sect. 3.7. Column 11 lists all cross-correlations with sources detected in earlier X-ray surveys of M 33 (Long et al. 1981a; Trinchieri et al. 1988b; Schulman & Bregman 1995; Long et al. 1996; Haberl & Pietsch 2001), including X-ray variability and other information presented in these catalogues. The detected USNO-B1 counterparts and corresponding X-ray to optical flux ratio (see Sect. 3.7) are listed in columns 12 and 13, respectively, while columns 14–17 present 2MASS counterparts and their J, H, and K-band magnitudes. Columns 18 and 19 list the identified radio counterparts from the NRAO VLA Sky Survey (Condon et al. 1998) and their catalogued 1.4 GHz flux. Column 21 gives all previous source identifications found in the lists of optically and radio selected SNRs

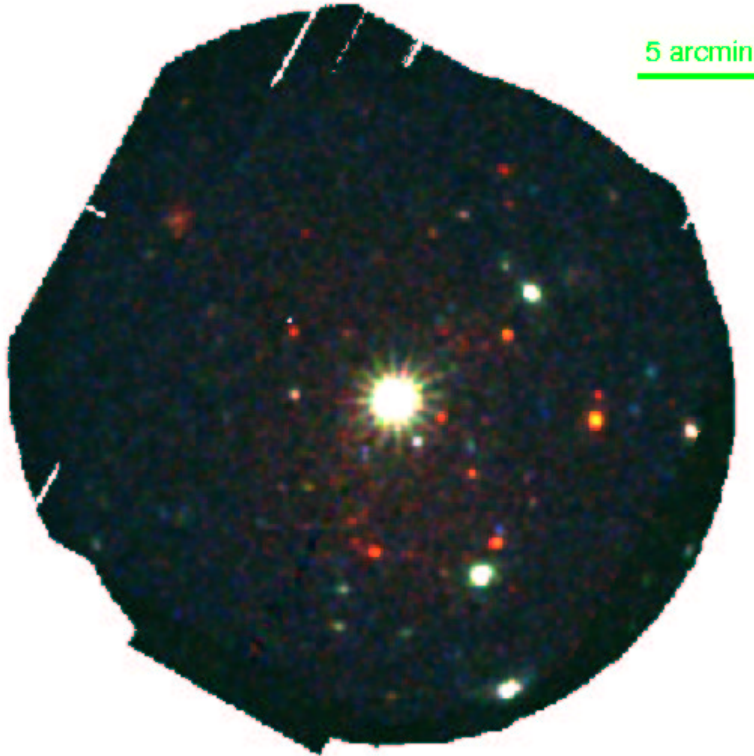


Figure 3.4: Linearly-scaled, three-colour XMM-Newton EPIC image of observation 1c combining PN, MOS1, and MOS2 data. Red, green, and blue show, respectively, the (0.2–1.0) keV, (1.0–2.0) keV and (2.0–12.0) keV bands. The data in each energy band were smoothed with a Gaussian of FWHM $6''$.

(Gordon et al. 1998, 1999), and also in SIMBAD and NED data bases. The final source classification is given in column 20, and we discuss it further in Sect. 3.9.

Table 3.5 presents the parameters of each source separately for each pointing. Most of the sources are listed in more than one row, each of which summarises the parameters of a single observation. If the source was not detected in a given observation (likelihood of detection < 7) but is included in the FoV, the vignetting corrected upper limits are listed. The columns are: the source number (1), observation (2), likelihood of existence (3), integrated count rate and error (4,5), flux and error in the 0.2–4.5 keV band (6,7), and hardness ratios and errors (8–15), all from the combined PN, MOS1, and MOS2 data. Note that hardness ratios were calculated only for the sources for which the significance of at least one of the contributing count rates is greater than 2σ . The EPIC PN parameters are listed in columns 16–29: exposure (16), likelihood of the source existence (17), count rate and error (18,19), XID flux and error (20,21), and hardness ratios and errors (22–29). The EPIC MOS1 and EPIC MOS2 parameters are listed in the same order in columns 30–44 and 45–59, respectively.

Sources #113 and #254 are detected as extended sources (see Sect. 3.3.1). Since they are the only two sources with a reliable estimate of the extent parameter in

all those fields in which they are detected (extent of $11''.2$ and $12''.3$ respectively), we list the parameters that were obtained assuming they are extended sources (see details in Sect. 3.3.1). While several other sources are detected as “extended” in some observations, we believe that their extent is the result of a poor modelling of the PSF at large off-axis angles, and therefore we list them as point sources in the catalogue.

The faintest source (#264) detected in our sample has the XID flux of 6.7×10^{-16} erg cm $^{-2}$ s $^{-1}$, which is slightly below the sensitivity threshold of the combined data catalogue. However, the source is only detected with PN, and its catalogued flux is calculated as the average flux of all three detectors, and hence reduced. We have only three such faint sources that were detected with PN (#264, #212, #292). The lowest XID flux detected with approximately the same likelihood in all three detectors is 1.8×10^{-15} erg cm $^{-2}$ s $^{-1}$ (#325). The brightest source, X-8 (#182), was detected with an XID flux in the range $(1.0-1.5) \times 10^{-11}$ erg cm $^{-2}$ s $^{-1}$. Sources #111, #153, #282, and #339, detected in the first run of `emldetect` when the detection program had fit the source positions, fell slightly below the detectability threshold of 7 in the ‘fixed position’ run of `emldetect`. This means that the actual positions of these sources are slightly different than our catalogued positions. However, since our detectability threshold is determined in the first run of `emldetect`, these sources are included in the catalogue. The XID fluxes of the rest of the detected sources are different by less than 5% in the two runs of `emldetect`.

3.5 Images

Figures A.1 to A.6 (Appendix A) show the broad band (0.2–12.0 keV) images of all 24 XMM-Newton observations, for PN, MOS1, and MOS2 data combined. The images were smoothed with a Gaussian of FWHM $6''$, with OOT events excluded from the PN data. The background levels are different in each image, because we cleaned the images to maximise the signal-to-noise ratio in each image individually (see Sect. 3.2). Onto each image we overlaid the sources detected in that field (big circles), together with the positions of the sources from our catalogue that are covered by that observation but are below the detection threshold (small circles).

Figure 3.4 illustrates the existence of sources with X-ray colours (*i.e.* spectra) that are different from the average population; some sources appear red because their X-ray emission is strongest at energies below 1.0 keV. Others are blue because they are more prominent in the hard band.

3.6 Comparison to the PMH2004 catalogue

We cross-correlated our final source list with the combined data catalogue of PMH2004. As expected, the majority of our sources (311) were also detected in the combined images. We also detected 39 sources that are not included in the PMH2004 list. All except 3 of these new sources (#180, #208 and #255) were detected in one field only, either because of relatively higher background in some images, or because these

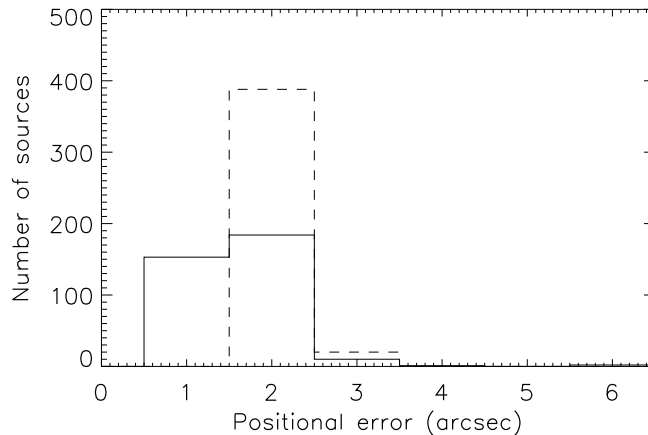


Figure 3.5: Histograms of the total positional errors in the individual (full line, this work) and combined (dashed line, PMH2004) data catalogues.

sources are variable or even transient. Several of the sources (e.g. #32, #92, #109, #140, #143, #208) were actually clearly visible in the combined image but too weak or smeared to be picked up by the detection algorithm. Sources #1 and #185 were detected near the edges of the two thick filter observations that were not included in the combined image.

With the method described in Sect. 3.3.2, we were able to improve on the X-ray positions with respect to PMH2004. This was confirmed when we compared ours and the PMH2004 RA and DEC offsets between the X-ray and optical positions for all stars identified as secure optical counterparts, and also for all identified 2MASS counterparts. Our positions were more evenly distributed around a value of 0 than those of PMH2004, which show consistent systematic RA and DEC shifts with respect to optical and infrared data, of approximately $-1''$ in RA, and $< 1''$ in DEC. The shifts are within the systematic error of $1.5''$ in the combined catalogue determined by PMH2004. The smaller systematic error that we estimate for our data also translates into an improved estimate of the total positional errors for most bright sources (Fig. 3.5).

We compared the XID fluxes and hardness ratios for the 311 sources in common with the PMH2004 catalogue. Figure 3.6 shows the result of the comparison for SNRs – sources that are expected to show no intrinsic flux variability. For each confirmed SNR and SNR candidate in our data and detected in more than one pointing, we plot the XID flux from PMH2004, and the maximum and minimum XID flux measured in the individual observations. The maximum and minimum flux values are consistent, as for most sources they are within the $\sim 1\sigma$ of the combined statistical flux errors. A dispersion of up to 2σ for a few SNRs is just the result of a normal statistical deviation in a sample of 10–15 measurements. For example, in Fig. 3.7 we show the measured fluxes in all 13 observations of one such SNRs (SRC #211). Only one measurement (the maximum) is slightly higher than the rest, but it is determined with a large error,

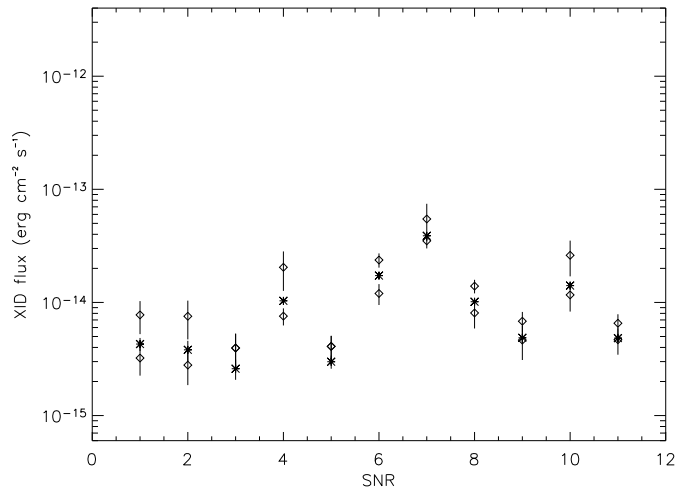


Figure 3.6: The maximum and minimum XID fluxes determined in the individual observations (marked as diamonds) for a sample of SNRs detected in both catalogues. The XID fluxes determined in the combined image (PMH2004) are marked as asterisks. As expected, SNRs show no significant variability, *i.e.* the maximum, minimum, and combined catalogue fluxes are within the 3σ of the statistical errors.

in an observation with short exposure and high background. Hence, the detected variability factor of 2.24 is not significant ($S = 1.49$). The light-curves of all other SNRs and candidates are similar, confirming their classification.

The situation is different for the sample of highly variable sources (Fig. 3.8). The flux measured in the combined data is not the intrinsic source flux, but it represents only the averaged high and low state flux measured in the individual images. Its value depends on how many low and high state observations are included in the combined image. For some sources that are in the low state in all or most observations, the combined data flux can even be below the upper limit of the minimum flux determined in individual images.

Due to better statistics, the flux errors in the combined data catalogue are significantly smaller, and hence, the hardness ratios could be more accurately determined for the majority of the detected sources.

There are 97 sources listed in the PMH2004 catalogue that are below the detection threshold in all individual images and, hence, not detected here. These sources, with fluxes in the range of $1.15 \times 10^{-15} \text{ erg cm}^{-2} \text{ s}^{-1}$ to $1.05 \times 10^{-14} \text{ erg cm}^{-2} \text{ s}^{-1}$, were detected in the regions in which the combined image is more sensitive, due to the much longer exposure.

3.7 Cross-correlations with other catalogues

We used the positions listed in Table 3.4 for a systematic cross-correlation with X-ray (Haberl & Pietsch 2001, and references therein), optical (USNO-B1, Monet 1998),

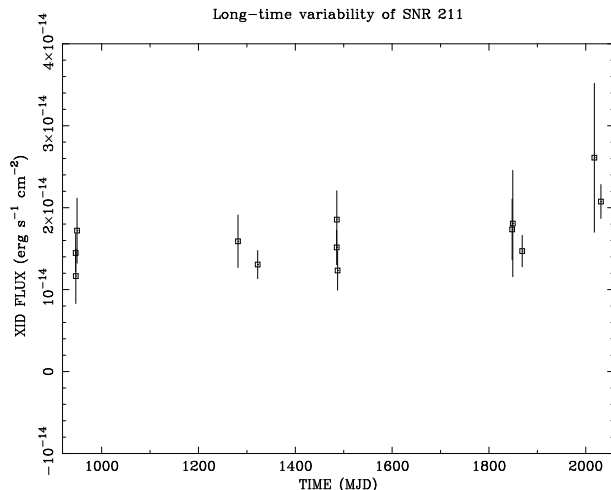


Figure 3.7: The long-term X-ray light-curve of an SNR (SRC #211), detected in 13 individual images. The time is given in days, with the reference day at JD 2450814.5. The maximum, minimum, and average (PMH2004) flux are also shown in Fig. 3.6 (SNR number 10). Only the maximum flux deviates slightly from the rest of the measurements. However, its error is large, so the calculated variability factor of 2.24 is not significant ($S=1.49$).

infrared (2MASS, Skrutskie et al. 1997), and radio (NRAO VLA Survey, Condon et al. 1998) catalogues, with a radius equal to the 3σ error (col. 5 of Table 3.4) of each source. The results are listed in Table 3.4. We confirm most of the identifications proposed by PMH2004, and only comment on a few differences and new entries.

The additional cross-correlations with the ROSAT M33 catalogue of Haberl & Pietsch (2001) are: HP6, HP68, HP90, HP128 (cross-correlated with new sources not detected in the combined data), and HP64 (a strong source also detected in the combined image but with the position just outside the 3σ distance from the ROSAT source).

In most cases we identified the X-ray source with the brightest of the sources in the USNO-B1 catalogue that falls within the search region. We then used the X-ray to optical flux ratio, calculated as $\log(\frac{f_x}{f_{opt}}) = \log(f_x) + (m_{B2} + m_{R2}) / (2 \times 2.5) + 5.37$, following Maccacaro et al. (1988), to distinguish foreground stars from SNRs and AGN (see Sect 3.9). For 10 sources in common with PMH2004, namely sources #8, 61, 81, 84, 90, 105, 183, 188, 220, and 270, we identified a different counterpart in the USNO-B1 catalogue, because of our new positions. We also found 7 new identifications (source #144, 186, 230, 245, 308, 310, and 343), but did not confirm the identifications of sources #241, 248 and 278, which are now without a USNO-B1 counterpart. In addition, there are 10 out of the 39 new sources for which we find an optical counterpart in the USNO-B1 catalogue.

PMH2004 did not do a systematic cross-correlation with the 2MASS catalogue (Cutri et al. 2003), but only listed one counterpart that was suggested by SIMBAD. We correlated our catalogue with 2MASS, and found 54 identifications, confirming the PMH2004 identification of the source #170 (196 in PMH2004).

The cross-correlation with the lists of optically and radio selected SNRs (Gordon

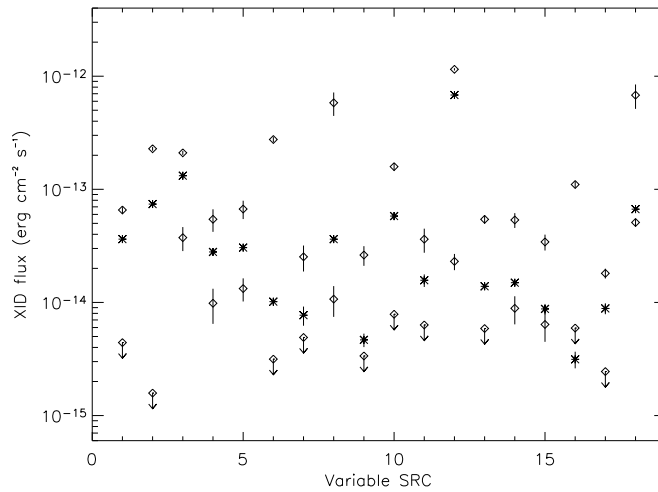


Figure 3.8: The maximum and minimum (or upper limit, indicated by a downward arrow) XID fluxes determined in the individual observations (marked as diamonds) for the sample of highly variable sources with the variability amplitude greater than 5. The asterisks show the XID fluxes determined in the combined image of PMH2004.

et al. 1998, 1999) and SIMBAD and NED data bases allowed us to obtain several new identifications, which are discussed in Sect. 3.9.

Finally, we detected 6 new radio counterparts in the NRAO VLA Sky Survey (Condon et al. 1998). Note that for some extended radio counterparts the positions of the radio and X-ray sources are separated by $\sim 15\text{-}20''$.

3.8 Variability

We detected significant long-term X-ray flux variability of 61 (20%) out of 301 sources covered by more than one pointing. Only 2 of these sources were known to be variable from previous variability studies of M33 using Einstein data (Peres et al. 1989). The variability factors (V , see Sect. 3.3.3), or lower limits detected here and defined as the ratio between the maximum and minimum flux (or upper limit), are in the range 1.2 to 144, on a time scale of a few hours to several months or years.

The long-term light-curve of the most variable source in our sample is shown in Fig. 3.9, while the light-curves of the remaining 60 variable sources are shown in Figures B.1 to B.4 (Appendix B). For each source we plot all measured fluxes in all observations that cover the source, or the 3σ upper limits, omitting only a few meaningless upper limits that are higher than the detected fluxes. Such high upper limits were determined only for a few sources in high background images. Some sources were detected in a large number of individual observations, and exhibited large flux variations on a relatively short time scale of (several) hours. In some sources the variability can be described as flares.

The long-term flux variability was used to further constrain the nature of these

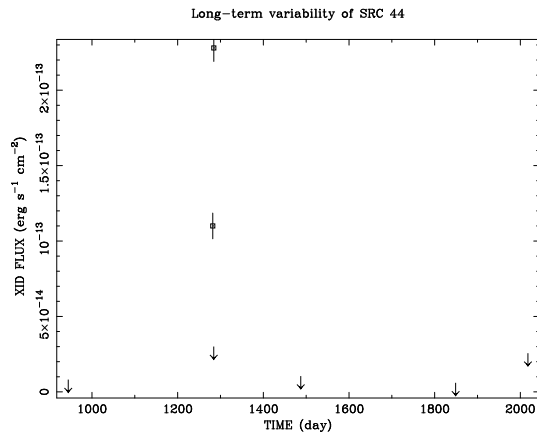


Figure 3.9: The long-term X-ray light-curve of source #44, showing an extreme flux variability by a factor of 144 on a time scale of several days and, hence, classified as an XRB candidate (see Sect. 3.9). The time is given in days after JD 2450814.5.

sources. The variability amplitudes and light curve shapes were used to classify eight relatively hard and luminous sources as XRB candidates, as they were observed changing their XID flux by a factor of ten to more than a hundred (Sect. 3.9).

We confirm the X-ray flux variability of both of the two previously known XRB – the eclipsing binary X-7 designated here as source #150 (Pietsch et al. 2004b, and references therein), and the ultra-luminous source near the nucleus X-8 or source #182 (Dubus et al. 1997; Dubus & Rutledge 2002; Dubus et al. 2004). Besides XRBs and candidates, the most variable sources detected in our sample are SSS candidates. The sample of the variable sources also includes 6 star candidates, 1 galaxy, 3 AGN candidates, 36 hard, 2 unclassified sources. Three optically identified SNRs were also found to be variable in our analysis, and we changed the classification of these sources (discussed in detail in Sect. 3.9.4).

Figure 3.10 (upper panel) shows the detected variability factor (or lower limit) as a function of the maximum flux, for all variable sources. As already noted, the most variable sources in our sample are XRB and SSS candidates, with an XID high state flux greater than $\sim 1 \times 10^{-13} \text{ erg cm}^{-2} \text{ s}^{-1}$, corresponding to a luminosity of $10^{36} - 10^{37} \text{ erg s}^{-1}$ at the distance of M33. Such luminosities are expected for X-ray binary systems. Since the faintest sources detected in the individual images have XID fluxes of about $\sim 1 \times 10^{-15} \text{ erg cm}^{-2} \text{ s}^{-1}$, determined with large errors, we could not detect any significant variability for such objects. Hence, the faintest variable source in our sample has an XID high state flux of $1.2 \times 10^{-14} \text{ erg cm}^{-2} \text{ s}^{-1}$. As expected, there is a correlation between the variability factor (and also variability significance) and maximum XID flux, since large flux variations could only be detected for luminous sources. However, as Fig. 3.10 shows, several highly luminous sources exhibit a small amplitude but highly significant variability (e.g. #182, 131, 112, 124, 237). The variability factors of these sources are in the range of 1.3 to 1.7, with the significance as high as 10 to 35. Clearly such behaviour can only be seen in luminous sources detected with small errors on the flux determination. Most of these sources

also showed some indications of variability in previous X-ray observations. As already noted, source #182 (X-8) is known from previous studies to be variable with small flux modulations. In addition, sources #131 (the Einstein source X-6, Long et al. 1981a; Trinchieri et al. 1988a) and #112 (X-4) showed flux variations of at least 40% in a BeppoSAX study, but since the detected variability was comparable to systematic uncertainties, it was regarded as tentative (Parmar et al. 2001).

In order to exclude a possible systematic error in our automatic flux determination, we compared the fluxes of all sources in overlapping fields. For example, we checked whether some observations show systematically higher (or lower) flux for all or most sources within the FoV. However, we could not detect any trends. The maximum and minimum XID fluxes seem to be distributed randomly between the observations, and they are not related to the filter used, or to the off-axis angle of the source. We also note that, although most of the brightest sources in our data show some degree of variability, there are also highly luminous sources (e.g. #288, 348) that show no significant variability.

The lower panel of Fig. 3.10 shows the relationships between the variability factor and hardness ratio HR1 determined in the high states. We plot only the sources with hardness ratio errors smaller than 0.2, and also mark the catalogue source number of the most variable sources. The HR plot shows that the sample of highly variable sources includes SSS and XRB candidates, which occupy two distinct regions on this plot. For example, sources #96 and 207, classified as SSS candidates, appear on the left hand side, while the rest of the marked sources have much harder spectra, in agreement with their proposed classification as XRB or candidates. We also identified two distinct spectral classes of sources with much smaller variability amplitudes: soft sources with the HR2 in the range -0.8 to -0.5 are most probably foreground stars; and sources with well-defined HR3 and HR4, we classified as ‘hard’.

3.9 Classification of the detected sources

We classified the sources detected in our data into different classes of X-ray emitting objects: foreground stars (fgStar), galaxies (GAL), AGN, super-soft sources (SSS), supernova remnants (SNR), and X-ray binaries (XRB), using the cross-correlation with catalogues at other wavelengths, together with the X-ray properties determined in this survey. In a few cases we were able to identify an X-ray source with a source already classified from optical, infrared, or radio data. However, in most cases we could not find this kind of information, so it is useful to define criteria to classify sources based on their X-ray characteristics. This is demonstrated by Haberl & Pietsch (2001), who have used the X-ray hardness ratio diagrams to define regions populated by different classes of X-ray sources, using well-studied sources in the Magellanic Clouds (Haberl & Pietsch 1999). PMH2004 have expanded it to the broader XMM-Newton energy range and applied it successfully to classify more than 350 sources detected in the XMM-Newton combined image of M33, and also more than 600 sources in M31 (Pietsch et al. 2005b).

Here we adopt the same classification criteria as defined in Table 3.5 of PMH2004,

and add the information derived from the X-ray variability and near-infrared colour and brightness that we derived in this work. We list our classifications in column 20 of Table 3.4. Similarly to PMH2004, we classify a source only if all criteria are fulfilled; otherwise, the source is a candidate for a particular class of objects (indicated by pointed brackets).

The majority (206) of the detected sources were classified as 'hard', using the selection criteria defined by PMH2004 as $HR2 - HR2 \text{ error} > -0.2$, or only HR3 and HR4 as defined and no other classification. From comparison with the X-ray background surveys (Brandt et al. 2001; Rosati et al. 2002), we estimate that approximately 100–150 of these sources would be background objects - AGN and galaxies - 13 of which we have already identified. There are also 28 foreground stars and star candidates in our catalogue and 54 sources that have relatively soft spectra and that we could not classify. The rest of the detected sources most probably belong to M 33 - 10 XRB and XRB candidates, 25 SNRs and SNR candidates, and 11 SSS candidates.

3.9.1 Foreground stars (fgStar)

We adopted the criteria defined in Table 2.5 of PMH2004 ($\log(f_x/f_{opt}) < -1.0$, $HR2 < 0.3$ and $HR3 < -0.4$) to classify foreground stars, and added near-infrared brightness and colour criteria: ($Jmag - Kmag < 0.8$), and ($Jmag < 12.5$) (Finlator et al. 2000).

Out of the 5 foreground stars and 30 star candidates classified by PMH2004, we confirm the detection and classification of 4 stars plus 21 foreground star candidates. We also classify one of the new sources (#189) and a previously listed source candidate (#174) as foreground stars, identified also with SIMBAD stars. The first star is listed in the catalogue of OB associations in the southern arm of M 33 and classified on the basis of UBV CCD photometry (Regan & Wilson 1993). The star classification of the second object is based on the measured proper motion and listed in The Tycho Reference Catalogue (Hog et al. 1998). We classify further 3 objects as foreground star candidates.

Only four stars and candidates do not have a 2MASS counterpart, and one star candidate (#110) has the infrared brightness and colour slightly out of range. The X-ray spectrum of this object is also found to be slightly harder than expected for a typical star. However, since the optical data confirm the stellar classification and its light-curve (Fig. B.1) resembles a flaring event, we leave the PMH2004 classification for this object.

There are three other foreground star candidates (#128, #170, and #309, see the light curves in Fig. B.2 and Fig. B.4) that show significant X-ray variability on the time scale of days to months, probably due to flaring. We also classify #133 and 186 as foreground stars, because the sources are variable; hence their previous SNR classification was not confirmed (see Sect. 3.9.4). Only one star candidate (#170) could not be associated with the USNO-B1 counterpart, although its HRs and infrared brightness and colour confirm the stellar classification. The source is also listed in the catalogue of blue and red giants in M 33 (Ivanov et al. 1993). All of the classified

foreground stars and candidates have the X-ray fluxes and hardness ratios in the range expected for this class of objects.

Sources #263 and #309 are classified as foreground star candidates by PMH2004. We identified these sources with the same USNO counterparts. However, in our data they have $\log(f_x/f_{opt}) > -1$ – outside the range assumed for stars, because we measured a higher X-ray flux (see Sect. 3.6 for possible explanations on differences in the flux measured in the two catalogues). Since the infrared data does not distinctively confirm the stellar classification of the first source and its spectrum is slightly harder, we leave it without classification. A relatively higher X-ray flux of the second source could be explained as flaring (see Fig. B.4). We keep the stellar classification of this source, because it is also confirmed by its HRs and infrared data.

Sources #8 and #11 have been suggested as possible foreground stars by PMH2004 based on their hardness ratios. However, they could not be associated with any optical counterpart. Due to our improved positions we identified the USNO counterparts, but the corresponding $\log(f_x/f_{opt})$ are larger than -1 and do not support the proposed classification. The hardness ratios, which are the same as calculated by PMH2004, classify the first source as an SNR candidate, while we could not classify the second one. According to its spectrum and $\log(f_x/f_{opt}) \sim 0$ the source could be either an SNR or a galaxy.

3.9.2 Galaxies (GAL) and AGN

The selection criteria used to classify galaxies and AGN are defined as either a radio source with a relatively hard X-ray spectrum compared to a SNR or an optical identification with a galaxy (Table 2.5, PMH2004). We detected and confirmed the classification of 11 out of 14 galaxies and AGN, and we classified one more source (#57) as AGN, because of its hard spectrum and spatial correlation with the NVSS source 013245+303859. Source #126 classified by PMH2004 as an SNR or AGN is found to be significantly variable in our data, with flux variations of a factor of 5 on a time scale of several days (Fig. B.2). We classified this source as AGN, as the detected variability would make a SNR classification unlikely.

3.9.3 Super-soft sources (SSS)

Luminous super-soft sources, discovered as a new class in the LMC by ROSAT (Trümper et al. 1991; Greiner et al. 1991), display extremely soft X-ray spectra, which can be represented by a blackbody model with the effective temperature of the emitting object below 50 eV. Luminous ($10^{36} - 10^{38} \text{ erg s}^{-1}$) super-soft sources are generally believed to be binary systems with white dwarfs accreting from more massive hydrogen-burning donors (van den Heuvel et al. 1992). They have been observed in our own and in nearby galaxies, sometimes showing significant variability on different time-scales, from several days to several months, while some other SSSs have been found to be recurrent transients (Greiner et al. 2004; Di Stefano et al. 2004; Osborne et al. 2001).

The selection criteria for SSSs in the combined XMM-Newton catalogue (HR1 < 0.2, HR2 - HR2 error < -0.99 or HR2 not defined, HR3 and HR4 not defined) were derived by calculating the HRs for an assumed 25 and 50 eV black body model (Table 2.5, PMH2004). We confirm 4 out of 5 SSS candidates. Two (#96, #207) are very luminous and also among the most variable sources detected in our data (variability factors of 87 and 44, respectively; Fig. B.1 and Fig. B.3), which makes their identification with super-soft accreting binary systems very likely. Super-soft source candidates #48 and #285 are slightly less luminous, and we could not detect any significant flux variability in our observations. Note that the fluxes given in Table 3.4 and Table 3.5 are calculated by assuming a power law spectrum and the galactic foreground absorption as for all other sources. However, due to their significantly different spectrum, we estimate that their fluxes are underestimated by as much as 30–40%.

In addition to these four SSSs, we propose 7 new SSS candidates, detected only in the individual images with luminosities of $\sim 10^{35} - 10^{36}$ erg s⁻¹, at the distance of M 33. Some of these SSS candidates may be low-luminosity objects, such as e.g. single, non-interacting white dwarfs, magnetic cataclysmic variables, or novae several years after outburst (Greiner 2000). Recently, Pietsch et al. (2005b) found that almost all of the 21 X-ray counterparts of optical novae detected in M 33 and M 31 were identified as SSS according to their HRs. However, none of the classified SSS sources in this or in the PMH2004 catalogue is associated with the known optical novae, probably due to the small number of detected optical novae in M 33.

3.9.4 Supernova remnants (SNR)

Many SNRs in M 33 were detected and classified in the optical (see Gordon et al. 1998, and references therein) and radio observations (see Gordon et al. 1999, and references therein). PMH2004 have identified a total of 21 of these known SNRs, and their X-ray properties confirm the optical/radio identification as an SNR. Further 23 SNR candidates, fulfilling either the HR criteria (HR1 > 0.1 and HR2 < -0.4) or coinciding with a classified radio or optical SNR, are also listed in the combined data catalogue.

We confirm the PMH2004 classification of 14 SNRs plus 11 candidates. We checked that the variability factors of these sources are consistent with no variability (see also Sect. 3.6). However, for sources #108, 133, and 186, identified and listed in the M 33 SNR catalogue of Gordon et al. (1998) as SNRs 21, 28, and 55, we detected small but significant flux variations.

Source #108 (SNR 21, Gordon et al. 1998) has an optical extent of approximately 6–7 arcsec (28 pc at the distance to M 33). We determined the parameters of this source from our point source run of `emldetect` (see Sect. 3.3), because the extended emission was detected only marginally in some observations when we tried to fit it. This could have caused the detected small flux variations with an amplitude of 1.24 (S=4.52, the light-curve is shown at Fig. B.1) in our data. However, some indications for possible variability of this source (the Einstein source X-3, Long et al. 1981a; Trinchieri et al. 1988a) were also found by Peres et al. (1989).

Source #186 (X-13, SNR 55) was reported to have different count rates in two

Einstein observations separated by 6 months, although the source was too weak to definitely confirm the detected variability (Peres et al. 1989). We found that #186 changes its XID flux by a factor of 2.2 (significance 4.12). As its light-curve shows, (Fig. B.3) the source goes through several 'high' states with the XID flux of $3-4 \times 10^{-14}$ erg cm⁻² s⁻¹ and 'low' states, when the flux decreases to below 2×10^{-14} erg cm⁻² s⁻¹. In a recent study of SNRs in M 33 with Chandra, Ghavamian et al. (2005) have found this X-ray source to be point-like in Chandra data, which also indicates that the detected X-ray emission is not associated with the optically selected SNR.

Finally, source #133 (SNR 28, not detected with Einstein) changed its flux by a factor of 1.67 ($S = 3.47$, see Fig. B.2). Ghavamian et al. (2005) report that this X-ray source has a flux, as determined in Chandra observations, that is two times smaller when compared to the PMH2004 XID flux.

A discrepancy between the XID flux measured with XMM-Newton and Chandra was also noted for #138 (SNR 29), which in our analysis has a variability factor of 1.98, but determined below the 3σ significance level ($S = 2.77$).

While the small variability amplitude of #108 might be explained by an error in the XID flux determination due to the large extent of this source, this certainly would not be the case for the other two (possibly three) sources. According to their hardness ratios, all four sources could also be classified as stars. Furthermore, we identified the USNO counterparts of #133 and #186, and the calculated $\log(f_x/f_{opt})$ is in the range expected for stars. Hence, we classified these two sources as possible foreground stars. We keep the proposed SNR classification for #138, and leave #108 without classification. However, further studies are needed to confirm the nature of the X-ray emission, which coincides with these optically selected SNRs.

For one source (#206) classified in PMH2004 as SNR candidate, we found significant variability (variability factor of almost 6, Fig. B.3). The HRs of this source (in PMH2004 and also in our data) are consistent with both the stellar and SNR classification, but since the source could not be associated with an optical counterpart, PMH2004 list it as an SNR candidate. However, the detected variability in our data is inconsistent with the proposed SNR classification, so we leave this source unclassified.

The giant HII region NGC 604, the brightest optical source in M 33, is also identified with an SNR candidate in PMH2004, based on its HRs. The source is detected in our analysis as the extended source #254. We confirm its HRs but found it to be variable, with a variability pattern similar to X-7 (Fig. B.4). Since the source is extended in all observations, we determined its parameters by fitting its extent in `emldetect`. However, high resolution Chandra archival images show that this complex HII region is resolved into a collection of point sources probably of different natures (SNRs, XRBs), and includes perhaps some diffuse hot gas emission. The same is true for the BCLMP 290 (Boulesteix et al. 1974), another optically bright extended region in M 33, which shows a hard X-ray spectrum and significant long-term X-ray variability (source #113, Fig. B.1). We classify this source as an XRB candidate (see next section).

Finally, we note that Ghavamian et al. (2005) have found optical counterparts of two SNR candidates (#61, and PMH2004 source 270 not detected in the individual observations) selected using the HR method. The optical data confirms the proposed

SNR classification.

3.9.5 X-ray binaries (XRB)

As discussed by PMH2004, HRs alone cannot be used to distinguish XRBs from AGN or plerions, because these classes of sources occupy the same regions in the HR diagrams. Therefore, PMH2004 introduced 'hard' sources as a new class. Both XRBs and AGN are known to be variable. However, XRB in general show much larger flux variations on significantly shorter time scales (of days or even hours), and could also show periodicity (e.g. due to eclipsing or pulsations), a behaviour not observed in AGN. Since some of our individual observations are separated by only several hours, it was possible to detect such extreme X-ray variability on short time scales and use the generated X-ray light-curves, in combination with X-ray luminosity, spectra, and other wavelength identifications, to classify sources as XRBs.

Two XRBs have already been identified in PMH2004 with known binary systems in M 33: the black hole XRB X-8 (#182) near the galactic nucleus, and the 3.4 day eclipsing HMXB X-7 (#150). We classify eight additional sources as XRB candidates (#41, 44, 75, 113, 134, 168, 180, and 254), mostly thanks to their light-curves.

The sources X-8 and X-7 are also variable in our data. The most luminous source X-8 was found to change its flux by 10% with a period of 106 days (Dubus et al. 1997). Although this periodicity was not confirmed later, all other surveys of this source also suggest that it is variable (see Sect. 3.8). Our analysis of X-8 (Fig. B.3) shows flux variations of small amplitude (factor of 1.52) but high significance (35.4). As the light-curve shows, this small flux modulation occurs on a time scale of several hours.

The most accurate binary period of X-7 (3.45 days) has been determined by Pietsch et al. (2004b), using the individual XMM-Newton observations, together with Chandra and optical data. Our light-curve (Fig. B.2) also includes two XMM-Newton observations not analysed by Pietsch et al. (2004b). However, the source is still found only in high or low state, with the shortest separation between the states less than two days, and no transit into or out of eclipse was observed.

The shape of the light-curve of one XRB candidates (#113) resembles that of X-7 (Fig. B.1). It shows the source in high and low states, with flux variations of a factor of at least 54. This source is one of the two extended sources in our catalogue, identified as the HII region BCLMP 290 in SIMBAD, and it is also listed as an SNR by Gordon et al. (1999). According to its HRs, the source was classified as 'hard' in the combined data catalogue. Inspection of archival Chandra images indicates that this complex region, which could not be resolved by XMM-Newton, contains different X-ray emitting objects. The light-curve shows that the transitions from low to high state occur in ~ 0.25 days.

Two other XRB candidates (#44 and 41) are shown in Fig. 3.11. Source #44 exhibits the highest variability in our sample, changing its flux by a factor of at least 144. As the images in Fig. 3.11 and the corresponding light-curve (Fig. 3.9) show, the source is very strong (with a luminosity of 2×10^{37} erg s⁻¹ in the high state) on two

images separated by ~ 2.4 days, but could not be detected in the other observations. Source #41 shows similar behaviour (Fig. B.1). The nearby source #37 is classified as 'hard', without significant variability.

As already noted, the complex HII region NGC 604 (#254) has an SNR spectrum, but its light-curve (Fig. B.4) shows several transitions from low to high state in a fraction of a day, so we also included it in the list of the XRB candidates, together with sources 75, 134, and 180, which have similar temporal characteristics (Fig. B.1, Fig. B.2, and Fig. B.3, respectively). Source #75 was also detected as a variable source in earlier X-ray surveys (see Haberl & Pietsch 2001, and references therein), and its luminosity is in the range expected for an XRB. Source #180, detected only in the present catalogue, has been identified in SIMBAD as a peculiar object of unknown nature (Fabrika & Sholukhova 1995). Finally, PMH2004 note several other objects as possible XRB candidates, because of their cross-correlation with variable stars. One of these sources (#168) is included in our list of the XRB candidates, because of its high variability amplitude (Fig. B.2), spectral characteristics, and luminosity. We also confirmed the X-ray variability of source #277 (Fig. B.4), identified with a variable star in SIMBAD. However, since its variability amplitude (slightly greater than 2) could also be observed in an AGN, we classify this source as 'hard'.

3.9.6 Spatial distribution

Figure 3.12 shows the spatial distribution of all 375 X-ray sources detected in the direction of M 33 and classified in the present catalogue, and/or by PMH2004. The majority of the sources in both surveys are classified as 'hard'; they are evenly distributed over the total field of view, and are probably AGN. Foreground stars and candidates are also distributed over the total surveyed region, and the optical counterparts of most of them show up as bright objects in the optical image.

However, in our analysis, we also significantly increased the number of the classified sources, which are most probably intrinsic to M 33 (shown with black symbols in Fig. 3.12). In addition to around 40 SNRs and candidates, we now have a significant population of XRB (10) and SSS (11) candidates in M 33. The spatial distribution of the XRB and SSS candidates detected here supports their classification – most of them seem to be associated with the galactic disk or spiral arms, except 2 SSS candidates that are further away from the central region and could be foreground objects. The figure also shows a region to the South of the M 33 nucleus (along the Southern spiral arm) with 8 SNRs and 1 SSS source concentrated very close to each other, which could indicate a region of a recent star-formation episode.

We also made use of a recent XMM-Newton survey of M 31 by Pietsch et al. (2005b) to compare the spatial distribution of the detected X-ray sources in these two spiral galaxies. In contrast to M 33, we clearly see a concentration of bright white and blue sources in the bulge of M 31 (see Fig. 4 in Pietsch et al. 2005b). To compare this further, we selected all 'white and blue' (i.e. 'hard', XRBs and XRB candidates, AGN and AGN candidates) sources with luminosities above $\sim 3 - 4 \times 10^{36}$ erg s⁻¹ (at that luminosity both surveys are complete over the whole area) in both catalogues - out of

the 30 such sources in M 33, 11 (or 37%) are detected in the central observation, while most of the remaining sources are further away but within the D_{25} area. In M 31 the hard luminous sources are concentrated around the galactic centre – in a sample of 108 bright hard sources, we found a total of 71 (66%) in the central observation.

3.9.7 Luminosity distribution

We present the luminosity distribution of the SNRs and XRBs in M 33 classified in both catalogues, and compare it with the same source populations detected in the XMM-Newton survey of M 31 (Pietsch et al. 2005b). The catalogues are directly comparable, since they were derived using the same source detection procedures and classification. They also have similar sensitivity, the M 31 survey covering approximately 1.2 deg^2 down to the (0.2–4.5) keV luminosity of $\sim 10^{35} \text{ erg s}^{-1}$. Figure 3.13 shows the result of this comparison for the 38 SNRs and SNR candidates in M 33, and 42 SNRs and candidates detected in M 31 (Pietsch et al. 2005b). The distribution of SNRs in both spiral galaxies is almost the same, with slopes of -23 ± 3 and -24 ± 2 for M 33 and M 31, respectively. The Kolmogorov-Smirnov test gives a probability of 97.5% that the two distributions are derived from the same population. Although M 33 and M 31 reveal the same SNR luminosity distribution, there are many more SNRs in M 33 per surveyed area detected in X-rays (the same number of detected SNRs in both galaxies, but the surveyed area of M 31 is almost 2 times larger).

Based on the multi-wavelength studies of the ISM in ours and the nearby galaxies Duric (2000b), suggested that the reason for the intrinsically faint X-ray emission of SNRs in M 31 could be a multi-phased ISM. Although the average gas density is relatively higher, SNRs are expanding into locally warm low-density regions. Previous studies suggest that the upper density limit of this ambient gas in M 31 is 0.1 cm^{-3} (Magnier et al. 1997). The similarity of the luminosity distribution of the detected SNRs in M 31 and M 33 seems to suggest that the ISM of M 33 also includes a low-density component.

The discrepancy between the relative number of bright SNRs in M 33 and the LMC, as found by Haberl & Pietsch (2001) in the ROSAT analysis of M 33, has been also recently discussed by Ghavamian et al. (2005). Ghavamian et al. (2005) use a sample of optically identified SNRs detected in Chandra and XMM-Newton data, and compare it with the SNRs detected in the ROSAT HRI survey (Sasaki et al. 2000). To check this result for our M 33 SNR sample, we also plot (Fig. 3.13) 40 SNRs brighter than $\sim 10^{35} \text{ erg s}^{-1}$ from the LMC PSPC catalogue (Haberl & Pietsch 1999). We converted the ROSAT PSPC count rates to fluxes ($\text{ECF} = 2.17 \times 10^{-11} \text{ erg cm}^{-2} \text{ ct}^{-1}$) by using the same model to approximate the LMC source spectra that was used in the analysis of M 33 and M 31 (see Sect. 3.3). The figure shows that the SNRs in the LMC have a slightly flatter distribution (with a slope of -18 ± 3) in agreement with the previous result, which was attributed to the relatively higher metallicity of the LMC (Haberl & Pietsch 2001). Ghavamian et al. (2005) use a much smaller ROSAT HRI subsample of SNRs from Sasaki et al. (2000) for their comparison, which could be the reason for their slightly steeper LMC slope (also shown in Fig. 3.13).

The sample of the classified binaries and XRB candidates in M 33 is still limited to performing detailed population studies, but it is now comparable to the relative number of XRBs detected in M 31 (Pietsch et al. 2005b). There are 7 XRB and 9 candidates in the M 31 catalogue, classified mainly from the optical cross-correlation and/or variability. However, there are 37 sources associated with the known globular clusters in M 31, most probably low mass X-ray binaries (LMXB). We could not detect any X-ray emission from the relatively smaller number of known globular clusters in M 33 (Mochejska et al. 1998). Figure 3.14 shows the luminosity distribution of the XRBs detected in M 33 and M 31. The globular cluster sources (LMXB) in M 31 are also shown. The distribution of the XRBs is clearly limited by the selection effect. It flattens just below the XID luminosity of $\sim 10^{37}$ erg s⁻¹ in both galaxies, because the extreme variability used for the XRB classification could only be detected in highly luminous sources. The globular cluster sources, on the other hand, can be classified down to fainter luminosities, and have a slightly steeper distribution.

3.10 Summary and conclusion

We analysed all 24 XMM-Newton observations of M 33 individually and compiled a catalogue of 350 point-like X-ray sources detected in those observations. A total of 39 of these objects were detected for the first time, while 311 had already been detected in PMH2004. For all sources we determined positions (improving on those reported in PMH2004, since we were able to correct for the relative offsets between the observations) and the most relevant X-ray parameters such as XID fluxes, HRs, long-term variability, and correlations with other wavelength counterparts.

A total of 61 sources in our sample exhibit significant variability up to a factor of more than 144 on time scales from hours to months or years. As expected, the most variable sources in our sample have extremely soft or hard spectra, and we classified them as SSS and XRB candidates. There are also several foreground stars or candidates, along with AGN candidates exhibiting moderate flux variations (by a factor of approximately 2 to 6); but the majority of variable sources are 'hard', probably unidentified XRBs or AGN. The brightest sources detected in our data (#182 or X-8, #131, #112) show small flux variations detected with a high significance.

The variability amplitudes and shapes of the long-term light-curves were used, together with the HR method of PMH2004 and optical, infrared, and radio data, to classify all detected sources. In particular, we have used the light-curves to classify 8 new XRB candidates in M 33 that could not be distinguished from AGN using only the HR method. The detected variability was also used to reject the SNR classification of several sources. We also classified 11 SSS candidates, 7 of which are reported here for the first time. The detected and classified XRB and SSS candidates have significantly increased the X-ray binary population in M 33.

In addition, we classified 14 SNRs and 11 SNR candidates, 6 foreground stars and 23 star candidates, 12 AGN candidates, 1 galaxy, and 206 'hard' sources. The remaining 54 sources could not be classified using the proposed classification criteria. As already discussed by PMH2004, at least 50 % of the 'hard' and unclassified sources

are background galaxies and AGN, while the remaining ~ 50 – 100 sources still await identification, most probably as XRBs or Crab-like SNRs within M 33.

The analysis of both the combined and individual observations of M 33 have significantly increased the number of classified sources in M 33. Using the deep combined image, it was possible to detect faint sources, in particular SNR and foreground star candidates. Approximately 50% more of these sources were detected in the combined data than in the individual images. In addition, due to much better statistics for determining hardness ratios, the HR plots could be calibrated, and the classification method was established based, to a great extent, only on the X-ray spectral characteristics. In the analysis of the individual observations, on the other hand, it was possible to systematically search for long-term X-ray variability, and then use it as an efficient tool for classifying XRBs and other source classes. Furthermore, by analysing the individual images, it was possible to detect faint variable and transient sources such as SSS.

The spatial distribution of the detected sources in M 33 confirms that there is no pronounced bulge in this late-type spiral galaxy, in contrast to e.g. M 31, where there is a clearly visible concentration of sources and diffuse emission around the galactic centre.

The relative contribution of the classified X-ray binary source population in M 33 is now almost comparable to M 31. Excluding the low mass XRBs associated with globular clusters, there are 7 XRB and 9 candidates classified in a recent XMM-Newton survey of M 31 (Pietsch et al. 2005b). However, the number of classified XRB (10) and candidates in M 33 is still small, and more sensitive observations are needed to detect variability of fainter objects, and use it for source classification. In addition, optical follow-up observations are needed to confirm the XRB classifications.

There is approximately the same number of detected and classified SNRs and candidates in both galaxies, although the surveyed area of M 31 and the total number of the detected sources are more than two times larger. The luminosity distribution of SNRs in both galaxies is similar, and has a slightly steeper slope than that of the LMC.

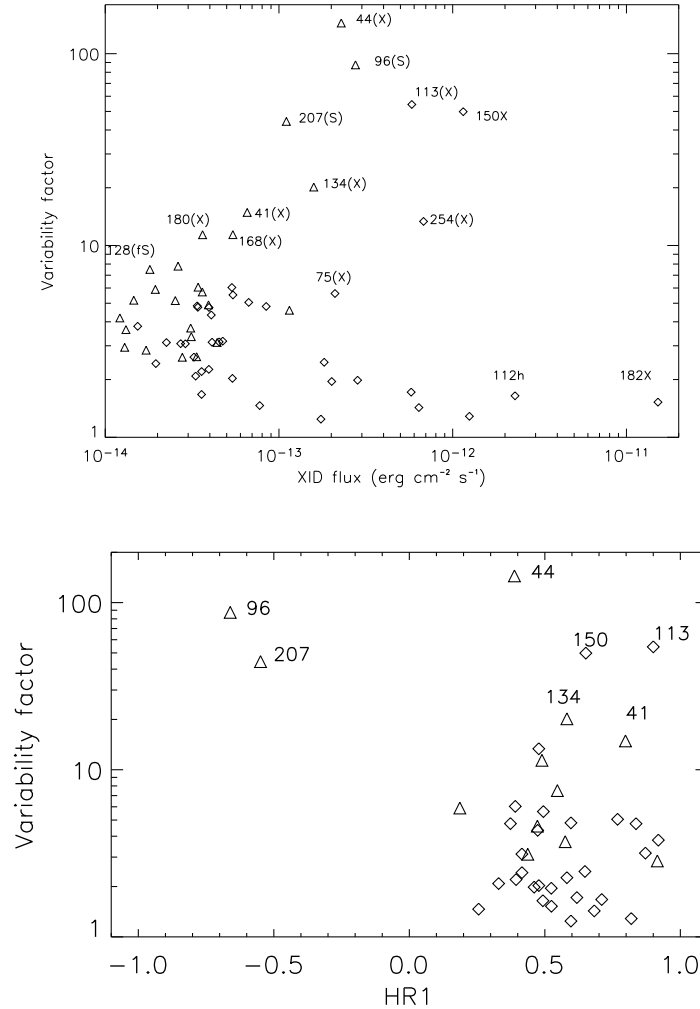


Figure 3.10: Upper panel: The variability factor as a function of the maximum XID flux for the 61 significantly variable sources from Table 3.4. The lower limits of the variability factors are marked as triangles pointing up, while values determined from measured minima are shown as diamonds. For the brightest and most variable sources, the catalogue source number and classification are also marked: X indicates X-ray binary, S supersoft source, fS foreground star and h 'hard' source. The same symbols in brackets denote candidates. **Lower panel:** The variability factor versus HR1. The lower limits are shown as triangles, while the calculated values are marked as diamonds. The catalogue source numbers are also marked. Sources #96 and #207 are classified as SSS candidates, while the rest of the marked sources are XRB or XRB candidates.

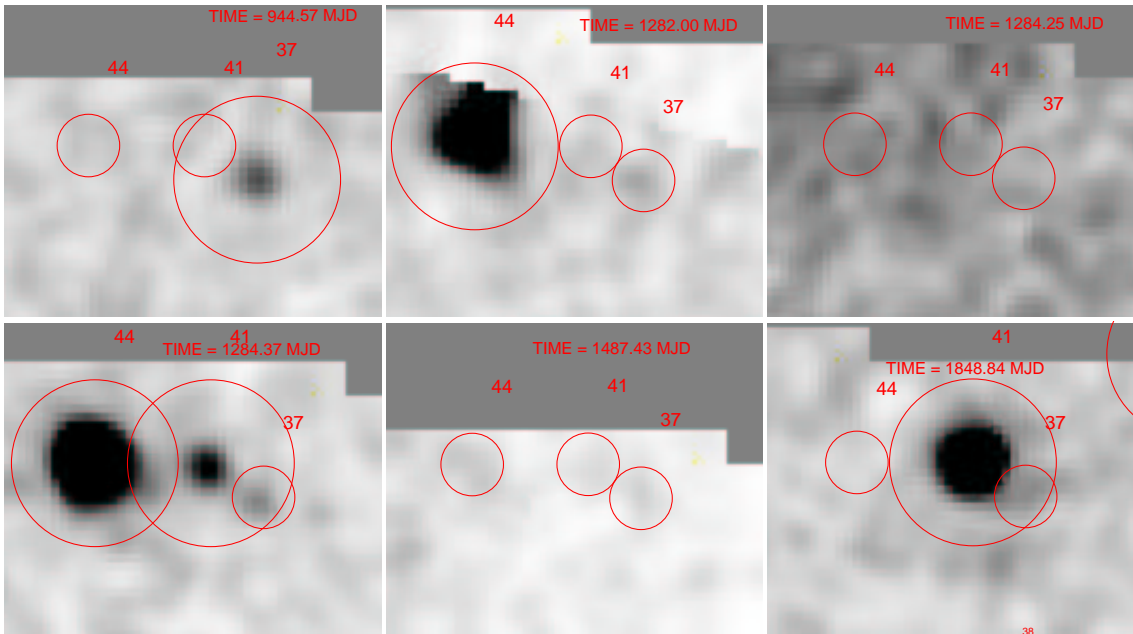


Figure 3.11: The broad band XMM-Newton EPIC gray scale images of the observations 4(a), 5(a), 10(a), 11(a), 15(a), and 4(b) (from upper left to lower right, respectively) showing the regions around sources #44, 41, and 37. The big circles mark the positions of the detected sources, while small circles mark the positions of the sources below the detection threshold. The intensity scale in all images is linear from 0 to $2.90472 \text{ ct s}^{-1} \text{ pixel}^{-1}$. The observation times in days after JD 2450814.5 are marked on each image.

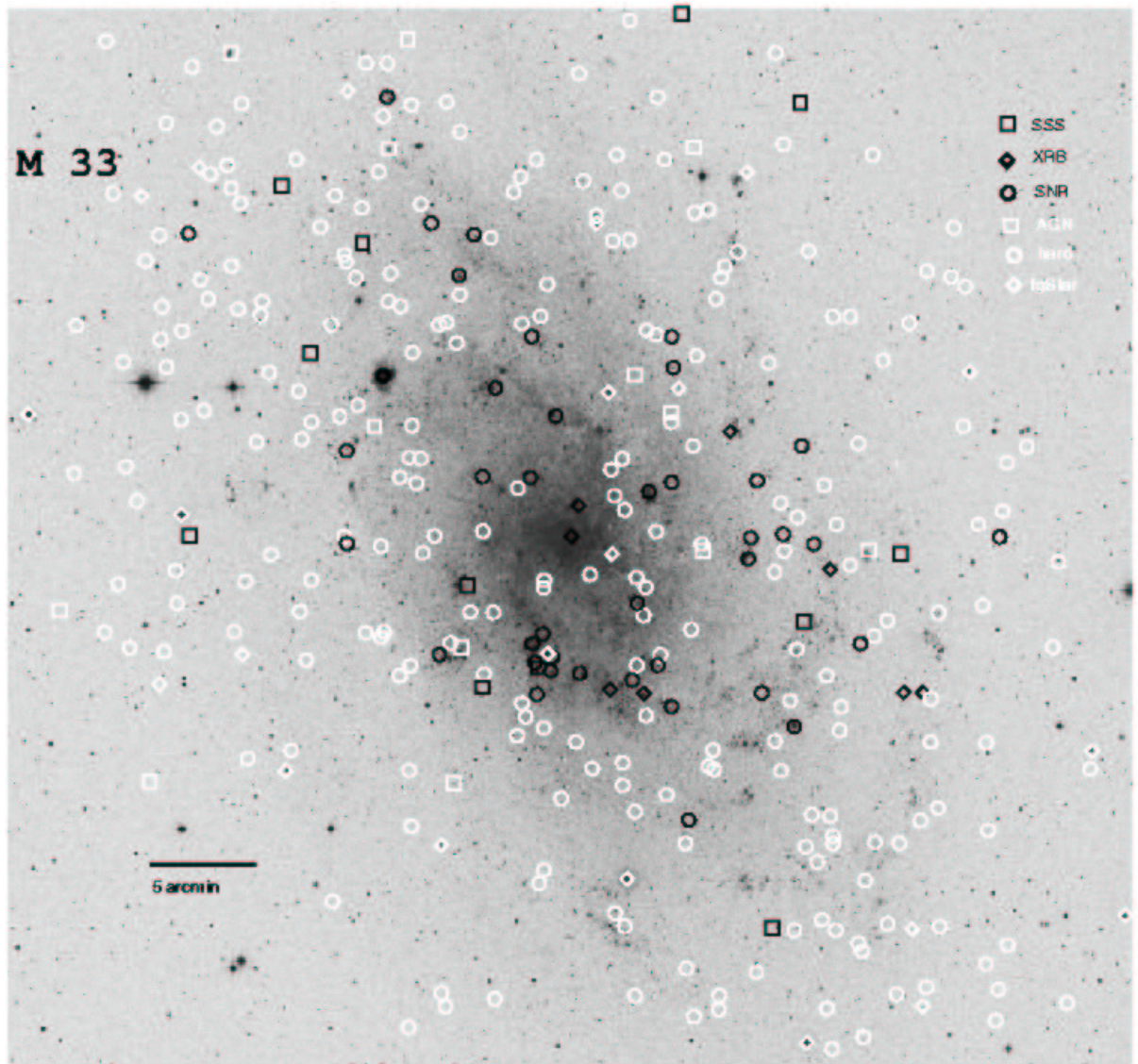


Figure 3.12: Spatial distribution of all 374 classified X-ray sources detected in the direction of M 33 in both the combined and individual data catalogues.

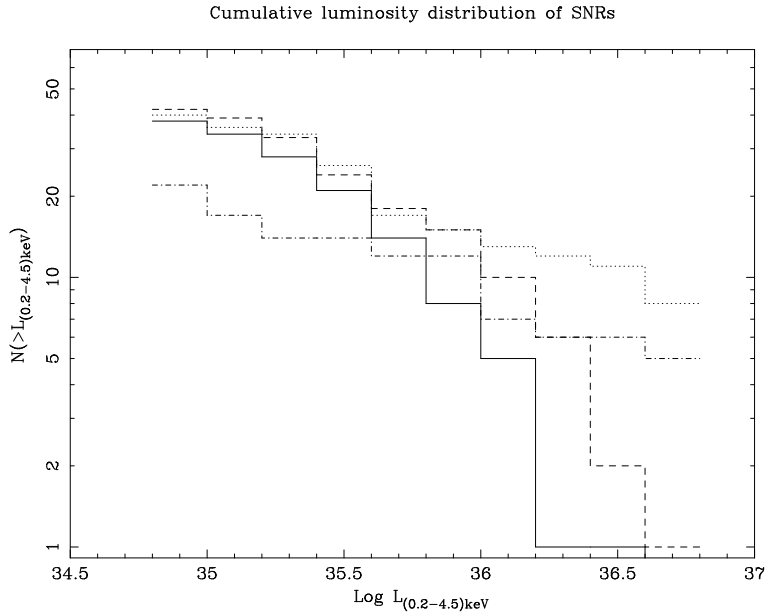


Figure 3.13: The cumulative luminosity distribution of the SNRs and SNR candidates detected and classified in both XMM Newton catalogues of M 33 (this work and PMH2004, solid line), in the catalogue of M 31 (Pietsch et al. 2005b, dashed line), and in the ROSAT catalogues of LMC (Sasaki et al. 2000; Haberl & Pietsch 1999, HRI dotted-dashed line; PSPC dotted line).

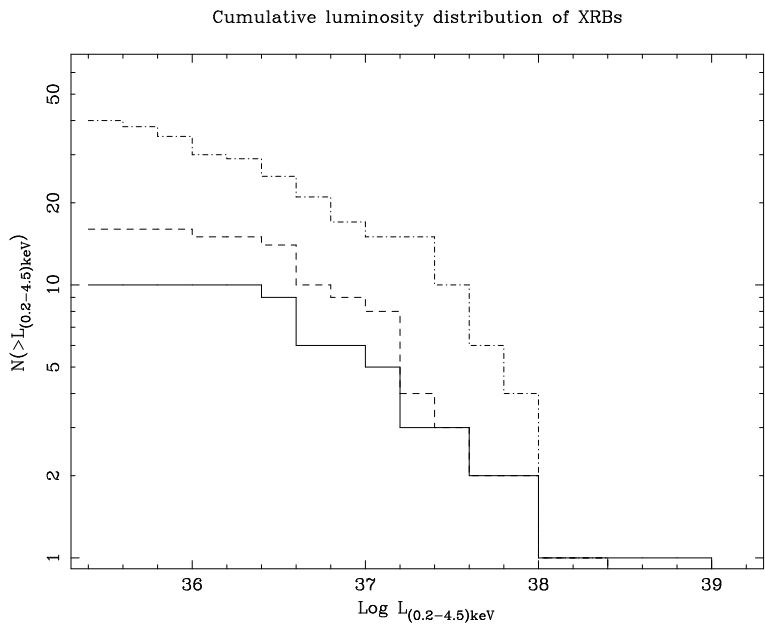


Figure 3.14: The cumulative luminosity distribution of the XRB and XRB candidates detected and classified in both XMM Newton catalogues of M 33 (this work and PMH2004, solid line), and in the catalogue of M 31 (Pietsch et al. 2005b, XRBs – dashed line; globular cluster sources – dotted-dashed line).

Chapter 4

XMM-Newton survey of the Local Group galaxy M 33 – bright individual sources

Z. Misanovic, W. Pietsch, F. Haberl, G. Trinchieri, M. Ehle, D. Hatzidimitriou,, 2005, Proceedings IAU Symposium No. 130, Dublin

Abstract: As shown in our first poster, in a recent survey of M 33 with XMM-Newton we detected the X-ray source population of this nearby spiral galaxy down to the (0.2-4.5) keV luminosity of 10^{35} erg s⁻¹, a factor of 10 deeper than in previous observations. The majority of the detected sources was classified using, in many cases, only their X-ray properties. In particular, 8 new X-ray binary (XRB) candidates were selected, based on their long-term X-ray light curves. We also classified supernova remnants (SNRs), super-soft sources (SSS), AGN, foreground stars and a population of 'hard' sources using the hardness ratio (HR) method. A detailed spectral and timing analysis of the brightest sources is in progress. We present a few examples of spectra for particular source classes. We find that bright 'hard' sources can be divided into two broad families: one best modelled by a powerlaw with photon index in the range of 1.0–2.0, and the other displaying disk blackbody spectra with kT of 0.8 to 1.5 keV.

4.1 Introduction

As demonstrated by Pietsch et al. (2004a), we can use HRs to distinguish very soft, soft and hard sources. SNRs and foreground stars exhibit soft spectra with the emission mainly below 1.0 keV, while SSS have extremely soft spectra (below 0.5 keV). XRBs, Crab-like SNRs and background AGN have significantly harder spectra. We perform detailed spectral and timing analysis of the brightest sources in all individual XMM-Newton observations of M 33. Below we show several examples of typical source spectra.

4.2 Source spectra

The first source in Fig. 4.1 is a SNR, which we fitted by a two-temperature plasma (MEKAL) model and an absorption column of $6 \times 10^{20} \text{ cm}^{-2}$. The variable source 253 also requires a two component model (MEKAL+POWERLAW). This source is identified as a late G-type star in optical follow up observations (Hatzidimitriou et al. 2005), and its relatively hard spectrum can, most probably, be attributed to flaring, although we do not have enough counts in any of the individual observations to confirm this. We fit an extremely variable SSS by an absorbed black body model with a kT of 62 eV.

The remaining sources from our selection display hard spectra. For M33 X-7, a known eclipsing high mass XRB (see e.g. Pietsch et al. 2004b), we extract a spectrum in the high state and fit it by an absorbed disk blackbody with an intrinsic absorption column of about $3 \times 10^{20} \text{ cm}^{-2}$ and a kT of 0.89 keV. A 'hard' source (Src 124) has a similar spectral shape – almost the same absorption and a temperature of 1.03 keV. The powerlaw model also gave acceptable fits for these two sources, however, requiring significantly higher absorption columns and spectral indices in the range 2.6–3.0.

We fit a source classified as an AGN and a 'hard' source (SRC 131) with the powerlaw models with spectral indices of 2.0 and 1.6 respectively.

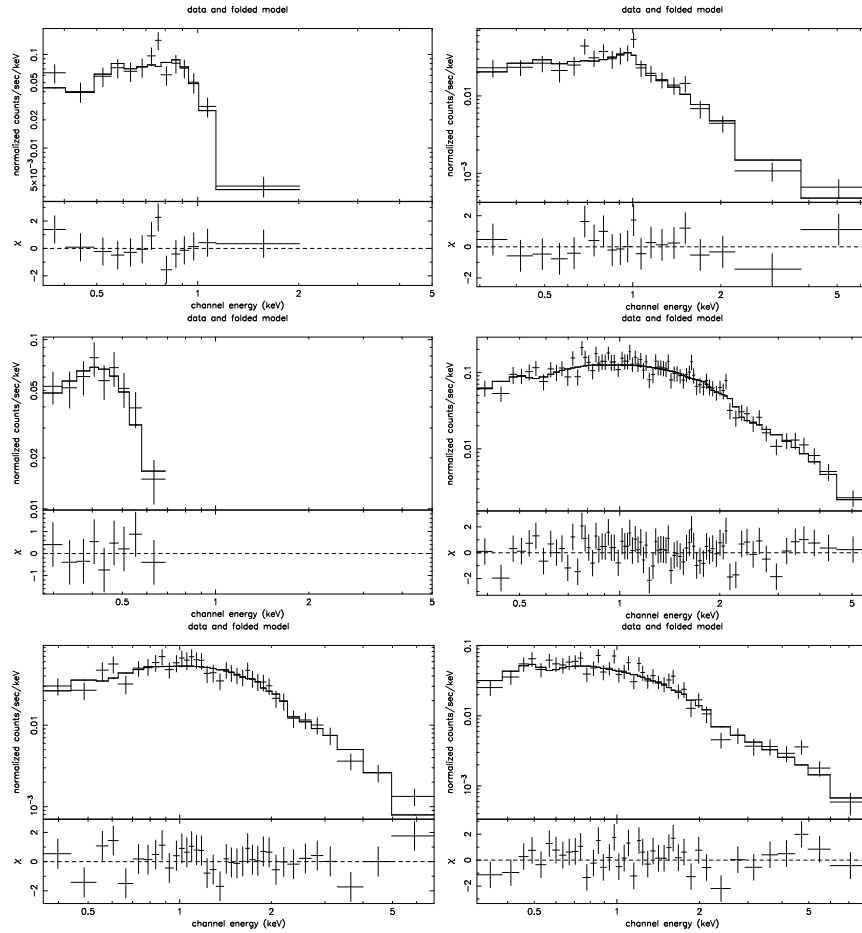


Figure 4.1: Spectra of bright X-ray sources detected in XMM-Newton survey of M 33. From upper left to lower right: Src 108 (SNR), 253 (fgStar), 207 (SSS), 150(XRB M 33 X-7), 124 ('hard') and 248 (AGN). The source number and classification are from Misanovic et al. (2005).



Chapter 5

Spectroscopy of the brightest optical counterparts of X-ray sources in the direction of M 31 and M 33

D. Hatzidimitriou, W. Pietsch, Z. Misanovic, P. Reig, F. Haberl, 2005, A&A, submitted

Abstract: Recent surveys of the Local Group spiral Galaxies M 31 and M 33 with XMM-Newton yielded a large number of X-ray sources. As part of the effort of identifying and classifying the objects responsible for this X-ray emission, we have undertaken the task of obtaining optical spectra of the brightest optical counterparts of the identified X-ray sources, using the 1.3m Skinakas Telescope. Most of these objects are foreground star candidates. The purpose of the present study is to confirm this and to explore the compatibility between the optical spectral classification and the observed X-ray properties of the sources. We have obtained optical spectra for the 14 brightest optical counterparts of X-ray sources identified by XMM-Newton in the direction of M 31 and for 21 in the direction of M 33, using the 1.3m Skinakas telescope in Crete, Greece. All of the M 31 sources and all but one of the M 33 sources were confirmed to be foreground stars, of spectral types between A and M. One of the stars is a late M dwarf with H $_{\alpha}$ emission, a flare star, also displaying strong X-ray variability. One of the M 33 sources (lying within the D25 ellipse) corresponds to a background galaxy, LEDA 5899.

5.1 Introduction

Recent surveys of the Local Group spiral Galaxies M 31 (Pietsch et al. 2005b, hereafter PFH2005) and M 33 (Pietsch et al. 2004a, hereafter PMH2004) with XMM-Newton yielded a large number of X-ray sources. With their moderate Galactic foreground absorption both galaxies are ideal for studying the X-ray source population and diffuse

emission in nearby spiral galaxies.

The Andromeda galaxy M 31 is a massive SA(s)b galaxy, located at a distance of 780 kpc and seen under an inclination of 78° . A total of 856 X-ray sources were detected in an area of 1.24 square degrees. Within M 31, 21 supernova remnants (SNR) and 23 SNR candidates were detected, as well as 18 super-soft source candidates, 7 X-ray binaries and 9 X-ray binary candidates and finally, 27 globular cluster sources and 10 globular cluster source candidates, which most likely are low mass X-ray binaries within the cluster. From 567 hard sources, some are expected to be X-ray binaries or Crablike SNRs within M 31, and the rest, background AGN. Besides the sources within M 31, there were also foreground and background sources: six sources were identified as foreground stars and 90 as foreground star candidates, one as a BL Lac type active galactic nucleus (AGN) and 36 as AGN candidates. One source coincided with the Local Group galaxy M 32, one with a background galaxy cluster and another is a background galaxy cluster candidate.

M 33, an Sc galaxy, is located at a distance of 795 kpc and is seen under a relatively low inclination of 56° . PMH2004 detected a total of 408 sources in a 0.8 square degree field combining the counts of all EPIC instruments. About half of the sources lie within M 33, while the rest are background AGNs or foreground stars. Cross-correlation with archival data led to the identification of 5 foreground stars and 30 foreground star candidates, as well as 12 AGN candidates. Within M 33, 21 supernova remnants (SNR) and 23 SNR candidates were identified, as well as 5 super-soft sources and 2 X-ray binaries. From the remaining 267 X-ray sources classified as "hard", those within M 33 may be low or high mass X-ray binaries, or, Crab-like SNRs, while a significant fraction of them are expected to be background AGN. Very recently, Misanovic et al. (2005), analyzed the individual observations of the XMM-Newton data of M 33, detecting 39 new sources and improving the positions of another 311. They also studied the variability of the sources on time scales of hours to months or years, their spectral characteristics and classification. For example, using the detected variability, they were able to classify 8 new X-ray binary candidates.

It should also be mentioned that Pietsch et al. (2005a) searched for X-ray counterparts of optical novae detected in M 31 and M 33 and discovered 21 X-ray counterparts for novae in M 31 - mostly identified as supersoft sources by their hardness ratios - and two in M 33.

As part of the effort of identifying and classifying the objects responsible for the observed X-ray emission in the direction of M 31 and M 33, we have undertaken the task of obtaining optical spectra of the brightest optical counterparts of the identified X-ray sources, using the 1.3m Skinakas Telescope. Most of these objects are foreground star candidates. The purpose of the present study is to confirm this and to explore the compatibility between the optical spectral classification and the observed X-ray properties of the sources. In the next section, we describe the optical observations, while in Sect. 5.3 we describe briefly the data reduction. In Sect. 5.4, the method followed for the classification of the spectra obtained is presented, while in Sect. 5.5 we discuss the results, including special mention of individual objects of interest.

5.2 Optical Observations

The optical observations used in this study were carried out during three observing runs, on September 6, 2003, on October 18-22, 2003 and on October 10-11, 2004, using the 1.3-m Ritchey-Cretien telescope at Skinakas Observatory, located on the island of Crete (Greece).

The telescope was equipped with a 2000x800 ISA SITe CCD camera and a 1302 lines/mm grating, giving a nominal dispersion of 1.04 Å/pixel, and a wavelength coverage from 4748 Å to 6828 Å. The spectral region was selected so as to include both H $_{\alpha}$ and H $_{\beta}$ spectral lines. For the three spectra that were obtained in September 2003, the wavelength region was somewhat different, shifted further to the blue (from 3900 Å to 6000 Å). One of these three spectra (of source number 3 in M33) was also observed in October 2003, with the wavelength coverage used for the bulk of the spectra. As will be discussed later, the two spectra obtained for this object served as a test of the compatibility between the spectral classes obtained in the two different wavelength regions.

Exposure times ranged from 600 to 7200 s, depending on the object's magnitude and on seeing and weather conditions. In most cases, two or more exposures were obtained per object. Each object observation was followed by an arc calibration exposure (CuAr).

A total of 18 standards, of spectral types ranging from O9.5 to M6 were also observed with exactly the same configuration as the targets.

In the first observing run three objects in the direction of M33 were observed (6/9/2003). In the second run another 19 targets in the direction of M33 were observed (one of them repeated from the first run, so a total of 21 targets in the direction of M33 were observed), while in the third, spectra for 14 objects in the direction of M31 were obtained. The first 6 columns of Table 5.1 list the details of the observations, for the M31 and M33 objects. Column 1 gives the X-ray source number of the target as it appears in the corresponding X-ray catalogue paper, i.e., in PFH2005 for M31 and in PMH2004 for M33. If available, Chandra source names are given in the footnotes of the table. For M31 only one source ([PFH2005] 31) has a Chandra identification, while for M33 two sources ([PMH2004] 196 and 200) have also been identified in existing Chandra catalogues. The second and third columns supply the co-ordinates of the objects (epoch 2000), while the fourth column gives the USNO-B1 identification derived from the cross-correlation between the X-ray catalogue and the USNO catalogue. The fifth column gives the R magnitude of the corresponding USNO object (as given in the USNO catalogue). The sixth column provides the 2MASS identification derived from the cross-correlation between the X-ray catalogue and the 2MASS catalogue, while the seventh column gives the corresponding J magnitude of the 2MASS counterpart (as given in the 2MASS catalogue). In the eighth column, the total exposure time for the specific spectrum is provided. Figure 5.1 illustrates how well the X-ray positions correlate with the coordinates of the optical counterparts observed.

Table 5.1: Log of objects observed in the direction of M 31 and M 33 and derived spectral types.

M 31									
ID*	RA (2000)	Dec (2000)	USNO-B1 ID	R (mag)	2MASS ID	J (mag)	Exp. (s)	Spectral type	
26	00 39 43.51	40 39 42.5	1306-0011237	12.43	00394351+4039425	11.57	3600	G0	
31 ¹	00 39 56.51	40 41 00.4	1306-0011322	10.31	00395652+4041003	9.78	1200	F0	
49	00 40 13.84	40 35 32.3	1305-0011683	11.46	00401383+4035322	10.69	2400	F5	
59	00 40 23.81	40 53 06.9	1308-0012001	10.21	00402380+4053069	9.70	1200	F5	
101	00 40 57.04	40 56 38.5	1309-0012722	11.42	00405703+4056384	10.81	2400	F5	
137	00 41 24.12	40 55 33.8	1309-0012839	11.49	00412410+4055333	12.09	2400	G8	
168	00 41 43.45	41 05 04.8	1310-0013030	11.17	00414345+4105047	10.35	2400	G0	
217	00 42 09.00	41 23 30.6	1313-0012724	9.78	00420901+4123306	8.38	1200	G8	
464	00 43 32.61	41 09 09.3	1311-0013521	9.96	00433260+4109092	8.62	1800	K0	
479	00 43 41.53	41 42 24.3	1317-0014537	10.27	00433892+4138472	15.58	1800	G8	
498	00 43 50.18	41 24 11.6	1314-0013364	10.92	00435017+4124115	10.58	2400	F7	
553	00 44 23.92	42 00 09.6	1320-0014047	10.70	00442392+4200095	10.21	1200	G0	
615	00 45 07.51	41 53 58.3	1318-0015195	11.95	00450752+4153581	10.22	2400	G9	
733	00 46 19.06	42 21 31.1	1323-0017450	12.16	00461905+4221308	10.53	2400	G0	
M 33									
3 ²	01 31 54.90	30 29 52.2	1204-0019506	11.34	01315500+3029522	9.73	2700	G9	
	01 31 52.62	30 29 26.2	1204-0019500	14.66			600	G9	
							2400	M3	
28	01 32 23.56	30 47 49.3	1207-0019732	11.65			1800	G9	
39 ³	01 32 30.41	30 36 18.8	1206-0019336	14.75	01323043+3036186	13.32	4800	K3::	
54	01 32 38.78	30 12 17.0	1202-0019688	10.99	01323878+3012167	11.34	1200	G4	
77	01 32 51.27	30 08 14.2	1201-0020193	10.89	01325128+3008140	11.23	1800	F5	
92	01 32 56.85	30 15 43.1	1202-0019784	9.50	01325685+3015429	8.20	600	G7	
							1200		
122	01 33 13.41	31 02 48.9	1210-0020531	13.84	01331353+3102527	14.58	3600	G0	
	01 33 13.6	31 02 53					3600	G5::	
142	01 33 23.26	30 56 53.4	1209-0020773	9.04	01332270+3056573	14.93	600	F4	
182	01 33 37.07	30 23 21.2	1203-0021390	7.96	01333708+3023213	7.58	480	A5	
196 ⁴	01 33 41.86	30 38 49.1			01334186+3038491	12.61	7200	M5	
200 ⁵	01 33 43.38	30 46 30.7	1207-0020534	11.13	01334337+3046307	9.77	1620	G5	
204	01 33 46.58	30 54 30.8	1209-0020967	10.46	01334657+3054308	9.91	1800	F4	
							3600		
206	01 33 46.69	30 54 55.1	1209-0020969	12.21	01334671+3054550	11.93	1800	K0	
							3600		
281	01 34 26.65	30 58 02.8	1209-0021391	10.48	01342664+3058028	9.56	1200	F8	
297	01 34 33.08	30 57 54.2	1209-0021478	12.28	01343309+3057538	11.89	2400	G8	
337	01 34 52.73	30 28 12.3	1204-0021198	11.92			1200	F5	
358	01 35 08.82	31 02 18.8	1210-0021425	9.99	01350881+3102189	13.48	4500	galaxy	
372	01 35 15.63	30 55 08.3	1209-0021845	10.98	01351564+3055084	10.53	1200	F8	
406	01 35 51.65	30 44 53.4	1207-0021551	9.38	01355164+3044531	8.66	600	F5	

* X-ray source numbers from PFH2005 (M 31) and PMH2004 (M 33)

¹ Chandra source s1-74, from Williams et al. (2004)

² The adopted spectral type for this object is the average of the spectral types obtained from the two observing runs.

³ far off-axis in Chandra observations 1730, not in source list of Grimm et al. (2005)

⁴ Chandra source CXO J013341.8+303848, from Grimm et al. 2005; no USNO-B1 position, 2MASS position given.

⁵ Chandra source CXO J013343.4+304630, from Grimm et al. 2005.

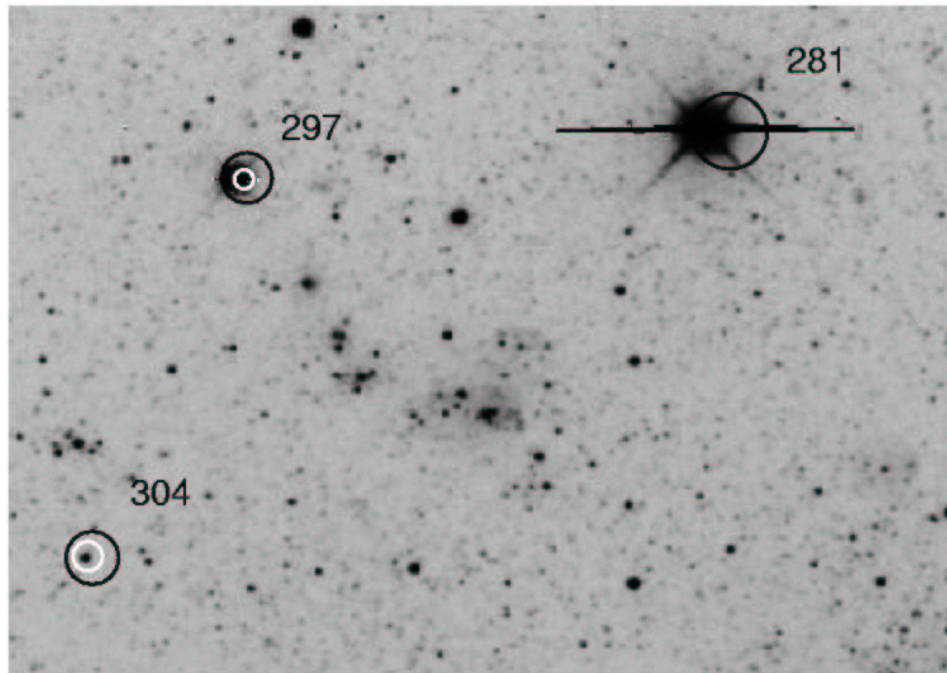


Figure 5.1: X-ray positions (3-sigma error circles in black) of PMH2004 sources overlaid on the optical image of Massey et al. (2002). The bright stellar counterparts with spectroscopic follow-up of [PMH2004] 297 and 281 are clearly visible. The smaller white circles show the improved positions and errors from the analysis of individual XMM-Newton observations (Misanovic et al. 2005). Note that object 281 was not detected in this latter study. The figure also shows one additional X-ray source in the FoV that was classified as 'hard' ([PMH2004] 304).

5.3 Data Reduction

The data reduction was performed using the *STARLINK* Figaro package (Shortridge 2001). The frames were bias subtracted, flat fielded and corrected for cosmic ray events. The 2-D spectra were subsequently sky subtracted using the *POLYSKY* command. A spatial profile was then determined for each 2-D spectrum, and, finally, the object spectra were optimally extracted using the algorithm of Horne (1986), with the *OPTEXTRACT* routine. Arc spectra were then extracted from the arc exposures, using exactly the same profiles as for the corresponding object spectra. The arc spectra were subsequently used to calibrate the object spectra. After calibration, spectra from individual exposures of the same object were co-added to yield the final spectrum.

This procedure was followed for almost all of the observations, with one exception, namely object USNO-B1 1210-0020531, in the M33 list. In this case, a second object was located very close to the target (see Sect. 5.5.2). The resulting spectra could not be extracted separately using the optimal extraction procedure described above. Due to the slight curvature of the spectra, single linear extraction along the lines of the CCD was not possible either. Thus we have resorted to a step extraction with sufficient wavelength overlap between subsequent extractions to ensure compatibility

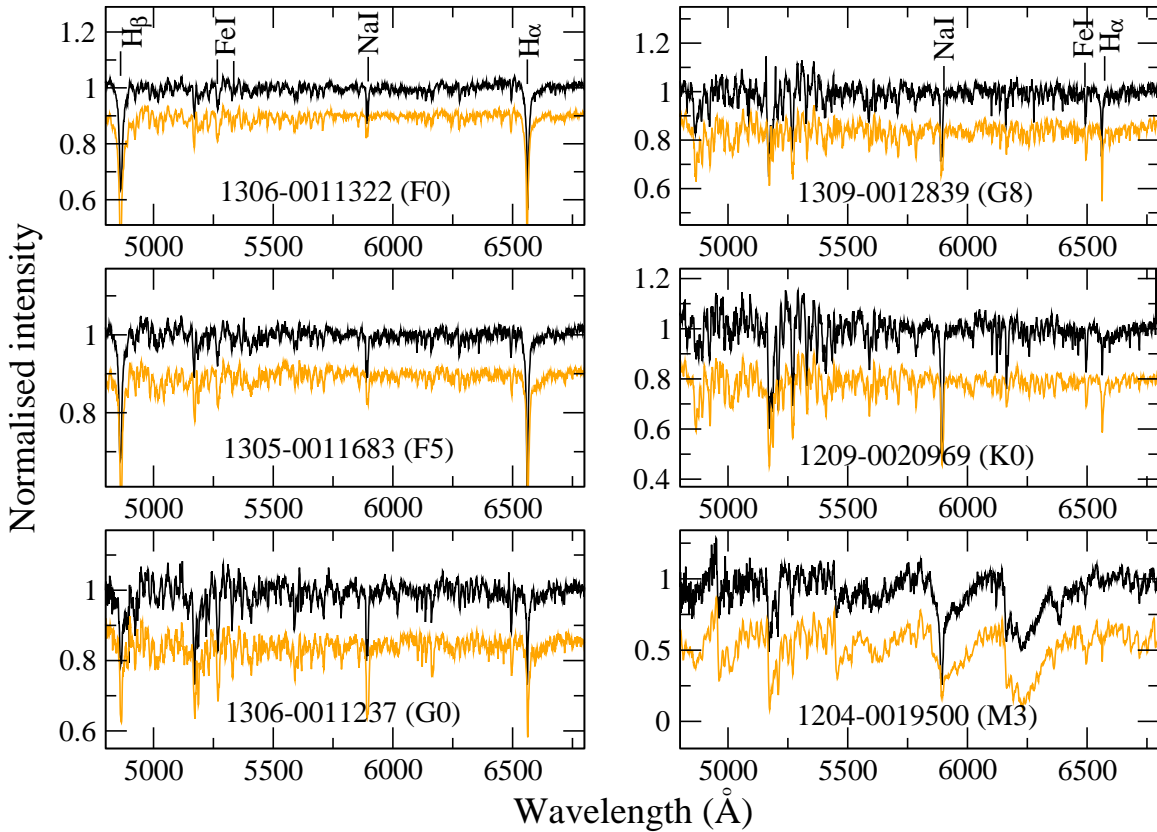


Figure 5.2: Six examples of spectra (flux normalized) of optical counterparts of X-ray sources in the direction of M 31 and M 33 (black lines). For comparison, we also show in grey the corresponding standard star spectrum (of the same spectral type) shifted in y by an arbitrary amount, for demonstration purposes. The identified lines are H_{α} (6563\AA), H_{β} (4861\AA), FeI (5270 , 5328 , 6495\AA) and NaI (5890\AA).

of the fluxes. The calibrating arc spectra were created in exactly the same way.

The signal-to-noise ratio (S/N) of the final spectra varied from 20 to about 350, with an average of 150.

The same reduction and calibration procedures were followed for the 18 spectroscopic standard stars. Most of the standard spectra have S/N ranging between 200 and 350, while two have somewhat lower S/N (around 130).

Figure 5.2 shows six examples of target spectra (black lines), all of foreground stars of different spectral types, which have been flux-normalized for presentation purposes. For comparison, we also show in grey the corresponding standard star spectrum (of the same spectral type) shifted in y by an arbitrary amount, for demonstration purposes.

5.4 Spectral Classification

Classification of the obtained spectra was achieved via cross-correlation with the 18 standard star spectra.

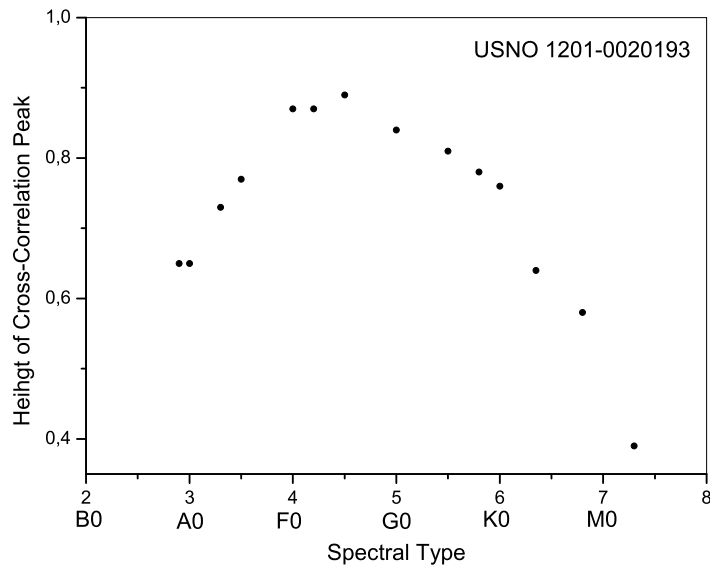


Figure 5.3: Results of cross-correlation between the spectrum of object USNO 1201-0020193 with each standard star spectrum. On the x-axis, the spectral type of the standard star is indicated, while on the y-axis the height of the corresponding cross-correlation peak is given.

Each object spectrum was cross-correlated with each standard spectrum, and the height of the corresponding cross-correlation peak (hereafter, ccp) was recorded. These ccp heights were plotted as a function of the spectral type of the standard, with the maximum of the curve yielding the adopted spectral type for the object spectrum. Figure 5.3 shows a typical example of such a plot, for object USNO 1201-0020193. As it can be seen in this figure, the highest ccp is about 0.9, corresponding to an F5 spectral type. For the entire sample, the highest ccp, on which the spectral classification was based, ranged from 0.7 to 0.95, with most being higher than 0.8.

In some cases there were two ccp (usually for adjoining spectral types in the standard star grid) with comparable heights. For these, we adopted the average spectral type as best representing the spectral class of the object.

As an additional check, we inspected the spectra visually and compared them against those of the standard stars. In very few cases the spectral type yielded by the cross-correlation method described above, had to be modified after visual inspection. These modifications were always within our estimated error of 0.3 of a spectral type (see below).

The adopted spectral type for each objects is reported in the last column of Table 5.1.

The accuracy of the spectral classification achieved in this manner depends clearly on the fineness of the grid of standard spectra used and on the signal-to-noise ratio of the cross-correlated spectra. We estimated the accuracy of the spectral classification in the following manner: We treated each standard star as an object spectrum. We cross-correlated it with all of the other standards, and determined its spectral type

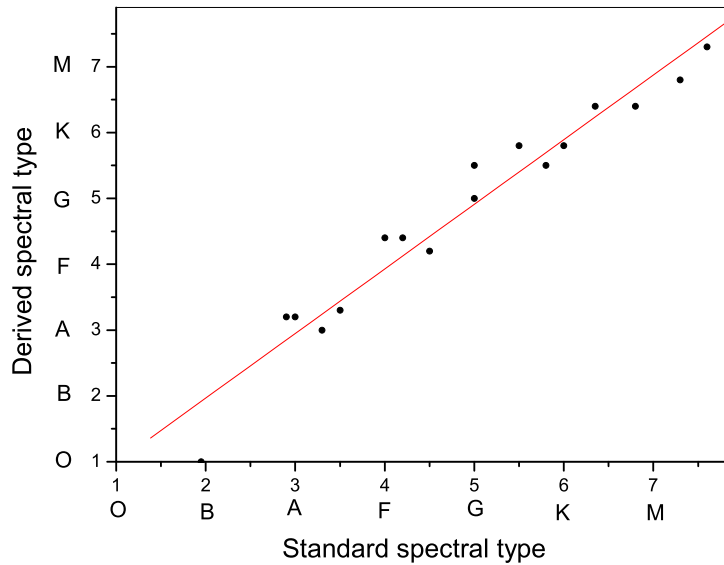


Figure 5.4: Derived versus standard spectral type for the standard stars

using the cross-correlation peak curves, as was done for the object spectra. In Fig. 5.4 we plot the derived spectral type for the standards as a function of the reference spectral type. A least-squares linear fit yields a slope of 0.98 ± 0.06 and a scatter of 0.3 in spectral type.

The effect of the S/N on the derived spectral type was estimated by utilizing the individual exposures of various targets. Following the same procedure as for the co-added spectra we derived spectral types and compared them to the spectral types adopted for the co-added spectra. Although the cross-correlation peaks were lower for the lower S/N spectra, the maximum value of the cross-correlation peaks was equally well defined and no differences in spectral classification were noted down to a S/N of about 30. There are two spectra for which the S/N is significantly lower and for these the spectral classification is less accurate (spectral type followed by the symbol “:”, in Table 5.1). Therefore, for practically all of our spectra the accuracy of the spectral classification depends on the fineness of the standard-star grid and is around 0.3 of a spectral type.

For the three spectra obtained in September 2003, the cross-correlation was performed over the common wavelength range between these spectra and the standards (that were obtained in the subsequent observing runs), i.e. over 1000\AA . Despite the shorter wavelength range, the cross-correlation peaks were very high, similar to those obtained for the rest of the spectra. As mentioned earlier, one of the stars ([PMH2004] 3 in M 33) was observed in both wavelength ranges. The spectral classes derived were in excellent agreement (within 0.1 of a spectral type).

5.5 Discussion of results

All the objects observed, except for [PMH2004] 358 in the direction of M 33 which is a known galaxy (LEDA 5899) and which is discussed separately below, are consistent with being foreground stars, the spectral types of which range from A5 to M5. Figure 5.5 shows the frequency distribution of the derived spectral types.

In Table 5.2, we list some of the X-ray properties of the sources (as given in PMH2004), namely the logarithm of the ratio of the X-ray flux to the optical flux, $\log(f_x/f_{opt})$, and hardness ratios 1 and 2 (HR1 and HR2, respectively). $\log(f_x/f_{opt})$ ranges from -5.9 to -2.5, with an average of -4.2 ± 0.8 , HR1 takes values between 0.16 and 0.94, with an average of 0.5 ± 0.2 , while HR2 ranges from -0.93 to 0.32, with an average of -0.5 ± 0.3 . There is no clear correlation between any of the three X-ray properties listed here and the derived spectral types of the optical counterparts. It is noteworthy, however, that the object with the lowest X-ray to optical flux ratio happens to be the only early type star in the sample (of A type).

The majority of the objects have X-ray hardness ratios and X-ray to optical flux ratios (see Table 5.2) that are consistent with them being foreground stars. In Fig. 5.6 we plot the hardness ratio HR2 against the X-ray to optical flux ratio [$\log(f_x/f_{opt})$], marking the different spectral classes in different colours. It is clear that all spectral classes in our sample (with enough stars to make the comparison meaningful) occupy the same locus on the $\log(f_x/f_{opt})$ -HR2 plane. However, there are three objects, i.e. [PFH2005] 464 in the direction of M 31 and [PMH2004] 206 and [PMH2004] 337 in the direction of M 33, that seem to differ significantly, with hardness ratios that appear to be too high. Two of these have K-type spectra and one is an F-type. These are discussed separately below.

5.5.1 [PFH2005] 464 in M 31 field (USNO1311-0013521)

This object has a hardness ratio (HR2) value that is too high compared to other stars in the sample with similar X-ray to optical flux ratios (as seen in Fig. 5.6). The optical spectrum of the star shows no indication of emission lines that might indicate flaring activity. However, it should be pointed out that the X-ray source itself is quite faint and close to hard sources which may disturb the X-ray detection program in the determination of the hard count rate and lead to a harder HR2.

5.5.2 Source south-west of [PMH2004] 3 in M 33 field

This object was not included in the catalogue of X-ray sources of PMH2004. It's position on a EPIC PN CCD boundary, about 30'' south-west of [PMH2004] 3 and far off-axis, prevented the detection by automatic procedures. However, the 0.2–1 keV X-ray image (see smoothed contour overlay in Fig. 5.7) clearly indicates X-ray emission most likely originating from the M3 star USNO 1204-0019500 (R magnitude 14.66).

The spectrum we obtained for this object is that of an M star.

Table 5.2: X-ray properties of the objects of Table 5.1.

M 31			
ID*	$\log(f_x/f_{opt})$	HR1	HR2
26	-3.6 ± 0.1	0.47 ± 0.08	-0.52 ± 0.09
31	-4.0 ± 0.1	0.71 ± 0.04	-0.60 ± 0.04
49	-4.2 ± 0.1	0.74 ± 0.08	-0.48 ± 0.07
59	-4.6 ± 0.2	0.39 ± 0.16	-0.39 ± 0.19
101	-4.1 ± 0.1	0.75 ± 0.05	-0.69 ± 0.06
137	-4.8 ± 0.4	0.16 ± 0.21	-0.47 ± 0.27
168	-3.6 ± 0.1	0.68 ± 0.03	-0.58 ± 0.04
217	-5.2 ± 0.2	0.50 ± 0.12	-0.93 ± 0.13
464	-5.1 ± 0.3	0.24 ± 0.24	0.07 ± 0.22
479	-4.6 ± 0.1	0.68 ± 0.08	-0.53 ± 0.08
498	-4.7 ± 0.2	0.72 ± 0.17	-0.60 ± 0.16
553	-4.0 ± 0.1	0.58 ± 0.07	-0.63 ± 0.08
615	-4.4 ± 0.3	0.30 ± 0.18	-0.79 ± 0.22
733	-4.5 ± 0.3	0.19 ± 0.23	-0.33 ± 0.27
M 33			
3	-4.1 ± 0.3	0.37 ± 0.21	-0.64 ± 0.26
28	-3.0 ± 0.1	0.44 ± 0.07	-0.33 ± 0.07
39	-2.6 ± 0.2	0.49 ± 0.10	-0.24 ± 0.11
54	-3.9 ± 0.2	0.64 ± 0.15	-0.75 ± 0.14
77	-3.6 ± 0.2	0.67 ± 0.11	-0.48 ± 0.12
92	-5.2 ± 0.4	0.85 ± 0.14	-0.75 ± 0.18
122	-3.0 ± 0.4	0.94 ± 0.32	-0.36 ± 0.29
142	-5.5 ± 0.3	0.73 ± 0.20	-0.51 ± 0.22
182	-5.9 ± 0.2	0.35 ± 0.13	-0.54 ± 0.16
196		0.38 ± 0.05	-0.65 ± 0.05
200	-3.9 ± 0.1	0.61 ± 0.05	-0.52 ± 0.05
204	-4.6 ± 0.1	0.46 ± 0.10	-0.73 ± 0.11
206	-3.5 ± 0.2	0.61 ± 0.32	0.32 ± 0.20
281	-5.0 ± 0.3	0.31 ± 0.17	-0.69 ± 0.18
297	-2.5 ± 0.1	0.56 ± 0.03	-0.10 ± 0.03
337	-3.3 ± 0.1	0.33 ± 0.12	0.30 ± 0.09
358		0.56 ± 0.20	-0.14 ± 0.16
372	-4.7 ± 0.3	0.80 ± 0.18	-0.54 ± 0.21
406	-3.6 ± 0.1	0.47 ± 0.04	-0.41 ± 0.03

*X-ray source, as in Table 5.1

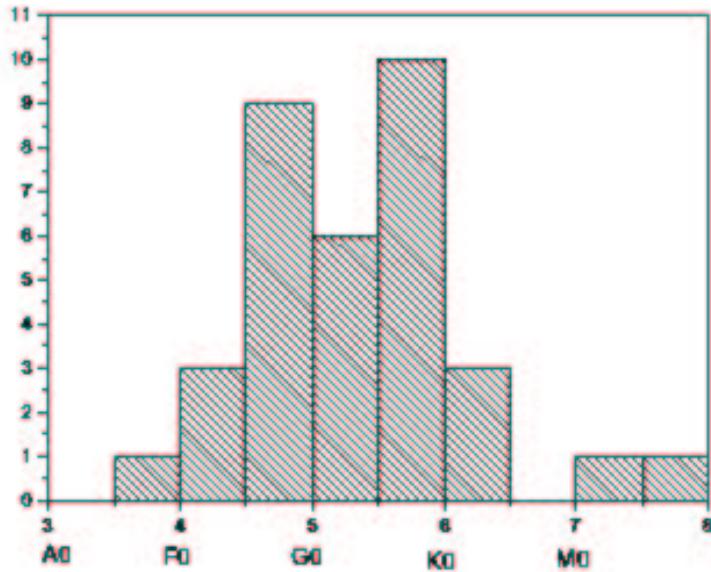


Figure 5.5: Frequency distribution of spectral types of the observed bright stellar counterparts of X-ray sources in M31 and M33.

5.5.3 [PMH2004] 122 in M33 field

This source correlates with the bright USNO star 1210-0020531. However, inspection of the deeper 4m Mosaic images of M33 from the Kitt Peak National Observatory archive (from the Local Group Survey of Massey et al. 2002), shows that there are actually two relatively bright stars separated by $\sim 6''$ in NNE/SSW direction which are probably blended into one star in the USNO catalogue. We have obtained spectra for both stars. They both have G-type spectra, i.e. both stars are compatible with the known X-ray properties of the X-ray source [PMH2004] 122 (see Table 5.2). Thus, it has not been possible to confirm which one of the two stars is the optical counterpart of the X-ray source. More accurate position of the X-ray source would help determine this question. Unfortunately, the source is outside the FOV of the archival *Chandra* observations.

5.5.4 [PMH2004] 196 in M33 field (2MASS01334186+3038491)

Due to the position of [PMH2004] 196 close to the center of M33 its optical counterpart was not catalogued in USNO B2 but only in 2MASS. We therefore give the 2MASS position in Table 5.1. The optical spectrum identifies it as a late M type star, which shows significant H_α emission (see Fig. 5.8). The emission line is clearly seen in all four separate exposures obtained for this star (the combined spectrum from all four exposures is shown in Fig. 5.8). The equivalent width of the emission line is estimated to be $5.7 \pm 0.3 \text{ \AA}$. The presence of Balmer emission lines in late M dwarfs is

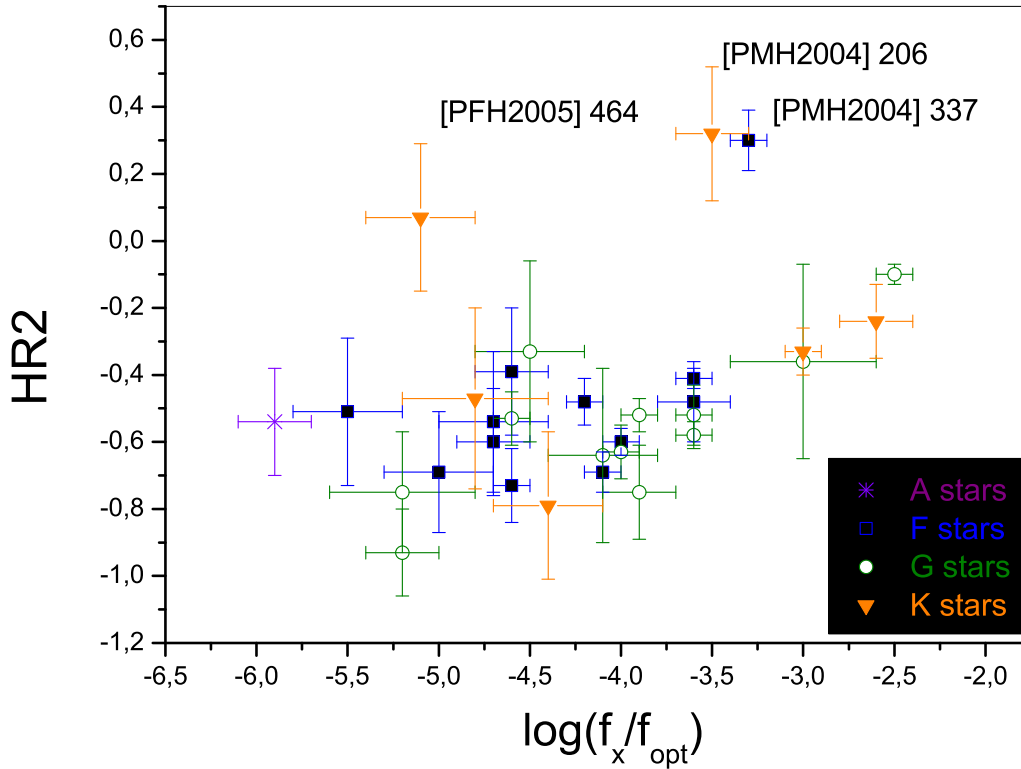


Figure 5.6: X-ray properties of the observed sample. Different spectral types are marked in different colours.

quite frequent and is linked to variability (e.g. Jaschek & Jaschek 1987). Flare stars are expected to exhibit a late spectral type (typically dwarf M-type) and to present emission in CaII (not included in our spectral range) and in the Balmer lines, during the quiescent phase. The strength of the Balmer emission reaches maximum during the second phase of a flaring event (i.e. after the first strong continuum phase).

The object displays long-term X-ray variability, changing its flux by a factor of 6, probably due to flaring. The light curve is presented in Misanovic et al. (2005, their source 170). The source is also found to be variable in the analysis of Chandra data (Grimm et al. 2005). Although the source is faint in X-rays we managed to produce an X-ray spectrum, by combining the counts from three observations. We have obtained an acceptable fit to the spectrum for a plasma with kT of 2.8 keV. Such a high temperature is expected during flares.

5.5.5 [PMH2004] 206 in M 33 field (USNO1209-0020969)

This is an early-K star which has a somewhat high hardness ratio and it was classified as a possibly hard source by PMH2004. The X-ray flux does not show significant variability within the errors, which are quite high due to the faintness of the source, however, the hardness ratio does show some evidence of variability between the ob-

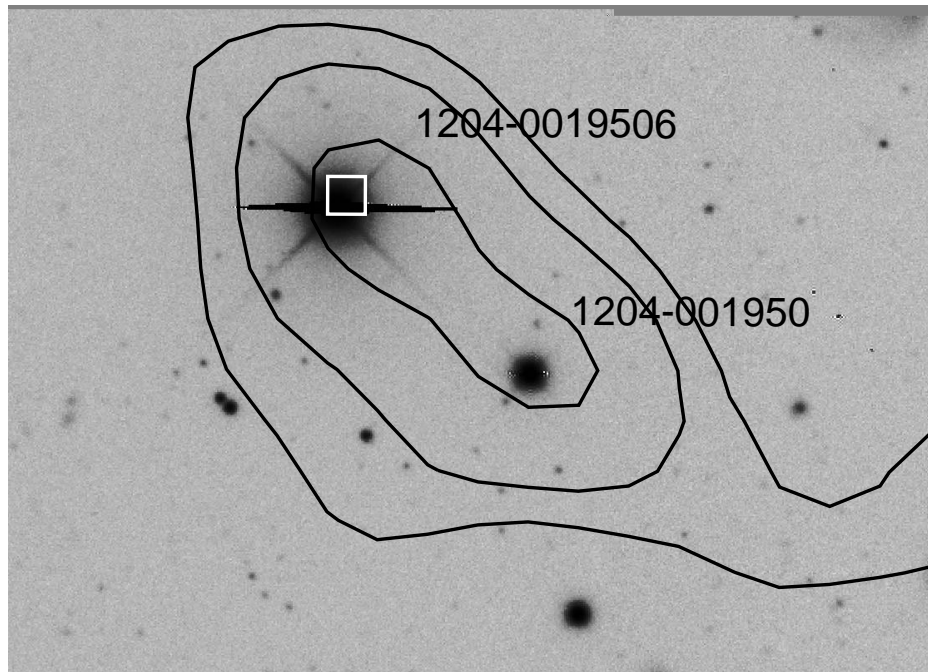


Figure 5.7: X-ray contours from the (0.2–1.0) keV combined image of PMH2004 overlaid on the optical R image of Massey et al. (2002). The contours are at levels $3, 4$ and 6×10^{-6} $\text{cts s}^{-1} \text{ pixel}^{-1}$, and indicate the position of additional X-ray emission coinciding with the USNO source 1204-0019500. The position on a pn CCD gap prevented the detection of this emission as an X-ray source. The nearby source [PMH2004] 3 is shown with a box which size corresponds to the 3 sigma error.

servations that are spread over three years (Fig. 5.9). On the other hand, the optical spectrum of the optical counterpart shows no indication of emission lines that might indicate flaring activity.

5.5.6 [PMH2004] 297 in M 33 field (USNO1209-0021478)

In PMH2004 this object was misidentified as a background elliptical galaxy (object MD 53 in Christian & Schommer 1982). It is actually a stellar source to the North of this galaxy. Indeed, the spectrum is certainly a stellar spectrum of late G-type.

The source displays significant long-term variability in X-rays, changing its flux by a factor of 4. The light curve is presented in Misanovic et al. (2005, their source 253). It so happens that [PMH2004] 297 is one of the two sources among the objects studied in the present paper, for which an X-ray spectrum could be produced. Preliminary analysis of the spectrum indicates that it is typical of very active stars (for example see Güdel et al. 2001b, 2004). We have obtained an acceptable fit with a combination of two temperature plasmas with kT of 0.8 and 2.3 keV. The high temperature component is most probably produced by flaring or some other type of stellar activity, which may also explain the significant X-ray variability of this source.

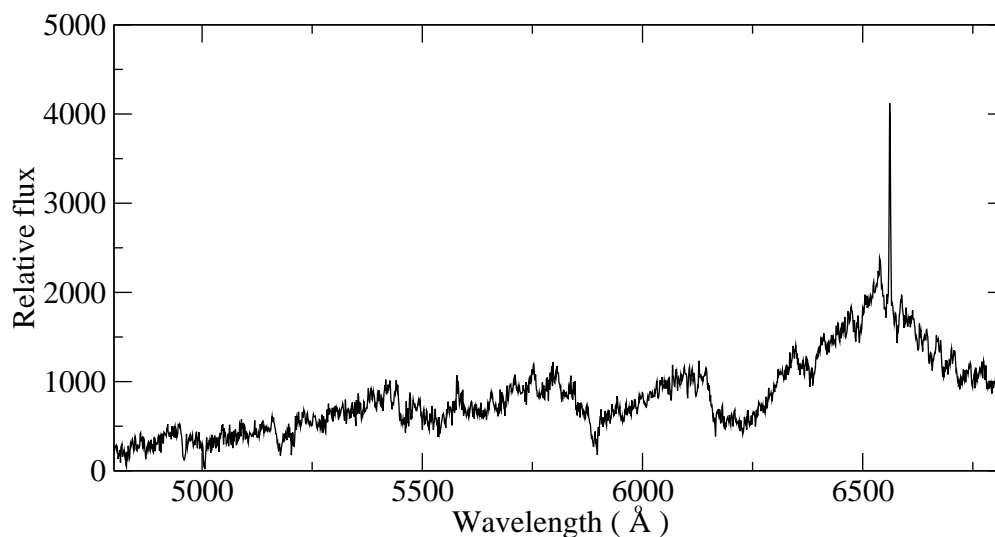


Figure 5.8: *Optical spectrum (not flux normalized) of the optical counterpart of [PMH2004] 196 in M33, identifying it as a late M star with H_{α} emission.*

5.5.7 [PMH2004] 337 in M 33 field (USNO 1204-0021198)

This object has a hardness ratio (HR2)¹ value that is too high compared to other stars in the sample with similar X-ray to optical flux ratios. The optical spectrum of the star shows no indication of emission lines that might indicate flaring activity. However, it should be pointed out that the X-ray source itself is close to a hard source which may disturb count rate and hardness ratio determination.

5.5.8 [PMH2004] 358 in M 33 field (LEDA 5899)

This source corresponds to the spiral galaxy LEDA 5899 (CGCG502-114) which is found within the M33 D25 ellipse and shows somewhat disturbed appearance. Figure 5.10, shows images of the galaxy in U and V (top and bottom panel respectively), extracted from the 4m Mosaic images of M33 from the Kitt Peak National Observatory archive (from the Local Group Survey of Massey et al. 2002). The overlaid circles show the X-ray positions of the source and the corresponding 3 sigma error boxes from PMH2004 (black circle) and Misanovic et al. 2005 (gray circle). The optical spectrum of the galaxy that we obtained here is presented in Fig. 5.11. Some characteristic lines are marked. Our determined redshift (0.034) agrees within the errors with the value of 0.035 given in Huchra et al. (1999). X-ray variability could not be established for this object, due to lack of data. The X-ray luminosity of the galaxy in the band (0.2-4.5)keV is found to be $2 - 3 \times 10^{40} \text{erg s}^{-1}$, a luminosity typical for normal spiral galaxies (see e.g. Fabbiano & Kim 1992).

¹The source is covered by three individual XMM-Newton observations and detected above the selected threshold in two of them. The HR2 seems to be approximately the same (0.24 and 0.28) in both observations separated by several months.

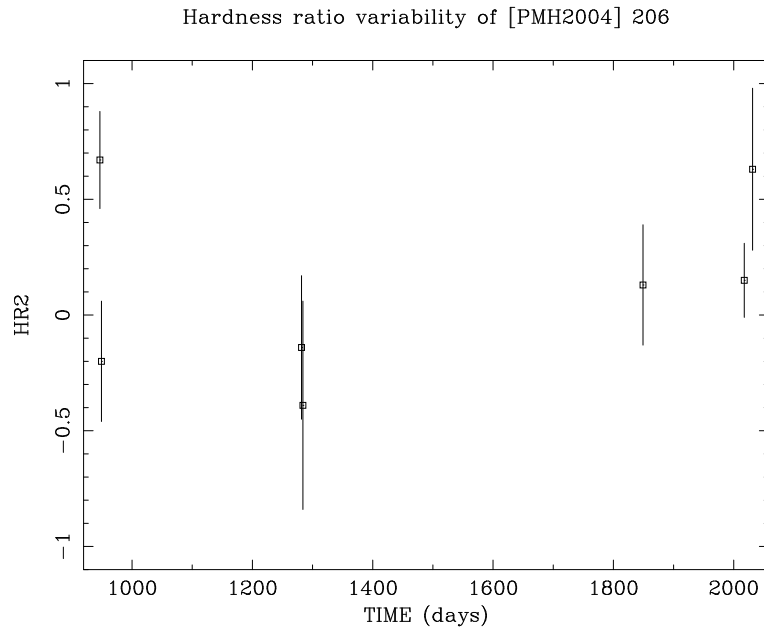


Figure 5.9: Hardness ratio ($HR2$ as defined in *PMH2004*) as a function of epoch of observation for [PMH2004] 206, which corresponds to source 176 in *Misanovic et al. (2005)*. The time is given in days, with the reference day at $JD\ 2450814.5$.

5.6 Summary

We have obtained optical spectra for the 14 brightest optical counterparts of the *XMM-Newton* source catalogue of the M 31 field (*PFH2005*) and the 21 brightest counterparts of the *XMM-Newton* source catalogue of the M 33 field (*PMH2004*), using the 1.3m Skinakas telescope in Crete, Greece. All of the M 31 sources and all but one of the M 33 sources were foreground stars, of spectral types between A5 and M5. One of the M 33 sources (lying within the D25 ellipse) is a background galaxy. The majority of the objects have X-ray hardness ratios and X-ray to optical flux ratios (see Table 5.2) that are consistent with the proposed foreground stars nature. One of the stars close to the M 33 center is a late M dwarf with H_{α} emission, probably a flare star, also displaying strong X-ray variability.

Acknowledgements:

The authors are thankful to T. Koutentakis and A. Strigachev who helped with the observations at Skinakas Observatory. Also, they are indebted to A. Zezas, for his help in determining the redshift of LEDA 5899.

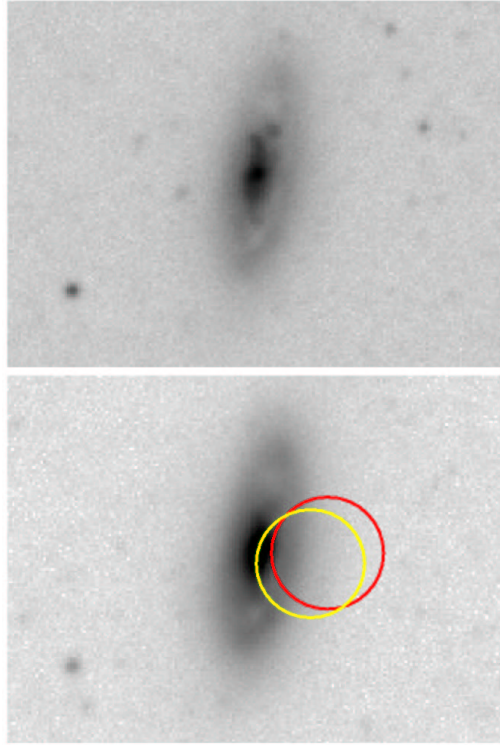


Figure 5.10: Images of the galaxy LEDA 5899, in U (top panel) and V (bottom panel). The circles show the X-ray positions of the source and the corresponding 3 sigma error boxes from PMH2004 (bright circle) and Misanovic et al. 2005 (dark).

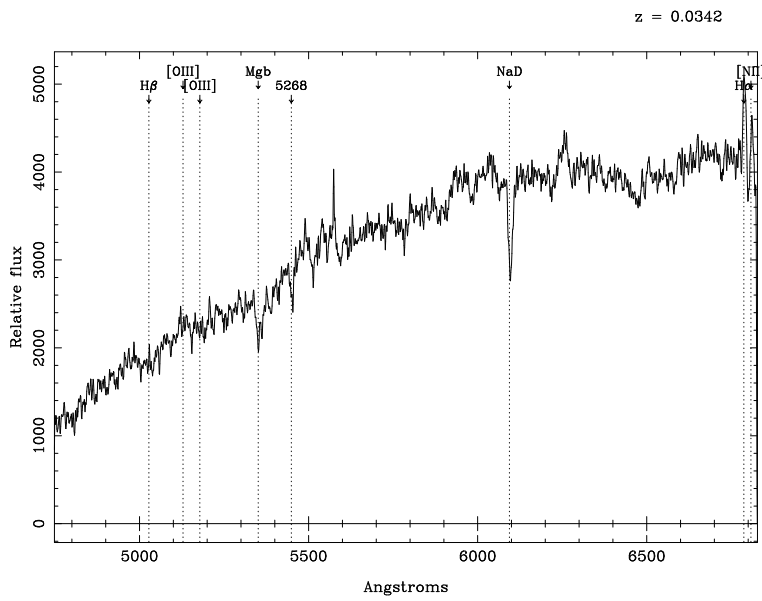


Figure 5.11: Optical spectrum (not flux normalised) of Galaxy LEDA 5899.

Chapter 6

The eclipsing massive X-ray binary M33 X-7: New X-ray observations and optical identification

W. Pietsch, B. J. Mochejska, Z. Misanovic, F. Haberl, M. Ehle, G. Trinchieri, 2004, A&A, 413, 879

Abstract: The eclipsing X-ray binary M33 X-7 was in the field of view during several observations of our XMM-Newton M33 survey and in the archival *Chandra* observation 1730 which cover a large part of the 3.45 d orbital period. We detect emission of M33 X-7 during eclipse and a soft X-ray spectrum of the source out of eclipse that can best be described by bremsstrahlung or disk blackbody models. No significant regular pulsations of the source in the range 0.25–1000 s were found. The average source luminosity out of eclipse is 5×10^{37} erg s⁻¹ (0.5–4.5 keV). In a special analysis of DIRECT observations we identify as optical counterpart a B0I to O7I star of 18.89 mag in V which shows the ellipsoidal heating light curve of a high mass X-ray binary with the M33 X-7 binary period. The location of the X-ray eclipse and the optical minima allow us to determine an improved binary period and ephemeris of mid-eclipse as HJD $(245\,1760.61 \pm 0.09) \pm N \times (3.45376 \pm 0.00021)$. The mass of the compact object derived from orbital parameters and the optical companion mass, the lack of pulsations, and the X-ray spectrum of M33 X-7 may indicate that the compact object in the system is a black hole. M33 X-7 would be the first detected eclipsing high mass black hole X-ray binary.

6.1 Introduction

M33 X-7 (hereafter X-7) was detected as a variable source with a luminosity brighter than 10^{38} erg s⁻¹ in *Einstein* observations (Long et al. 1981a; Markert & Rallis 1983; Trinchieri et al. 1988a,b). Peres et al. (1989) suggested that the X-7 variability pattern

can be explained by an eclipsing X-ray binary (XRB) with an orbital period of 1.7 d and an eclipse duration of ~ 0.4 d. This finding was the first identification of a close accreting binary system with an X-ray source in an external galaxy other than the Magellanic Clouds. It was confirmed combining *Einstein* observatory and first ROSAT data (Schulman et al. 1993, 1994). With the inclusion of more ROSAT and ASCA data (Larson & Schulman 1997; Dubus et al. 1999, hereafter D99) the orbital period turned out to be twice as long. The shape of the eclipse could be described by a slow ingress ($\Delta\Phi_{\text{ingress}} = 0.10 \pm 0.05$), an eclipse duration of $\Delta\Phi_{\text{eclipse}} = 0.20 \pm 0.03$, and a fast eclipse egress ($\Delta\Phi_{\text{egress}} = 0.01 \pm 0.01$) with an ephemeris for the mid-eclipse time of $\text{HJD } 244\,8631.5 \pm 0.1 + N \times (3.4535 \pm 0.0005)$. In addition, D99 discovered evidence for a 0.31 s pulse period. The orbital period, pulse period and observed X-ray luminosity are remarkably similar to those of the Small Magellanic Cloud neutron star XRB SMC X-1 (Liu et al. 2000). However, if the pulse period of X-7 can not be confirmed, the source could also resemble high mass black hole XRBs (BHXB) like LMC X-1 or LMC X-3. It would be the first eclipsing object within this rare class of XRBs.

The position of X-7 correlates with the dense O-B association HS13 (Humphreys & Sandage 1980) and therefore no individual counterpart could be identified based on position only. However, its location in HS13 is consistent with the expectation of a massive companion. As D99 point out, the optical counterpart is likely to show ellipsoidal and/or X-ray heating variations (Tjemkes et al. 1986) which can be used for the optical identification. Variable optical sources within M 33 were systematically searched for in the DIRECT project (see e.g. Mochejska et al. 2001b, hereafter M01b). Many eclipsing binaries, Cepheids, and other periodic, possibly long-period or nonperiodic variables were detected. X-7 is located in DIRECT field M33B. The variability of the optical counterpart was not detected in the previous analysis due to the limitations of the variable search strategy for such small amplitude variables in crowded regions.

As a follow-up of our study of the X-ray source population of M 33 based on all archival ROSAT observations (Haberl & Pietsch 2001, hereafter HP01), we planned a deep XMM-Newton raster survey of M 33 based on 22 Telescope Scientist guaranteed time (proposal no 010264) and AO2 (proposal no 014198) observations, each with a duration of about 10 ks (for first results see Pietsch et al. 2003a). X-7 was covered in 13 of these observations at varying off-axis angles and covering different orbital phases.

In this paper we report on time and spectral variability of X-7 within the XMM-Newton raster survey. We add results from an archival *Chandra* observation, which covered the source, and a dedicated timing analysis of the DIRECT data of the HS13 region.

6.2 X-ray observations and results

For the detailed analysis of X-7 we mostly used data from XMM-Newton EPIC. From the M 33 observations in the *Chandra* archive only the observation with identification no 1730 covered the X-7 field. Table 6.1 summarizes the observation identifications (Col. 1), observation dates (2), elapse time (3), extraction radius R_{ext} used for count

Table 6.1: M 33 X-7 observations with the observatories XMM-Newton (proposal numbers 010264 and 014198) and *Chandra* (1730). Besides observation 010264210, where M 33 X-7 was only in the field of view of the MOS detectors, for XMM-Newton we give EPIC PN count rates, hardness ratios and luminosities. For the low state observations, no hardness ratio could be determined.

Obs. id.	Obs. dates	Elapse time	R_{ext}	Count rate**	HR	L_{x}^*	Offax	Binary phase
(1)	(2)	(ks)	($''$)	(ct ks $^{-1}$)	(10^{37} erg s $^{-1}$)	($^{\circ}$)	(8)	(9)
0102641201	2000-08-02	13.1	30.0	172 ± 4	$1.40 \pm 0.38^{\dagger}$		8.7 10.4	0.54–0.58
0102640401	2000-08-02	13.1	40.0	163 ± 5	$1.27 \pm 0.23^{\dagger}$	8.5	10.4	0.6–0.66
0102640101	2000-08-04	13.3	22.5	4.0 ± 1.2		0.2	8.3	0.1–0.16
0102640501	2001-07-05	11.8	45.0	57 ± 2	2.27 ± 0.30	8.3	7.1	0.33–0.36
0102640601	2001-07-05	8.2 $^{+}$	35.0	75 ± 5	1.09 ± 0.45	6.0	15.7	0.23–0.26
0102640701	2001-07-05	11.7	35.0	54 ± 2	2.10 ± 0.26	7.8	9.3	0.28–0.31
0102541101	2001-07-08	12.5	35.0	101 ± 1.7	0.3	11.1	0.05	
0102642101	2002-01-25	2.3*	35.0	115 ± 3	$1.61 \pm 0.35^*$	8.5	13.1	0.25–0.29
0102642301	2002-01-27	12.3	35.0	316 ± 6	1.17 ± 0.20	7.0	0.9	0.8–0.85
0141980501	2003-01-22	8.1	35.0	114 ± 10	0.20 ± 0.15	9.0	8.3	0.18–0.21
41980601	2003-01-23	13.6	37.5	153 ± 4	1.23 ± 0.28	7.3	10.4	0.46–0.50
41980701	2003-01-24	13.7	35.0	164 ± 6	1.12 ± 0.34	7.3	10.4	0.2–0.56
0801	2003-02-12	10.2	35.0	221 ± 6	1.16 ± 0.28	8.6	8.3	0.20–0.23
	2000-12-07	52.0	15.0	100 ± 2	1.89 ± 0.09	6.3	8.6	0.49–0.65

Notes and references:

+ : M 33 X-7 only in PN field of view.

* : M 33 X-7 only in MOS field of view, integrated MOS count rate, hardness ratio and luminosity given.

† : The on average higher HR during observations 0102641201 and 0102640401 compared to the other observations reflects the difference between thick and medium filter and most likely not a change of the spectrum of M 33 X-7.

** : raw count rate and luminosity in the 0.5–4.5 keV band assuming the best fitting thermal bremsstrahlung spectrum (see Table 6.3) corrected for a Galactic foreground absorption of $N_H = 6.38 \times 10^{20}$ (Dickey & Lockman 1990) and a distance of M 33 of 795 kpc (van den Bergh 1991), which we use throughout the paper.

rates, light curves, and spectra (4), X-7 raw count rates in the 0.5–4.5 keV band (5), hardness ratios (6), and luminosities in the 0.5–4.5 keV band (7). For the XMM-Newton observations, values in columns 4 to 7 correspond to the EPIC PN detector if not indicated differently, since it gives about twice the number of photons than the EPIC MOS cameras. Off axis angle of X-7 (8) and phase coverage within the binary orbit according to the ephemeris of D99 (9) are also given. As hardness ratio (HR) we use the ratio of the counts in the 1.2–3.0 keV band to the counts in the 0.5–1.2 keV band. Luminosities were determined from thermal bremsstrahlung spectra (see Sect. 6.2.3). During observations 0102640101 and 0102641101 X-7 was in low state and source statistics did not allow us to derive hardness ratios. For these observations we assumed that the source spectrum was similar to the spectrum during observation 0102642301 and scaled the source luminosity from the vignetting corrected count rates.

In the XMM-Newton observations (Jansen et al. 2001) the EPIC PN and MOS instruments (Strüder et al. 2001; Turner et al. 2001) were mostly operated in the full frame mode resulting in a time resolution of 73.4 ms and 2.6 s, respectively. Only for the first two observations in Table 6.1, the PN detector was operated in the extended full frame mode (time resolution 200 ms) and during observation 0102640101 the MOS detectors were operated in the small window mode (0.3 s time resolution for the inner CCDs). The medium filter was in front of the EPIC cameras in all but the first two observations which were performed with the thick filter. We used all EPIC instruments for imaging, position determination and for the timing and spectral investigations of X-7. In most of the observations the source is located at high off-axis angle (see Table 6.1), and could be outside of the field of view in some of the cameras. Also, the cameras normally cover different times. The XMM-Newton point spread function (PSF) required extraction radii R_{ext} larger than $22''5$ to encircle $> 80\%$ of the source photons. Depending on the location of the source, counts could be missing due to CCD gaps. Many of the XMM-Newton observations suffer from times of high particle background. To be able to also use these times to cover as much as possible of the X-7 binary orbit, we restricted the energy band for light curve and hardness ratio analysis to 0.5–3.0 keV where the source is brightest.

Four *Chandra* ACIS observations (Weisskopf et al. 2000) of M 33 were obtained from the *Chandra* Data Archive (<http://asc.harvard.edu/cgi-gen/cda>). However, only the ACIS I observation 1730 (see Table 6.1) covered the X-7 field. The instrument was operated in the full frame mode (3.2 s time resolution). X-7 is positioned in the outer corner of the front-illuminated CCD chip I2 during the observation.

The deep space orbits of the satellites XMM-Newton and *Chandra* led to long continuous observation times of X-7. The low earth orbits of the *Einstein*, ROSAT, ASCA and *BeppoSAX* observatories on the other hand, led to observations split in many short intervals of typically less than 1 500 s.

The data analysis was performed using tools in the SAS v5.4.0, CIAO v2.3, EXSAS MIDAS 1.2/1.4, and FTOOLS v5.2 software packages, the imaging application DS9 v2.1b4, the timing analysis package XRONOS v5.19 and spectral analysis software XSPEC v11.2.

For the time variability investigations all X-7 event times were corrected to solar

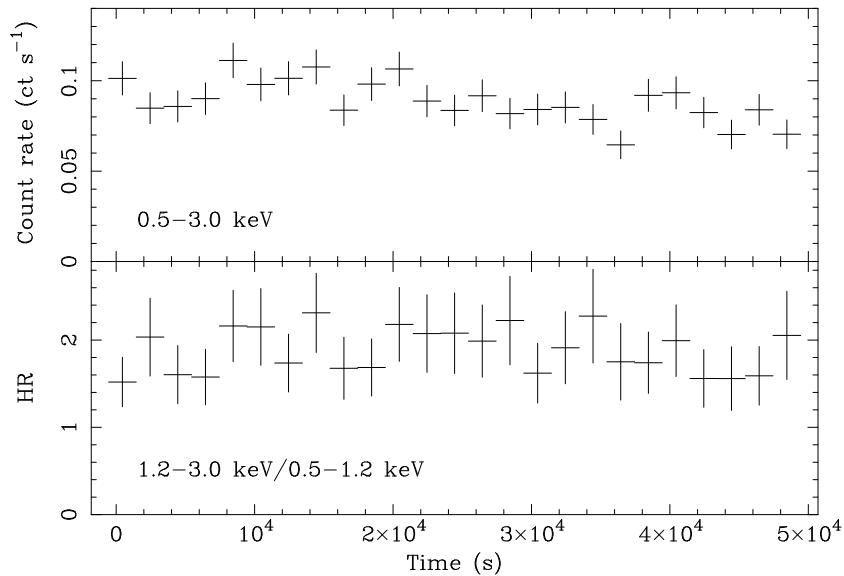


Figure 6.1: *Chandra ACIS I* light curve and hardness ratio of M33 X-7 during observation 1730 integrated over 2000 s. Time zero corresponds to HJD 245 1737.88019 (solar system barycenter corrected). The light curves cover orbital phases 0.49–0.65 (ephemeris of D99).

system barycenter arrival times.

6.2.1 Time variability

The X-ray light curve of X-7 was sampled with a time resolution of 1000 s for EPIC PN and with 2000 s for MOS. While we give raw count rate in Table 6.1, the light curves in Fig. 6.2 and 6.4 are corrected for vignetting and EPIC MOS count rates for the difference in instrument efficiency compared to EPIC PN (i.e. increased by a factor of 2.5). The vignetting corrections for far off-axis positions is up to a factor of 3.5 and may include systematic errors of up to 20%. The source extraction radii chosen assure that more than 80% of the PSF are covered. EPIC PN as well as MOS show X-7 at low intensity for XMM-Newton observations 0102640101 and 0102641101 which covered binary phase 0.01 to 0.16 according to the ephemeris of D99. During the other XMM-Newton observations (covering binary phase 0.18 to 0.85 according to the ephemeris of D99, see Fig. 6.2 and 6.4), the source was in high state. The high state intensity did not vary by more than $\pm 20\%$ between the observations. Within the observations the intensities changed by up to 30% on time scales as short as 1000 s (see Fig. 6.2). No significant variability in hardness ratio was detected between the observations. However, there seems to be variability on shorter time scales. Some of the observations suffer from strong particle background flares which show vignetting effects by the telescope mirrors. We did not exclude these times from the light curves but tried to correct by subtracting this variable background determined as close to X-7 as allowed by CCD configuration and emission from other nearby sources. Our selection of the background regions should minimize spurious effects on source count rate and hardness ratio. Nevertheless, residual effects may explain the count rate

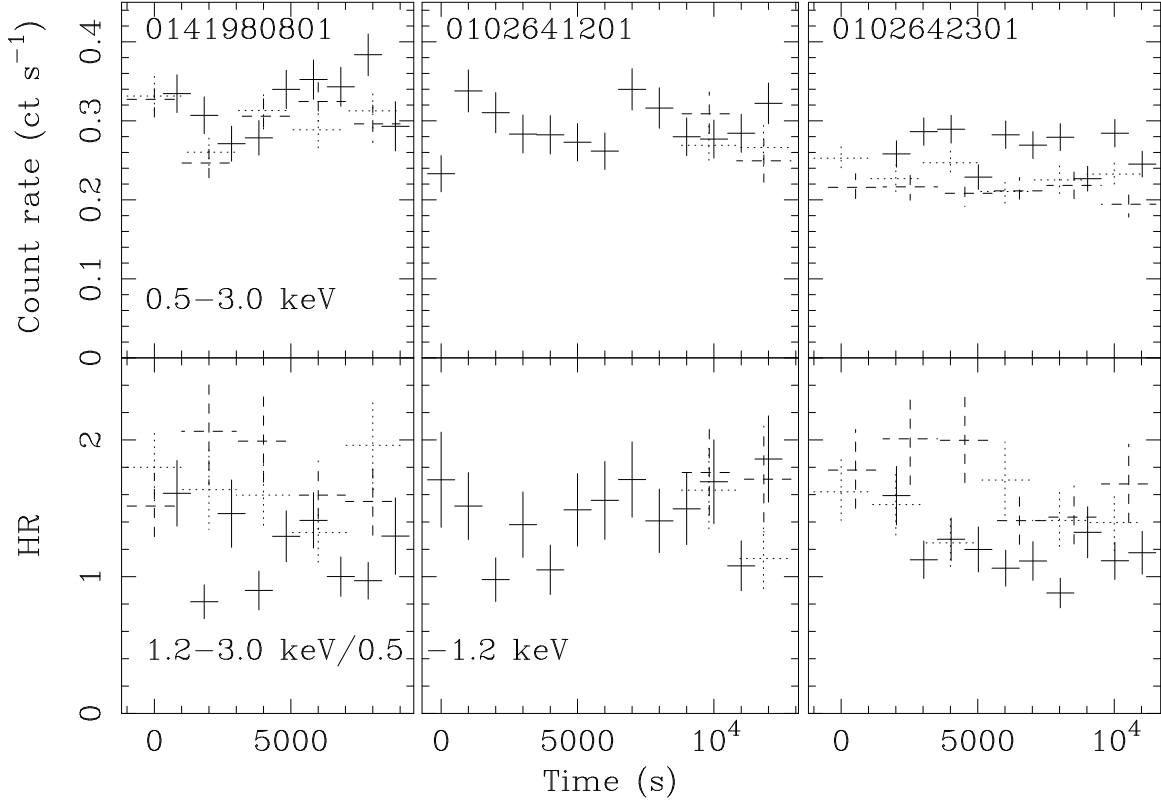


Figure 6.2: XMM-Newton EPIC light curves and hardness ratio of M33 X-7 during observations 0141980801, 0102641201, and 0102642301 with time zero corresponding to HJD 245 2683.14827, 245 1758.79473, 245 2301.91542, respectively (solar system barycenter corrected). Count rates were corrected for vignetting. EPIC MOS rates were scaled by a factor of 2.5 to approximately correct for the difference in instrument efficiency compared to EPIC PN. EPIC PN, MOS1 and MOS2 data are marked with solid, dotted, and dashed error bars. The light curves cover orbital phases 0.20–0.23, 0.54–0.58, and 0.81–0.85 (left to right, ephemeris of D99).

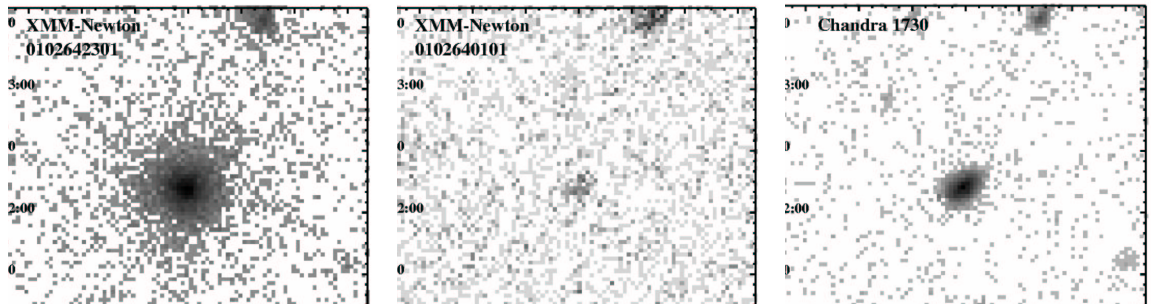


Figure 6.3: Logarithmically-scaled, grey-scale images of the M33 X-7 region of the XMM-Newton EPIC observations 0102642301, 0102640101, and Chandra ACIS I observation 1730 (from left to right). The images (RA, Dec J2000.0) were accumulated with a pixel size of $2''$, in the 0.5–4.5 keV band. EPIC PN and MOS images were selected for times of low background and added. Integration times for observation 0102642301 are 9.0, 12.1, and 12.2 ks for PN, MOS1, and MOS2, respectively, and the maximum in the image is 193 counts per pixel. The corresponding numbers for observation 0102640101 are 11.7, 10.6, and 12.4 ks and 12 counts per pixel. In this image M33 X-7 is close to a CCD gap in PN and there is no MOS exposure in the upper left corner of the image. For the Chandra image the integration time was 49.4 ks and the maximum in the image is 919 counts per pixel. M33 X-7 is the source in the center of the images and was in a low state (eclipse) during observation 0102640101. HP01 X67 is the source to the NW of M33 X-7.

increase in observation 0141980701 around binary phase 0.55 seen in Fig. 6.4.

The light curve for the Chandra observation 1730 shows the source out of eclipse. While the count rate in the 0.5–3.0 keV band decreased during the observation by about 20% and there is also variability down to the the sampling time scale of 2000 s, the hardness ratio did not change significantly (Fig. 6.1).

One has to keep in mind that the EPIC MOS count rates and HRs of X-7 can not directly be compared to the PN one as they originate from a CCD with a different energy response function. The same is even more true if one wants to compare Chandra and XMM-Newton count rates and HRs.

Figure 6.3 shows images ($3'$ to a side) of the X-7 area in the 0.5–4.5 keV band during the high and low state (XMM-Newton EPIC cameras are combined). X-7 is clearly detected also during the low state ($\sim 3\%$ of the average high state emission).

We searched for pulsations within the bright state XMM-Newton low background observations and the Chandra observation in the frequency range 10^{-3} –4 Hz following the Rayleigh Z_n^2 method (Buccheri et al. 1983) as described in Haberl & Zavlin (2002). No signal was found with more than 94% ($< 2\sigma$) confidence level. This includes the previously suggested period of 0.31 s (D99) although the time resolution of 0.073 s of the PN detector in the full frame mode may not be sufficient to clearly detect such a short period.

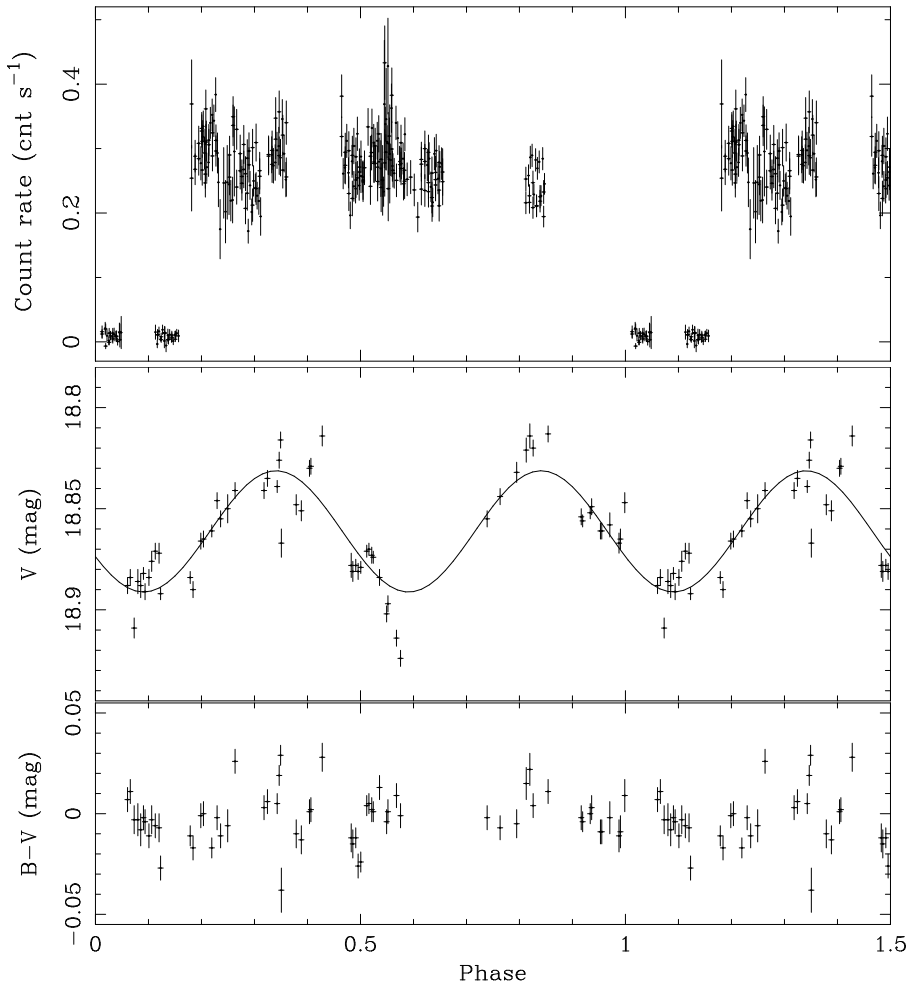


Figure 6.4: Light curve of the XRB M33 X-7 in the 0.5–3.0 keV band and in optical V and B-V folded over the 3.45 d orbital period using ephemeris of D99. Data for phase 0. to 0.5 are repeated at 1.0 to 1.5 for clarity. Added is a double-sinusoidal approximation to the V-data (full line, see text).

6.2.2 Improved position

HP01 give the position of X-7 with a 90% error radius of $2''.0$ which is fully determined by the assumed remaining systematic error of $2''.0$. The much higher number of photons detected with the *Chandra* ACIS I detectors and the good PSF even at an off-axis angle of $8'.6$ allow us to determine a significantly improved source position in observation 1730. Systematic errors can be reduced by adjusting the positions using the well determined radio position of a supernova remnant (SNR) close to X-7 (source 57 in Gordon et al. 1999) which is also detected in X-rays (X67 in HP01), the X-ray source $\sim 1'.5$ to the NNW of X-7 in Fig. 6.3. We get a significantly improved position for X-7: $\alpha=01^{\text{h}}33^{\text{m}}34.^{\text{s}}21$, $\delta=+30^{\circ}32'11''.7$ (J2000), with a remaining error radius of $0''.3$ mainly determined from the statistical uncertainty of the X67 position.

Several XMM-Newton EPIC observations cover X-7 and in addition X67. The

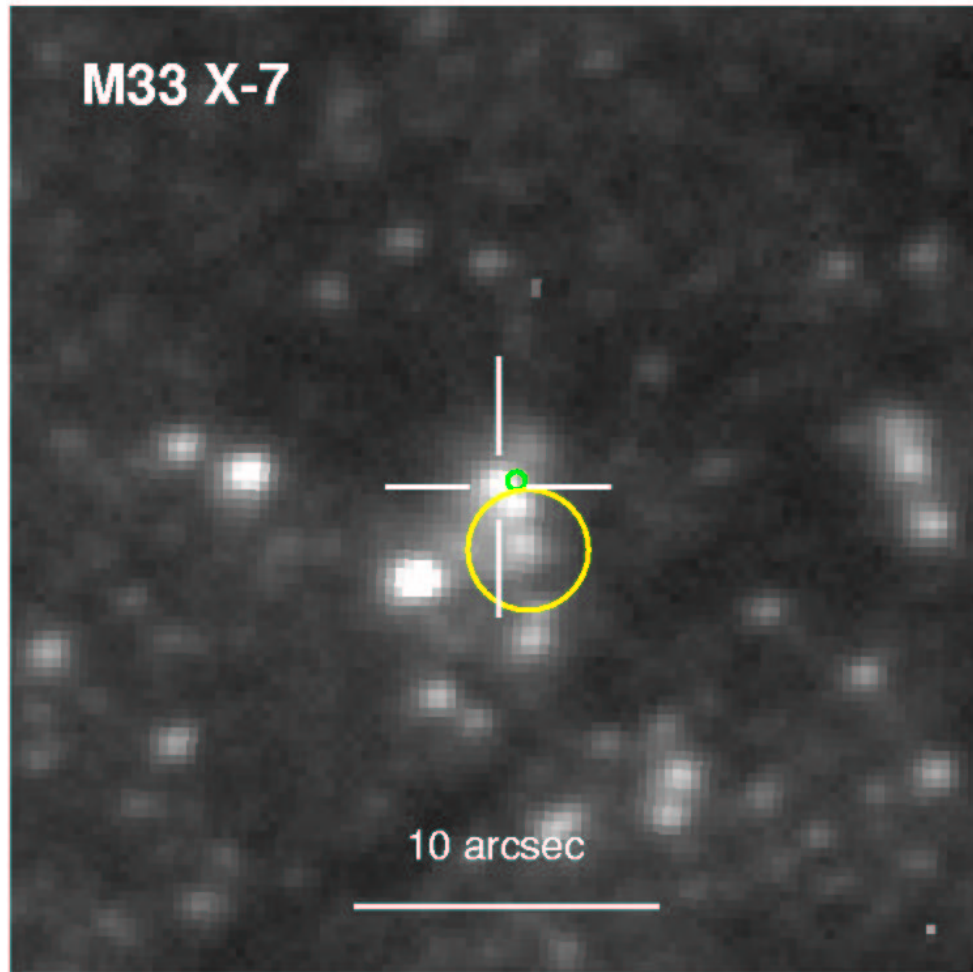


Figure 6.5: Position of M 33 X-7 is shown on a V image of the *DIRECT* survey. The *ROSAT* position and error from *HP01* is marked by the big circle, *Chandra* position by the small circle. The optical identification, i.e. the star showing the 3.4 d variability, is marked by the cross hair.

integration times of the individual observations are much shorter than for the *Chandra* observation and the XMM-Newton PSF is worse. XMM-Newton determined positions of X-7 have individual error radii of $1''.0$ or greater for the PN and MOS cameras and are within the errors consistent with the *Chandra* position. See Fig. 6.5 for an overlay of the improved position on a deep optical V -band image.

6.2.3 Energy spectra

Spectra for the low background XMM-Newton EPIC observation 0102642301 and for the *Chandra* observation were approximated with simple spectral models (see Table 6.2). Individual EPIC PN and MOS spectra were simultaneously fitted with the same model parameters correcting for vignetting and the fraction of the PSF covered by the source extraction area. Energy independent normalization factors for each

Table 6.2: Spectral modeling results for M33 X-7 for the on-axis XMM-Newton EPIC observation 0102641201 (all EPIC instruments fitted together) and the Chandra ACIS I observation 1730. The degradation of the ACIS was taken into account using model ACISABS in XSPEC. For each instrument, we give the effective integration time T_{int} and the raw count rate. The number of energy bins reduced by the number of free parameters defines the degrees of freedom ν . In the case of $\chi^2/\nu \leq 2.0$, 90% errors are given.

Observation	Inst.	T_{int} (ks)	Raw count rate (10^{-2} ct s $^{-1}$)	ν	Model*	N_{HM33}^{**} (10^{20} cm $^{-2}$)	Γ	kT (keV)	L_X^{***} (10^{37} erg s $^{-1}$)	χ^2/ν
<i>XMM-Newton</i>	PN	9.0	32.0 \pm 0.6	119	POWL	19.3 $^{+3.1}_{-2.8}$	2.24 $^{+0.09}_{-0.09}$		6.9 $^{+0.6}_{-0.6}$	0.95
EPIC	MOS1	12.1	10.5 \pm 0.3		BREMS	8.8 $^{+2.0}_{-2.0}$		2.93 $^{+0.32}_{-0.27}$	7.0 $^{+0.5}_{-0.5}$	0.79
0102642301	MOS2	12.2	9.2 \pm 0.3		THPL	2.3 $^{+1.5}_{-1.4}$		4.7 $^{+0.4}_{-0.2}$	7.0 $^{+0.3}_{-0.3}$	1.47
					DISKBB	< 0.8		0.96 $^{+0.04}_{-0.03}$	7.1 $^{+1.0}_{-0.8}$	0.87
<i>Chandra</i>	ACIS I	49.4	10.2 \pm 0.2	101	POWL	28.4 $^{+4.1}_{-3.8}$	2.33 $^{+0.11}_{-0.08}$		6.2 $^{+0.6}_{-0.6}$	1.23
1730					BREMS	15.3 $^{+2.8}_{-2.6}$		2.82 $^{+0.27}_{-0.24}$	6.3 $^{+0.4}_{-0.4}$	0.98
					THPL	7.1		4.7	6.3	2.1
					DISKBB	3.2 $^{+2.4}_{-2.3}$		1.01 $^{+0.04}_{-0.05}$	6.5 $^{+1.3}_{-1.1}$	0.97

* : THPL = thin thermal Plasma with solar abundance (XSPEC model MEKAL), BREMS = thermal bremsstrahlung, POWL = power law, DISKBB = disk blackbody

** : Absorption exceeding the fixed Galactic foreground

***: In the 0.5–4.5 keV band, corrected for Galactic absorption, corrected for extraction radii and vignetting

Table 6.3: Spectral modeling results for the remaining out of eclipse XMM-Newton EPIC observations of M33 X-7 using thermal bremsstrahlung and disk blackbody spectra. In the last row, five EPIC PN spectra of low background observations (Σ EPIC PN; combining 0102640501, 0102640701, 0102642301, 0141980601, and 0141980801) are simultaneously fitted. Model parameters are given with 90% errors (see Table 6.2).

Observation	ν	Thermal bremsstrahlung			Disk blackbody		
		N_{HM33} (10^{20} cm^{-2})	kT (keV)	χ^2/ν	N_{HM33} (10^{20} cm^{-2})	kT (keV)	χ^2/ν
0102641201	53	$16.0^{+3.3}_{-3.3}$	$2.16^{+0.26}_{-0.22}$	0.79	$4.2^{+3.1}_{-2.8}$	$0.87^{+0.06}_{-0.05}$	0.96
0102640401	68	$12.3^{+3.1}_{-3.0}$	$2.66^{+0.33}_{-0.27}$	1.05	< 2.6	$0.99^{+0.04}_{-0.06}$	1.20
0102640501	53	$13.5^{+3.8}_{-3.6}$	$2.72^{+0.39}_{-0.33}$	1.00	< 4.6	$0.99^{+0.06}_{-0.06}$	0.99
0102640601 ⁺	18	$11.4^{+10.4}_{-9.3}$	$2.87^{+4.29}_{-1.26}$	0.88	< 11.7	$0.90^{+0.25}_{-0.23}$	0.99
0102640701	41	$10.8^{+4.3}_{-4.0}$	$2.90^{+0.61}_{-0.47}$	0.91	< 3.3	$0.98^{+0.06}_{-0.07}$	0.93
0102642101 [*]	30	$14.4^{+5.1}_{-4.6}$	$3.00^{+0.87}_{-0.61}$	0.97	< 8.4	$0.97^{+0.11}_{-0.10}$	0.97
0141980501	45	$12.7^{+4.6}_{-4.3}$	$2.54^{+0.48}_{-0.39}$	0.61	< 4.8	$0.94^{+0.07}_{-0.08}$	0.79
0141980601	75	$17.0^{+2.9}_{-2.7}$	$2.14^{+0.21}_{-0.18}$	1.25	$4.8^{+2.6}_{-2.4}$	$0.88^{+0.05}_{-0.05}$	1.15
0141980701	87	$9.4^{+4.1}_{-3.9}$	$2.83^{+0.89}_{-0.58}$	1.06	< 3.9	$0.90^{+0.08}_{-0.09}$	1.04
0141980801	80	$14.7^{+3.9}_{-2.8}$	$2.13^{+0.20}_{-0.17}$	1.01	< 4.4	$0.89^{+0.04}_{-0.05}$	0.92
Σ EPIC PN	251	$11.6^{+1.6}_{-1.5}$	$2.47^{+0.17}_{-0.15}$	1.07	< 1.7	$0.94^{+0.03}_{-0.03}$	1.04

Notes and references:

⁺ : M33 X-7 only in PN field of view.

^{*} : M33 X-7 only in MOS field of view.

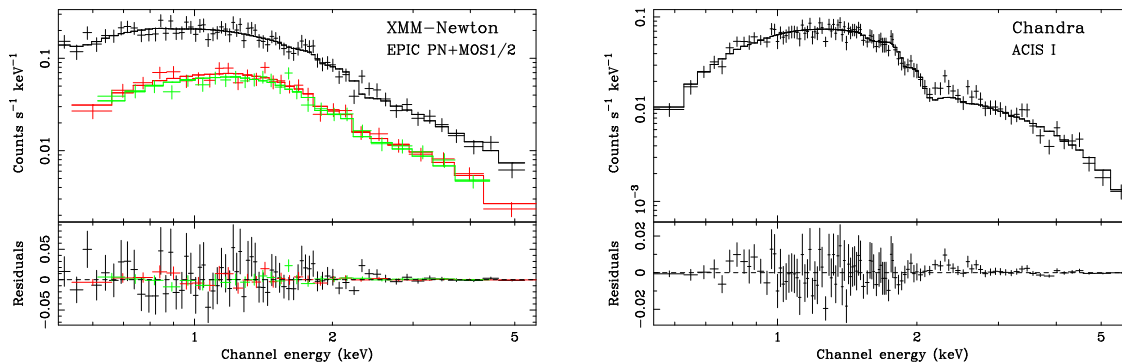


Figure 6.6: *M 33 X-7 spectrum of XMM-Newton EPIC PN observation 0102641201 (left) and of Chandra ACIS I observation 1730 (right). Data and best fitting bremsstrahlung model are shown in the upper panels, residuals between data and model below. For the model parameters see Table 6.2.*

spectrum separately take into account possible differences in source coverage. Model components were the fixed Galactic foreground absorption plus additional absorption within M 33 or in the immediate surrounding of the source using XSPEC model component WABS. A thin thermal (MEKAL) model could be rejected due to the high χ^2/ν , and also a power law (POWL) model still shows large residuals. Bremsstrahlung (BREMS) and also variable temperature disk blackbody (DISKBB) models on the other hand yield acceptable χ^2/ν values. We used the latter models to fit all high state observations of X-7 (see Table 6.3). For all observations, absorbed BREMS or DISKBB models give acceptable fits. The BREMS model needs comparably high absorption outside the Galaxy. The model temperatures are the same within the errors. For the DISKBB model, on the other hand, the additional absorption is very low or absent and inner disk temperatures also don't vary significantly.

6.3 Optical observations and results

6.3.1 Observations

The data were obtained as part of the DIRECT project¹ (Mochejska et al. 2001a,c, M01b) at the Kitt Peak National Observatory² 2.1m telescope during two separate runs, from September 29th to October 5th, 1999 and from November 1st to 7th, 1999. The telescope was equipped with a Tektronix 2048 × 2048 CCD (T2KA camera) having a pixel scale 0.305"/*pixel*. We collected 74 × 600 s exposures in the *V* filter and 30 × 600 s in *B*. The exposure times varied slightly to compensate for the changes of seeing conditions. The typical seeing was 1".5.

¹For information on the DIRECT project see <http://cfa-www.harvard.edu/~kstanek/DIRECT/>.

²Kitt Peak National Observatory is a division of NOAO, which are operated by the Association of Universities for Research in Astronomy, Inc. under cooperative agreement with the National Science Foundation.

6.3.2 Data reduction and calibration

The preliminary processing of the CCD frames was performed with the standard routines in the IRAF ccdproc package.³ The data were corrected for CCD non-linearity at this stage, as described by Mochejska et al. (2001a).

Photometry was extracted using the ISIS image subtraction package (Alard & Lupton 1998; Alard 2000). A brief outline of the method is presented here. For a more detailed description of the reduction procedure the reader is referred to Mochejska et al. (2001a).

The ISIS reduction procedure consists of the following steps: (1) transformation of all frames to a common (x, y) coordinate grid; (2) construction of a reference image from several best exposures; (3) subtraction of each frame from the reference image and (4) extraction of profile photometry from the subtracted images.

All computations were performed with the frames internally subdivided into four sections (`sub_x=sub_y=2`). Differential brightness variations of the background were fit with a second degree polynomial (`deg_bg=2`). A convolution kernel varying quadratically with position was used (`deg_spatial=2`). The PSF width (`psf_width`) was set to 15 pixels. We used a photometric radius (`radphot`) of 3 pixels.

Due to residual non-linearity, our photometry could not be calibrated from observations of standard stars. The coefficients for the color terms of the transformation were derived from the comparison of our NGC 6791 photometry with the data from the KPNO 0.9m telescope (Kaluzny & Udalski 1992). The offsets were determined relative to 735 stars above $V = 20$ mag from the DIRECT catalog of stellar objects in M33 (Macri et al. 2001b). The calibration coefficients can be found in M01b.

The transformation from rectangular to equatorial coordinates was derived using 894 transformation stars with $V < 19.5$ mag from the DIRECT catalog of stellar objects in M33 (Macri et al. 2001b). The average difference between the catalog and the computed coordinates for the transformation stars was $0''.06$ in right ascension and $0''.06$ in declination.

6.3.3 Results

We have searched within a radius of $36''$ around the SIMBAD position of X-7 for stars with a period of around 3.45 d. From the 715 stars examined only one was a binary with a period of about 3.46-3.48 days. It is a star at position $\alpha=01^{\text{h}}33^{\text{m}}34^{\text{s}}.20$, $\delta=+30^{\circ}32'11''.08$ (J2000), with an average V magnitude of 18.86, and an amplitude of variation in this band of about 0.11 mag. From the images it seems to be located in a small star cluster (see Fig. 6.5). Measured V and B magnitudes are given in Table 6.4.

The binary light curve in the V band using the ephemeris of D99 (Fig. 6.4) shows two maxima and minima of different depth as expected for an ellipsoidal and X-ray heating light curve for a high mass XRB (HMXB) together with a double-sinusoidal fit

³IRAF is distributed by the National Optical Astronomy Observatories, which are operated by the Association of Universities for Research in Astronomy, Inc., under cooperative agreement with the NSF.

Table 6.4: Optical light curve of the star identified with M33 X-7. Magnitude with error in the V or B filter (column F) and heliocentric Julian date (HJD) of the observation are given.

F	HJD - 2451400	Mag	F	HJD - 2451400	Mag
V	52.721458	18.854(4)	B	56.793912	18.887(4)
V	52.730637	18.856(3)	V	56.811296	18.884(4)
V	52.780012	18.852(3)	B	56.820741	18.873(4)
V	52.788819	18.849(4)	V	56.829560	18.876(5)
B	52.798183	18.852(3)	B	56.840301	18.865(4)
V	52.846146	18.861(4)	V	56.853021	18.871(4)
V	52.854931	18.861(4)	V	56.877454	18.872(5)
V	52.907662	18.858(6)	V	56.887141	18.892(3)
B	52.916632	18.856(5)	V	57.674028	18.867(7)
V	52.967407	18.867(5)	B	57.699340	18.829(8)
V	52.976493	18.865(5)	V	57.771528	18.848(5)
V	53.005012	18.847(5)	V	57.804664	18.851(5)
V	53.919248	18.841(4)	B	57.814074	18.838(4)
V	54.676273	18.878(6)	V	57.857789	18.830(4)
V	54.686343	18.881(5)	V	57.866620	18.829(4)
B	54.696771	18.866(3)	B	57.875891	18.831(4)
V	54.705671	18.878(3)	V	57.940764	18.814(5)
V	54.720822	18.881(4)	B	57.950278	18.842(4)
B	54.729942	18.855(3)	B	84.699097	18.873(3)
V	54.738519	18.879(3)	V	84.708727	18.884(3)
V	54.777199	18.871(3)	V	84.726852	18.890(4)
V	54.791528	18.870(3)	V	84.777234	18.866(4)
B	54.800428	18.875(3)	B	84.785775	18.865(4)
V	54.809769	18.873(4)	V	84.794618	18.865(4)
V	54.819468	18.874(3)	V	84.849259	18.861(3)
V	54.860521	18.884(4)	V	84.883831	18.846(4)
B	54.869780	18.897(4)	B	84.895440	18.844(3)
B	54.878403	18.898(4)	V	84.906539	18.855(4)
V	54.906435	18.902(4)	V	84.952697	18.850(7)
V	54.915324	18.897(4)	B	86.634097	18.853(3)
V	54.971019	18.914(4)	V	86.643438	18.855(4)
B	54.987986	18.923(4)	V	86.727384	18.844(4)
V	54.997303	18.924(4)	B	86.742824	18.837(4)
V	55.753866	18.832(5)	V	86.897975	18.821(6)
B	55.762789	18.827(4)	V	86.921400	18.814(6)
V	55.861551	18.820(4)	V	88.643009	18.841(4)
B	55.870822	18.824(3)	B	88.652106	18.843(3)
V	55.958808	18.813(4)	V	88.664965	18.835(4)
V	56.672176	18.888(4)	V	88.728738	18.839(3)
B	56.680891	18.895(3)	V	88.741968	18.826(4)
V	56.690012	18.884(4)	V	88.750914	18.816(4)
B	56.701400	18.883(3)	B	88.760104	18.845(2)
V	56.715382	18.909(5)	B	88.780637	18.824(3)
B	56.724583	18.906(4)	V	88.878808	18.826(6)
V	56.739606	18.886(6)	V	88.893958	18.830(7)
B	56.748368	18.883(5)	V	88.927685	18.813(7)
V	56.757824	18.888(6)	V	89.698310	18.912(4)
B	56.766597	18.880(4)	V	89.710938	18.912(3)
V	56.775752	18.882(3)	V	90.841655	18.838(5)
V	56.786528	18.891(4)	V	90.886076	18.835(6)

to the data (average V magnitude of 18.862 ± 0.001 , amplitude $(33 \pm 1) \times 10^{-3}$ mag). The phase of the shallower minimum is shifted by $+0.0956 \pm 0.0028$ with respect to the eclipse center of D99 in the same direction as also indicated by the X-ray light curve (see Sect. 6.2.1). The double-sinusoidal fit is only a crude approximation to the data and the model parameters certainly are affected by non-uniform sampling of the optical light curve. The data suggest a deeper secondary minimum (around phase 0.6) which according to Tjemkes et al. (1986) might point at the effect of an accretion disk in the system. V magnitude and B-V color at X-ray eclipse are 18.890 and -0.005 mag.

6.4 Discussion

6.4.1 Improved ephemeris

D99 determined the eclipse parameters for X-7 using in total 50 ks and 325 ks of archival ROSAT PSPC and HRI data, respectively, integrated over one satellite orbit (~ 3 ks time bins). The XMM-Newton and *Chandra* low and high state observations of X-7 can naturally be explained by finding the source within and out of eclipse. Unfortunately, neither of the observations covered eclipse ingress or egress. However, from the XMM-Newton light curves we can deduce that the eclipse egress lasts < 0.02 and the ingress < 0.16 in phase (well within the parameter range given by D99). These values are only poorly determined due to gaps in the phase sampling over the orbit. More observations are needed to further constrain the binary ephemeris.

Nevertheless, we can restrict the time of eclipse egress to HJD ($245\,1760.935 \pm 0.035$) assuming that it is constrained by the end of observation 0102640101 (when X-7 is still in eclipse) and the beginning of observation 0141980501 (when, 261 binary orbits later, X-7 is already out of eclipse). With the eclipse shape parameters of D99 we then derive a mid-eclipse epoch of HJD ($245\,1760.61 \pm 0.09$). The new X-ray mid-eclipse time corresponds to binary phase 0.07 in Fig. 6.4. Combining this result with the mid-eclipse epoch of D99 we get an improved orbital period for X-7 of (3.45376 ± 0.00021) d well within the period errors given by D99.

6.4.2 The optical companion

The spectral classification of the optical companion can be deduced from the absolute optical magnitude and color during X-ray eclipse when we see the optical surface that is mostly undisturbed by gravitational effects, an expected accretion disk and heating by the X-ray source. To derive the absolute magnitude the measured brightness has to be corrected for the distance (-24.502 mag for the assumed distance of 795 kpc) and for interstellar extinction, the color has to be corrected for reddening. These corrections can be estimated from the Galactic N_H in the direction of X-7 as $A_{V\text{Gal}} = 0.36$ mag and $E(B - V)_{\text{Gal}} = -0.12$ (Predehl & Schmitt 1995). The N_H column depth of the M33 disk in the direction of X-7 is varying significantly on small scales. X-7 is not located in one of the HI holes catalogued by Deul & den Hartog (1990). The absorbing

column within M 33 can be determined to $\sim 2.2 \times 10^{21} \text{ cm}^{-2}$ from a 47×93 arcsec half power beam width HI map (Newton 1980b). The absorbing columns derived from the spectral fits to the X-ray spectra indicate half or less than this absorbing column depending on the spectral model. Assuming that we see X-7 through half of this column and that the same conversion applies as used above, we get $A_{V \text{ M}33} = 0.62$ mag and $E(B - V)_{\text{M}33} = -0.21$. The companion star therefore should have an absolute V magnitude of -6.0 to -6.6 and $(B-V)_0$ of -0.12 to -0.33, which would correspond to a star of spectral type B0I to O7I and masses M_2 of 25 to 35 M_{\odot} (see e.g. Aller et al. 1982). Optical companions of similar spectral type were proposed by D99 based on binary orbit and eclipse length, assuming a 1.4 M_{\odot} neutron star as the compact object.

6.4.3 M 33 X-7, an eclipsing black hole XRB?

We can use the mass of the optical companion as determined in the previous subsection and the mass ratios determined from binary orbit and eclipse length (see D99 and Paczyński 1971; Eggleton 1983) to determine the mass M_X of the compact object. For a binary inclination of 90° , the mass ratio $q (= M_X/M_2)$ is 0.085 yielding M_X of 2.1–3.0 M_{\odot} , significantly higher than expected masses of neutron stars. For an inclination of 70° , q is 0.036 and $M_X = 0.9 - 1.2 M_{\odot}$ well in the range of typical neutron star masses. The inclination can not be constrained by our measurements and the mass estimates above do not exclude a neutron star for the compact object in the system.

Further information on the nature of the compact object may be inferred from the X-ray spectrum. Before XMM-Newton and *Chandra*, the X-ray spectrum of X-7 was investigated using ROSAT and *BeppoSAX* observations. HP01 found that the X-7 spectrum in the ROSAT band can be described by an absorbed power law ($N_H = (1.9 \pm 0.9) \times 10^{21} \text{ cm}^{-2}$ and $\Gamma = 1.86 \pm 0.52$). Thin thermal plasma models did not give acceptable fits. Parmar et al. (2001) reported that *BeppoSAX* detected X-7 in the 2–8 keV band. The spectrum could be described equally well by a power law ($N_H < 9.8 \times 10^{22} \text{ cm}^{-2}$ and photon index $\Gamma = 2.9_{-1.3}^{+1.7}$) or a Bremsstrahlung model ($N_H < 11 \times 10^{22} \text{ cm}^{-2}$ and $kT = 3.7_{-2.4}^{+9.7} \text{ keV}$). If the absorption is fixed to $5.6 \times 10^{20} \text{ cm}^{-2}$, the power law photon index is constrained to 1.7 ± 0.6 and the Bremsstrahlung temperature to $< 3.7 \text{ keV}$. Keeping in mind the large uncertainties in the parameters, these results are consistent with the XMM-Newton and *Chandra* spectra reported for this persistent source in Sect. 6.2.3. In the following we therefore concentrate on these higher quality spectral results.

Thermal Bremsstrahlung and disk blackbody models yield acceptable fits to the XMM-Newton and *Chandra* spectra (see Sect. 6.2.3). For the first model an absorbing column comparable to half the HI values at the position of X-7 within M 33 (see above) is needed to fit the X-7 spectra. The second model only allows us to determine upper limits for the M 33 absorbing column in front of X-7 which are smaller than half the M 33 column depth at that position. The X-7 X-ray spectra are steeper in the 2–10 keV band than typical for HMXB (flat power law shapes with photon indices of $0.8 < \Gamma < 1.5$, White et al. 1983b) and better resemble the spectra of persistent black hole XRBs like LMC X-1 and Cyg X-1 (see e.g. Cui et al. 2002).

Therefore, the spectral results, our unsuccessful search for X-ray pulsations and the high mass estimate of the compact object, inferred from the identified optical companion indicate a black hole as the compact object. These findings make M 33 X-7 a very interesting source for further investigation as it could be the first eclipsing HMXB with a black hole as the compact object.

6.5 Conclusions

XMM-Newton and Chandra observations of the persistent eclipsing HMXB M 33 X-7 allowed us to improve on the orbital period and investigate the X-ray spectrum in unprecedented detail. No X-ray pulsations were detected. A special investigation of the optical variability of DIRECT data of the region revealed in the optical the orbital light curve of a high mass companion. X-ray and optical data point at a black hole as the compact object in the system. Optical spectroscopy and high sensitivity X-ray pulsation searches are needed to clarify the situation.



Chapter 7

Conclusions

7.1 Results

Classification of individual sources of X-ray emission in a galaxy plays a crucial role in understanding its structure, dynamical history and evolution. Complete, uniform samples of detected and classified sources (XRBs, SNRs) in galaxies of different types are needed to investigate how the global properties of these source classes correlate with various galactic environments. In particular, the X-ray source populations in a galaxy provide an insight into its star formation history. Hence, it is necessary to obtain large samples of classified X-ray sources and to establish this relationship for nearby galaxies, which then can be applied to more distant galaxies.

In this dissertation the analysis of a deep XMM-Newton survey of the bright face-on Local Group spiral galaxy M 33 is presented. The survey consists of 24 10-ks raster observations made in the period between August 2000 and July 2003, giving us an opportunity to detect and classify point-like X-ray sources in M 33 (XRBs, SNRs, SSSs) down to the luminosity of 10^{35} erg s⁻¹ in the 0.2–4.5 keV band, which is more than a factor of 10 deeper than in earlier ROSAT observations, and to separate them from foreground stars and background objects (AGN and galaxies). Two catalogues were compiled, containing positions, fluxes in five energy bands, hardness ratios (X-ray colours) derived from these fluxes, flux variability amplitudes, and cross-correlations with optical, infrared and radio data, for all of the 447 sources detected in the combined (Chapter 2) and individual (Chapter 3) observations. The catalogues are available in electronic form at the CDS.

The analysis of both the combined and individual observations has significantly increased the number of classified sources in the M 33 field, compared to previous studies. Using the deep combined data, it was possible to detect fainter sources, in particular SNRs and foreground stars. In addition, with a large number of collected photons, we were able to calibrate hardness ratio plots. Hence, a classification method was established based, to a great extent, only on the X-ray spectral characteristics. In the analysis of the individual observations, on the other hand, it was possible to systematically search for long-term X-ray flux variability, and then use it as an efficient tool for classifying XRBs (8 new XRB candidates are presented in this work)

and other source classes. Furthermore, by analysing the individual images, it was possible to detect and classify faint variable and transient sources such as SSSs.

The XMM-Newton source catalogue derived from the combined images lists 408 sources in the M 33 field, while the analysis of the individual observations revealed a total of 350 objects, 39 of which were new sources. As objects in M 33 we identified or classified a total of 18 SNRs and 20 SNR candidates, 8 XRB candidates (only the 2 brightest XRBs in M 33 were known from previous studies), and 12 SSS candidates (7 of which are reported here for the first time). In addition, a total of 15 AGN and galaxies, and 7 foreground Galactic stars and 30 star candidates were detected in the field of view. A total of 271 sources could only be classified as 'hard', half of which are either XRBs or Crab-like SNRs in M 33, while the other half are, most probably, background objects.

The compiled catalogues contain the largest sample of classified X-ray sources in the M 33 field to date, including a significant number of objects intrinsic to M 33. The classified samples of SNRs and XRBs were used to investigate the spatial and luminosity distributions of these source classes. The results were compared with those obtained previously for other nearby galaxies like M 31, and the LMC. The luminosity distribution of SNRs in the two spiral galaxies is almost the same, although the number of the detected SNRs in M 33 remains much higher. SNRs in the LMC have a slightly flatter luminosity distribution, probably due to the relatively higher metallicity of the LMC, in agreement with previous results. The sample of the classified binaries and XRB candidates in M 33 is still too small for performing detailed population studies. One of the binary systems in our sample is classified as a high mass XRB. Further studies are needed to determine the nature of the remaining objects. Most of the XRBs detected in M 31 are classified as low mass systems, and many of them are associated with globular clusters. The classified XRBs in M 33, on the other hand, do not seem to be connected with globular clusters, indicating that the population of XRBs in this late type spiral may be different than that of M 31.

The spatial distribution of SNRs, XRBs and SSSs supports their classification – most of them seem to be associated with the galactic disk or spiral arms. We detected a region to the South of the M 33 nucleus (along the Southern spiral arm) with 8 SNRs concentrated very close to each other, which could indicate a region of a recent star-formation episode. The spatial distribution of the detected sources in M 33 confirms that there is no pronounced bulge in this late-type spiral galaxy, in contrast to e.g. M 31, where there is a clearly visible concentration of sources and diffuse emission around the galactic centre.

As part of this project, optical follow-up observations were undertaken using the 1.3m Skinakas telescope in Crete, Greece. Optical spectra for the 21 brightest optical counterparts confirmed our proposed X-ray classifications. One of the observed sources corresponds to a background galaxy, LEDA 5899, while the remaining sources are Galactic foreground stars of spectral types between A and M.

Chapter 6 presents detailed spectral and temporal properties of one of the brightest X-ray sources in M 33 - the high mass eclipsing binary X-7. In a special analysis of DIRECT observations, we identified a B0I to O7I star of 18.89 mag in V as the optical

counterpart of this source. Using the optical light-curve, together with our XMM-Newton observations and a set of archived *Chandra* data, we determined an improved binary period and ephemeris of mid-eclipse. Our analysis indicates that the compact object of this binary system is most probably a black hole. Confirmation of this result would make this object the first detected eclipsing high mass black hole X-ray binary.

Finally, we present a few examples of X-ray spectra for source classes detected in this work (Chapter 4). These detailed spectra of the brightest objects are consistent with our catalogued classifications. We find that bright 'hard' sources can be divided into two broad families: one best modelled by a powerlaw model with photon index in the range of 1.0–2.0, and the other displaying multicolour disk blackbody spectra with the inner region disk temperatures kT_{in} of 0.8 to 1.5 keV. This illustrates how the detailed spectral analysis can be used to further distinguish the 'hard' sources that we could not separate with our HR method. However, this is only possible for a small number of sufficiently bright sources. Detailed X-ray properties of a sample of about ~ 20 sources is in progress, and will be presented in a future work.

7.2 Future prospects

The future work on X-ray properties of M 33 also includes the detailed spectral analysis of the ULX M 33 X–8. We propose a more physical model to fit the X-ray spectrum of this source. We also detect spectral variability by analysing all 15 observations that cover this ULX. Our preliminary results indicate that, contrary to previous studies, the mass of the compact object is $\sim 20\text{--}50 M_{\odot}$, and no beaming is required to account for the observed luminosity.

The work presented in this dissertation significantly increased our knowledge about the X-ray source populations in M 33, increasing the sample of not only detected, but also classified sources in this Local Group galaxy. However, deeper, more sensitive data are certainly needed to further explore the X-ray properties of this nearest face-on spiral. While XMM-Newton spectral capabilities were heavily exploited in the work presented here, *Chandra's* superior spatial resolution is needed to resolve crowded regions and complex structures.

Part of existing *Chandra* archived data, which covers significantly smaller part of M 33, were also included in this work (for source X–7). In addition, recent studies of these observations by Grimm et al. (2005, source list and luminosity function), and Ghavamian et al. (2005, the SNR population study) confirm our results.

Moreover, with a very large *Chandra* proposal that has just been accepted, the X-ray studies of M 33 are continuing (see *Chandra* webpage¹). This new *Chandra* survey will cover the whole central region of the galaxy with a sensitivity of at least a factor of two deeper than our XMM-Newton data. These two complementary data sets together, will provide complete census of the X-ray source population of this late-type, nearby spiral galaxy.

¹<http://chandra.harvard.edu>



Bibliography

Alard, C. 2000, A&AS, 144, 363

Alard, C. & Lupton, R. H. 1998, ApJ, 503, 325

Aller, L. H., Appenzeller, I., Baschek, B., et al., eds. 1982, Landolt-Börnstein: Numerical Data and Functional Relationships in Science and Technology - New Series " Gruppe/Group 6 Astronomy and Astrophysics " Volume 2

Angelini, L., Loewenstein, M., & Mushotzky, R. F. 2001, ApJ, 557, L35

Antonucci, R. 1993, ARA&A, 31, 473

Aschenbach, B. 2002, in Neutron Stars, Pulsars, and Supernova Remnants, 13

Baganoff, F. K., Bautz, M. W., Brandt, W. N., et al. 2001, Nature, 413, 45

Becker, W. 2001, AIP Conf. Proc. 599: X-ray Astronomy: Stellar Endpoints, AGN, and the Diffuse X-ray Background, 599, 13

Becker, W. & Pavlov, G. G. 2001, The Century of Space Science, eds. J.Bleeker, J.Geiss, M.Huber, Kluwer Academic Publishers, (astro-ph/0208356)

Becker, W. & Trümper, J. 1999, A&A, 341, 803

Begelman, M. C. 2002, ApJ, 568, L97

Bender, R., Kormendy, J., Bower, G., et al. 2005, ApJ, 631, 280

Bildsten, L. 1998, ApJ, 501, L89

Bildsten, L., Chakrabarty, D., Chiu, J., et al. 1997, ApJS, 113, 367

Boller, T., Tanaka, Y., Fabian, A., et al. 2003, MNRAS, 343, L89

Boulesteix, J., Courtes, G., Laval, A., Monnet, G., & Petit, H. 1974, A&A, 37, 33

Bradt, H. V., Levine, A. M., Remillard, R. A., & Smith, D. A. 2000, in Rossi2000: Astrophysics with the Rossi X-ray Timing Explorer, meeting abstract

Brandt, W. N., Alexander, D. M., Hornschemeier, A. E., et al. 2001, AJ, 122, 2810

- Brandt, W. N. & Hasinger, G. 2005, *ARA&A*, 43, 827
- Bregman, J. N. & Pildis, R. A. 1992, *ApJ*, 398, L107
- Buccheri, R., Bennett, K., Bignami, G. F., et al. 1983, *A&A*, 128, 245
- Chakrabarty, D. & Morgan, E. H. 1998, *Nature*, 394, 346
- Christian, C. A. & Schommer, R. A. 1982, *ApJ*, 253, L13
- Colbert, E., Heckman, T., Ptak, A., Strickland, D., & Weaver, K. 2003, *AAS/High Energy Astrophysics Division*, 7
- Colbert, E. J. M. & Miller, M. C. 2003, Proceedings edited by M. Novello, S. Perez-Bergliaffa and R. Ruffini, World Scientific, Singapore, 2005. (astro-ph/0402677)
- Colbert, E. J. M. & Mushotzky, R. F. 1999, *Advances in Space Research*, 23, 847
- Colbert, E. J. M. & Ptak, A. F. 2002, *ApJS*, 143, 25
- Condon, J. J., Cotton, W. D., Greisen, E. W., et al. 1998, *AJ*, 115, 1693
- Corcoran, M. F., Swank, J., Rawley, G., et al. 1994, in *AIP Conf. Proc. 313: The Soft X-ray Cosmos*, 159
- Cowley, A. P., Schmidtke, P. C., Crampton, D., & Hutchings, J. B. 1996, in *IAU Symp. 165: Compact Stars in Binaries*, 439
- Crampton, D., Gussie, G., Cowley, A. P., & Schmidtke, P. C. 1997, *AJ*, 114, 2353
- Cui, W., Feng, Y. X., Zhang, S. N., et al. 2002, *ApJ*, 576, 357
- Cutri, R. M., Skrutskie, M. F., van Dyk, S., et al. 2003, *VizieR Online Data Catalog*, 2246
- Davidson, K. & Ostriker, J. 1972, *Nature*, 236, 46
- de Vaucouleurs, G., de Vaucouleurs, A., Corwin, H. G., et al. 1991, *Third Reference Catalogue of Bright Galaxies (Volume 1-3, XII, 2069 pp. 7 figs.. Springer-Verlag Berlin Heidelberg New York)*
- den Herder, J. W., Brinkman, A. C., Kahn, S. M., et al. 2001, *A&A*, 365, L7
- Deul, E. R. & den Hartog, R. H. 1990, *A&A*, 229, 362
- Di Stefano, R. & Kong, A. K. H. 2003, *ApJ*, 592, 884
- Di Stefano, R. & Kong, A. K. H. 2004, *ApJ*, 609, 710
- Di Stefano, R., Kong, A. K. H., Greiner, J., et al. 2004, *ApJ*, 610, 247

- Di Stefano, R. & Rappaport, S. 1995, in ASP Conf. Ser. 72: Millisecond Pulsars. A Decade of Surprise, 155
- Dickey, J. M. & Lockman, F. J. 1990, ARA&A, 28, 215
- Dove, J. B., Wilms, J., & Begelman, M. C. 1997, ApJ, 487, 747
- Dubus, G., Charles, P. A., & Long, K. S. 2004, A&A, 425, 95
- Dubus, G., Charles, P. A., Long, K. S., & Hakala, P. J. 1997, ApJ, 490, L47
- Dubus, G., Charles, P. A., Long, K. S., Hakala, P. J., & Kuulkers, E. 1999, MNRAS, 302, 731
- Dubus, G., Hameury, J.-M., & Lasota, J.-P. 2001, A&A, 373, 251
- Dubus, G. & Rutledge, R. E. 2002, MNRAS, 336, 901
- Duric, N. 2000a, in Proceedings 232. WE-Heraeus Seminar, 179
- Duric, N. 2000b, in Proceedings 232. WE-Heraeus Seminar, 127
- Eardley, D. M., Lightman, A. P., & Shapiro, S. L. 1975, ApJ, 199, L153
- Ebisawa, K., Mitsuda, K., & Hanawa, T. 1991, ApJ, 367, 213
- Eckart, A., Baganoff, F. K., Morris, M., et al. 2004, A&A, 427, 1
- Eggleton, P. P. 1983, ApJ, 268, 368
- Ehle, M., Pietsch, W., & Haberl, F. 2001, in ASP Conf. Ser. 251: New Century of X-ray Astronomy, 300
- Esin, A. A., McClintock, J. E., & Narayan, R. 1997, ApJ, 489, 865
- Fabbiano, G. 1989, ARA&A, 27, 87
- Fabbiano, G. 1995, Bulletin of the American Astronomical Society, 27, 877
- Fabbiano, G. 2003, Chinese Journal of Astronomy and Astrophysics, 3, 193
- Fabbiano, G. 2004, in Revista Mexicana de Astronomia y Astrofisica Conference Series, 46–49
- Fabbiano, G. & Kim, D.-W. 1992, in Frontiers Science Series, 423
- Fabbiano, G., Krauss, M., Zezas, A., Rots, A., & Neff, S. 2003, ApJ, 598, 272
- Fabbiano, G. & Trinchieri, G. 1987, ApJ, 315, 46

- Fabbiano, G. & White, N. E. 2003, Compact stellar X-ray sources, book in preparation for Cambridge University press, eds. W. Lewin and M. van der Klis (astro-ph/0307077)
- Fabian, A. C., Iwasawa, K., Reynolds, C. S., & Young, A. J. 2000, PASP, 112, 1145
- Fabian, A. C. & Terlevich, R. 1996, MNRAS, 280, L5
- Fabrika, S. & Sholukhova, O. 1995, Ap&SS, 226, 229
- Fabrika, S. N., Sholukhova, O. N., & Zakharova, S. A. 1997, Bull. Special Astrophys. Obs., 43, 133
- Feldmeier, A., Puls, J., & Pauldrach, A. W. A. 1997, A&A, 322, 878
- Fender, R. 2002, LNP Vol. 589: Relativistic Flows in Astrophysics, 589, 101
- Fender, R. & Maccarone, T. 2004, in ASSL Vol. 304: Cosmic Gamma-Ray Sources, 205
- Fender, R. P., Garrington, S. T., McKay, D. J., et al. 1999, MNRAS, 304, 865
- Finlator, K., Ivezić, Ž., Fan, X., et al. 2000, AJ, 120, 2615
- Fleming, T. A., Gioia, I. M., & Maccacaro, T. 1989, ApJ, 340, 1011
- Foschini, L., Rodriguez, J., Fuchs, Y., et al. 2004, A&A, 416, 529
- Frank, J., King, A., & Raine, D. 1992, Accretion Power in Astrophysics (Cambridge University Press)
- Frank, J., King, A., & Raine, D. J. 2002, Accretion Power in Astrophysics: Third Edition (Accretion Power in Astrophysics, by Juhan Frank and Andrew King and Derek Raine, pp. 398. Cambridge, UK: Cambridge University Press)
- Freyberg, M. J., Briel, U. G., Dennerl, K., et al. 2004, in X-Ray and Gamma-Ray Instrumentation for Astronomy XIII. Edited by Flanagan, Kathryn A.; Siegmund, Oswald H. W. Proceedings of the SPIE, Volume 5165, 112–122
- Gaetz, T. J. & Salpeter, E. E. 1983, ApJS, 52, 155
- Gallo, L. C., Boller, T., Tanaka, Y., et al. 2004, MNRAS, 347, 269
- Garcia, M. R., Primini, F. A., Williams, B., & Yuan, F. 2004, American Astronomical Society Meeting Abstracts, 204
- Gebhardt, K., Lauer, T. R., Kormendy, J., et al. 2001, AJ, 122, 2469
- Ghavamian, P., Blair, W. P., Long, K. S., et al. 2005, AJ, 130, 539
- Gierliński, M., Zdziarski, A. A., Poutanen, J., et al. 1999, MNRAS, 309, 496

- Gilfanov, M. 2004, MNRAS, 349, 146
- Gilfanov, M., Grimm, H.-J., & Sunyaev, R. 2004, MNRAS, 347, L57
- Giovagnoli, A. & Mould, J. 1994, PASP, 106, 376
- Gordon, S. M., Duric, N., Kirshner, R. P., Goss, W. M., & Viallefond, F. 1999, ApJS, 120, 247
- Gordon, S. M., Kirshner, R. P., Long, K. S., et al. 1998, ApJS, 117, 89
- Green, D. A. 2004, Bulletin of the Astronomical Society of India, 32, 335
- Greiner, J. 2000, New Astronomy, 5, 137
- Greiner, J., Di Stefano, R., Kong, A., & Primini, F. 2004, ApJ, 610, 261
- Greiner, J., Hasinger, G., & Kahabka, P. 1991, A&A, 246, L17
- Greiner, J., Hasinger, G., & Thomas, H.-C. 1994, A&A, 281, L61
- Greiner, J., Supper, R., & Magnier, E. A. 1996, Supersoft X-Ray Sources, Lecture Notes in Physics, Vol. 472, edited by Jochen Greiner. Springer-Verlag, Berlin Heidelberg New York, 472, 75
- Grimm, H.-J., Gilfanov, M., & Sunyaev, R. 2002, A&A, 391, 923
- Grimm, H.-J., Gilfanov, M., & Sunyaev, R. 2003, MNRAS, 339, 793
- Grimm, H.-J., McDowell, J., Zezas, A., Kim, D.-W., & Fabbiano, G. 2005, ApJS, 161, 271
- Güdel, M., Audard, M., Briggs, K., et al. 2001a, A&A, 365, L336
- Güdel, M., Audard, M., Magee, H., et al. 2001b, A&A, 365, L344
- Güdel, M., Audard, M., Reale, F., Skinner, S. L., & Linsky, J. L. 2004, A&A, 416, 713
- Gürkan, M. A., Freitag, M., & Rasio, F. A. 2004, ApJ, 604, 632
- Haardt, F. & Maraschi, L. 1991, ApJ, 380, L51
- Haberl, F., Dennerl, K., & Pietsch, W. 2003, A&A, 406, 471
- Haberl, F. & Pietsch, W. 1999, A&AS, 139, 277
- Haberl, F. & Pietsch, W. 2001, A&A, 373, 438
- Haberl, F. & Pietsch, W. 2005, A&A, 438, 211
- Haberl, F. & White, N. E. 1990, in Astronomische Gesellschaft Abstract Series, 52

- Haberl, F., White, N. E., & Kallman, T. R. 1989, *ApJ*, 343, 409
- Haberl, F. & Zavlin, V. E. 2002, *A&A*, 391, 571
- Haisch, B., Strong, K. T., & Rodono, M. 1991, *ARA&A*, 29, 275
- Harnden, F. R., Golub, L., Rosner, R., et al. 1979, *BAAS*, 11, 775
- Hasinger, G. 1994, *Reviews of Modern Astronomy*, 7, 129
- Hasinger, G., Altieri, B., Arnaud, M., et al. 2001, *A&A*, 365, L45
- Hasinger, G., Miyaji, T., & Schmidt, M. 2005, *A&A*, 441, 417
- Hasinger, G. & van der Klis, M. 1989, *A&A*, 225, 79
- Hatzidimitriou, D., Pietsch, W., Misanovic, Z., Reig, P., & Haberl, F. 2005, *A&A*, submitted
- Hinz, J. L., Rieke, G. H., Gordon, K. D., et al. 2004, *ApJS*, 154, 259
- Hippelein, H., Haas, M., Tuffs, R. J., et al. 2003, *A&A*, 407, 137
- Hog, E., Kuzmin, A., Bastian, U., et al. 1998, *A&A*, 335, L65
- Horne, K. 1986, *PASP*, 98, 609
- Hubble, E. P. 1926, *ApJ*, 63, 236
- Huchra, J. P., Vogele, M. S., & Geller, M. J. 1999, *ApJS*, 121, 287
- Hughes, J. P. 1998, *Bulletin of the American Astronomical Society*, 30, 876
- Humphrey, P. J., Fabbiano, G., Elvis, M., Church, M. J., & Bałucińska-Church, M. 2003, *MNRAS*, 344, 134
- Humphreys, R. M. & Sandage, A. 1980, *ApJS*, 44, 319
- Illarionov, A. F. & Sunyaev, R. A. 1975, *A&A*, 39, 185
- Immler, S., Pietsch, W., & Aschenbach, B. 1998, *A&A*, 331, 601
- Irwin, J. A., Athey, A. E., & Bregman, J. N. 2003, *ApJ*, 587, 356
- Israel, F. P. & van der Kruit, P. C. 1974, *A&A*, 32, 363
- Ivanov, G. R., Freedman, W. L., & Madore, B. F. 1993, *ApJS*, 89, 85
- Jansen, F., Lumb, D., Altieri, B., et al. 2001, *A&A*, 365, L1
- Jaschek, C. & Jaschek, M. 1987, *The classification of stars* (Cambridge: University Press)

- Kaaret, P., Prestwich, A. H., Zezas, A., et al. 2001, MNRAS, 321, L29
- Kahabka, P. & Trümper, J. 1996, in IAU Symp. 165: Compact Stars in Binaries, 425
- Kahabka, P. & van den Heuvel, E. P. J. 1997, ARA&A, 35, 69
- Kaluzienski, L. J., Holt, S. S., Boldt, E. A., & Serlemitsos, P. J. 1976, ApJ, 208, L71
- Kaluzny, J. & Udalski, A. 1992, Acta Astronomica, 42, 29
- Kardashev, N. S. 1962, Soviet Astronomy, 6, 317
- King, A. R. 1995, in ASP Conf. Ser. 85: Magnetic Cataclysmic Variables, 21
- King, A. R. 2002, MNRAS, 335, L13
- King, A. R., Davies, M. B., Ward, M. J., Fabbiano, G., & Elvis, M. 2001, ApJ, 552, L109
- King, A. R., Osborne, J. P., & Schenker, K. 2002, MNRAS, 329, L43
- Koerding, E., Falcke, H., Markoff, S., & Fender, R. 2001, in Astronomische Gesellschaft Meeting Abstracts, 176
- Kong, A. K. H., DiStefano, R., Garcia, M. R., & Greiner, J. 2003, ApJ, 585, 298
- Koyama, K., Kawada, M., Takeuchi, Y., et al. 1990, ApJ, 356, L47
- Koyama, K., Kunieda, H., Takeuchi, Y., & Tawara, Y. 1991, ApJ, 370, L77
- Koyama, K., Petre, R., Gotthelf, E. V., et al. 1995, Nature, 378, 255
- Kubota, A. 1998, in IAU Symp. 188: The Hot Universe, 388
- Kubota, A., Mizuno, T., Makishima, K., et al. 2001, ApJ, 547, L119
- La Parola, V., Damiani, F., Fabbiano, G., & Peres, G. 2003, ApJ, 583, 758
- La Parola, V., Peres, G., Fabbiano, G., Kim, D. W., & Bocchino, F. 2001, ApJ, 556, 47
- Lamb, F. K. & Miller, M. C. 1995, ApJ, 439, 828
- Larson, D. T. & Schulman, E. 1997, AJ, 113, 618
- Lasota, J.-P. 2001, New Astronomy Review, 45, 449
- Lehmann, I., Becker, T., Fabrika, S., et al. 2005, A&A, 431, 847
- Lewin, W. H. G., van Paradijs, J., & Taam, R. E. 1993, Space Science Reviews, 62, 223

- Li, L.-X., Zimmerman, E. R., Narayan, R., & McClintock, J. E. 2005, *ApJS*, 157, 335
- Liedahl, D. A. & Torres, D. F. 2005, *Canadian Journal of Physics*, in press (astro-ph/0510093)
- Liu, Q. Z., van Paradijs, J., & van den Heuvel, E. P. J. 2000, *A&AS*, 147, 25
- Liu, Q. Z., van Paradijs, J., & van den Heuvel, E. P. J. 2001, *A&A*, 368, 1021
- Livio, M. 1994, *Memorie della Societa Astronomica Italiana*, 65, 49
- Long, K. S., Charles, P. A., Blair, W. P., & Gordon, S. M. 1996, *ApJ*, 466, 750
- Long, K. S., Dodorico, S., Charles, P. A., & Dopita, M. A. 1981a, *ApJ*, 246, L61
- Long, K. S., Helfand, D. J., & Grabelsky, D. A. 1981b, *ApJ*, 248, 925
- Longair, M. S. 1981, *High energy astrophysics* (Cambridge and New York, Cambridge University Press, 1981. 420 p.)
- Longair, M. S. 1994, *High energy astrophysics. Vol.2: Stars, the galaxy and the interstellar medium* (Cambridge: Cambridge University Press, —c1994, 2nd ed.)
- Lozinskaya, T. A. 1992, *Supernovae and stellar wind in the interstellar medium* (New York: American Institute of Physics)
- Maccacaro, T., Gioia, I. M., Wolter, A., Zamorani, G., & Stocke, J. T. 1988, *ApJ*, 326, 680
- Macri, L. M., Stanek, K. Z., Sasselov, D. D., Krockenberger, M., & Kaluzny, J. 2001a, *AJ*, 121, 870
- Macri, L. M., Stanek, K. Z., Sasselov, D. D., Krockenberger, M., & Kaluzny, J. 2001b, *AJ*, 121, 861
- Madau, P. & Rees, M. J. 2001, *ApJ*, 551, L27
- Magnier, E. A., Primini, F. A., Prins, S., van Paradijs, J., & Lewin, W. H. G. 1997, *ApJ*, 490, 649
- Magrini, L., Cardwell, A., Corradi, R. L. M., Mampaso, A., & Perinotto, M. 2001, *A&A*, 367, 498
- Makishima, K., Kubota, A., Mizuno, T., et al. 2000, *ApJ*, 535, 632
- Makishima, K., Maejima, Y., Mitsuda, K., et al. 1986, *ApJ*, 308, 635
- Markert, T. H. & Rallis, A. D. 1983, *ApJ*, 275, 571
- Mason, K. O., Breeveld, A., Much, R., et al. 2001, *A&A*, 365, L36

- Massey, P. 1998, *ApJ*, 501, 153
- Massey, P., Bianchi, L., Hutchings, J. B., & Stecher, T. P. 1996, *ApJ*, 469, 629
- Massey, P. & Conti, P. S. 1983, *ApJ*, 273, 576
- Massey, P., Hodge, P. W., Holmes, S., et al. 2002, *Bulletin of the American Astronomical Society*, 34, 1272
- Matsumoto, H. & Tsuru, T. G. 2001, in *Two Years of Science with Chandra*, Abstracts from the Symposium held in Washington, DC, meeting abstract.
- Matsumoto, H., Tsuru, T. G., Koyama, K., et al. 2001, *ApJ*, 547, L25
- McClintock, J. E. & Remillard, R. A. 2004, *Compact stellar X-ray sources*, book in preparation for Cambridge University press, eds. W. Lewin and M. van der Klis (astro-ph/0306213)
- Merloni, A. & Fabian, A. C. 2002, *MNRAS*, 332, 165
- Meszaros, P. 1992, *High-energy radiation from magnetized neutron stars (Theoretical Astrophysics)*, Chicago: University of Chicago Press, —c1992)
- Meyer, F. & Meyer-Hofmeister, E. 1994, *A&A*, 288, 175
- Miller, J. M., Fabbiano, G., Miller, M. C., & Fabian, A. C. 2003, *ApJ*, 585, L37
- Miller, M. C. & Colbert, E. J. M. 2004, *International Journal of Modern Physics D*, 13, 1
- Miller, M. C. & Hamilton, D. P. 2002, *MNRAS*, 330, 232
- Mirabel, I. F. & Rodriguez, L. F. 1998, *Nature*, 392, 673
- Mirabel, I. F. & Rodríguez, L. F. 2000, *Nuclear Physics B Proceedings Supplements*, 80, 143
- Misanovic, Z., Cram, L., & Green, A. 2002, *MNRAS*, 335, 114
- Misanovic, Z., Pietsch, W., Haberl, F., et al. 2005, *A&A*, in press,
- Mitsuda, K., Inoue, H., Koyama, K., et al. 1984, *PASJ*, 36, 741
- Mochejska, B. J., Kaluzny, J., Krockenberger, M., Sasselov, D. D., & Stanek, K. Z. 1998, *Acta Astronomica*, 48, 455
- Mochejska, B. J., Kaluzny, J., Stanek, K. Z., Sasselov, D. D., & Szentgyorgyi, A. H. 2001a, *AJ*, 121, 2032
- Mochejska, B. J., Kaluzny, J., Stanek, K. Z., Sasselov, D. D., & Szentgyorgyi, A. H. 2001b, *AJ*, 122, 2477

- Mochejska, B. J., Kaluzny, J., Stanek, K. Z., Sasselov, D. D., & Szentgyorgyi, A. H. 2001c, *AJ*, 121, 3284
- Monet, D. G. 1998, *Bulletin of the American Astronomical Society*, 30, 1427
- Mushotzky, R. F. 1984, *Advances in Space Research*, 3, 157
- Mushotzky, R. F., Cowie, L. L., Barger, A. J., & Arnaud, K. A. 2000, *Nature*, 404, 459
- Nagase, F. 1989, *PASJ*, 41, 1
- Narayan, R. 1996, *ApJ*, 462, 136
- Nazé, Y., Antokhin, I. I., Rauw, G., et al. 2004, *A&A*, 418, 841
- Newton, K. 1980a, *MNRAS*, 190, 689
- Newton, K. 1980b, *MNRAS*, 191, 615
- Nomoto, K., Nariai, K., & Sugimoto, D. 1979, *PASJ*, 31, 287
- Novikov, I. D., Thorne, K. S. in Dewitt, C., & Dewitt, B. S. 1973, *Black holes (Black holes, by C. DeWitt and B.S. DeWitt. New York: Gordon and Breach, 1973.)*
- Nowak, M. A., Wilms, J., & Dove, J. B. 2002, *MNRAS*, 332, 856
- Orio, M., della Valle, M., Massone, G., & Ogelman, H. 1994, *A&A*, 289, L11
- Orosz, J. A., Groot, P. J., van der Klis, M., et al. 2002, *ApJ*, 568, 845
- Osborne, J. P., Borozdin, K. N., Trudolyubov, S. P., et al. 2001, *A&A*, 378, 800
- Osterbrock, D. E. 1998, in *Revista Mexicana de Astronomia y Astrofisica Conference Series*, 180
- Paczynski, B. 1971, *ARA&A*, 9, 183
- Pakull, M. W. 1981, *A&A*, 104, 33
- Pakull, M. W. & Mirioni, L. 2001, in *Astronomische Gesellschaft Meeting Abstracts*, 112
- Parmar, A. N., Sidoli, L., Oosterbroek, T., et al. 2001, *A&A*, 368, 420
- Pavlov, G. G., Sanwal, D., & Teter, M. A. 2004, in *IAU Symposium*, 239
- Peres, G., Reale, F., Collura, A., & Fabbiano, G. 1989, *ApJ*, 336, 140
- Peterson, B. M. 1997, *An Introduction to Active Galactic Nuclei (An introduction to active galactic nuclei, Publisher: Cambridge, New York Cambridge University Press, 1997 Physical description xvi, 238 p. ISBN 0521473489)*

- Pickles, A. J. 1998, PASP, 110, 863
- Pietsch, W., Ehle, M., Haberl, F., Misanovic, Z., & Trinchieri, G. 2003a, AN, 324, 85
- Pietsch, W., Fliri, J., Freyberg, M. J., et al. 2005a, A&A, 442, 879
- Pietsch, W., Freyberg, M., & Haberl, F. 2005b, A&A, 434, 483
- Pietsch, W. & Haberl, F. 2000, in The interstellar medium in M31 and M33. Proceedings 232. WE-Heraeus Seminar, 22-25 May 2000, Bad Honnef, Germany. Edited by Elly M. Berkhuijsen, Rainer Beck, and Rene A. M. Walterbos. Shaker, Aachen, 2000, p. 149
- Pietsch, W., Haberl, F., & Vogler, A. 2003b, A&A, 402, 457
- Pietsch, W., Misanovic, Z., Haberl, F., et al. 2004a, A&A, 426, 11
- Pietsch, W., Mochejska, B. J., Misanovic, Z., et al. 2004b, A&A, 413, 879
- Pietsch, W., Vogler, A., Klein, U., & Zinnecker, H. 2000, A&A, 360, 24
- Porquet, D., Predehl, P., Aschenbach, B., et al. 2003, A&A, 407, L17
- Portegies Zwart, S. F., Baumgardt, H., Hut, P., Makino, J., & McMillan, S. L. W. 2004, Nature, 428, 724
- Pounds, K. A., Nandra, K., Stewart, G. C., George, I. M., & Fabian, A. C. 1990, Nature, 344, 132
- Predehl, P. & Schmitt, J. H. M. M. 1995, A&A, 293, 889
- Prestwich, A. H., Irwin, J. A., Kilgard, R. E., et al. 2003, ApJ, 595, 719
- Priedhorsky, W. C. & Holt, S. S. 1987, Space Science Reviews, 45, 291
- Primini, F. A., Forman, W., & Jones, C. 1993, ApJ, 410, 615
- Pringle, J. E. & Rees, M. J. 1972, A&A, 21, 1
- Psaltis, D. 2004, Compact stellar X-ray sources, book in preparation for Cambridge University press, eds. W. Lewin and M. van der Klis (astro-ph/0410536)
- Psaltis, D., Lamb, F. K., & Miller, G. S. 1995, ApJ, 454, L137
- Quataert, E. & Narayan, R. 1999, ApJ, 520, 298
- Rappaport, S., Di Stefano, R., & Smith, J. D. 1994, ApJ, 426, 692
- Raymond, J. C. & Smith, B. W. 1977, ApJS, 35, 419
- Regan, M. W. & Wilson, C. D. 1993, AJ, 105, 499

- Reynolds, C. S. & Nowak, M. A. 2003, *Physics Reports*, 377, 389
- Roberts, T. P. & Colbert, E. J. M. 2003, *MNRAS*, 341, L49
- Roberts, T. P. & Warwick, R. S. 2000, *MNRAS*, 315, 98
- Roberts, T. P., Warwick, R. S., Ward, M. J., & Murray, S. S. 2002, *MNRAS*, 337, 677
- Rosati, P., Tozzi, P., Giacconi, R., et al. 2002, *ApJ*, 566, 667
- Rowe, J. F., Richer, H. B., Brewer, J. P., & Crabtree, D. R. 2005, *AJ*, 129, 729
- Rybicki, G. B. & Lightman, A. P. 1979, *Radiative processes in astrophysics* (New York, Wiley-Interscience, 1979. 393 p.)
- Sanford, P. W., Mason, K. O., Hawkins, F. J., Murdin, P., & Savage, A. 1974, *ApJ*, 190, L55
- Sasaki, M., Haberl, F., & Pietsch, W. 2000, *A&AS*, 143, 391
- Sasaki, M., Haberl, F., & Pietsch, W. 2002, *A&A*, 392, 103
- Schmitt, J. H. M. M. 2000, *Reviews of Modern Astronomy*, 13, 115
- Schödel, R., Ott, T., Genzel, R., et al. 2002, *Nature*, 419, 694
- Schulman, E. & Bregman, J. N. 1995, *ApJ*, 441, 568
- Schulman, E., Bregman, J. N., Collura, A., Reale, F., & Peres, G. 1993, *ApJ*, 418, L67
- Schulman, E., Bregman, J. N., Collura, A., Reale, F., & Peres, G. 1994, *ApJ*, 426, L55
- Schulz, N. S., Canizares, C. R., Lee, J. C., & Sako, M. 2002, *ApJ*, 564, L21
- Seward, F. D. & Mitchell, M. 1981, *ApJ*, 243, 736
- Shakura, N. I. & Sunyaev, R. A. 1973, *A&A*, 24, 337
- Shapiro, S. L. & Teukolsky, S. A. 1983, *Black holes, white dwarfs, and neutron stars: The physics of compact objects* (Research supported by the National Science Foundation. New York, Wiley-Interscience, 1983, 663 p.)
- Shklovskii, I. S. 1976, *Soviet Astronomy Letters*, 2, 95
- Shklovsky, I. S. 1967, *ApJ*, 148, L1
- Shortridge, K. 2001, *Astronomical Software Strategies* (ASSL Vol. 266: Organizations and Strategies in Astronomy, Vol. II), 163
- Sivakoff, G. R., Sarazin, C. L., & Irwin, J. A. 2003, *ApJ*, 599, 218
- Skinner, G. K., Bedford, D. K., Elsner, R. F., et al. 1982, *Nature*, 297, 568

- Skrutskie, M. F., Schneider, S. E., Stiening, R., et al. 1997, in *ASSL Vol. 210: The Impact of Large Scale Near-IR Sky Surveys*, 25
- Slane, P. 2000, in *Chandra Proposal ID #02500349*, 508
- Soria, R. 2003, in *IAU Symposium*, 59
- Soria, R., Cropper, M., & Motch, C. 2005a, *Chinese Journal of Astronomy and Astrophysics*, 5, 153
- Soria, R., Cropper, M., Pakull, M., Mushotzky, R., & Wu, K. 2005b, *MNRAS*, 356, 12
- Soria, R. & Wu, K. 2002, *A&A*, 384, 99
- Soria, R. & Wu, K. 2003, *A&A*, 410, 53
- Stark, A. A., Gammie, C. F., Wilson, R. W., et al. 1992, *ApJS*, 79, 77
- Stella, L., Priedhorsky, W., & White, N. E. 1987, *ApJ*, 312, L17
- Stella, L. & Rosner, R. 1984, *ApJ*, 277, 312
- Stelzer, B. & Burwitz, V. 2003, *A&A*, 402, 719
- Strüder, L., Briel, U., Dennerl, K., et al. 2001, *A&A*, 365, L18
- Streblyanska, A., Hasinger, G., Finoguenov, A., et al. 2005, *A&A*, 432, 395
- Strohmayer, T. & Bildsten, L. 2003, *Compact stellar X-ray sources*, book in preparation for Cambridge University press, eds. W. Lewin and M. van der Klis (astro-ph/0301544)
- Strohmayer, T. E. & Mushotzky, R. F. 2003, *ApJ*, 586, L61
- Sunyaev, R. A. & Titarchuk, L. G. 1980, *A&A*, 86, 121
- Swartz, D. A., Ghosh, K. K., & Tennant, A. F. 2003, *American Astronomical Society Meeting Abstracts*, 202
- Swartz, R. 2002, *American Astronomical Society Meeting Abstracts*, 201
- Takano, M. & Mitsuda, K. 1994, in *New Horizon of X-Ray Astronomy. First Results from ASCA*, 521
- Tanaka, Y. 1991, *LNP Vol. 385: Iron Line Diagnostics in X-ray Sources*, 385, 98
- Tanaka, Y. 1995, in *Seventeenth Texas Symposium on Relativistic Astrophysics and Cosmology*, 206

- Tanaka, Y. I. & Lewin, F. 1995, The black hole binaries (X-ray Binaries, eds. W.H.G. Lewin, J. van Paradijs, and E.P.J. van den Heuvel (Cambridge: Cambridge Univ. Press))
- Tanimori, T., Hayami, Y., Kamei, S., et al. 1998, *ApJ*, 497, L25
- Tennant, A. F., Wu, K., Ghosh, K. K., Kolodziejczak, J. J., & Swartz, D. A. 2001, *ApJ*, 549, L43
- Thilker, D. A., Hoopes, C. G., Bianchi, L., et al. 2005, *ApJ*, 619, L67
- Tjemkes, S. A., van Paradijs, J., & Zuiderwijk, E. J. 1986, *A&A*, 154, 77
- Trinchieri, G., Fabbiano, G., & Peres, G. 1988a, *ApJ*, 325, 531
- Trinchieri, G., Fabbiano, G., & Peres, G. 1988b, *ApJ*, 329, 1037
- Trudolyubov, S., Kotov, O., Priedhorsky, W., Cordova, F., & Mason, K. 2005, *ApJ*, 634, 314
- Trümper, J. 1986, in NATO ASIC Proc. 162: Cosmic Radiation in Contemporary Astrophysics, 217–225
- Trümper, J., Hasinger, G., Aschenbach, B., Braeuninger, H., & Briel, U. G. 1991, *Nature*, 349, 579
- Tully, R. B. 1988, Nearby galaxies catalog (Cambridge and New York, Cambridge University Press)
- Turner, M. J. L., Abbey, A., Arnaud, M., et al. 2001, *A&A*, 365, L27
- Vacca, W. D., Sztajno, M., Lewin, W. H. G., et al. 1987, *A&A*, 172, 143
- Vaiana, G. S., Cassinelli, J. P., Fabbiano, G., et al. 1981, *ApJ*, 245, 163
- van den Bergh, S. 1991, *PASP*, 103, 609
- van den Heuvel, E. P. J., Bhattacharya, D., Nomoto, K., & Rappaport, S. A. 1992, *A&A*, 262, 97
- van der Klis, M. 2004, Compact stellar X-ray sources, book in preparation for Cambridge University press, eds. W. Lewin and M. van der Klis (astro-ph/0410551)
- van Paradijs, J. & McClintock, J. E. 1995, Optical and Ultraviolet Observations of X-ray Binaries (X-ray Binaries, eds. W.H.G. Lewin, J. van Paradijs, and E.P.J. van den Heuvel (Cambridge: Cambridge Univ. Press))
- von Kap-Herr, A., Berkhuijsen, E. M., & Wielebinski, R. 1978, *A&A*, 62, 51
- Wang, Q. & Wu, X. 1992, *ApJS*, 78, 391

- Wang, Y.-M. & Welter, G. L. 1981, *A&A*, 102, 97
- Waters, L. B. F. M. & van Kerkwijk, M. H. 1989, *A&A*, 223, 196
- Watson, M. G., Warwick, R. S., & Ricketts, M. J. 1981, *MNRAS*, 195, 197
- Weisskopf, M. C., Tananbaum, H. D., Van Speybroeck, L. P., & O'Dell, S. L. 2000, in *Proc. SPIE Vol. 4012, p. 2-16, X-Ray Optics, Instruments, and Missions III*, Joachim E. Trümper; Bernd Aschenbach; Eds., 2–16
- White, N. E. 1989, *A&A Rev.*, 1, 85
- White, N. E., Kallman, T. R., & Swank, J. H. 1983a, *ApJ*, 269, 264
- White, N. E., Nagase, F., & Parmar, A. N. 1995, *The properties of X-ray Binaries (X-ray Binaries, eds. W.H.G. Lewin, J. van Paradijs, and E.P.J. van den Heuvel (Cambridge: Cambridge Univ. Press))*
- White, N. E., Swank, J. H., & Holt, S. S. 1983b, *ApJ*, 270, 711
- Williams, B. F., Garcia, M. R., Kong, A. K. H., et al. 2004, *ApJ*, 609, 735
- Wu, K. 2001, *Publications of the Astronomical Society of Australia*, 18, 443
- Zaritsky, D., Elston, R., & Hill, J. M. 1989, *AJ*, 97, 97
- Zdziarski, A. A. 2000, in *IAU Symp. 195: Highly Energetic Physical Processes and Mechanisms for Emission from Astrophysical Plasmas*, 153
- Zdziarski, A. A. 2001, in *X-ray Emission from Accretion onto Black Holes*
- Zdziarski, A. A. & Gierliński, M. 2004, *Progress of Theoretical Physics Supplement*, 155, 99
- Zezas, A. & Fabbiano, G. 2002, *ApJ*, 577, 726
- Zezas, A., Ward, M. J., & Murray, S. S. 2003, *ApJ*, 594, L31

Appendix A

Full band images

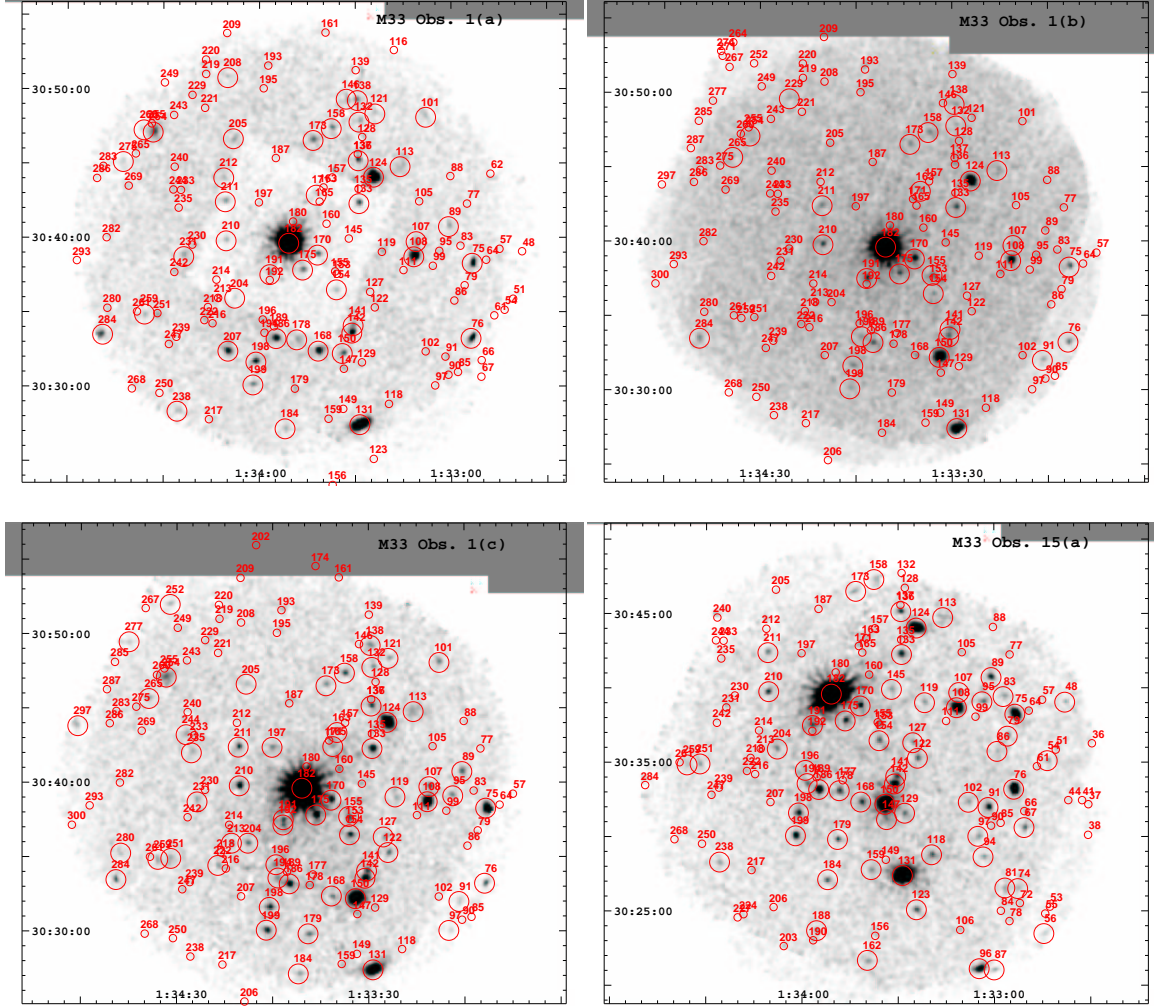


Figure A.1: The broad band (0.2-12.0 keV) gray scale XMM-Newton EPIC images of the observations 1(a) (upper left), 1(b) (upper right), 1(c) (lower left), and 15(a) (lower right), combining PN, MOS1, and MOS2 data. The images are smoothed with a Gaussian of FWHM $6''$. The intensity scale is linear from 0.00765 to 3.0785 $\text{ct s}^{-1} \text{pixel}^{-1}$ (upper left, lower right, lower left), and from 0.00765 to 6.7785 $\text{ct s}^{-1} \text{pixel}^{-1}$ (upper right). The pixel size is $4''$. The big circles represent the sources detected above the likelihood threshold of 7, while the small circles mark the positions of the sources that are below the detection threshold in that observation, for which we determine only the upper limits of the count rates (see text). The numbers correspond to the SRC Id from Table 3.4.

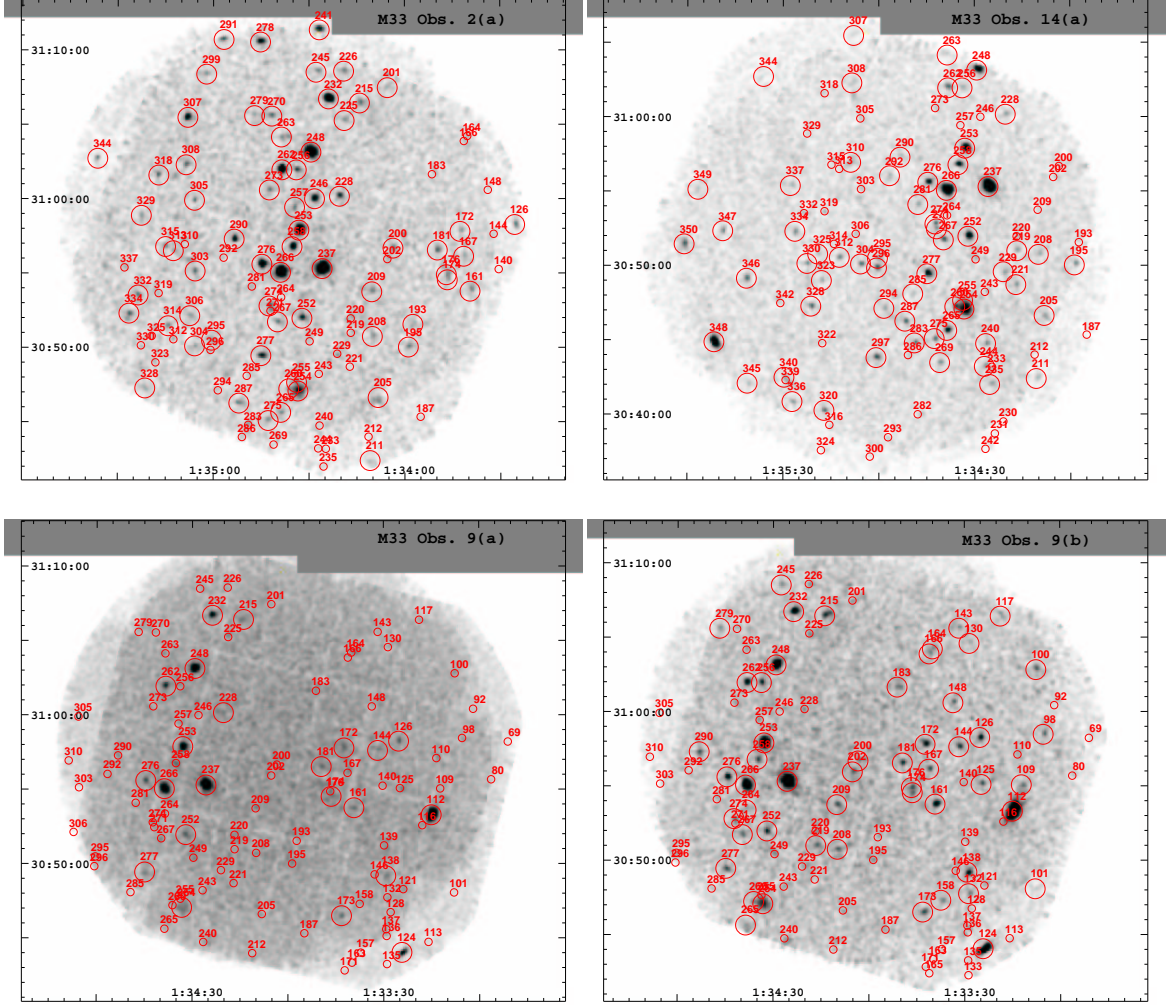


Figure A.2: The broad band (0.2-12.0 keV) gray scale XMM-Newton EPIC images of the observations 2(a) (upper left), 14(a) (upper right), 9(a) (lower left), and 9(b) (lower right), combining PN, MOS1, and MOS2 data. The images are smoothed with a Gaussian of FWHM $6''$. The intensity scale is linear from 0.00513 to 3.36775 $\text{ct s}^{-1} \text{pixel}^{-1}$ (upper left, upper right, lower right), and from 0.00513 to 8.2400775 $\text{ct s}^{-1} \text{pixel}^{-1}$ (lower left). The pixel size is $4''$. The big circles represent the sources detected above the likelihood threshold of 7, while the small circles mark the positions of the sources that are below the detection threshold in that observation, for which we determine only the upper limits of the count rates (see text). The numbers correspond to the SRC Id from Table 3.4.

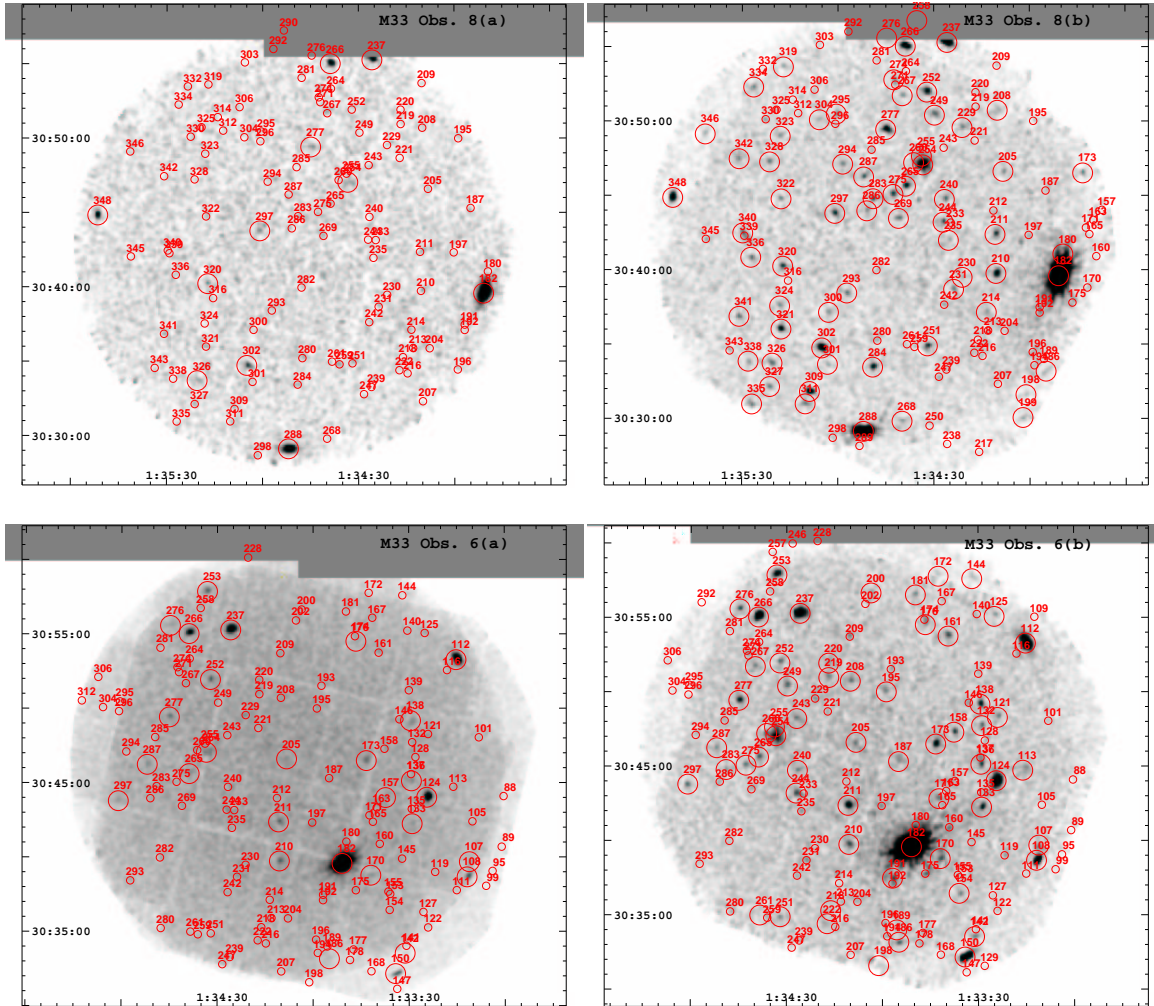


Figure A.3: The broad band (0.2-12.0 keV) gray scale XMM-Newton EPIC images of the observations 8(a) (upper left), 8(b) (upper right), 6(a) (lower left), and 6(b) (lower right), combining PN, MOS1, and MOS2 data. The images are smoothed with a Gaussian of FWHM $6''$. The intensity scale is linear from 0.00153 to 1.55803 (upper left), 0.001527 to 3.02803 (upper right), 0.001527 to 15.65901 (lower left), and from 0.001527 to 3.99803 $\text{ct s}^{-1} \text{pixel}^{-1}$ (lower right). The pixel size is $4''$. The big circles represent the sources detected above the likelihood threshold of 7, while the small circles mark the positions of the sources that are below the detection threshold in that observation, for which we determine only the upper limits of the count rates (see text). The numbers correspond to the SRC Id from Table 3.4.

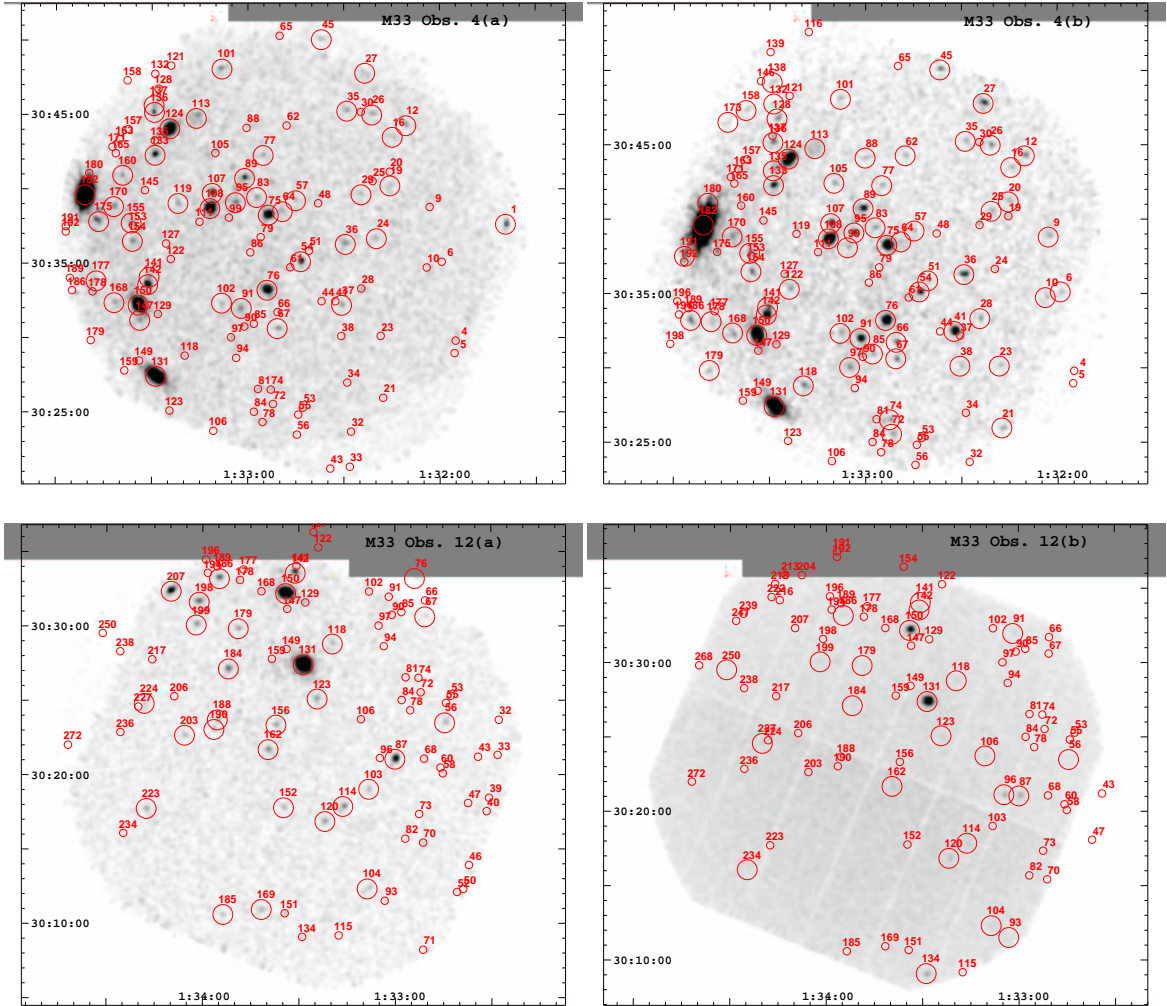


Figure A.4: The broad band (0.2-12.0 keV) gray scale XMM-Newton EPIC images of the observations 4(a) (upper left), 4(b) (upper right), 12(a) (lower left), and 12(b) (lower right), combining PN, MOS1, and MOS2 data. The images are smoothed with a Gaussian of FWHM $6''$. The intensity scale is linear from 0.02276 to 4.18462 (upper left, upper right and lower left), and 0.02276 to 30.74765 $\text{ct s}^{-1} \text{pixel}^{-1}$ (lower right). The pixel size is $4''$. The big circles represent the sources detected above the likelihood threshold of 7, while the small circles mark the positions of the sources that are below the detection threshold in that observation, for which we determine only the upper limits of the count rates (see text). The numbers correspond to the SRC Id from Table 3.4.

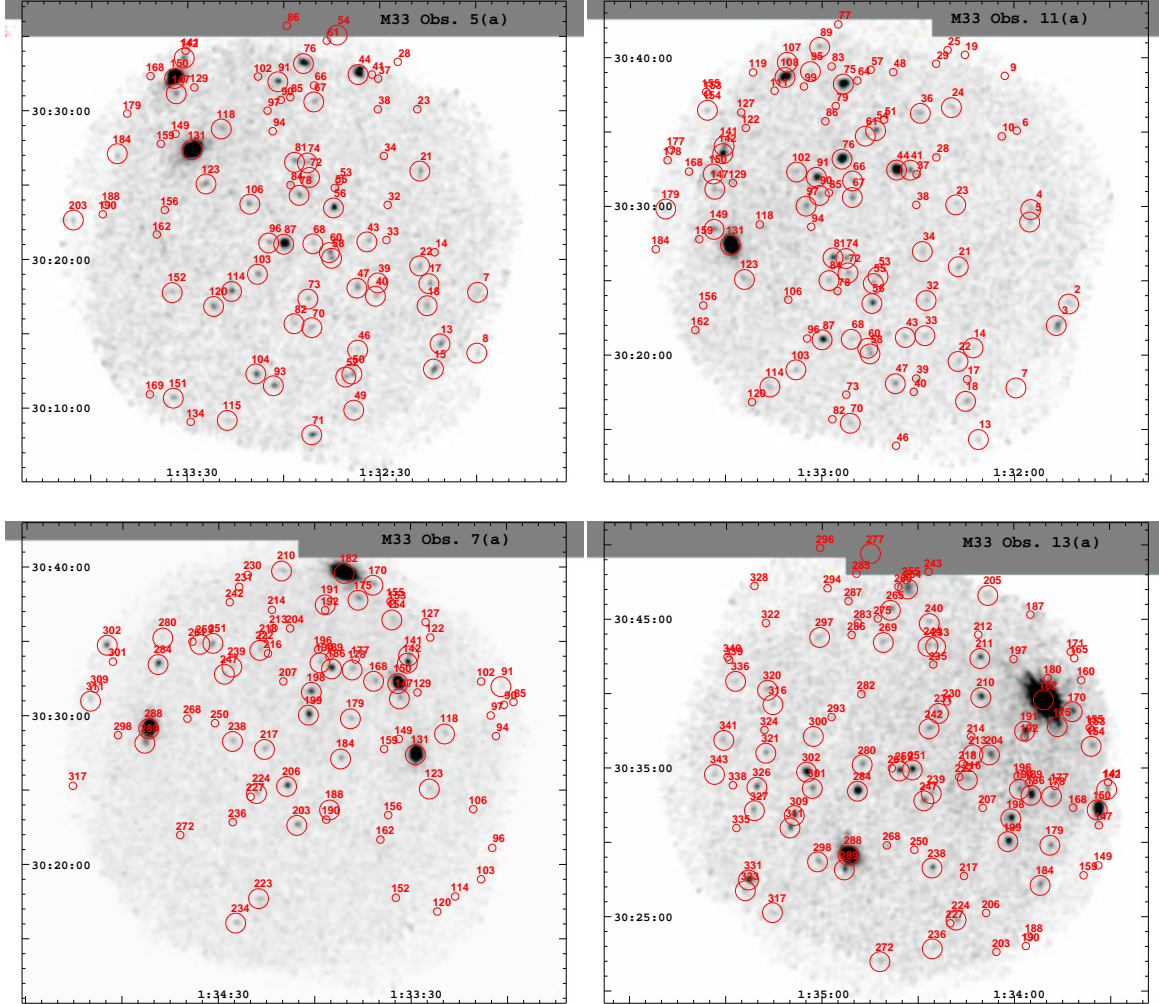


Figure A.5: The broad band (0.2-12.0 keV) gray scale XMM-Newton EPIC images of the observations 5(a) (upper left), 11(a) (upper right), 7(a) (lower left), and 13(a) (lower right), combining PN, MOS1, and MOS2 data. The images are smoothed with a Gaussian of FWHM $6''$. The intensity scale is linear from 0.02343 to 3.94374 $\text{ct s}^{-1} \text{pixel}^{-1}$. The pixel size is $4''$. The big circles represent the sources detected above the likelihood threshold of 7, while the small circles mark the positions of the sources that are below the detection threshold in that observation, for which we determine only the upper limits of the count rates (see text). The numbers correspond to the SRC Id from Table 3.4.

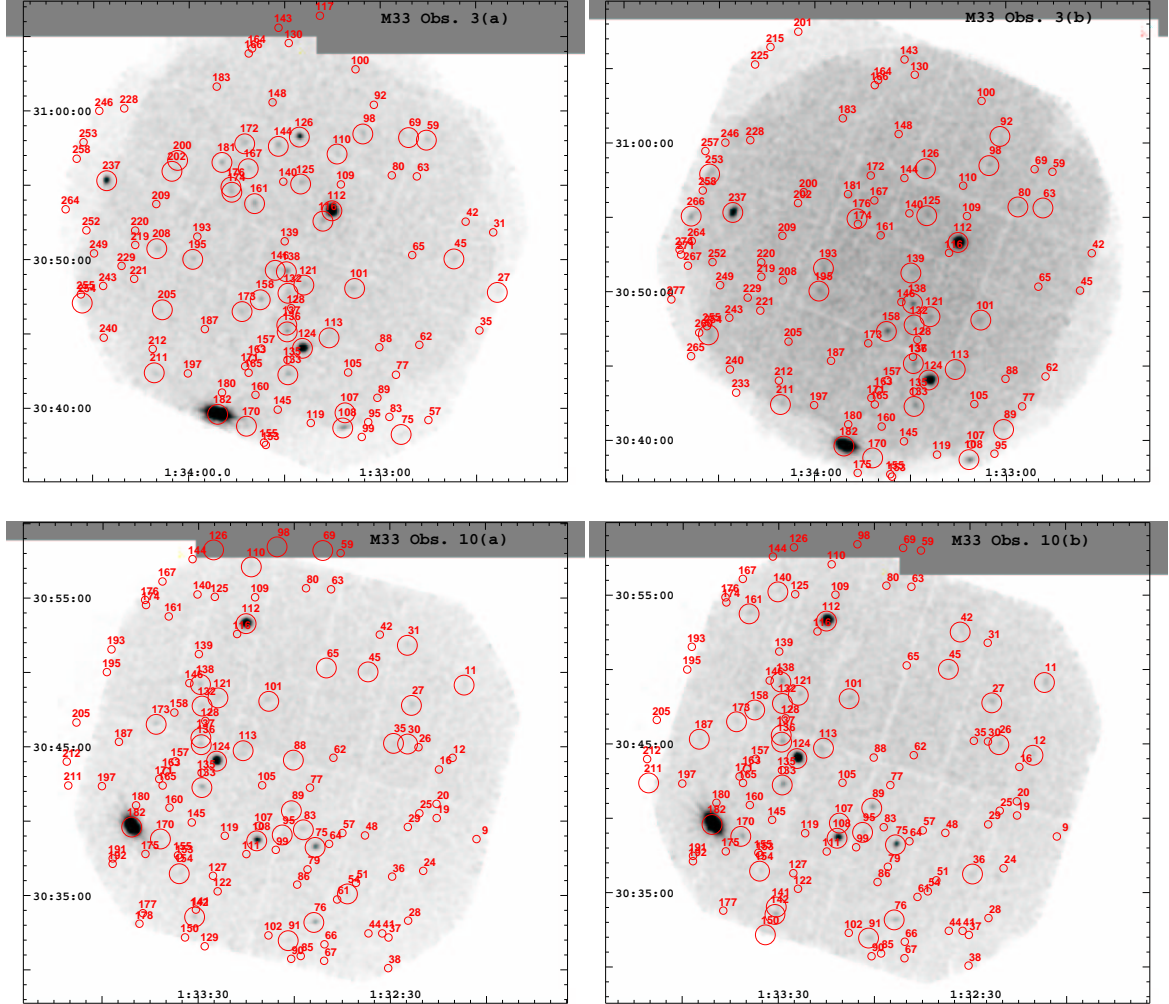


Figure A.6: The broad band (0.2-12.0 keV) gray scale XMM-Newton EPIC images of the observations 3(a) (upper left), 3(b) (upper right), 10(a) (lower left), and 10(b) (lower right), combining PN, MOS1, and MOS2 data. The images are smoothed with a Gaussian of FWHM $6''$. The intensity scale is linear from 0.11473 to 15.81277 $\text{ct s}^{-1} \text{pixel}^{-1}$. The pixel size is $4''$. The big circles represent the sources detected above the likelihood threshold of 7, while the small circles mark the positions of the sources that are below the detection threshold in that observation, for which we determine only the upper limits of the count rates (see text). The numbers correspond to the SRC Id from Table 3.4.

Appendix B

Light-curves of the individual sources

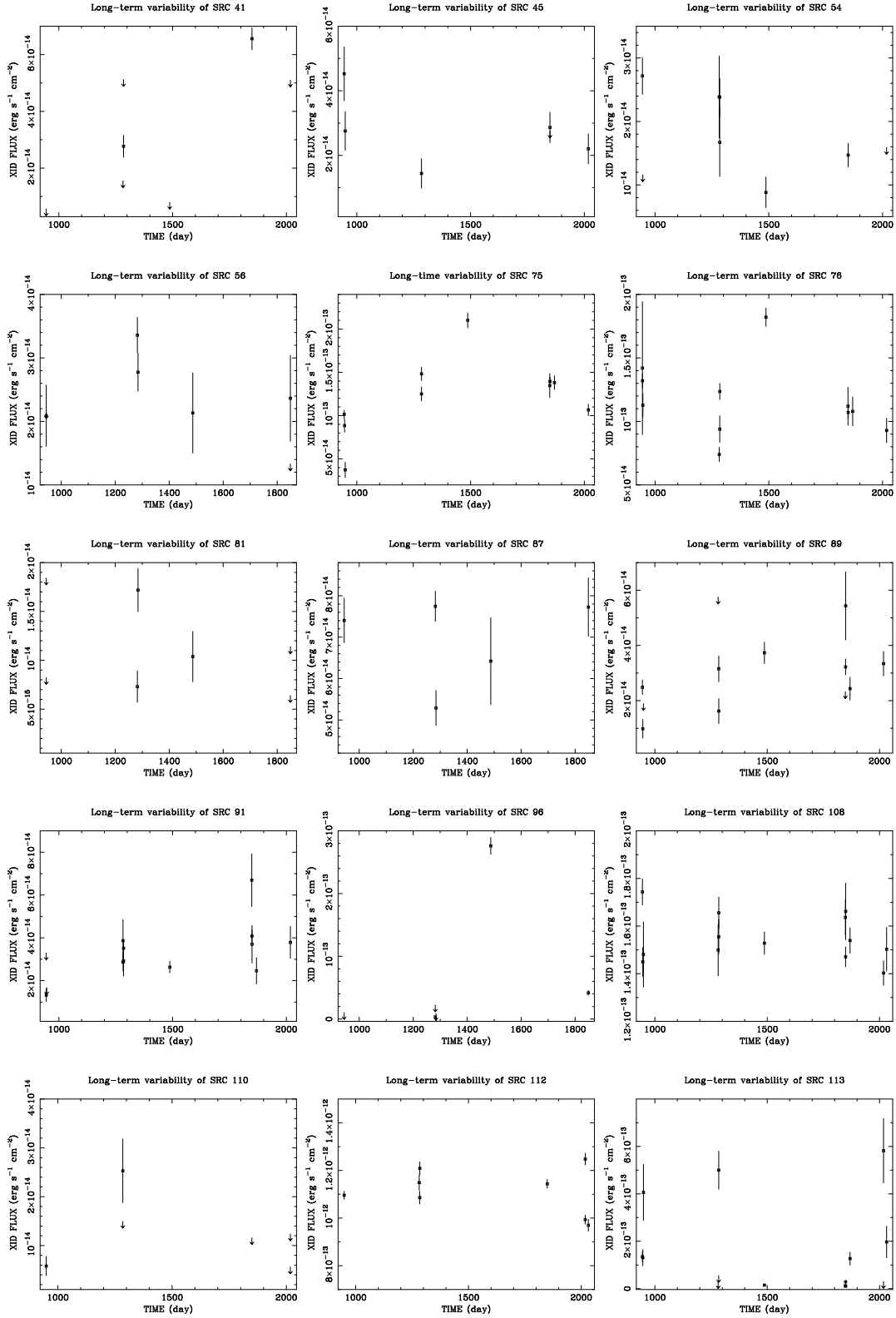


Figure B.1: The long-term X-ray light-curves of sources #41, #45, #54, #56, #75, #76, #81, #87, #89, #91, #96, #108, #110, #112, and #113. The downward arrows represent the 3σ upper limits of the XID flux. The time is given in days after JD 2450814.5.

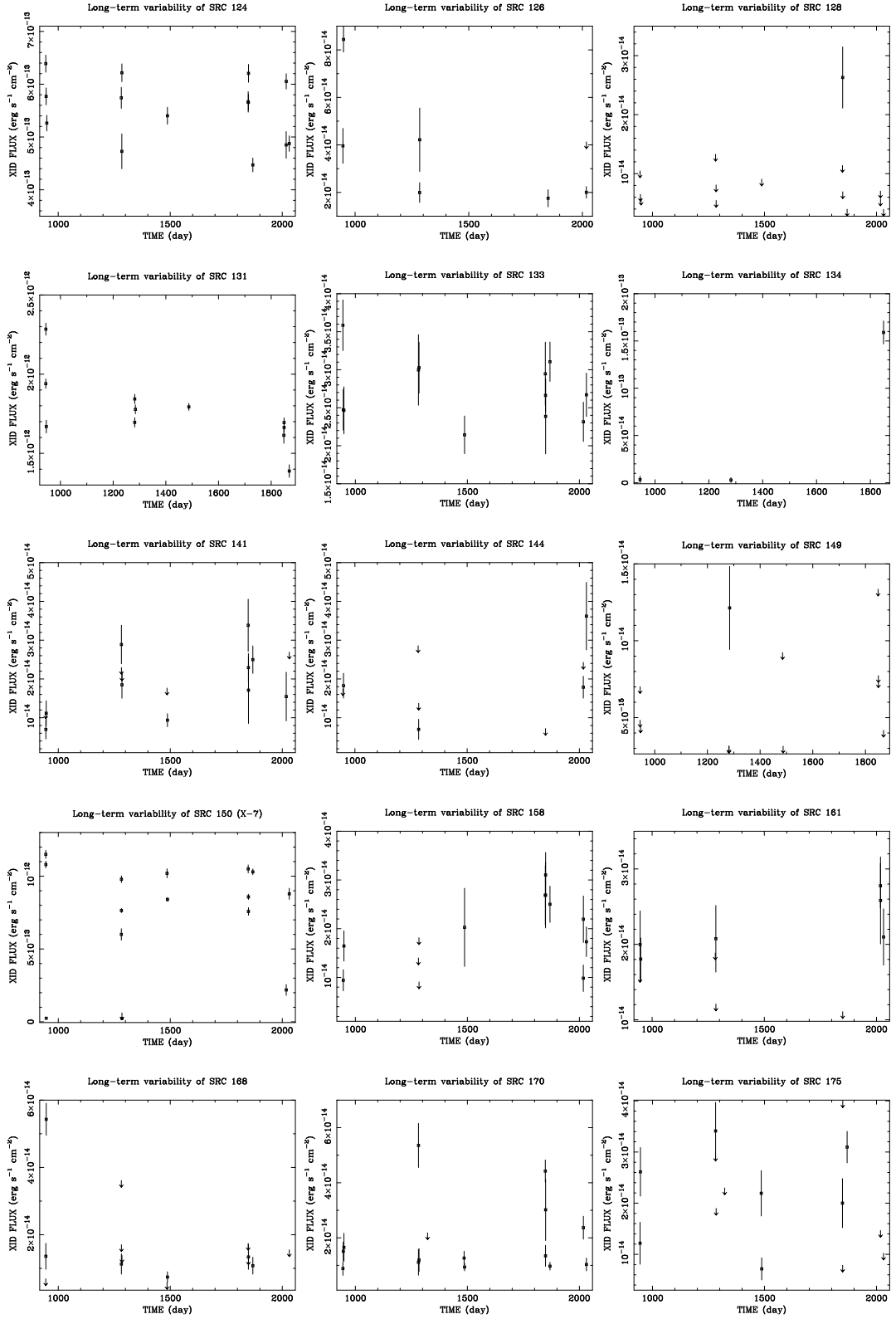


Figure B.2: The long-term X-ray light-curves of sources #124, #126, #128, #131, #133, #134, #141, #144, #149, #150, #158, #161, #168, #170, and #175. The downward arrows represent the 3σ upper limits of the XID flux. The time is given in days after JD 2450814.5.

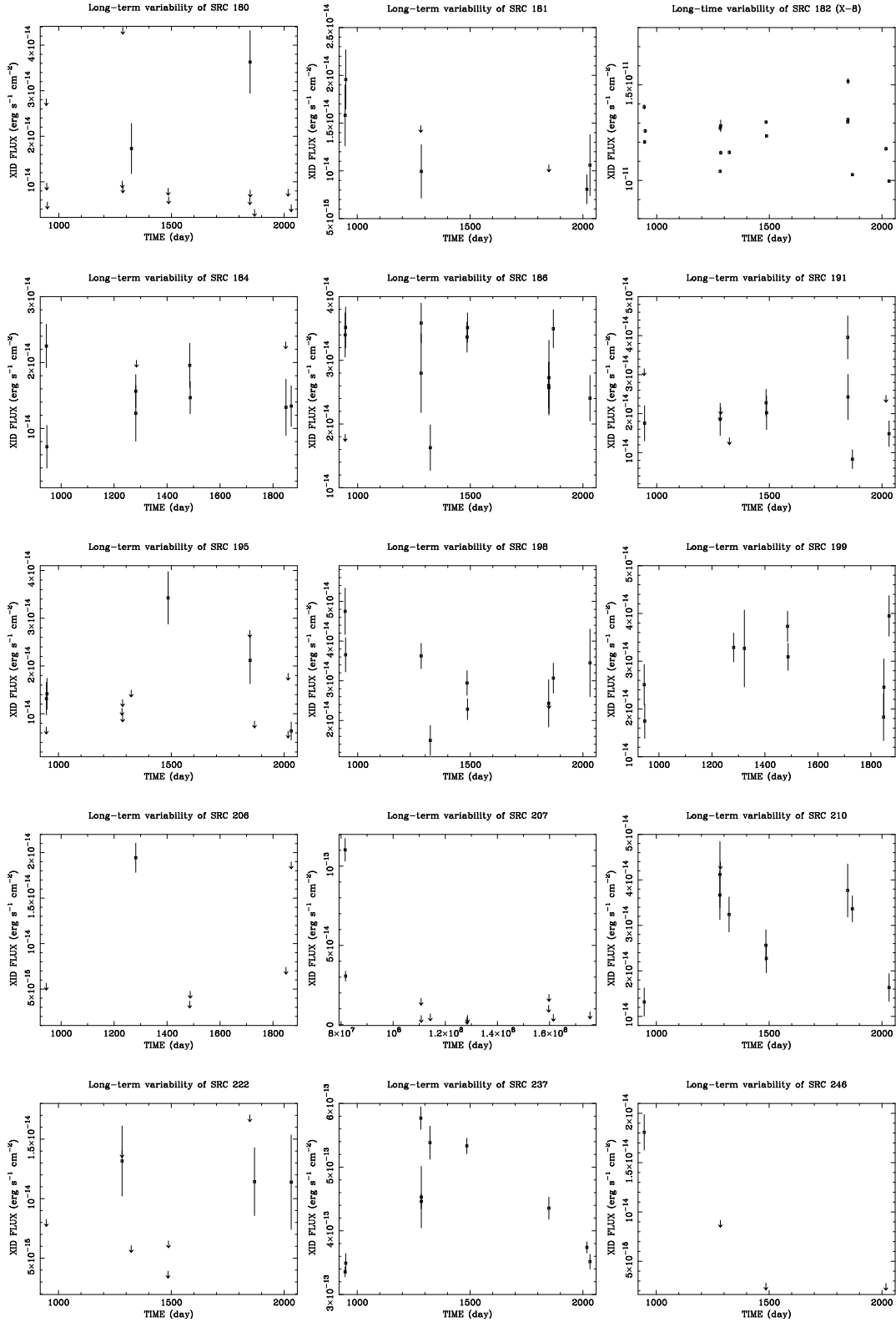


Figure B.3: The long-term X-ray light-curves of sources #180, #181, #182, #184, #186, #191, #195, #198, #199, #206, #207, #210, #222, #237, and #246. The downward arrows represent the 3σ upper limits of the XID flux. The time is given in days after JD 2450814.5.

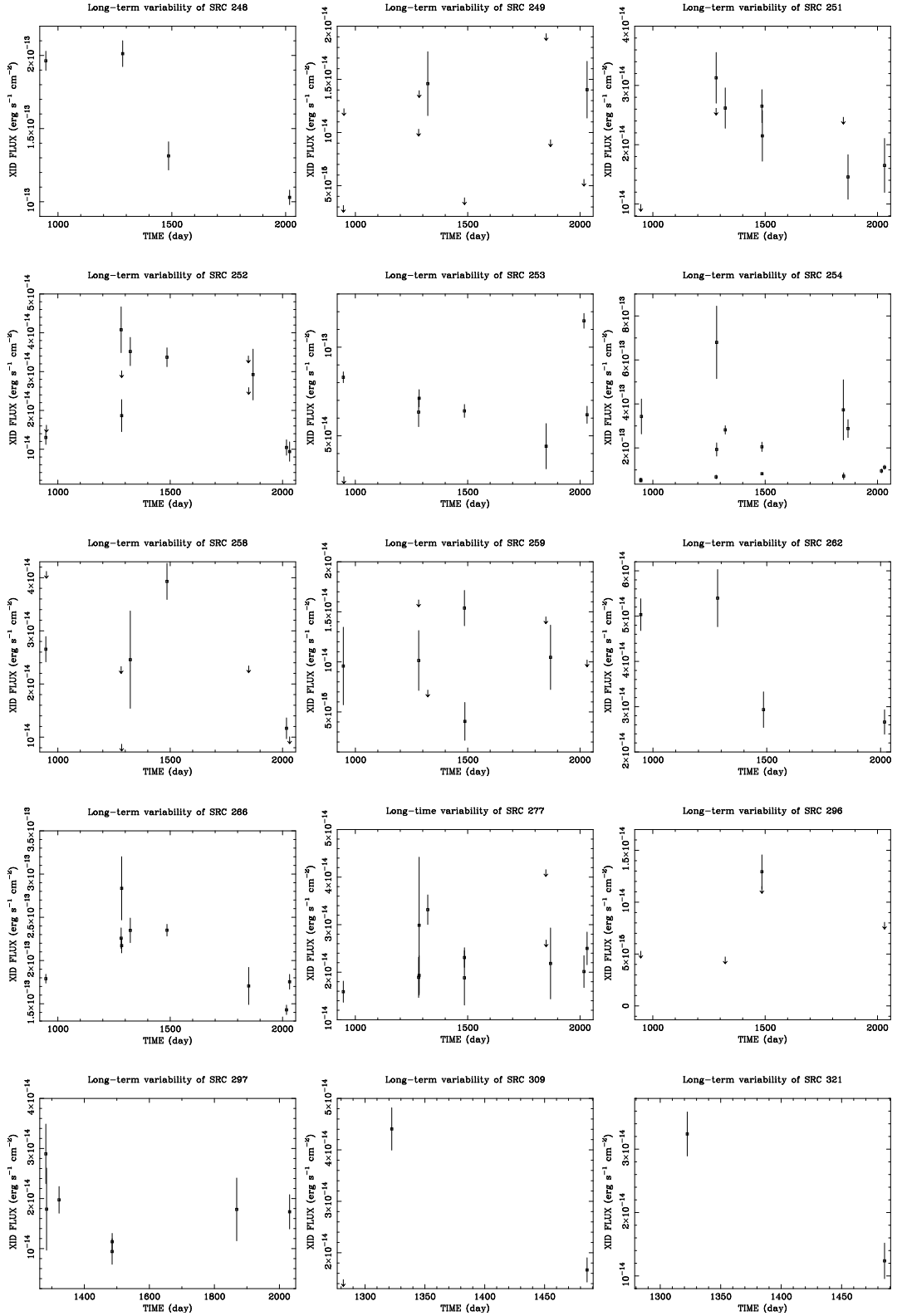


Figure B.4: The long-term X-ray light-curves of sources #248, #249, #251, #252, #253, #254, #258, #259, #262, #266, #277, #296, #297, #309, and #321. The downward arrows represent the 3σ upper limits of the XID flux. The time is given in days after JD 2450814.5.

Appendix C

Read-Me file Table 2.3

J/A+A/426/11 XMM-Newton survey of M33 (Pietsch+, 2004)

=====

XMM-Newton survey of the Local Group galaxy M 33.

Pietsch W., Misanovic Z., Haberl F., Hatzidimitriou D., Ehle M.,
Trinchieri G.

<Astron. Astrophys. 426, 11 (2004)>

=2004A&A...426...11P (SIMBAD/NED BibCode)

=====

ADC_Keywords: Galaxies, nearby ; X-ray sources

Mission_Name: XMM-Newton

Keywords: Galaxies: individual: M 33 - X-rays: galaxies

Abstract:

In an XMM-Newton raster observation of the bright Local Group spiral galaxy M 33 we study the population of X-ray sources (X-ray binaries, supernova remnants) down to a 0.2-4.5keV luminosity of 10^{35} erg/s - more than a factor of 10 deeper than earlier ROSAT observations. EPIC hardness ratios and optical and radio information are used to distinguish between different source classes. The survey detects 408 sources in an area of 0.80 square degree. We correlate these newly detected sources with earlier M 33 X-ray catalogues and information from optical, infra-red and radio wavelengths. As M 33 sources we detect 21 supernova remnants (SNR) and 23 SNR candidates, 5 super-soft sources and 2 X-ray binaries (XRBs). There are 267 sources classified as hard, which may either be XRBs or Crab-like SNRs in M 33 or background AGN. The 44 confirmed and candidate SNRs more than double the number of X-ray detected SNRs in M 33. 16 of these are proposed as SNR candidates from the X-ray data for the first time. On the other hand, there are several sources not connected to M 33: five foreground stars, 30 foreground star candidates, 12 active galactic nucleus

candidates, one background galaxy and one background galaxy candidate. Extrapolating from deep field observations we would expect 175 to 210 background sources in this field. This indicates that about half of the sources detected are within M 33.

File Summary:

FileName	Lrecl	Records	Explanations
ReadMe	80	.	This file
table3.dat	552	408	X-ray source catalogue of the XMM-Newton EPIC M 33 raster observation

See also:

J/A+A/373/438 : The X-ray view of M33 after ROSAT (Haberl+ 2001)

Byte-by-byte Description of file: table3.dat

Bytes	Format	Units	Label	Explanations
1-	3	I3	---	[PHM2004] Source Number
	5	I1	h	RAh Right Ascension J2000 (hours)
7-	8	I2	min	RAm Right Ascension J2000 (minutes)
10-	14	F5.2	s	RAs Right Ascension J2000 (seconds)
	17	A1	---	DE- Declination J2000 (sign)
18-	19	I2	deg	DEd Declination J2000 (degrees)
21-	22	I2	arcmin	DEm Declination J2000 (minutes)
24-	27	F4.1	arcsec	DEs Declination J2000 (seconds)
29-	33	F5.2	arcsec	PosErr Positional error
35-	42	E8.2	---	LH Source detection likelihood (combined EPIC)
44-	51	E8.2	ct/s	CRate Combined EPIC count rate (1)
53-	59	E7.1	ct/s	e_CRate Error in CRate
61-	68	E8.2	mW/m2	CFlux Combined EPIC flux in erg/cm2/s (1)
70-	76	E7.1	mW/m2	e_CFlux Error in CFlux
78-	82	F5.2	---	CHR1 ? Combined EPIC hardness ratio 1 (2)
84-	87	F4.2	---	e_CHR1 ? Error in CHR1
89-	93	F5.2	---	CHR2 ? Combined EPIC hardness ratio 2 (2)
95-	98	F4.2	---	e_CHR2 ? Error in CHR2
100-	104	F5.2	---	CHR3 ? Combined EPIC hardness ratio 3 (2)
106-	109	F4.2	---	e_CHR3 ? Error in CHR3
111-	115	F5.2	---	CHR4 ? Combined EPIC hardness ratio 4 (2)
117-	120	F4.2	---	e_CHR4 ? Error in CHR4

122-124	A3	---	VAL	EPIC instruments contributing to source detection (3)
126-129	F4.1	ks	PN_Expo	? Exposure of EPIC pn instrument
131-138	E8.2	---	PN_LH	? EPIC pn source detection likelihood
140-147	E8.2	ct/s	PNRate	? EPIC pn count rate (1)
149-155	E7.1	ct/s	e_PNRate	? Error in PNRate
157-164	E8.2	mW/m2	PNFlux	? EPIC pn flux in erg/cm ² /s (1)
166-172	E7.1	mW/m2	e_PNFlux	? Error in PNFlux
174-178	F5.2	---	PNHR1	? EPIC pn hardness ratio 1 (2)
180-183	F4.2	---	e_PNHR1	? Error in PNHR1
185-189	F5.2	---	PNHR2	? EPIC pn hardness ratio 2 (2)
191-194	F4.2	---	e_PNHR2	? Error in PNHR2
196-200	F5.2	---	PNHR3	? EPIC pn hardness ratio 3 (2)
202-205	F4.2	---	e_PNHR3	? Error in PNHR3
207-211	F5.2	---	PNHR4	? EPIC pn hardness ratio 4 (2)
213-216	F4.2	---	e_PNHR4	? Error in PNHR4
218-221	F4.1	ks	M1_Expo	? Exposure of EPIC MOS1 instrument
223-230	E8.2	---	M1_LH	? EPIC MOS1 source detection likelihood
232-239	E8.2	ct/s	M1Rate	? EPIC MOS1 count rate (1)
241-247	E7.1	ct/s	e_M1Rate	? Error in M1Rate
249-256	E8.2	mW/m2	M1Flux	? EPIC MOS1 flux in erg/cm ² /s (1)
258-264	E7.1	mW/m2	e_M1Flux	? Error in M1Flux
266-270	F5.2	---	M1HR1	? EPIC MOS1 hardness ratio 1 (2)
272-275	F4.2	---	e_M1HR1	? Error in M1HR1
277-281	F5.2	---	M1HR2	? EPIC MOS1 hardness ratio 2 (2)
283-286	F4.2	---	e_M1HR2	? Error in M1HR2
288-292	F5.2	---	M1HR3	? EPIC MOS1 hardness ratio 3 (2)
294-297	F4.2	---	e_M1HR3	? Error in M1HR3
299-303	F5.2	---	M1HR4	? EPIC MOS1 hardness ratio 4 (2)
305-308	F4.2	---	e_M1HR4	? Error in M1HR4
310-313	F4.1	ks	M2_Expo	? Exposure of EPIC MOS2 instrument
315-322	E8.2	---	M2_LH	? EPIC MOS2 source detection likelihood
324-331	E8.2	ct/s	M2Rate	? EPIC MOS2 count rate (1)
333-339	E7.1	ct/s	e_M2Rate	? Error in M2Rate
341-348	E8.2	mW/m2	M2Flux	? EPIC MOS2 flux in erg/cm ² /s (1)
350-356	E7.1	mW/m2	e_M2Flux	? Error in M2Flux
358-362	F5.2	---	M2HR1	? EPIC MOS2 hardness ratio 1 (2)
364-367	F4.2	---	e_M2HR1	? Error in M2HR1
369-373	F5.2	---	M2HR2	? EPIC MOS2 hardness ratio 2 (2)
375-378	F4.2	---	e_M2HR2	? Error in M2HR2
380-384	F5.2	---	M2HR3	? EPIC MOS2 hardness ratio 3 (2)
386-389	F4.2	---	e_M2HR3	? Error in M2HR3
391-395	F5.2	---	M2HR4	? EPIC MOS2 hardness ratio 4 (2)
396-399	F4.2	---	e_M2HR4	? Error in M2HR4

401-440	A40	---	XID	? X-ray identification (4)
442-453	A12	---	USNO-B1.0	? Name of brightest USNO-B1.0 (<I/284>) source within search area
455	I1	---	USNOMul	? Number of USNO-B1.0 correlations
457-459	F3.1	arcsec	USNOdis	? Distance of source USNO-B1.0
461-464	F4.1	mag	USNOB2	? B2 magnitude of source USNO-B1.0
466-469	F4.1	mag	USNOR2	? R2 magnitude of source USNO-B1.0
471-474	F4.1	mag	USNOI2	? I2 magnitude of source USNO-B1.0
476-479	F4.1	---	logfX/fo	? Logarithm of fX/fopt
481-500	A20	---	Class	? Classification of X-ray source (5)
502-551	A50	---	Remarks	? Additional remarks (6)

Note (1): Count rate and flux in XID band (0.2-4.5keV)

Note (2): $HR_i = (R(i+1) - R(i)) / (R(i+1) + R(i))$ where R_i are the count rates in the energy bands 1 to 5 and
band 1 = 0.2-0.5keV,
band 2 = 0.5-1.0keV,
band 3 = 1.0-2.0keV,
band 4 = 2.0-4.5keV,
band 5 = 4.5-12keV

Note (3): First character for EPIC PN, second for MOS1, third for MOS2;
character = T : source is in field of view of instrument
F : otherwise

Note (4): References in XID:

X-n : Long et al., 1981ApJ...246L..61L;
Trinchieri et al., 1988ApJ...329.1037T
SBn : Schulman & Bregman, 1995ApJ...441..568S
LCBn : Long et al., 1996ApJ...466..750L
DCL97: Dubus et al., 1997ApJ...490L..47D
DCL99: Dubus et al., 1999MNRAS.302..731D
HPn : Haberl & Pietsch, 2001A&A...373..438H

Note (5): Classifications used (see Table 5)

fg Star = foreground star
<fg Star> = foreground star candidate
AGN = active galactic nucleus
<AGN> = AGN candidate
GAL = galaxy
<GAL> = galaxy candidate
SSS = supersoft source in M 33
<SSS> = supersoft source candidate in M 33
SNR = supernova remnant in M 33
<SNR> = supernova remnant candidate in M 33
XRB = X-ray binary in M 33
<hard> = HR2-e_HR2>-0.2 or only HR3 and HR4 defined, and no other

classification

Note (6): References in remarks:

SIM : SIMBAD Database
NED : NASA Extragalactic Database
NVSS : Condon et al., 1998AJ....115.1693C
CS82 : Christian & Schommer, 1982ApJ...253L..13C
[MC83]25 : Massey & Conti, 1983ApJ...273..576M
IFM* : Ivanov et al., 1993ApJS...89...85I
GKLn : Gordon et al., 1998ApJS..117...89G
GDKn : Gordon et al., 1999ApJS..120..247G
IV74 : Israel & van der Kruit, 1974A&A....32..363I
VBW78 : von Kap-Herr et al., 1978A&A....62...51V
M98 : Massey, 1998ApJ...501..153M
MCM2001 : Magrini et al., 2001A&A...367..498M
MBH96 : Massey et al., 1996ApJ...469..629M
PMM2004 : Pietsch et al., 2004A&A...413..879P
GM94 : Giovagnoli & Mould, 1994PASP..106..376G
FSZ : Fabrika et al., 1997BSAO...43..133F
D33 : Macri et al., 2001AJ....121..870M;
Mochejska et al., 2001AJ....121.2032M
RW93 : Regan & Wilson, 1993AJ....105..499R
VHK : Hubble, 1926ApJ....63..236H
CGC97 : Crampton et al., 1997AJ....114.2353C
BCLMP : Boulesteix et al., 1974A&A....37...33B

Acknowledgements: Wolfgang Pietsch <wnp@mpe.mpg.de>

=====
(End)

Wolfgang Pietsch [MPE, Germany]

07-Dec-2004

Appendix D

Read-Me file Table 3.4

J/A+A/vol/page XMM-Newton Survey of M33 (Misanovic+, 2005)

=====

XMM-Newton survey of the Local Group galaxy M33 - variability of the detected sources

Misanovic Z., Pietsch W., Haberl F., Ehle M., Hatzidimitriou D.,
Trinchieri G

<Astron. Astrophys. vol, page (year)>
=2005A&A...VVV.ppppI (SIMBAD/NED BibCode)

=====

ADC_Keywords: Galaxies, nearby ; X-ray sources

Mission_Name: XMM-Newton

Keywords: Galaxies: individual: M33 - X-rays: galaxies

Abstract:

We present an analysis of the individual observations of a deep XMM-Newton survey of the Local Group spiral galaxy M\,33. We detected a total of 350 sources with fluxes (in the 0.2--4.5 keV energy band) in the range 6.7×10^{-16} - 1.5×10^{-11} erg s⁻¹. This comprehensive study considers flux variability, spectral characteristics, and classification of the detected objects. Thirty-nine objects in our catalogue are new sources, while 311 were already detected in a previous analysis of most of the same data using combined images. We present improved positions of these sources and the X-ray parameters of each source in each individual observation that covers the source. We then used these parameters to systematically search for flux variability on time scales of hours to months or years. The long-term light-curves were generated for the 61 sources showing a significant variability of the (0.2--4.5) keV flux, by a factor of

1.2 to 144. The detected variability was then used to classify 8 new X-ray binary candidates in M\,33. Together with the hardness ratio method and cross-correlation with optical, infrared, and radio data, we also classify or confirm previous classification of 25 supernova remnants and candidates, 2 X-ray binaries, and 11 super-soft source candidates (7 of which are new SSS candidates). In addition, we classify 13 active galactic nuclei and background galaxies, 6 stars, and 23 foreground star candidates in the direction of M\,33. Further 206 objects are classified as 'hard', approximately half of which are sources intrinsic to M\,33. The relative contribution of the classified XRB and SSS in M\,33 is now comparable to M\,31. The luminosity distribution of SNRs in both spiral galaxies is almost the same, although the number of the detected SNRs in M\,33 remains much higher.

File Summary:

```
-----
```

FileName	Lrecl	Records	Explanations
ReadMe	80	.	This file
table4.dat	251	350	X-ray variability of the sources detected in the XMM-Newton EPIC M33 raster observations

```
-----
```

See also:

- J/A+A/373/438 : The X-ray view of M33 after ROSAT (Haberl+ 2001)
- J/A+A/426/11 : XMM-Newton survey of the Local Group galaxy M33 (Pietsch+ 2004)

Byte-by-byte Description of file: table4.dat

```
-----
```

Bytes	Format	Units	Label	Explanations
1- 3	I3	---	SRC_ID	Source Number
5- 7	I3	---	PMH04	Source Number in J/A+A/426/11 (1)
9- 18	A10	h:m:s	RA	Right Ascension J2000 (in hours:minutes:seconds)
20- 30	A11	d:m:s	DEC	Declination J2000 (in degrees:minutes:seconds)
32- 36	F5.2	arcsec	TOTAL_POS_ERR	Positional error

```
-----
```

38- 45	F8.2	mW/m2	F_MAX	Maximum EPIC flux in erg/cm2/s (2)
47- 53	F7.1	mW/m2	eF_MAX	Error in F_MAX
55- 60	F6.2	---	V	Variability factor (3)
62- 67	F6.2	---	S	Variability significance (4)
69- 70	I2	---	V_FLAG	Variability flag (5)
72-109	A38	---	XID	X-ray identification (6)
111-122	A12	---	USNO_B1	USNO_B1 cross-correlation (<I/284>)
124-127	F4.1	---	logx_opt	Logarithm of fx/fopt
129-145	A17	---	2MASS	2MASS cross-correlation (<II/246>)
147-151	F5.2	mag	Jmag	2MASS J magnitude
153-157	F5.2	mag	Hmag	2MASS H magnitude
159-163	F5.2	mag	Kmag	2MASS K magnitude
165-178	A14	---	NVSS	NVSS cross-correlation (<VIII/65>)
180-184	F5.2	mJy	S1_4	NVSS 1.4 GHz flux
186-200	A15	---	TYPE	Classification of X-ray source (7)
202-251	A50	---	COMM	Additional comments (8)

Note (1): Source number from J/A+A/426/11 (Pietsch+ 2004)

Note (2): Maximum flux in XID band (0.2-4.5keV)

Note (3): $V = F_{MAX}/F_{MIN}$ where F_{MAX} and F_{MIN} are the maximum and minimum XID flux. If source is not detected at the minimum then F_{MIN} is determined as 3σ XID flux upper limit.

Note (4): $S = (F_{MAX} - F_{MIN}) / \sqrt{eF_{MAX} * eF_{MAX} + eF_{MIN} * eF_{MIN}}$ where eF_{MAX} and eF_{MIN} are errors in F_{MAX} and F_{MIN} .

Note (5): $V_FLAG = 1$ if F_{MIN} is a non-detection
 $V_FLAG = 0$ otherwise

Note (6): References in XID:

X-n : Long et al., 1981ApJ...246L..61L;
Trinchieri et al., 1988ApJ...329.1037T
SBn : Schulman & Bregman, 1995ApJ...441..568S
LCBn : Long et al., 1996ApJ...466..750L
DCL97: Dubus et al., 1997ApJ...490L..47D
DCL99: Dubus et al., 1999MNRAS.302..731D
HPn : Haberl & Pietsch, 2001A&A...373..438H

Note (7): Classifications used (see J/A+A/426/11 (Pietsch+ 2004))

fgStar = foreground star
<fgStar> = foreground star candidate
AGN = active galactic nucleus
<AGN> = AGN candidate
GAL = galaxy
<GAL> = galaxy candidate
SSS = supersoft source in M33
<SSS> = supersoft source candidate in M33
SNR = supernova remnant in M 33
<SNR> = supernova remnant candidate in M33
XRB = X-ray binary in M 33
<hard> = HR2-e_HR2>-0.2 or only HR3 and HR4 defined, and no other classification

Note (8): References in comm:

SIM : SIMBAD Database
NED : NASA Extragalactic Database
NVSS : Condon et al., 1998AJ...115.1693C
CS82 : Christian & Schommer, 1982ApJ...253L..13C
[MC83]25 : Massey & Conti, 1983ApJ...273..576M
IFM* : Ivanov et al., 1993ApJS...89...85I
GKLn : Gordon et al., 1998ApJS..117...89G
GDKn : Gordon et al., 1999ApJS..120..247G
TYC2293-810-1 : Hog et al., 1998A&A...335L..65H
IV74 : Israel & van der Kruit, 1974A&A....32..363I
VBW78 : von Kap-Herr et al., 1978A&A....62...51V
M98 : Massey, 1998ApJ...501..153M
MCM2001 : Magrini et al., 2001A&A...367..498M
MBH96 : Massey et al., 1996ApJ...469..629M
PMM2004 : Pietsch et al., 2004A&A...413..879P
GM94 : Giovagnoli & Mould, 1994PASP..106..376G
FS95b : Fabrika et al., 1995Ap&SS.226..229F
FSZ : Fabrika et al., 1997BSAO...43..133F
D33 : Macri et al., 2001AJ....121..870M;
Mochejska et al., 2001AJ....121.2032M
RW93 : Regan & Wilson, 1993AJ....105..499R
VHK : Hubble, 1926ApJ....63..236H
CGC97 : Crampton et al., 1997AJ....114.2353C
BCLMP : Boulesteix et al., 1974A&A....37...33B

Acknowledgements: Zdenka Misanovic <zdenka@mpe.mpg.de>

======(End)

1998A&A . . . 335L . . 65H,

Appendix E

Read-Me file Table 3.5

J/A+A/vol/page XMM-Newton Survey of M33 (Misanovic+, 2005)

=====

XMM-Newton survey of the Local Group galaxy M33 - variability of the detected sources

Misanovic Z., Pietsch W., Haberl F., Ehle M., Hatzidimitriou D.,
Trinchieri G

<Astron. Astrophys. vol, page (year)>
=2005A&A...VVV.ppppI (SIMBAD/NED BibCode)

=====

ADC_Keywords: Galaxies, nearby ; X-ray sources

Mission_Name: XMM-Newton

Keywords: Galaxies: individual: M33 - X-rays: galaxies

Abstract:

We present an analysis of the individual observations of a deep XMM-Newton survey of the Local Group spiral galaxy M\,33. We detected a total of 350 sources with fluxes (in the 0.2--4.5 keV energy band) in the range 6.7×10^{-16} - 1.5×10^{-11} erg s⁻¹. This comprehensive study considers flux variability, spectral characteristics, and classification of the detected objects. Thirty-nine objects in our catalogue are new sources, while 311 were already detected in a previous analysis of most of the same data using combined images. We present improved positions of these sources and the X-ray parameters of each source in each individual observation that covers the source. We then used these parameters to systematically search for flux variability on time scales of hours to months or years. The long-term light-curves were generated for the 61 sources showing a

significant variability of the (0.2--4.5) keV flux, by a factor of 1.2 to 144. The detected variability was then used to classify 8 new X-ray binary candidates in M\,33. Together with the hardness ratio method and cross-correlation with optical, infrared, and radio data, we also classify or confirm previous classification of 25 supernova remnants and candidates, 2 X-ray binaries, and 11 super-soft source candidates (7 of which are new SSS candidates). In addition, we classify 13 active galactic nuclei and background galaxies, 6 stars, and 23 foreground star candidates in the direction of M\,33. Further 206 objects are classified as 'hard', approximately half of which are sources intrinsic to M\,33. The relative contribution of the classified XRB and SSS in M\,33 is now comparable to M\,31. The luminosity distribution of SNRs in both spiral galaxies is almost the same, although the number of the detected SNRs in M\,33 remains much higher.

File Summary:

FileName	Lrecl	Records	Explanations
ReadMe	80	.	This file
table5.dat	374	2658	X-ray source catalogue of the individual XMM-Newton EPIC M33 raster observations

See also:

- J/A+A/373/438 : The X-ray view of M33 after ROSAT (Haberl+ 2001)
- J/A+A/426/11 : XMM-Newton survey of the Local Group galaxy M33 (Pietsch+ 2004)

Byte-by-byte Description of file: table5.dat

Bytes	Format	Units	Label	Explanations
1- 3	I3	---	SRC_ID	Source Number
5- 11	A7	---	OBS	Observation
13- 20	E8.2	---	DET_ML	Source detection likelihood (combined EPIC)
22- 29	E8.2	ct/s	XID_RATE	Combined EPIC count rate (1)
31- 37	E7.1	ct/s	eXID_RATE	Error in XID_RATE

39- 46	E8.2	mW/m2	XID_FLUX	Combined EPIC flux in erg/cm2/s (1)
48- 54	E7.1	mW/m2	eXID_FLUX	Error in XID_FLUX
56- 60	F5.2	---	HR1	Combined EPIC hardness ratio 1 (2)
62- 65	F4.2	---	eHR1	Error in HR1
67- 71	F5.2	---	HR2	Combined EPIC hardness ratio 2 (2)
73- 76	F4.2	---	eHR2	Error in HR2
78- 82	F5.2	---	HR3	Combined EPIC hardness ratio 3 (2)
84- 87	F4.2	---	eHR3	Error in HR3
89- 93	F5.2	---	HR4	Combined EPIC hardness ratio 4 (2)
95- 98	F4.2	---	eHR4	Error in HR4
100-103	F4.1	ks	pn_EXP_MAP	Exposure of EPIC pn instrument
105-112	E8.2	---	pn_DET_ML	EPIC pn source detection likelihood
114-121	E8.2	ct/s	pn_XID_RATE	EPIC pn count rate (1)
123-129	E7.1	ct/s	pn_XID_RATE_ERR	Error in pn_XID_RATE
131-138	E8.2	mW/m2	pn_XID_FLUX	EPIC pn flux in erg/cm2/s (1)
140-146	E7.1	mW/m2	pn_XID_FLUX_ERR	Error in pn_XID_FLUX
148-152	F5.2	---	pn_HR1	EPIC pn hardness ratio 1 (2)
154-157	F4.2	---	pn_HR1_ERR	Error in pn_HR1
159-163	F5.2	---	pn_HR2	EPIC pn hardness ratio 2 (2)
165-168	F4.2	---	pn_HR2_ERR	Error in pn_HR2
170-174	F5.2	---	pn_HR3	EPIC pn hardness ratio 3 (2)
176-179	F4.2	---	pn_HR3_ERR	Error in pn_HR3
181-185	F5.2	---	pn_HR4	EPIC pn hardness ratio 4 (2)
187-190	F4.2	---	pn_HR4_ERR	Error in pn_HR4
197-204	E8.2	---	m1_DET_ML	EPIC MOS1 source detection likelihood
206-213	E8.2	ct/s	m1_XID_RATE	EPIC MOS1 count rate (1)
215-221	E7.1	ct/s	m1_XID_RATE_ERR	Error in m1_XID_RATE
223-230	E8.2	mW/m2	m1_XID_FLUX	EPIC MOS1 flux in erg/cm2/s (1)
232-238	E7.1	mW/m2	m1_XID_FLUX_ERR	Error in m1_XID_FLUX
240-244	F5.2	---	m1_HR1	EPIC MOS1 hardness ratio 1 (2)
246-249	F4.2	---	m1_HR1_ERR	Error in m1_HR1
251-255	F5.2	---	m1_HR2	EPIC MOS1 hardness ratio 2 (2)
257-260	F4.2	---	m1_HR2_ERR	Error in m1_HR2
262-266	F5.2	---	m1_HR3	EPIC MOS1 hardness ratio 3 (2)
268-271	F4.2	---	m1_HR3_ERR	Error in m1_HR3
273-277	F5.2	---	m1_HR4	EPIC MOS1 hardness ratio 4 (2)
279-282	F4.2	---	m1_HR4_ERR	Error in m1_HR4
284-287	F4.1	ks	m2_EXP_MAP	Exposure of EPIC MOS2 instrument
289-296	E8.2	---	m2_DET_ML	EPIC MOS2 source detection likelihood
298-305	E8.2	ct/s	m2_XID_RATE	EPIC MOS2 count rate (1)
307-313	E7.1	ct/s	m2_XID_RATE_ERR	Error in m2_XID_RATE
315-322	E8.2	mW/m2	m2_XID_FLUX	EPIC MOS2 flux in erg/cm2/s (1)
324-330	E7.1	mW/m2	m2_XID_FLUX_ERR	Error in m2_XID_FLUX
332-336	F5.2	---	m2_HR1	EPIC MOS2 hardness ratio 1 (2)

338-341	F4.2	---	m2_HR1_ERR	Error in m2_HR1
343-347	F5.2	---	m2_HR2	EPIC MOS2 hardness ratio 2 (2)
349-352	F4.2	---	m2_HR2_ERR	Error in m2_HR2
354-358	F5.2	---	m2_HR3	EPIC MOS2 hardness ratio 3 (2)
360-363	F4.2	---	m2_HR3_ERR	Error in m2_HR3
365-369	F5.2	---	m2_HR4	EPIC MOS2 hardness ratio 4 (2)
371-374	F4.2	---	m2_HR4_ERR	Error in m2_HR4

 Note (1): Count rate and flux in XID band (0.2-4.5keV)

Note (2): $HR_i = (R(i+1) - R(i)) / (R(i+1) + R(i))$ where R_i are the count rates in the
 energy bands 1 to 5 and
 band 1 = 0.2-0.5keV,
 band 2 = 0.5-1.0keV,
 band 3 = 1.0-2.0keV,
 band 4 = 2.0-4.5keV,
 band 5 = 4.5-12keV

 Acknowledgements: Zdenka Misanovic <zdenka@mpe.mpg.de>

======(End)

Curriculum Vitae

- Name: Zdenka Misanovic
- Current address: Max-Planck-Institut für extraterrestrische Physik
Giessenbach Strasse 1, D-85741, Garching, Germany
- E-mail: zdenka@mpe.mpg.de

Education

- 1996–1998 University of Sydney, Sydney, Australia
School of Physics, Department of Astrophysics
Bachelor of Science (with Honours)
- 1999–2001 University of Sydney, Sydney, Australia
School of Physics, Department of Astrophysics
Master of Science (by research)
MSc thesis topic: “A search for young supernova remnants”
- 2002–2006 Ludwig-Maximilians-Universität, München, Germany
Department of Physics
International Max Planck Research School on Astrophysics (IMPRS) at
Max-Planck-Institut für extraterrestrische Physik
PhD on Astrophysics
PhD thesis topic: “Classification of the X-ray source population
in the M33 field”